

Modelling and Characterization of Laterally-Coupled Distributed Feedback Laser and Semiconductor Optical Amplifier

By

Julie Efiok Nkanta

Thesis submitted to the
Faculty of Graduate and Postdoctoral Studies in partial fulfillment of the
requirements for the **Doctor of Philosophy degree in Physics**

Department of Physics
Ottawa-Carleton Institute of Physics
University of Ottawa
Ottawa, Canada

©Julie Efiok Nkanta, Ottawa, Canada, 2016

Abstract

There is an increasing need for tuneable spectrally pure semiconductor laser sources as well as broadband and polarization insensitive semiconductor optical amplifiers based on the InGaAsP/InP material system, to be monolithically integrated with other active and passive components in a photonic integrated circuit. This thesis aims to contribute to finding a solution through modelling, experimental characterization and design improvements.

In this thesis we have analyzed laterally-coupled distributed feedback (LC-DFB) lasers. These lasers have the gratings etched directly out of the ridge sidewalls thus lowering the cost associated with the re-growth process required if the gratings were otherwise embedded above the active region. The performance characteristics are analyzed for the LC-DFB lasers partitioned into 1-, 2-, and 3-, electrodes with individual bias control at various operating temperatures. The laser exhibits a stable single mode emission at 1560 nm with a current tuning rate of ~ 14 pm/mA for a tuning of 2.25 nm. The side modes are highly suppressed with a maximum side-mode suppression ratio of 58 dB. The light-current characteristics show a minimum 40 mA threshold current, and power saturation occurring at higher injection currents. The linewidth characteristics show a minimum Lorentzian linewidth of 210 kHz under free-running and further linewidth reduction under feedback operation. The multi-electrode LC-DFB laser devices under appropriate and selective driving conditions exhibit a flat frequency modulation response from 0 to above 300 MHz. The multi-electrode configuration can thus be further exploited for certain requirements. Simulation results and design improvements are also presented.

The experimental characterization of semiconductor optical amplifier (SOA) and Fabry-Perot (FP) laser operating in the E-band are also presented. For the SOA, the linear vertical and horizontal states of polarization corresponding to the transverse electric (TE) and transverse magnetic (TM) modes were considered. For various input power and bias, performance characteristics shows a peak gain of 21 dBm at 1360 nm, gain bandwidth of 60 nm and polarization sensitivity of under 3 dB obtained for the entire wavelength range

analyzed from 1340 to 1440 nm. The analysis presented in this thesis show good results with room for improvement in future designs.

...to my son Akwa, and all the single mothers going to school

Acknowledgments

I am very grateful to my supervisor Prof. Trevor J. Hall for the opportunity to do my research in the field of photonics, also for his support and understanding throughout the course of my studies. I am also grateful to Prof. Karin Hinzer for her enthusiasm and support.

This thesis research was carried out at the Photonics Technology Laboratory (PTLab), Center for Research in Photonics, at the University of Ottawa, Canada. My appreciation goes to Dr Ramon Maldonado-Basilio for his research support and advice and to my other colleagues in PTLab for their friendly chat and support. My appreciation goes to Teraxion Inc especially Simon Ayotte and Maryse Aube, for allowing the frequency modulation experiment/analysis to be carried out in their facilities. I acknowledge the support in part of this research work by Natural Sciences and Research Council of Canada, CMC Microsystems, Teraxion Inc and Enablence.

My gratitude goes to my immediate and extended family all the way in Nigeria, especially my dear mother, Lady Margaret Nkanta and my siblings, Mary, Francis, Maureen and their families for their unwavering love, support and encouragement. To my good friends, especially Ofonmbuk, Minaso and their families for their kind support.

Most importantly, during the first year my PhD studies I had been blessed to have become a mother, my son has been my motivation and a happy distraction. Especially this past year he has been such a good sport and well-behaved while following me to my ‘workplace’ on weekends so I can write up this thesis. I am very grateful to the City of Ottawa for providing subsidized daycare space for my child so I can go to school. I am also grateful to the YMCA/YWCA Ottawa for the same reason.

Table of Content

<i>Abstract</i>	<i>II</i>
<i>Acknowledgments</i>	<i>V</i>
<i>Table of Content</i>	<i>VI</i>
<i>List of Figures</i>	<i>IX</i>
<i>List of Tables</i>	<i>XVII</i>
<i>Acronyms</i>	<i>XVIII</i>
<i>List of Related Publications</i>	<i>XXI</i>
Chapter 1 Introduction	1
1.1 Objective	1
1.2 Thesis Overview	2
1.2.1 Laterally-coupled distributed feedback laser	2
1.2.2 Semiconductor Optical Amplifiers	3
1.2.3 Thesis outline	4
1.2.4 Thesis original contributions.....	7
Chapter 2 III-V Semiconductor Properties Modelling and Simulation	9
2.1 Introduction	9
2.2 Crystal Structure and Electronic Energy Band Gap	10
2.3 Carrier Concentrations	12
2.3.1 Intrinsic Carrier Concentrations.....	13
2.3.2 Extrinsic Carrier Concentrations.....	16
2.4 Carrier Transport	18
2.4.1 Maxwell Equation and Continuity Equation.....	19
2.4.2 Drift and Diffusion.....	21
2.5 Carrier Recombination and Generation Mechanisms	22
2.5.1 Radiative recombination	23
2.5.2 Shockley-Read-Hall recombination.....	24
2.5.3 Auger recombination	25
2.6 Heterostructures and Quantum Confinement	26
2.6.1 Energy Eigenvalues and Density of states	26
2.6.2 Quantum Well Structure	28
2.6.3 Strain in Quantum Wells.....	30
2.6.4 InGaAsP/InP Band Gap Engineering.....	31
2.7 Simulation of InGaAsP/InP multi-quantum well Laser	35
2.7.1 Band structure and the quantum well wavefunction.....	38
2.7.2 Carrier densities	41

2.7.3 Optical mode and photon density	44
2.7.4 Gain and loss.....	45
2.7.5 Optical power and heat flow	47
2.8 Summary.....	50
Chapter 3 <i>Laterally-Coupled Distributed Feedback Laser</i>.....	52
3.1 Introduction.....	52
3.2 Bragg Grating and Couple Wave Equations.....	52
3.3 LC-DFB Laser Simulations.....	55
3.3.1 Grating design.....	55
3.3.2 Grating Simulation.....	58
3.3.3 Time-Domain Travelling Wave Model	66
3.4 Design Considerations for the Quantum Dot LC-DFB laser	76
3.4.1 Epitaxial Design.....	78
3.4.2 Mask Layout	82
3.4.3 Fabrication	86
3.5 Summary.....	88
Chapter 4 <i>Quantum Well Distributed Feedback Laser Characterization</i>.....	90
4.1 Introduction.....	90
4.2 Laser Device	91
4.3 Experimental Set-up	99
4.4 Light-Current.....	101
4.5 Optical Spectra.....	110
4.6 Side Mode Suppression Ratio	113
4.7 Linewidth Characterization.....	115
4.7.1 Measurement Technique	116
4.7.2 Linewidth in free-running.....	118
4.7.3 Linewidth in optical feedback.....	120
4.8 Frequency Modulation Response and Relative Intensity Noise	121
4.8.1 Measurement Technique	122
4.8.2 Frequency Modulation Response.....	123
4.8.3 Relative Intensity Noise.....	128
4.9 Summary.....	130
Chapter 5 <i>Semiconductor Optical Amplifier and Fabry-Perot Laser</i>	134
5.1 Introduction.....	134
5.2 SOA vs other Optical Amplifiers.....	134
5.3 Motivation of Research.....	135
5.4 SOA Device Structure.....	138

5.5	Fabry-Perot Laser Characterization.....	142
5.5.1	Experimental Set-up.....	143
5.5.2	Light-Current	144
5.5.3	Slope and Quantum Efficiencies.....	151
5.5.4	Optical Spectra.....	157
5.5.5	Optical Gain and Loss.....	162
5.6	SOA Characterization Parameters	166
5.6.1	Experimental Set-up.....	167
5.6.2	Amplified Spontaneous Emission.....	168
5.6.3	Optical Spectrum	170
5.6.4	Gain and Polarization Insensitivity	170
5.6.5	Saturation Output Power.....	175
5.6.6	Signal-to-Noise ratio and Noise Figure	177
5.7	Summary.....	179
<i>Chapter 6</i>	<i>Conclusions and Future Work</i>	<i>183</i>
6.1	Introduction.....	183
6.2	Summary.....	183
6.3	Recommendation and Future Work	189
<i>Appendix A:</i>	<i>Laser Design Variation Table.....</i>	<i>193</i>
<i>References</i>	<i>.....</i>	<i>197</i>

List of Figures

Figure 1-1. Schematic of the multi-electrode LC-DFB laser. SCH: separate confinement heterostructure	3
Figure 1-2. Cross-section schematic of the SOA: AMQW: asymmetric multi-quantum well, SCH: separate confinement heterostructure.	4
Figure 2-1. Band Structure of a semiconductor from k.p method in Kane’s model	12
Figure 2-2. The energy bands, density of states, Fermi distribution function and the carrier concentrations as a function of energy.	14
Figure 2-3. Energy band diagram showing the ionization process	16
Figure 2-4. Photon absorption and generation through radiative (band-to-band) recombination	23
Figure 2-5. Shockley-Read-Hall recombination	24
Figure 2-6. Auger recombination.....	25
Figure 2-7. Schematic of a single quantum well and its transition energies.....	29
Figure 2-8. Conduction and valence band edges for semiconductors under compressive strain, no strain and tensile strain.....	30
Figure 2-9. Schematic representation of an InGaAsP MQW SCH.....	32
Figure 2-10 Refractive index variation of InGaAsP as a function of wavelength for different y values	38
Figure 2-11 The conduction band, valence band and the Fermi levels at threshold.....	39
Figure 2-12 The conduction band, valence band and the Fermi levels within the quantum well region.	40
Figure 2-13 Electron well potential and the wavefunction of the lowest energy electron state in the 6 QWs	40
Figure 2-14 Heavy and light hole in the 6 QWs	41
Figure 2-15 The net recombination rates for the 6 QWs at threshold. Stimulated (red), spontaneous (blue), Auger (green), SRH (very negligible).	42
Figure 2-16 Comparison of the various recombination rates within the laser as a function of applied bias	42

Figure 2-17 Electrons (blue) and holes (green) carrier density in the QWs	43
Figure 2-18 Electrons (blue) and holes (green) current density	43
Figure 2-19 The vertical profile of the fundamental optical mode	44
Figure 2-20 The vertical profile of the optical mode	45
Figure 2-21 Longitudinal profiles photon density versus (a) electron density (b) hole density in the z-direction.....	45
Figure 2-22 Gain as a function of bias current	46
Figure 2-23 Free carrier loss as a function of bias current	46
Figure 2-24 Gain spectra at different current densities.....	47
Figure 2-25 Broadened gain and Spontaneous recombination spectrum vs wavelength..	47
Figure 2-26 Photon Energy vs wavelength.....	48
Figure 2-27 Comparison of the various power dissipation mechanisms	48
Figure 2-28 Heat sources from joule effect, non-radiative and free career absorption	49
Figure 2-29 Thermal characteristics	49
Figure 3-1. Schematic representation of the grating parameters	56
Figure 3-2. Reflection and transmission spectrum for different number of grating periods in the laser longitudinal direction	57
Figure 3-3. Schematic of the QW LC-DFB laser	58
Figure 3-4. Mode profile of the transverse cross-section for the wide ridge.....	60
Figure 3-5. Mode profile of the transverse cross-section for the narrow ridge	60
Figure 3-6. Farfield mode profile of the 3 μm ridge width laser structure	61
Figure 3-7. Farfield mode profile of the 1.5 μm ridge width laser structure	62
Figure 3-8. Top view of the light propagation through the grating for (a) one period, (b) 10 periods, and (c) 100 periods.....	63
Figure 3-9. Forward mode power in the longitudinal direction of the laser device.....	64
Figure 3-10. Total energy density along the laser device	64

Figure 3-11. Loss and power diagnostics in the laser cavity	65
Figure 3-12. Gain spectra (imported data is green and fitted is blue).....	69
Figure 3-13. Maximum gain vs carrier density. Imported (green) and fitted (blue).....	70
Figure 3-14. Peak wavelength vs carrier density. Imported (green) and fitted (blue).....	70
Figure 3-15 Light-current characteristic	71
Figure 3-16 Output power in the time domain at constant current injection of 50mA.....	72
Figure 3-17 Intensity spectra of the laser.....	72
Figure 3-18 Time evolving spectra of the laser	73
Figure 3-19 Longitudinal profile of the total optical power (blue), forward (red) and backward (green).	74
Figure 3-20 Longitudinal spatial profile of the carrier density.....	74
Figure 3-21 Longitudinal spatial profile of the current density.....	75
Figure 3-22 Longitudinal profile of the material gain	75
Figure 3-23 Lateral profile of the carrier density.....	76
Figure 3-24 Lateral profile of the current density.....	76
Figure 3-25. Schematic of 5 layers of InAs QDs.....	78
Figure 3-26. Typical quantum dot laser wafer PL map	79
Figure 3-27. Schematic of the QD LC-DFB laser	80
Figure 3-28. Mode profile of the transverse cross-section of the laser.....	82
Figure 3-29. DFB laser PCell with the rectangular grating indicating details for the lithography process	85
Figure 3-30. Layout of the mask on DW-2000 with colour coded regions to indicate the 4 different design variations	86
Figure 3-31. LC-DFB laser fabrication process: (1) Growth of epitaxial layers, (2) patterning of the gratings, (3) dielectric deposition and via etching, and (4) top and bottom metal contact deposition.	88
Figure 4-1. Schematic of the LC-DFB laser in different electrode configurations	91

Figure 4-2. Single point PL at the center of a wafer	94
Figure 4-3. Photoluminescence mapping of the six fabricated wafers	95
Figure 4-4. SEM slanted view images of the 3 rd order rectangular gratings showing the shape of the grating.....	96
Figure 4-5. SEM top view images of the rectangular gratings showing the 1(narrow), 2 (wide) ridge widths dimensions	97
Figure 4-6. Side view of the rectangular gratings showing the surface tilt	98
Figure 4-7 Microscope top view images of the fabricated laser devices on 2 bars, from the top L21-L40 (1500 μm), L41-L60 (1250 μm).....	98
Figure 4-8. Experimental stage set up showing the laser device with probe pins for current injection	100
Figure 4-9. Schematic of the experimental setup.....	101
Figure 4-10. L-I-V characteristic of (a) Single electrode 1500 μm LC-DFB laser device (b)1-, and 2-electrode 1500 μm LC-DFB laser device	102
Figure 4-11. L-I characteristic for 2-electrode 1500 μm LC-DFB laser device. (a) varying electrode1, and electrode2 fixed at 100 mA (b) varying electrode2, and electrode1 fixed at 100 mA	103
Figure 4-12. L-I characteristic for 2-electrode 750 μm LC-DFB laser device (a) varying electrode1, electrode2 is fixed at 30 mA, 40 mA, 50 mA and 60 mA (b) varying electrode2, electrode1 is fixed at 30 mA, 40 mA, 50 mA and 60 mA.....	104
Figure 4-13. L-I characteristic for 3-electrode 1500 μm LC-DFB laser device	105
Figure 4-14. L-I characteristic plot for varying temperature for the 2-electrode LC-DFB laser device	108
Figure 4-15. Threshold current as a function of temperature	109
Figure 4-16. IV plot as a function of (a) first electrode (b) second electrode.....	109
Figure 4-17. Output spectra of the 2-electrode 750 μm laser device at 30/30 mA bias .	111
Figure 4-18. Output spectra of the 2-electrode 750 μm laser device at various uniform current injection	111
Figure 4-19. Output spectra of the 2-electrode 750 μm laser device at 50/50 mA bias at different temperatures	112
Figure 4-20. Peak wavelength as a function of uniform current injection.....	113

Figure 4-21. SMSR as a function of temperature for the 2-electrode 750 μm laser device for various bias currents.....	114
Figure 4-22. SMSR as a function of current for the 2-electrode 750 μm laser device at various operating temperatures.....	115
Figure 4-23. Schematic of the experimental setup for delayed Self-heterodyne interferometric technique for measuring the linewidth. AOM: acoustic-optic modulator, PC: polarization controller, PD: photodiode, ESA: electrical spectrum analyzer, OSA: optical spectrum analyzer.....	117
Figure 4-24: Schematic of the experimental setup for optical feedback operation. VOA: variable optical attenuator, AOM: acousto-optic modulator, PC: polarization controller, PD: photodiode, ESA: electrical spectrum analyzer, OSA: optical spectrum analyzer	118
Figure 4-25. Measured RF beat note spectrum of the 2-electrode 750 μm laser device at 50/50 mA bias under free-running.....	119
Figure 4-26. Linewidth variation at symmetric bias control under free-running for various operating temperatures 25°C, 35°C, 45°C, and 55°C. I_T is the total current.....	120
Figure 4-27. Linewidth variations at symmetric bias control under optical feedback for various feedback powers -5, -10, -15 and -20 dB. I_T is the total current.....	121
Figure 4-28. A 3-electrode laser device mounted on a printing circuit board with 3 wire bonded electrodes	122
Figure 4-29. Schematic of the experimental setup.....	123
Figure 4-30. Light-current in the single electrode 1500 μm LC-DFB laser. Green-color rectangular boxes indicate regions with flat FM response. Inset plot shows the wavelength tuning range.....	124
Figure 4-31. Flat FM response map for the 2-electrode 1500 μm laser device with varying current injection.....	125
Figure 4-32. Flat FM response map for the 3-electrode L29 1500 μm laser device with varying current injection and under different operation temperatures.....	126
Figure 4-33. Frequency modulation response measured in the four tested multi-electrode MQW LC-DFB lasers.....	127
Figure 4-34. Phase modulation response measured in the four tested multi-electrode MQW LC-DFB lasers.....	127
Figure 4-35. PSD of the frequency noise measured in the 1-, 2- and 3-electrode laser devices of same 1500 μm cavity lengths and 750 μm (L62).....	128

Figure 4-36. RIN measured in the 2- and 3-electrode MQW LC-DFB lasers devices of same 1500 μm cavity length	129
Figure 5-1. Optical amplifier to extend reach of a network and/or add more users	136
Figure 5-2. Optical amplifier to improve quality of service (QoS)	136
Figure 5-3. Attenuation/Dispersion in low water peak fiber in E-band wavelength regime ¹⁰¹	137
Figure 5-4. Cross-section diagram of the asymmetric MQW SOA. SCH is the separate confinement heterostructure	138
Figure 5-5. Mask layout of the SOAs and FP lasers.....	140
Figure 5-6. Photoluminescence for SOA from wafer surface.....	140
Figure 5-7. Calculated reflectance at the 7° incidence angle.....	142
Figure 5-8. Schematic of the experimental setup.....	144
Figure 5-9. LI characteristic plots with varying ridge widths (RW) for (a) 600 μm (b) 900 μm (c) 1200 μm and (d) 1500 μm cavity lengths respectively.....	146
Figure 5-10. VI characteristic plots with varying ridge widths (RW) for (a) 600 μm (b) 900 μm (c) 1200 μm and (d) 1500 μm cavity lengths respectively.....	147
Figure 5-11. Maximum output power vs cavity length of the laser.....	148
Figure 5-12. Threshold current vs cavity length of the laser devices.	149
Figure 5-13. Threshold current density versus the reciprocal cavity length.....	151
Figure 5-14. The slope efficiency and external quantum vs of cavity length for the 2 μm ridge width laser devices.....	154
Figure 5-15. The slope efficiency and external quantum vs of cavity length for the 4 μm ridge width laser devices.....	154
Figure 5-16. The reciprocal of external quantum efficiency as a function of cavity length for the 2.0 μm ridge width laser devices.....	156
Figure 5-17. Optical emission spectra for the 600 μm long laser with (a)2 μm (b)4 μm (c)6 μm and (d)8 μm ridge widths respectively.....	158
Figure 5-18. Optical emission spectra for the 900 μm long laser with (a)2 μm (b)4 μm and (c)6 μm ridge widths respectively.....	159

Figure 5-19. Optical emission spectra for the 1200 μm long laser with (a)2 μm (b)4 μm (c)6 μm and (d)8 μm ridge widths respectively.....	160
Figure 5-20. Optical emission spectra for the 1500 μm long laser with (a)2 μm and (b)4 μm ridge widths	160
Figure 5-21. Peak wavelength as a function of the injection current for the 2 x 900 μm laser device	161
Figure 5-22. Net peak gain vs wavelength for the 2 x 900 μm laser device.....	162
Figure 5-23. The Fabry-Perot resonance of the spontaneous emission from the 2 x 900 μm laser device. Biased at 50mA	165
Figure 5-24. Schematic representation of the experimental setup.....	167
Figure 5-25. Experimental setup.....	168
Figure 5-26. Epitaxial structure of the $\text{In}_{1-x}\text{Ga}_x\text{As}_y\text{P}_{1-y}/\text{InP}$ SOA device	168
Figure 5-27. Amplified spontaneous emission collected at the output facet of the SOA for various bias currents	169
Figure 5-28. Output spectra for different input wavelengths with a linear vertical polarization and power of -10 dBm	170
Figure 5-29. Single-pass (chip) gain versus wavelength for an input power of -20 dBm @ 150mA. For as-cleaved facets.....	172
Figure 5-30. Chip gain versus wavelength for an input power of -20 dBm. For AR coated facets	173
Figure 5-31. Chip gain and noise figure versus wavelength for an input power of -10 dBm. For AR coated facets.....	173
Figure 5-32. Polarization sensitivity of the chip gain for input powers of -10 and -20 dBm at bias currents of 150 and 200 mA.	174
Figure 5-33. Single pass (chip) gain versus optical input power at 1360 nm. Bias current is set at 150 mA. For as-cleaved facets.....	176
Figure 5-34. Chip gain versus output power for TE and TM polarizations at 1360 nm. Bias currents set at 150 and 200 mA. For AR coated facets	176
Figure 5-35. Signal-to-noise ratio vs wavelength for the different currents and input powers combinations for TE and TM polarizations	177
Figure 5-36. Noise figure versus wavelength for input power of -10 dBm.....	178

Figure 5-37. Noise figure versus wavelength for input power of -20 dBm 178

Figure 6-1 Light propagation through an apodized sampled grating..... 190

Figure 6-2 Mode profile of a potential hybrid III-V/ silicon laser..... 191

List of Tables

Table 2-1. Quantum structures and confinement with associated energy and density of states.....	28
Table 2-2 Material parameters for some III-V binary compounds.	34
Table 2-3. Epitaxial layer composition of the laser	37
Table 2-4. Composition of some InGaAsP material layers	38
Table 3-1. Mode properties of the fundamental mode.....	61
Table 3-2. Material composition of the laser	81
Table 3-3. QD LC-DFB laser design variations with laser device labels	83
Table 3-4. Some mask layer definitions for the lithography process of the QD LC-DFB laser	84
Table 4-1. Material composition of the laser	92
Table 4-2. LC-DFB grating design variations	93
Table 4-3. Wavelength and temperature tuning as a function of bias current	113
Table 4-4. Current injection for a achieving a flat FM response in the laser devices	126
Table 5-1. Description of the SOA composition	139
Table 5-2. Cleaved SOA and FP laser devices on bars.....	141
Table 5-3. Laser devices dimension with their corresponding threshold current/density.	150
Table 5-4. The calculated slope and external quantum efficiencies	153
Table 5-5. Peak Wavelength and peak intensity with varying current for the 2 x 900 μm laser device	161
Table 5-6. Polarization sensitivity bandwidth	175
Table 6-1: Mode properties.....	191

Acronyms

1D	One dimensional
2D	Two dimensional
3D	Three dimensional
AMQW	Asymmetric multi-quantum well
AOM	Acousto-optic modulator
AR	Anti-reflection
ARC	Anti-reflection coating
ASE	Amplified spontaneous emission
CL	Cavity length
CPFC	Canadian Photonics Fabrication Center
C.S	Compressive strain
CW	Continuous wave
DC	Direct current
DFB	Distributed feedback
DSHI	Delayed self-heterodyne interferometer
DUT	Device under test
DWDM	Dense wavelength division multiplex
EDFA	Erbium doped fiber amplifier
EME	Eigenmode expansion method
ESA	Electrical spectrum analyzer
FM	Frequency response
FP	Fabry-Perot
FWHM	Full wave at half maximum
HH	Heavy hole
InGaAsP	Indium gallium arsenide phosphide

InP	Indium phosphide
IP	Internet protocol
IV	Current-Voltage
LC-DFB	Laterally-coupled distributed feedback
LASER	Light Amplification by the Stimulated Emission of Radiation
LH	Light-hole
L-I	Light-current
MBE	Molecular beam epitaxy
MOCVD	Metalorganic chemical vapour deposition
MQW	Multiple quantum well
NF	Noise figure
NRC	National Research Council
OSA	Optical spectrum analyzer
PC	Polarization controller
PD	Photodiode
PL	Photoluminescence
PML	Perfectly matched layers
PON	Passive optical network
PSDFN	Power spectral density of the frequency noise
QD	Quantum dot
QoS	Quality of Service
QW	Quantum well
RCMT	Rigorous coupled mode theory
RF	Radio Frequency
RIN	Relative Intensity Noise
RW	Ridge width
SCH	Separate confinement heterostructure
SEM	Scanning electron microscope

SMSR	Side mode suppression ratio
SNR	Signal-to-noise ratio
SO	Split orbit
SOA	Semiconductor Optical Amplifier
SRH	Shockley-Read-Hall
TDTW	Time-domain traveling wave
TE	Transverse electric
TEC	Thermo-electric Cooler
TM	Transverse magnetic
T.S	Tensile strain
U.S	Unstrained
VOA	Variable optical attenuator
VoIP	Voice over IP

List of Related Publications

1. **Julie E. Nkanta**, Ramón Maldonado-Basilio, Sawsan Abdul-Majid, Jessica Zhang, and Trevor J. Hall, ‘*Asymmetric MQW Semiconductor Optical Amplifier with Low-polarization Sensitivity of over 90-nm Bandwidth*’, Photonics West, 1-6 February 2014, San Francisco, USA, Proc. SPIE. (8 pages)
2. **Julie E. Nkanta**, Ramón Maldonado-Basilio, Kaiser Khan, Abdessamad Benhsaien, Sawsan Abdul-Majid, Jessica Zhang, Trevor J. Hall, ‘*Low polarization-sensitive asymmetric multi-quantum well semiconductor amplifier for next-generation optical access networks*’, Opt. Lett. , **38**(16), 2013, pp. 3165-3168.
3. **Julie E. Nkanta**, Ramón Maldonado-Basilio, Sawsan Abdul-Majid, Jessica Zhang, and Trevor J. Hall, ‘*Broadband Multi Quantum Well Semiconductor Optical Amplifier*’, CMC TEXPO, 15-16 October 2013, Gatineau, Canada
4. **Julie E. Nkanta**, Ramón Maldonado-Basilio, Abdessamad Benhsaien, Kaiser Khan, Sawsan Abdul-Majid, Jessica Zhang, Trevor J. Hall, ‘*Asymmetric MQW Semiconductor Optical Amplifier for Next-Generation Optical Access Networks*’, OSA Conference on Lasers and Electro-Optics (CLEO), 9-14 June 2013, San Jose, California, USA. Technical Digest, 2013. (2 pages)
5. **Julie E. Nkanta**, Ramón Maldonado-Basilio, Kaiser Khan, Abdessamad Benhsaien, Sawsan Abdul-Majid, Jessica Zhang, and Trevor J. Hall, ‘*Characterization of an Asymmetric InGaAsP/InP Multi-Quantum Well Semiconductor Optical Amplifier*’, Photonics North, 3-5 June 2013, Ottawa, Canada, Proc. SPIE. (8 pages)
6. Ramón Maldonado-Basilio, Vahid Eslamdoost, **Julie E. Nkanta**, and Trevor J. Hall “*Experimental Analysis of Laterally-Coupled MQW-DFB Lasers in Optical Feedback*” CLEO, June 8-13, 2014, San Jose, USA
7. Kais Dridi, Abdessamad Benhsaien, **Julie E. Nkanta**, Jessica Zhang, Sawsan Abdul-Majid, and Trevor J. Hall “*Multi-electrode Semiconductor Corrugated*

- Ridge Waveguide DFB Lasers*” Faculty of Engineering Graduate Student Poster 2014 (1st Prize)
8. A. Benhsaien, A. Assadihaghi, **J. Nkanta**, D. Iaon, K. Dridi, T. Hall, H. Schriemer and K. Hinzer “*Laterally-Coupled Grating Distributed Feedback Laser Sources*” Faculty of Engineering Graduate Student Poster 2010 (2nd Prize)
 9. **Julie E. Nkanta**, Ramón Maldonado-Basilio, Maryse Aubé, Simon Ayotte, Trevor J. Hall “*Laterally-Coupled Multi-Electrode DFB Lasers with Flat FM-Response*” (Drafted)
 10. **Julie E. Nkanta**, Ramón Maldonado-Basilio, Trevor J. Hall “*Modelling and Experimental Analysis of Laterally-Coupled Distributed Feedback Laser*” (In preparation)

Chapter 1 Introduction

1.1 Objective

There are two main goals of this thesis; the first is to analyze cost effective narrow linewidth laterally-coupled distributed feedback lasers. The test and analysis carried out on these laser devices shows that our laterally-coupled distributed feedback (LC-DFB) lasers exhibit stable single mode operation, reasonable threshold current and emission power, high side mode suppression ratio, narrow spectral linewidth, low noise and flat frequency modulation response. Because of the promising results obtained thus far, and with the quest to make better high-performance lasers, this thesis also includes changing our existing laser design to fit a quantum dot (QD) active region which is currently being fabricated. The choice of the QD is due to the added benefit such as the broader gain the quantum dot laser has over its quantum well counterpart.

The second aim is to analyze the broadband and polarization insensitive semiconductor optical amplifiers that is low cost, compact size and low energy consumption with possibility of being monolithically integrated with other optoelectronic components. Our tested asymmetric multi-quantum well (AMQW) semiconductor optical amplifier (SOA) devices exhibit broadband amplification, low polarization sensitivity, high gain, good signal-to-noise-ratio, and low noise figure.

All these have been motivated by the increasing need for low-cost, tunable and spectrally pure semiconductor laser sources to be used as optical transceiver at the end user in an optical access network. Also motivated by the low-cost and compact semiconductor optical amplifiers needed for both in-line and/or boost applications to extend the reach of the networks, add more users and to improve the quality of service.

1.2 Thesis Overview

1.2.1 Laterally-coupled distributed feedback laser

The semiconductor laser is a key component of an optical communication system. Recent advances in design and fabrication techniques is pushing it to be more high-performance and fabrication-tolerant. In current markets different gain media and cavity structures are utilized such as the quantum well structure and the quantum dot structure.

In this thesis the laterally-coupled distributed feedback laser was modelled and characterized. The InGaAsP/InP LC-DFB laser emitting in the 1560 nm wavelength consists of a multi-quantum well active region made up of six lightly compressively-strained (-0.64 %) 5 nm thick InGaAsP quantum wells and equally six lattice matched 8 nm thick InGaAsP barriers. This active region is sandwiched between two 200 nm thick separate confinement heterostructure (SCH) layers. The ridge waveguide is defined by 800 nm ridge height and a 5 nm thick etch-stop. The third-order rectangular grating uniformly etched along the laser cavity on the ridge sidewalls is 800 nm deep with an average period of ~720 nm and a duty cycle of 50 %. The gratings were etched by a 5× i-line stepper lithography process. After the etching process, the wafer is passivated with an insulated dielectric SiO₂ layer. Then follows etching of the via areas where electrical injection will be provided, multi-electrode devices are segmented into 2 and 3 lengths with electrically isolated regions separated by a few microns, ohmic contacts are formed, n-contact below the device and heavily doped p-contact above the device. A schematic to illustrate the structure of 3-electrode LC-DFB laser is shown in Figure 1-1

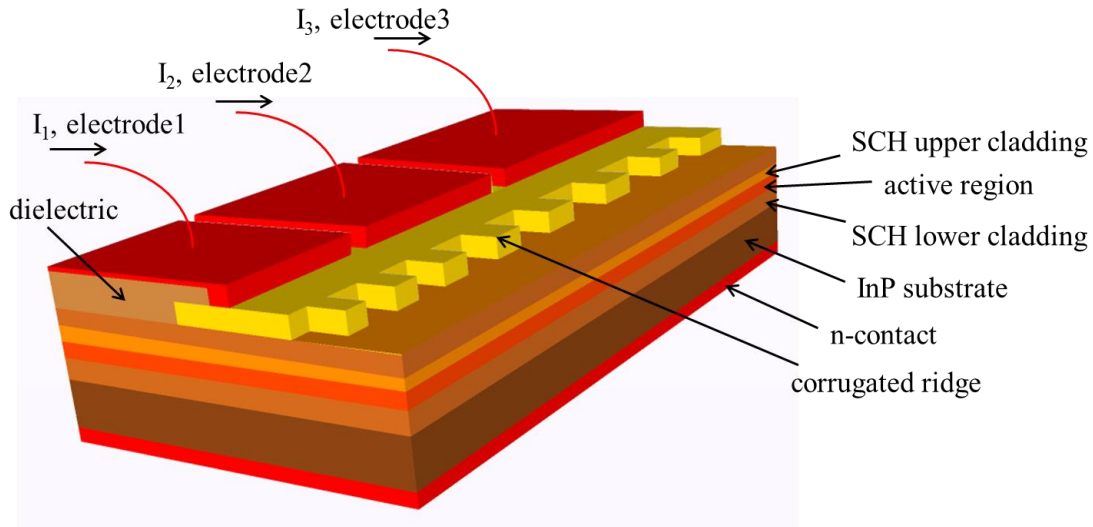


Figure 1-1. Schematic of the multi-electrode LC-DFB laser. SCH: separate confinement heterostructure

The aim is to continually improve upon existing laser designs. The quantum well laser version of these devices have been characterized and the resulting analysis presented. We further adapted our existing quantum well design to fit a quantum dot version. This was done by changing the epitaxy and the grating design to fit a quantum dot (QD) active region provided by a third party, National Research Council (NRC), this is because we have limited available resources in the research group to model a QD active region. QD is a promising emerging technology with improved benefit than the quantum well cavity because the injected carriers have more confinement and the recombination efficiency is more enhanced.

1.2.2 Semiconductor Optical Amplifiers

Semiconductor optical amplifiers (SOAs) have been studied for as long as semiconductor lasers because of the similarity in technology. In other words, semiconductor optical amplifiers are semiconductor lasers with anti-reflection coated facets. A semiconductor optical amplifier (SOA) amplifies an input signal, which is achieved by current injection into the device to achieve optical gain of this signal. The structure has an active region which is index guiding and confines the light, surrounded by p-doped upper cladding

layers and n-doped lower cladding layers. The amplification of the light is accompanied by an unavoidable amplification noise which is desirable to be kept at a minimum. InGaAsP/InP material system is popularly used because of the ability to easily integrate it with other components of same material system.

The tested SOA operating in the E-band (1360 – 1440 nm) range consists of nine 6 nm $\text{In}_{1-x}\text{Ga}_x\text{As}_y\text{P}_{1-y}$ 0.2% tensile strained asymmetric quantum well (AMQW) layers sandwiched between nine latticed matched 6 nm InGaAsP barriers. The asymmetry of the active region is based on the difference of the molar concentrations equivalent to bandgap wavelengths of $\lambda_g=1.1 \mu\text{m}$ for the barriers and $\lambda_g = 1.23 - 1.44 \mu\text{m}$ for the QW layers. The active region is grown on an n-doped InP substrate and buried by p-doped InGaAsP layers. The structure is shown in Figure 1-2 below. The SOA was characterized and results analysis is presented in this thesis. Fabry-Perot lasers of the same material composition as the SOA was also characterized and the result is presented.

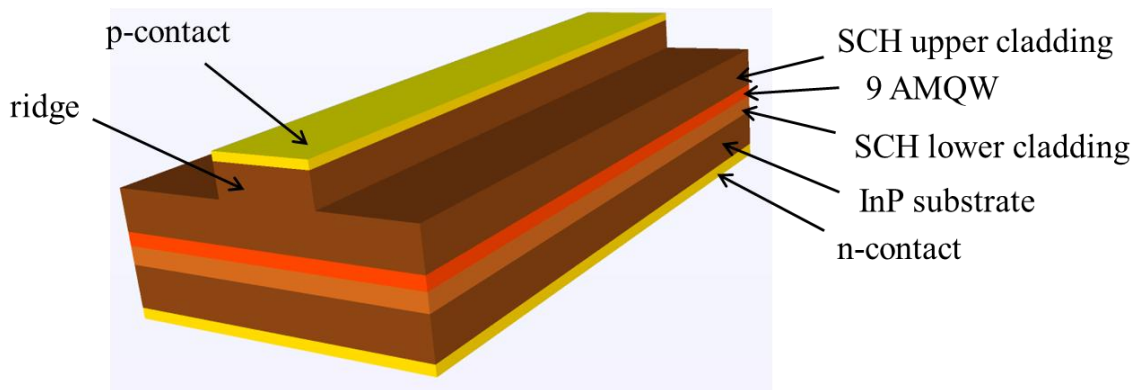


Figure 1-2. Cross-section schematic of the SOA: AMQW: asymmetric multi-quantum well, SCH: separate confinement heterostructure.

1.2.3 Thesis outline

This thesis is outlined below starting with the introduction as Chapter 1, the remaining major parts contains four chapters grouped under similar subject matter, then follows the last chapter with the conclusion and discussion for future work.

Chapter 2

This chapter explores the different properties associated with semiconductor materials, especially those peculiar to III-V materials. It starts with the crystal structure of the semiconductor compounds and its energy band gap. It delves more into the carrier dynamics; the intrinsic and extrinsic carrier concentrations, density of states, the carrier transport and its associated semiconductor electronic equations, as well as the different carrier generation and recombination mechanisms. Section 2.6 discusses the semiconductor heterostructures and quantum confinement: the energy eigenvalues, quantum wells materials, as well as the energy bandgap engineering of the InGaAsP/InP material system. Also in this chapter, the last section 2.7 is focused on the material modelling of the above properties of an InGaAsP/InP laser using Harold® heterostructure simulator to model the physics of the multi-quantum well InGaAsP/InP laser.

Chapter 3

This chapter begins in section 3.2 with discussion about Bragg grating and the couple wave equations. Section 3.3 is focused on the simulations of the LC-DFB laser starting with the grating design, the grating simulation using FIMMPROP and the time-domain travelling wave modelling using PICWave. The success of the current multi-quantum well LC-DFB laser led us to consider further design variations, one of which is using the quantum dot (QD) active region. Section 3.4 is therefore focused on adapting/changing our available epitaxy to fit a QD active region supplied by the National Research Council of Canada. This section also includes the development of the mask layout and the fabrication process. The chapter concludes with a summary in section 3.5

Chapter 4

In this chapter, section 4.2 is the description of the laser device under test, with details of surface grating dimensions, the SEM pictures, and the PL mapping of the wafer. Section 4.3 describes the experimental set-up used. Sections 4.4 and beyond presents results of the tests carried out to analysis the different characterization parameters of the laser

devices. Section 4.4 discusses the L-I-V characteristics of these lasers under symmetric and asymmetric bias control at various operating temperatures. The emission spectra and its red-shift behaviour under different driving current and temperature is presented in section 4.5 and the subsequent side mode suppression ratio in section 4.6. Section 4.7 discusses the linewidth analysis of these laser devices using the delayed self-heterodyne interferometer method in the free-running and under optical feedback operation. Section 4.8 discusses the frequency modulation response and the relative intensity noise of these lasers. The chapter concludes with a summary of the results analyzed.

Chapter 5

This chapter is on the semiconductor optical amplifier (SOA) operating in the E-band wavelength region. It begins with an overview of the advantages of SOAs which is due to its versatility, it has become a key enabling component in the fast growing optical communication system. This chapter presents the device structure for the asymmetric multi-quantum well SOA. Fabry-Perot (FP) lasers of same material compositions as the SOA were included on the same wafer as test structures for the SOA. Section 5.6 presents characterizations such as light-currents, threshold current density, slope efficiency, internal and external quantum efficiencies, optical spectra, gain/loss. The result analysis helped to narrow down the SOA devices based on the geometry that will give the best performance. Overall performance analysis of this ‘best performance’ SOA was carried out and presented in section 5.7. Parameter extraction of its characteristics such as its amplified spontaneous emission and spectrum, gain, broad bandwidth, output saturation power, polarization sensitivity and noise figure were performed. A summary of the results is presented in section 5.8.

Chapter 6

This chapter concludes the thesis with a summary of the results obtained and recommendations for future work

These devices were designed and the test/measurements were carried out at device station facilities available in the Photonics Technology Laboratory (PTLab), at the Center for

Research in Photonics (CRPuO), University of Ottawa, Canada (the frequency modulation and noise experiments were carried out at Teraxion Inc, Quebec City, Canada). Fabrications of these devices were done at the Center for Photonics Fabrication (CPFC) within the National Research Council (NRC), Canada.

1.2.4 Thesis original contributions

This thesis contributes to the advancement of knowledge in the field of photonics by some of my contributions below

- Modelling and simulation of InGaAsP/InP semiconductor laser properties to include, but not limited to, the carrier/charge density, the recombination rates, the material and modal gain, temperature and optical mode
- Modelling and simulation of the 3rd order gratings as well as the time domain traveling wave analysis of the LC-DFB lasers
- Modification of the surrounding epitaxial layers to fit a quantum dot active region (3rd party recipe) and modifying the grating to allow mode overlap and coupling into the active region. Development of the mask layout for the lithography process.
- Characterization of the 3rd order laterally-coupled distributed feedback lasers
- Characterization of the asymmetric multi-quantum well Fabry-Perot lasers,
- Characterization of the asymmetric multi-quantum well semiconductor optical amplifiers
- Recommendation and showing a possibility of a hybrid laterally-coupled distributed feedback III-V/Si laser

Positive outcomes from this thesis research

- The quantum dot LC-DFB lasers are presently being fabricated at the Canadian Photonics Fabrication Center (CPFC).
- Teraxion Inc have shown interest in the LC-DFB lasers due to the flat FM response which is of interest to them for their applications, and they are interested in seeing the results for the quantum dot LC-DFB lasers.

- I was directly contacted by a company in Quebec called AEPONYX because they were impressed with the work I published on the SOA results and therefore were interested in us collaborating with them on a project involving hybridization of SOA. This collaborative project is currently ongoing in the research group.

Chapter 2 III-V Semiconductor Properties Modelling and Simulation

2.1 Introduction

There are three kinds of solid-state materials based on electrical conductivity; metals, semiconductors and insulators. Metals are good conductors because they produce a large amount of free electrons with an applied electrical field and as such there is no band gap energy required. Insulators are poor conductors and because of the large energy bandgap between the conduction band and the valence band, a large amount of electrical current is required to overcome the bandgap which in most cases destroy the material. Semiconductors, as the name implies have electrical properties between a conductor and an insulator, the conductivity of semiconductors varies with the temperature and material properties. The conductivity and electronic properties are controlled during the growth of the elemental compounds by intentionally introducing impurities in a process otherwise known as the doping. The conduction of electrical current is a result of the flow of electrons. Some electrons are free to jump from the valence band to conduction band separated by an energy gap E_g , a valence electron needs at least the bandgap energy in order to successfully move to the conduction band leaving behind holes. Both electrons and holes can carry electrical current and thus are called carriers. The energy bandgap of semiconductor material, E_g is in the order of 1 eV, thereby electrons can easily be excited to the conduction band. The energy bandgap is essential in understanding semiconductor concepts such as free carrier concentrations, quasi-Fermi levels and carrier dynamics within a semiconductor. Manipulation and exploiting the properties of the semiconductor compounds has led to the manufacture of many devices such as lasers, light-emitting diodes, photodiodes, transistors etc.

This chapter explores the different properties associated with semiconductor materials, especially those peculiar to III-V materials. It starts with the crystal structure of the semiconductor compounds and its energy band gap. It delves more into the carrier dynamics; the intrinsic and extrinsic carrier concentrations, density of states, the carrier

transport and its associated semiconductor electronic equations, as well as the different carrier generation and recombination mechanisms, section 2.6 discusses the semiconductor heterostructures and quantum confinement: the energy eigenvalues, quantum well materials, as well as the energy bandgap engineering of the InGaAsP/InP material system. Also in this chapter, the material modelling of the properties of an InGaAsP/InP laser is presented in the last section 2.7 using Harold® heterostructure simulator to model the physics of the multi-quantum well InGaAsP/InP laser.

2.2 Crystal Structure and Electronic Energy Band Gap

A semiconductor is made up of element(s). A III-V semiconductor is composed of elements from group III and group V of the periodic table. The atoms in these elements bind together to form the crystal structure. A crystal lattice is formed when these atoms form a repeated pattern. The unit cell within a lattice is the smallest unit of volume that contains the repeat pattern, the unit cell of a semiconductor therefore establishes the periodicity of the atomic potentials of the lattice. There are different types of unit cells such as the simple cubic, body centered cubic, face centered cubic, diamond cubic etc. The III-V compounds form crystals with Zinc blend arrangement exhibiting a face-centered cubic (fcc) lattice¹. There are different types of semiconductor alloys, from the III-V group of the periodic table, we have the binary (e.g., InP), ternary (e.g., InGaAs) and quaternary (e.g., In_{1-x}G_xaAs_yP_{1-y}).

The energy dispersion relation of semiconductors strongly depends on the crystal lattice structure because in semiconductors the atoms in the crystal lattice have built up a periodic lattice potential. The unit cell of a semiconductor establishes the periodicity of the atomic potentials of the lattice. This periodic potential is important in solving the single-particle Schrödinger equation where the solution to the wavefunction, ψ for a single-particle within such a periodic potential takes the form of the Bloch function¹ as

$$n,k(\mathbf{r}) = u_{n,k}(\mathbf{r})e^{i\mathbf{k}\cdot\mathbf{r}} \quad 2-1$$

where \mathbf{k} is the wavevector, n is the index of the energy band (the n^{th} solution for the given wavevector) and $u_{n,\mathbf{k}}(\mathbf{r})$ is the periodic Bloch function, and $e^{i\mathbf{k}\cdot\mathbf{r}}$ is the plane wave. Note that the periodicity of the Bloch function is the same as the atomic potentials in the lattice. The eigenvalues of the Bloch functions is the energy, $E_n(\mathbf{k})$, which is the \mathbf{k} dependent allowed energy levels in the semiconductor. These energies are periodic in the reciprocal space associated with the unit cell geometry also called the first Brillouin zone. The solution of these energies as a function of the wavevector \mathbf{k} gives the energy-momentum (E - k) diagram of the semiconductor, which shows the characteristics of this semiconductor material as well as the relationship between the energy and momentum of available quantum mechanical states for electrons in this material. There are different numerical methods used to compute this energy band structure such as the pseudo-potential method, augmented plane wave, tight-binding method and the $\mathbf{k}\cdot\mathbf{p}$ perturbation method^{1,2} whereby if the wavefunctions and energies are known at band extrema, the perturbation methods can be applied to find the wavefunctions and energies at other points of the Brillouin zones. The $\mathbf{k}\cdot\mathbf{p}$ (Kronig-Penney) method is therefore useful for analyzing the band structure near a particular point of \mathbf{k} especially near the extremum for example $\mathbf{k} = 0$. The $\mathbf{k}\cdot\mathbf{p}$ method for a single or two bands only considers the band structure of either a single band such as the band edge of a conduction band or both the conduction and valence band edges thus the coupling to other bands is negligible. The $\mathbf{k}\cdot\mathbf{p}$ method for multi-bands such as four bands, considers the conduction band, the heavy-hole, light-hole and the spin-orbit split off bands. The $\mathbf{k}\cdot\mathbf{p}$ method was introduced by Bardeen³ and Seitz⁴.

To calculate energy dispersion for specific compounds, the multi-band $\mathbf{k}\cdot\mathbf{p}$ method is used whereby the spin-orbit interaction is taken into consideration in the Kane's model⁵ and the Luttinger-Kohn's models⁶ for degenerate bands. Figure 2-1 illustrates the InP band structure in the first Brillouin zone (where the wavevector, k is between $-\pi/a_0 < k_x < \pi/a_0$, and a_0 is the lattice constant) showing the different conduction band valleys, X , Γ , and L . The direct band gap, E_g of the Γ -valley exists at the center of the first Brillouin zone Γ where the important minima of the conduction band and maxima of the

valence band is present. The band structure near the band edges of the direct band gap shows the conduction, heavy-hole, light-hole, and spin-orbit split-off bands which have double degeneracy with their spin counterparts. The E_{SO} is the spin-orbit split-off band energy, the E_X and E_L are the indirect band gap energies at the X and L valleys. $\langle 100 \rangle$ and $\langle 111 \rangle$ are the crystal planes direction. In light-matter interaction, the band gap determines the wavelength of the light.

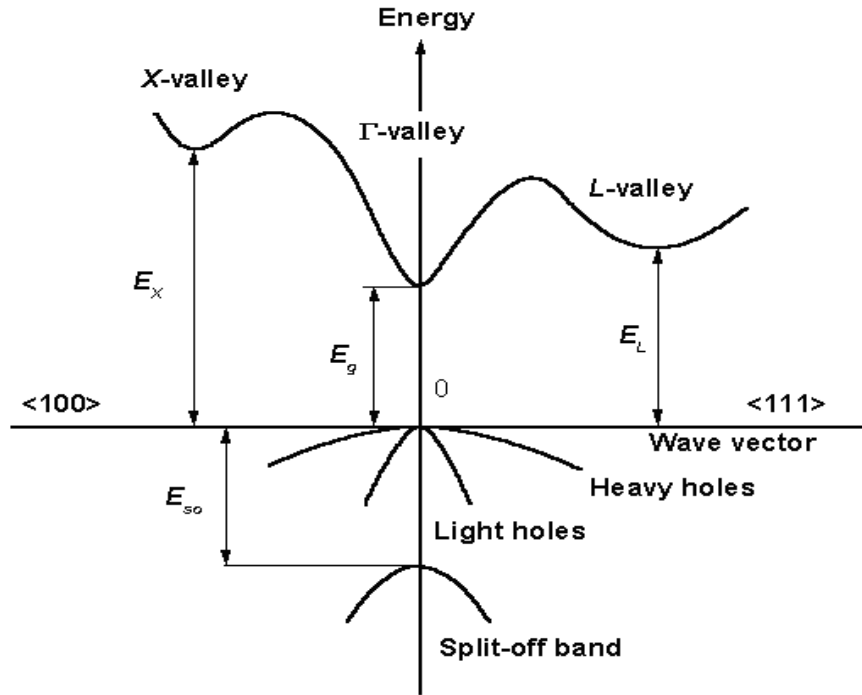


Figure 2-1. Band Structure of a semiconductor from $\mathbf{k}\cdot\mathbf{p}$ method in Kane's model⁷

2.3 Carrier Concentrations

Electrical conductivity or resistivity is determined by the concentration of free carriers in a semiconductor material given by

$$\sigma = q(\mu_n n + \mu_p p) = \frac{1}{\rho} \quad 2-2$$

where σ is the conductivity and ρ is the resistivity, n and p are the conduction band electrons and valence band holes concentrations respectively. μ_n and μ_p are electron and holes carrier mobilities respectively.

2.3.1 Intrinsic Carrier Concentrations

The number of electrons occupying each energy level in the conduction band depends on the number of available electron states and the probability that an electron occupies a state. This can be expressed as the product of the total number of states and the probability of finding an electron at an energy E , integrated over all possible energy levels in the band

$$n = \int_{E_c}^{\infty} N(E)f(E)dE \quad 2-3$$

where $N(E)$ is the density of states and $f(E)$ is the Fermi-Dirac distribution given by

$$f(E) = \frac{1}{1+\exp\left[\frac{E-E_F}{k_B T}\right]} \quad 2-4$$

where E_F is the Fermi energy level (highest energy level at $T = 0K$), k_B is the Boltzmann constant and T is the temperature in Kelvin. In intrinsic (pure) semiconductors, E_F is in the middle of the band gap thereby balancing the electron and hole concentrations. The density of electron state is determined by the energy dispersion function, $E(k)$ as illustrated in Figure 2-2 in which case the electrons and holes are considered to be (quasi) free particles.

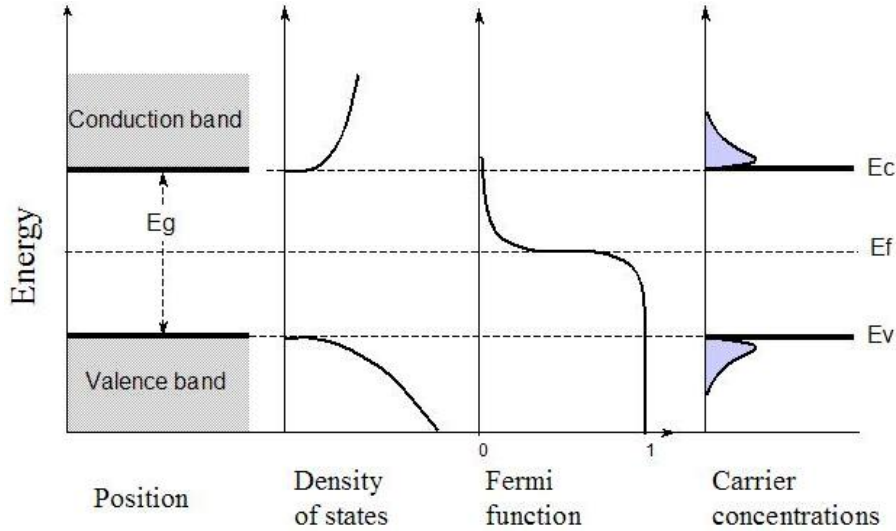


Figure 2-2. The energy bands, density of states, Fermi distribution function and the carrier concentrations as a function of energy.

The carrier concentration depends on the density of electron states, $N(E)$, and therefore certain approximations are necessary. The parabolic band approximations assume the bands near the band edges are parabolic, in other words only the electrons located near the minimum of the conduction band and the maxima of the valence bands are considered. In the parabolic band approximation, a Taylor series of the energy dependence on wavevector is taken to second order with respect to k as below

$$E(k) = E_c + \frac{\hbar^2 k^2}{2m^*} \quad 2-5$$

where m^* represents the density of effective mass of the electrons and \hbar is the Planck's constant. The density of states in both bands thereby becomes a parabolic function of the energy, E :

$$N_c(E) = \frac{1}{2\pi^2} \left(\frac{2m_e^*}{\hbar^2} \right)^{3/2} \sqrt{E - E_c} \quad (E > E_c) \quad 2-6$$

and

$$N_v(E) = \frac{1}{2\pi^2} \left(\frac{2m_h^*}{\hbar^2} \right)^{3/2} \sqrt{E_v - E} \quad (E < E_v) \quad 2-7$$

for the conduction band and the valence band respectively, where m_e^* and m_h^* are the effective masses of electrons and holes. E_c and E_v are the energy of conduction and valence band edges. Integrating the Fermi-Dirac function with the density of states gives the carrier concentration. This integral is approximated using Boltzmann statistics for intrinsic semiconductors where the Fermi level is at the middle (as shown in Figure 2-2) far from both the conduction and valence band edges, otherwise the Fermi-Dirac integral of the order of $1/2$ will be included.

$$n \approx N_c \exp\left(\frac{E_F - E_c}{k_B T}\right) \quad 2-8$$

$$p \approx N_v \exp\left(\frac{E_v - E_F}{k_B T}\right) \quad 2-9$$

where $N_c = 2\left(\frac{2m_e^*k_B T}{2\pi\hbar^2}\right)^{3/2}$ and $N_v = 2\left(\frac{2m_h^*k_B T}{2\pi\hbar^2}\right)^{3/2}$ are the effective density of states for the conduction and the valence band, respectively. In the valence band, the density of states effective mass of the hole is

$$m_h^* = (m_{lh}^{*3/2} + m_{hh}^{*3/2})^{2/3} \quad 2-10$$

where m_{lh}^* and m_{hh}^* are the light and heavy hole effective masses respectively. From the carrier concentration equations above, the Fermi level is derived to be

$$E_F = E_{Fi} = \frac{E_c + E_v}{2} + \frac{kT}{2} \ln\left(\frac{N_v}{N_c}\right) \quad 2-11$$

The intrinsic carrier concentration is the electron carrier concentration due to thermal excitation which is equivalent to the hole concentration in the valence band. It is given by

$$\begin{aligned} n_i &= N_c \exp(E_{Fi} - E_c/k_B T) = N_v \exp(E_{Fi} - E_v/k_B T) \\ n_i &= \sqrt{N_c N_v} \exp(-E_g/2k_B T) \end{aligned} \quad 2-12$$

Where at a particular temperature, equation 2-12 can be generalized to imply that the product of the electron and hole concentrations equals the square of the intrinsic carrier concentration and do not change in a material. This is otherwise known as the mass action law given as

$$np = n_i^2 = N_c N_v \exp(-E_g/2k_B T) \quad 2-13$$

This relation is very useful because if the electron concentration is known, the hole concentration can be easily deduced and vice versa

2.3.2 Extrinsic Carrier Concentrations

When impurity atoms are introduced to an intrinsic semiconductor through a process known as doping, it changes the electrical properties of the semiconductor. A doped semiconductor is called an extrinsic semiconductor. Dopant atoms can act as a donor by donating an extra valence electron to the conduction band or act as an acceptor by accepting electrons from the valence band, both changes the intrinsic carrier concentration of the semiconductor. Donor impurities increase electron carrier concentration and results in an *n*-type semiconductor, while acceptor atoms increase hole carrier concentration and results in a *p*-type semiconductor. However, these dopant atoms must be ionized implying that in order for the dopant atoms to donate or accept electrons, these electrons must be thermally excited. The ionization energy for the donor is E_D and the acceptor E_A . Figure 2-1 illustrates the ionization process in a doped semiconductor where dopant atoms donate electrons to the conduction band or accept valence electrons.

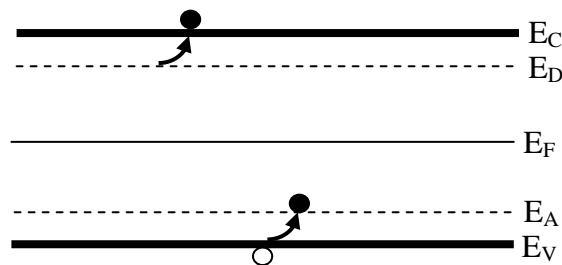


Figure 2-3. Energy band diagram showing the ionization process

The ionized donor concentrations is given by

$$N_D^+ = \frac{N_D}{1 + g_D \exp[(E_F - E_D)/k_B T]} \quad 2-14$$

where g_D is the ground state degeneracy of the donor impurity level and has a value 2 due to the spin degeneracy. Also the ionized acceptor concentration is given by

$$N_A^+ = \frac{N_A}{1 + g_A \exp[(E_A - E_F)/k_B T]} \quad 2-15$$

where g_A is the ground state degeneracy of the acceptor impurity level and has a value 4 due to having spin degeneracy and also double degeneracy of the defect state for heavy and light holes in the valence band.

Due to doping, the Fermi level moves away from the intrinsic energy of the semiconductor. The location of the Fermi level is dependent on the carrier concentration and the ionization level of the dopant atoms. The charge neutrality condition can then be used to determine the Fermi level

$$n_0 + N_A^- = p_0 + N_D^+ \quad 2-16$$

where n_0 and p_0 are electron and hole concentrations at thermal equilibrium. At thermal equilibrium $n_0 p_0 = n_i^2$.

For n-type semiconductor where $N_D^+ - N_A^- \gg n_i$, then the charge neutrality can be simplified to

$$n_0 \approx N_D^+ - N_A^- \quad 2-17$$

$$p_0 \approx \frac{n_i^2}{N_D^+ - N_A^-} \quad 2-18$$

The electron concentration is much higher than the thermal equilibrium intrinsic electron concentration. From equation 2-13, it shows that the hole concentration is greatly reduced, thereby the electrons are considered majority carriers, and holes minority carriers. However, at high temperatures, the intrinsic carrier concentrations overtake the dopant concentrations and then dominate the carrier concentrations, such that the charge neutrality condition cannot be simplified. Resistivity measurements as a function of the reciprocal of temperature, are used often to observe the extrinsic and intrinsic regimes of a semiconductor.

For p-type semiconductor where $N_A^+ - N_D^- \gg n_i$, then the charge neutrality can be simplified to

$$p_0 \approx N_A^+ - N_D^- \quad 2-19$$

$$n_0 \approx \frac{n_i^2}{N_A^+ - N_D^-} \quad 2-20$$

With the assumption that heavy holes dominate the p value and we neglect the contribution from light holes. In general, for n-type semiconductors, the Fermi level moves closer to the conduction band and for p-type semiconductor, the Fermi level is closer to the valence band

Depending on the proximity of the Fermi level to the conduction band, in heavily doped semiconductors, the Boltzmann approximation may not necessarily hold rather it fails if the Fermi-Dirac integral, $\eta_F > -1$ where $\eta_F = (E_F - E_c)/k_B T$. This happens when the donor/acceptor doping concentration are closer to the effective density of states of the conduction and valence bands. Heavy doping also shrinks band gap.

2.4 Carrier Transport

The flow of electrons and holes is the current in semiconductor devices. This happens when the semiconductor device is under an external perturbation, such as carrier injection or light injection. When this happens the semiconductor's equilibrium is slightly disturbed and no longer under thermodynamics equilibrium. The carriers then relax to a state of quasi-thermal equilibrium. The electrons and holes under these perturbations have split Fermi levels called quasi-Fermi levels, there are two of these levels one for electrons in the conduction band and one for holes in the valence band.

There are two types of carrier transport mechanisms; carrier drift which is as a result of externally applied current/voltage. Carrier diffusion is another type, which occurs due to thermal energy and associated random motion of carriers, in which carriers move from

regions of high carrier density to regions of low carrier density. The total current in a semiconductor equals the sum of the drift and the diffusion current.

2.4.1 Maxwell Equation and Continuity Equation

Maxwell's equations are fundamental equations from which important semiconductor electronics equations can be derived. It is given below in MKS units

$$\nabla \times \mathbf{E} = -\frac{\partial \mathbf{B}}{\partial t} \quad 2-21$$

$$\nabla \times \mathbf{H} = \mathbf{J} + \frac{\partial \mathbf{D}}{\partial t} \quad 2-22$$

$$\nabla \cdot \mathbf{D} = \rho \quad 2-23$$

$$\nabla \cdot \mathbf{B} = 0 \quad 2-24$$

where \mathbf{E} is the applied electric field, \mathbf{H} is the magnetic field, \mathbf{D} is the electric displacement flux density, \mathbf{B} is the magnetic flux density, \mathbf{J} is the current density, ρ is the free charge density. In isotropic materials, the following relations exist

$$\mathbf{D} = \varepsilon \mathbf{E} \quad \mathbf{B} = \mu \mathbf{H} \quad 2-25$$

where ε is the dielectric permittivity of the material and μ is the magnetic permeability of the material. For devices with a low dc or low-frequency bias, we can approximate $\partial/\partial t \approx 0$, so equation becomes $\nabla \times \mathbf{E} = 0$. Assuming no external magnetic field is applied $\mathbf{H} \cong 0$ and $\mathbf{B} = 0$.

Poisson's Equation

The solution of the electric can then be expressed in the form of the gradient of an electrostatic field potential

$$\mathbf{E} = -\nabla \phi \quad 2-26$$

and

$$\nabla \cdot (\varepsilon \nabla \phi) = -\rho \quad 2-27$$

This is the Poisson's equation where ϕ is the electrostatic potential and ρ is the free charge density given by

$$\rho = q(p - n + N_D^+ - N_A^-) \quad 2-28$$

where n is electron concentration, p the hole concentration, q is the magnitude of the charge, N_D^+ the ionized donor concentration and N_A^- the ionized acceptor concentration. The above equations can be seen in p - n junctions where the electric field is responsible for separating charge carriers.

Continuity Equation

From equation 2-22 (Ampere's law) and equation 2-28,

$$0 = \nabla \cdot (\nabla \times \mathbf{H}) = \nabla \cdot \mathbf{J} + \frac{\partial}{\partial t} \nabla \cdot \mathbf{D} \quad 2-29$$

$$\nabla \cdot \mathbf{J} + \frac{\partial}{\partial t} \rho = 0 = \nabla \cdot \mathbf{J} + q \frac{\partial}{\partial t} (p - n + N_D^+ - N_A^-) \quad 2-30$$

where $\mathbf{J} = \mathbf{J}_p + \mathbf{J}_n$, is the sum of the hole and electron current densities. And assuming the ionized acceptor and donor concentrations are constant over time, equation 2-30 becomes

$$\nabla \cdot \mathbf{J}_n - q \frac{\partial}{\partial t} n = +qR \quad 2-31$$

$$\nabla \cdot \mathbf{J}_p + q \frac{\partial}{\partial t} p = -qR \quad 2-32$$

where R represents the net generation and recombination rates, for both the electrons ($R = R_n - G_n$) and holes ($R = R_p - G_p$). Thus the carrier continuity equations in semiconductors are given as below

$$\frac{\partial n}{\partial t} = G_n - R_n + \frac{1}{q} \nabla \cdot \mathbf{J}_n \quad 2-33$$

$$\frac{\partial p}{\partial t} = G_p - R_p + \frac{1}{q} \nabla \cdot J_p \quad 2-34$$

2.4.2 Drift and Diffusion

The flow of electrons and holes in a semiconductor occurs randomly due to the interactions with lattice atoms of the crystal structure. This random motion does not result in a net motion of carriers and therefore does not contribute to current, however, with carrier or light injection, a gradient in carrier concentration forms, and the flow of carriers due to this gradient is called the diffusion process in which carriers move from high concentration region to low concentration region. The flux of carriers results in diffusion current given as

$$J_{n,diff} = qD_n \nabla n \quad 2-35$$

$$J_{p,diff} = qD_p \nabla p \quad 2-36$$

Where the electron and hole diffusion coefficients D_n and D_p are related to the electron, μ_n and hole, μ_p mobilities by

$$qD_n = \mu_n k_B T \quad qD_p = \mu_p k_B T \quad 2-37$$

Phonon scattering, carrier-carrier scattering and ionized impurity scattering contribute to carrier mobility. Studies of mobility have been carried out experimentally and theoretically and empirical mobility models have been developed by combining these theories with experimental observation on mobility measured by the Hall Effect. An accurate model suitable for III-V materials is the low-field Caughey-Thomas-like mobility model ⁸. In this model, carrier mobility is a function of carrier concentration (due to doping) and temperature.

Applying electric field in the form of voltage results in drift motion. For low electric current, the drift velocity of carriers is proportional to the electric field however for high

electric fields, the drift velocity overshoots before saturation. The drift-current is proportional to the electron and hole conductivities and is given by

$$J_{n,drift} = \sigma E = q\mu_n n E \quad 2-38$$

$$J_{p,drift} = \sigma E = q\mu_p p E \quad 2-39$$

In a uniform semiconductor, combining the drift current and diffusion current gives the total current density of electrons and holes

$$J_n = qD_n \nabla n + q\mu_n n E \quad 2-40$$

$$J_p = qD_p \nabla p + q\mu_p p E \quad 2-41$$

The total current density through the semiconductor device is the sum of equations 2-40 and 2-41. This is also called the carrier transport equations.

2.5 Carrier Recombination and Generation Mechanisms

Carriers in semiconductor lasers are created by forward biasing the p-n junction thus creating excitation for the onset of lasing. The photons are generated by the recombination (destruction of an electron-hole pair due to electron jump from the conduction to valence band) of both the majority and minority carriers. The injected carriers recombine in different forms, the radiative recombination which uses band-to-band transition between energy levels to release energy corresponding to the bandgap of the semiconductor, and the non-radiative recombinations Shockley-Read-Hall via centers in the forbidden gap or Auger recombinations in which the energy is released as a phonon. The emission efficiency of the laser and subsequent threshold condition therefore relies heavily on these recombinations. The creation and annihilation of photons is only present in the radiative recombination, while the other 2 kinds of recombinations involve interaction with phonons and other forms of energy.

2.5.1 Radiative recombination

Radiative recombination is a process whereby electrons spontaneously recombine with a hole through the emission of a photon. In laser operation the stimulated emission is very necessary and the spontaneous emission occurs naturally thereby dominating the carrier recombination paths. Figure 2-4 shows the photon absorption and generation through band-to-band radiative transitions.

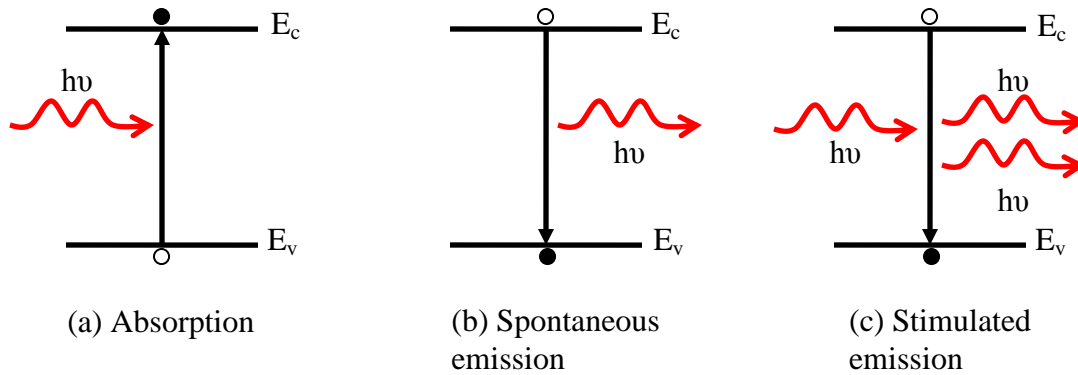


Figure 2-4. Photon absorption and generation through radiative (band-to-band) recombination

The recombination rate of electrons and holes is given by

$$R_n = R_p = Bnp \quad 2-42$$

and the generation rate by

$$G_n = G_p = e \quad 2-43$$

where B is the material dependent radiative recombination coefficient and e is the emission rate. The net recombination is

$$R_{rad} = R_n - G_n = R_p - G_p \quad 2-44$$

The excess carrier concentration vanishes at thermal equilibrium when there is no current or optical injection therefore

$$R_{rad} = B(np - n_i^2) \quad 2-45$$

Where $n_i^2 = n_0 p_0$. The carrier concentrations can deviate from thermal equilibrium and when under low current injections. The electron and holes radiative lifetime is given by

$$\tau_{rad} = \frac{1}{B(n_0 + p_0)} \quad 2-46$$

2.5.2 Shockley-Read-Hall recombination

Shockley-Read-Hall (SRH) recombination involves interaction between electrons and ionized energy levels deep inside the semiconductor band gap. Those energy levels are normally generated by crystal defects (deep traps) and is significant only in low quality crystals and in semi-insulating materials. Its rate is proportional to the trap density that is parameterized by carrier life times of τ_n and τ_p . The properties of existing traps can be very different depending on their local environment. Figure 2-5 illustrates the SRH recombination process where E_t is the energy level of the trap is caused by the presence of a structural defect, E_C and E_V are the energy levels of the conduction band and valence band respectively.

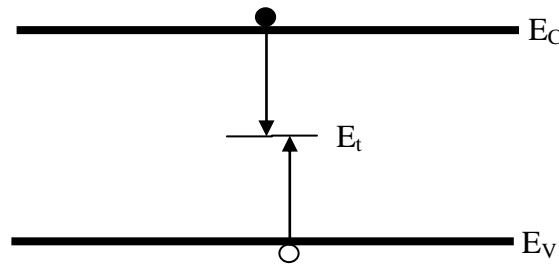


Figure 2-5. Shockley-Read-Hall recombination

SRH has four processes for generation and recombination. Electron capture and hole capture (recombination), as well as electron emission and hole emission (generation). The calculation of the SRH recombination rate can be a very complicated process. However, in good quality crystals where the deep trap density is much less than the doping concentration, at thermal equilibrium, the net SRH recombination rate can be approximated as

$$R_{SRH} = \frac{np - n_i^2}{\tau_p(n + n_1) + \tau_n(p + p_1)} \quad 2-47$$

where n_1 and p_1 depends on the intrinsic carrier density and the energy level of the trap and is given as

$$n_1 = n_i \exp\left(\frac{E_{trap}}{k_B T}\right) \quad 2-48$$

$$p_1 = n_i \exp\left(\frac{-E_{trap}}{k_B T}\right) \quad 2-49$$

2.5.3 Auger recombination

In Auger recombination, the excess energy is transferred to another electron within either the valence band or conduction band through an elastic scattering process, the now excited electron then releases its excess kinetic energy through phonon scattering in the form of heat. Figure 2-6 illustrates the Auger recombination process where E_C and E_V are the energy levels of the conduction band and valence band respectively.

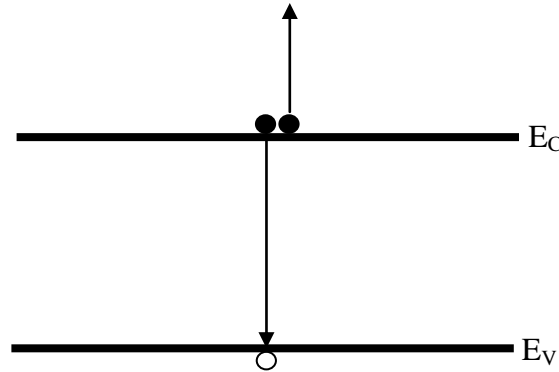


Figure 2-6. Auger recombination

Three particles are involved in an Auger event therefore Auger recombination rate is determined by the third-order polynomial fit to the recombination rate measurement and it is a function of carrier concentration. The total net Auger recombination is given as

$$R_{Aug} = (c_n n + c_p p)(np - n_i^2) \quad 2-50$$

where c_n and c_p are temperature dependent coefficient

The overall effective lifetime of a minority carrier is therefore a combination of all the recombination lifetimes

$$\frac{1}{\tau} = \frac{1}{\tau_{rad}} + \frac{1}{\tau_{SRH}} + \frac{1}{\tau_{Aug}} \quad 2-51$$

2.6 Heterostructures and Quantum Confinement

Heterostructures in semiconductors are junctions formed when two semiconductor materials of different band gaps are physically grown together. The different electron affinity between two heterojunctions can lead to differences in energy band alignment, and coupling such two heterojunctions can lead to the formation of potential barriers for carriers in one or both electronic bands. The carriers in the small bandgap semiconductor material will experience an additional potential as the thickness of the small band gap material decreases further to the atomic scale. This confines the carriers and leads to quantization effects. Carriers can be confined in either or all of the three dimensions or not at all.

2.6.1 Energy Eigenvalues and Density of states

From Schrödinger equation, the energy of a quantized particle is given by

$$E = \frac{\hbar^2 k^2}{2m^*} \quad 2-52$$

where k is the wavevector.

To solve this **for carriers confined in 1D**, a simple square well potential with an infinite barrier is used. Near the boundaries (at the barrier) the wavefunction approaches zero. The n^{th} solution of the electronic energy eigenvalues is given as

$$E_n = \frac{\hbar^2 \pi^2 n^2}{2m^* L_z^2} \quad 2-53$$

where L is the dimension of confinement (L_x , L_y and L_z), E_n is the n^{th} eigenenergy, and $\frac{\pi^2 n^2}{L_z^2} = k^2$. This results in a 2D density of states

$$N_{2D}(E) = \frac{m^*}{\pi \hbar^2 L_z} \sum_n H(E - E_n) \quad 2-54$$

where $H(E)$ is the Heaviside step function. This is a quantum well structure

For carriers confined in 2D, the energy eigenvalues is

$$E_{n_x, n_y} = \frac{\hbar^2 \pi^2}{2m^*} \left(\frac{n_x}{L_x} + \frac{n_y}{L_y} \right)^2 \quad 2-55$$

The resulting density of states is

$$N_{1D}(E) = \frac{1}{\pi L_x L_y} \sqrt{\frac{2m^*}{\hbar^2}} \sum_{n_x, n_y} \frac{1}{\sqrt{E - E_{n_x} - E_{n_y}}} \quad 2-56$$

This in a quantum structure is known as quantum wire

For carriers confined in 3D, the energy eigenvalues is given as

$$E_{n_x, n_y, n_z} = \frac{\hbar^2 \pi^2}{2m^*} \left(\frac{n_x}{L_x} + \frac{n_y}{L_y} + \frac{n_z}{L_z} \right)^2 \quad 2-57$$

The resulting density of states is

$$N_{0D}(E) = \frac{g_s}{\pi L_x L_y} \delta(E - E_{n_x} - E_{n_y} - E_{n_z}) \quad 2-58$$

Where g_s is the spin degeneracy $\delta(E)$ is the Dirac delta function. This is a quantum dot structure

There exists another quantum structure known as bulk, where the carrier wavefunctions exist in bands (continuous wavefunctions). This results in a 3D density of states

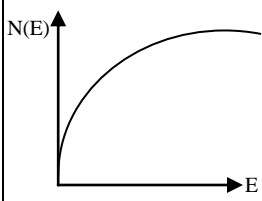
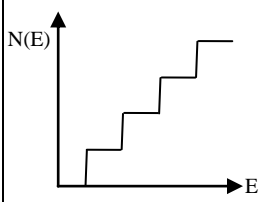
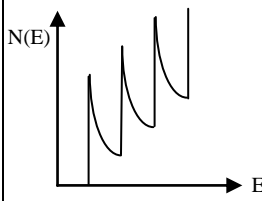
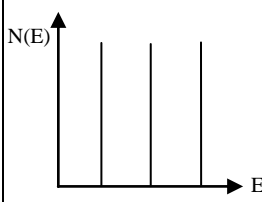
$$N_{3D}(E_n) = \frac{1}{2\pi^2} \left(\frac{2m^*}{\hbar^2} \right)^{3/2} \sqrt{E} \quad 2-59$$

At $E = E_n$ then

$$N_{3D}(E_n) = \frac{1}{2\pi^2} \left(\frac{2m^*}{\hbar^2} \right)^{3/2} \left(\frac{\hbar^2 \pi^2 n^2}{2m^* L_z^2} \right)^{1/2} \quad 2-60$$

These different structures and their respective confinement/density of states is shown in Table 2-1 below

Table 2-1. Quantum structures and confinement with associated energy and density of states

Structure	Quantum confinement	Number of free dimensions	Confinement Energy and Density of States
Bulk	None	3	
Quantum well	1	2	
Quantum wire	2	1	
Quantum Dot	3	0	

2.6.2 Quantum Well Structure

A quantum well structure is formed by sandwiching a narrow bandgap semiconductor material between two wider bandgap semiconductor materials. This heterostructure is formed during epitaxial growth of alternating layers where the middle layer with the smaller band gap semiconductor forms the quantum well, while the two layers

sandwiching the middle layer from the potential barriers. The semiconductor materials are lattice matched to reduce the interface defects due to mismatch of crystal dimensions between the materials.

In the QW structure, one potential well is formed for the conduction band electrons, and another is formed for valence band holes. The changes in the bandgap, E_g at the interface results in discontinuities in the conduction band (E_c) and the valence band (E_v). These conduction and valence band offsets correspond to the well depth for both the conduction band electrons and valence band holes. This offset is dependent on the doping of the semiconductor materials⁹. The schematic representation of a quantum well with its transition energies is shown below in the Figure 2-7. The emission wavelength, $E_{c1}-E_{hh(lh)}$, is not the same as the bandgap energy, $E_{g(w)}$, of the semiconductor material. As illustrated the quantum well layer is surrounded by two barrier layers on each side

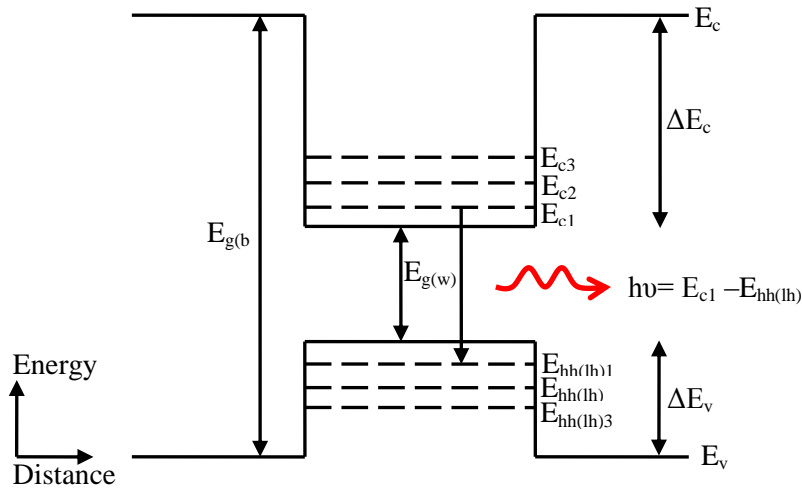


Figure 2-7. Schematic of a single quantum well and its transition energies

The discrete transition energy levels in quantum well allow tuning of the desired wavelength of emission. The gain region in a quantum well in contrast with a bulk semiconductor is a thin region and is embedded inside a larger optical confinement region. As discussed in previous section, carriers in the quantum wells are confined in one dimension. An extension of the single quantum well is the multiple quantum well

(MQW) structures as shown in Figure 2-9. It is comprised of a series of alternating layers of wells and barriers. The barrier thickness between adjacent wells is just sufficient to keep the well region electronically isolated and prevent significant coupling between the wells. The carrier and gain nonlinearities in QW structures are determined largely by the properties of the confinement region^{10,11,12}.

2.6.3 Strain in Quantum Wells

Strain changes the band structure of the heterostructure as well as the optical properties of the semiconductor. This occurs when there is lattice mismatch at the interface of the heterojunction. The induced strain does not cause serious defects if it is kept within an acceptable value. There are two types of strain that can be applied; compressive and tensile strains. Figure 2-8 illustrates the different strain effects on the conduction and valence band edges of a semiconductor.

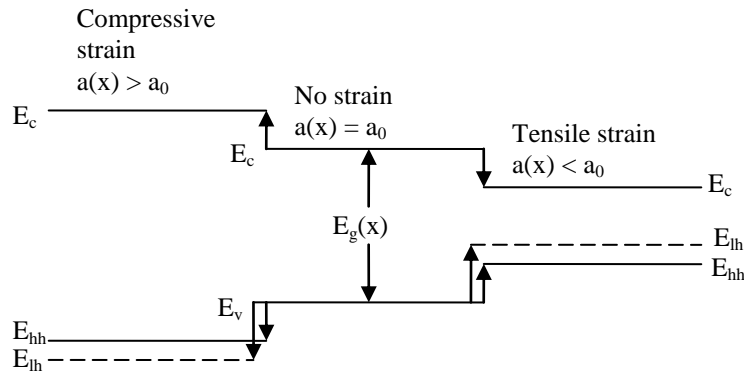


Figure 2-8. Conduction and valence band edges for semiconductors under compressive strain, no strain and tensile strain.

where $a(x)$ is the lattice constant of the unstrained alloy, x is the mole fraction, a_0 is the lattice constant of the substrate and $E_g(x)$ is the bandgap of the unstrained alloy. At $x = 0.468$, $a(0.468) = a_0$ and the strain is zero, if $x < 0.468$, the lattice constant increases i.e., $a(x) > a_0$ resulting in compressive strain, when $x > 0.468$, the lattice constant decreases i.e., $a(x) < a_0$ resulting in tensile strain¹³.

The magnitude of strain ε_{ij} is proportional to the relative change of lattice period $\varepsilon_{ij} = \Delta a_i/a_j$. The amount of energy shifts in the conduction and valence band edges are related to hydrostatic deformation potentials a_c , a_v and the shear deformation potential b as:

$$E_{hh}(0) = E_v^0 + a_v(\varepsilon_{xx} + \varepsilon_{yy} + \varepsilon_{zz}) + \frac{b}{2}(\varepsilon_{xx} + \varepsilon_{yy} - 2\varepsilon_{zz}) \quad 2-61$$

$$E_{lh}(0) = E_v^0 + a_v(\varepsilon_{xx} + \varepsilon_{yy} + \varepsilon_{zz}) + \frac{b}{2}(\varepsilon_{xx} + \varepsilon_{yy} - 2\varepsilon_{zz}) \quad 2-62$$

in valence bands, and

$$E_c(0) = E_c^0 = E_v^0 + E_g + a_c(\varepsilon_{xx} + \varepsilon_{yy} + \varepsilon_{zz}) \quad 2-63$$

in the conduction band

Strain affects both the conduction and valence bands in different ways by shifting the position of the band edges. Considering the three different scenarios in electron-hole recombinations; conduction band to heavy-hole (C-HH), conduction band to light-hole (C-LH) and conduction band to split-off band (C-SO). When a quantum well is tensile strained, the light-hole band is shifted upwards in energy and the C-LH transition is favoured, alternatively using compressive strained layer the heavy-hole band is shifted upward, favouring the C-HH transition. Compressive strains moves the bands apart while tensile strain tends to push the bands closer to degeneracy.

The gain spectrum of the light for TE polarization is usually higher than the TM polarization in an unstrained quantum well, this gain spectrum is also observed in compressive strain but the difference between the TE and TM is bigger, however in tensile strain, the TM polarization dominates the TE polarization².

2.6.4 InGaAsP/InP Band Gap Engineering

The $\text{In}_{1-x}\text{Ga}_x\text{As}_y\text{P}_{1-y}$ alloy can be grown lattice matched to InP substrate where x and y are parameters defining the composition of gallium and arsenide respectively. The energy

bandgap and band offset structure of alloys used in the active region of a QW material is the basis of the operational wavelength and the device performance.

A schematic presentation of an InGaAsP QW is shown in Figure 2-9 below.

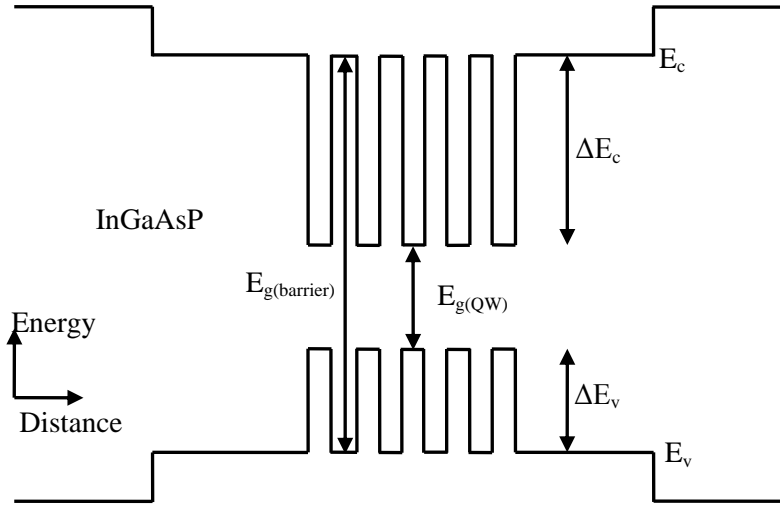


Figure 2-9. Schematic representation of an InGaAsP MQW SCH.

The general interpolation formula for quaternary compound parameters P, is given by

$$P(A_xAB_{1-x}C_yD_{1-y}) = xyP(AC) + (1-x)(1-y)P(BD) + (1-x)yP(BC) + x(1-y)P(AD) \quad 2-64$$

The energy gap of $In_{1-x}Ga_xAs_yP_{1-y}$ lattice matched quaternary system, at 298K, is dependent on the Ga and As fraction of the alloy, and is expressed using the following equations. where x is the Ga mole concentration, and y the As mole concentration, of the material

$$E_g(x, y) = 1.35 - 0.668x - 1.068y + 0.758x^2 + 0.078y^2 - 0.069xy - 0.3222x^2y + 0.03xy^2 \quad (eV) \quad 2-65$$

Or if latticed matched to InP

$$E_g(y) = 1.35 - 0.775y + 0.149y^2 \quad (eV) \quad 2-66$$

where

$$x = \frac{0.1894y}{0.4184 - 0.013y}$$

The band gap of the quaternary material could also be determined if the operating wavelength is given and using the formula:

$$E_g = \frac{hc}{\lambda} \quad (eV) \quad 2-67$$

where c is the speed of light and h is the Plank constant.

To obtain some of the other parameters for the $\text{In}_{1-x}\text{Ga}_x\text{As}_y\text{P}_{1-y}\text{As}$ material system, a linear interpolation between the four different binary semiconductors, GaAs, InP, InAs, and GaP is used (see equation 2-64), the formula is also used to calculate all physical parameters P used in the calculation of the band edge, except for the bandgap:

$\text{In}_{1-x}\text{Ga}_x\text{As}$ Ternary

The energy bandgap E_g for $\text{In}_{1-x}\text{Ga}_x\text{As}$ is given as follows:

$$E_g(\text{In}_{1-x}\text{Ga}_x\text{As}) = 0.36 + 0.505x + 0.555x^2 \quad (eV) \quad 2-68$$

The material parameters, M , of $\text{In}_{1-x}\text{Ga}_x\text{As}$ are interpolated using those for InAs and GaAs by using the following formula:

$$M(\text{In}_{1-x}\text{Ga}_x\text{As}) = (1 - x)M(\text{InAs}) + xM(\text{GaAs}) \quad (eV) \quad 2-69$$

InP Binary

InP is a direct bandgap binary alloy commonly used as a substrate for the InGaAsP material system. The energy bandgap for InP is given below, using a temperature, T, dependent equation:

$$E_g(T) = 1.421 - \frac{T^2 \times 3.63 \times 10^{-2}}{T + 162} \quad (eV) \quad 2-70$$

The energy bandgap calculated at room temperature is 1.351eV.

Reference^{14,15} lists the parameters for the common III-V binary, ternary and quaternary materials. Many ternary and quaternary alloy parameters are obtained by linear interpolation between the parameters of the relevant binary materials. A list of the basic physical parameters for III-V binary compounds is presented in Table 2-2.

Table 2-2 Material parameters for some III-V binary compounds.

	Unit	InAs	GaAs	AlAs	InP	GaP	AlP
E_g^Γ	eV	0.354	1.414	3.099	1.424	2.886	3.63
α^Γ	meV/K	0.276	0.541	0.885	0.363	----	0.577
β^Γ	K	93	204	530	162	----	372
Δ_{so}	eV	0.39	0.341	0.28	0.108	0.08	0.07
m_c^*	m_0	0.023	0.067	0.15	0.08	0.13	0.22
E_p	eV	21.5	28.8	21.1	20.7	31.4	17.7
F	----	-2.9	-1.94	-0.48	-1.31	-2.04	-0.65
γ_1	----	20	6.98	3.76	5.08	4.05	3.35
γ_2	----	8.5	2.06	0.82	1.6	0.49	0.71
γ_3	----	9.2	2.93	1.42	2.10	2.93	1.23
a_c	eV	-5.08	-7.17	-5.64	-6.0	-8.2	-5.7
a_v	eV	1.0	1.16	-2.47	-0.6	-1.7	-3.0
b	eV	-1.8	-2.0	-2.3	-2.0	-1.6	-1.5
c_{11}	GPa	832.9	1221	1250	1011	1405	1330

c_{12}	GPa	452.6	566	534	561	620.3	630
σ_T	cmK/W	3.7	2.27	1.1	1.47	1.3	0.77
ε	-----	14.6	13.1	10.06	12.56	11.1	9.8
a_0	\AA	6.058	5.653	5.661	5.870	5.451	5.467

where;

m_e is the electron mass

γ_1 , γ_2 and γ_3 are Luttinger parameters.

C_{11} and C_{12} are the elastic stiffness constants

F is the matrix element count for the higher band contributions to the conduction band

E_p is the matrix element count for the interaction between s-like conduction bands and p-like valence bands

Δ_{so} is the quantity for the interaction of electron spin and spin-orbit

2.7 Simulation of InGaAsP/InP multi-quantum well Laser

The simulation was carried out using HAROLD® simulator which is part of the Photon Design¹⁶ family of photonics CAD tools used for active and passive component designs.

HAROLD is a two-dimensional simulator which uses well-known physical models (optical, electrical, thermal, capture/escape, recombination, gain etc.) to self-consistently solve the Poisson equation, the current continuity equations, drift-diffusion equation, the capture/escape balance equations, the photon rate equation, the heat flow equation, as well as the vertical and longitudinal wave equation and Schrödinger's equation. As a result of this, HAROLD can model the vertical structure of quantum well lasers using its layer compositions. Laser devices can be simulated as one-dimensional (1D) or two-dimensional (2D) under self-heating (continuous wave) and isothermal (pulsed) operating conditions. Material model such as gain and the epitaxial layer structure can then be exported into Photon Design's circuit simulator PICWave whereby these results can be

incorporated into building complex devices for time domain simulations as will be presented in the next chapter.

Harold interface is user friendly with a Layers Editor that allows specification of the epitaxial layer structure of the laser device such as the quantum well and barrier layers, the bulk layers, the substrate layer and the metal contact/heat sink layers. For each layer the composition can be specified such as the thickness, doping level, material type, strain, and the alloy compositions (or refractive index). The Harold Device Editor is used to define the basic properties of the laser such as the geometry (cavity length and width), facet reflectivities/absorption, scattering loss, heat sink properties etc. Harold also allows one to define their own advanced parameters such as the trap definitions which models the non-radiation and Shockley-Read-Hall recombinations. Harold has a built in Scigraph post-processing graphical user interface (GUI) which is quite broad with many graphical options. These reasons and especially because the results generated in Harold such as the gain models and the device structure can be exported to other Photon Design suites of photonics software tools for further analysis of the grating and the time domain travelling wave model of the laser dynamics in a very small characteristic time scale as will be presented in Chapter 3 makes Harold a software of choice for use in this thesis. However, some issues remain as Harold cannot be used as a standalone tool to fully model certain laser structures, although it defines the epitaxial structure, however, this structure has to be exported to FIMMWAVE and PICWave in order to extend it to a ridge waveguide or be able to define the grating of a distributed feedback laser. Also, the gain curves generated in Harold has parabolic fitting and needs a wide-band gain fitting available in PICWave, this wide-band gain fitting makes the gain fitting more accurate over a wider range of wavelengths as compared to the parabolic gain fitting. Thus Harold lays the foundation and is very complementary with the other software tools used in this thesis.

The InGaAsP/InP laser under simulation consists of a multi-quantum well active region made up of six lightly compressively-strained (-0.64 %) 5 nm thick InGaAsP quantum wells and equally six lattice matched 8 nm thick InGaAsP barriers. This active region is sandwiched between p-doped upper layers and n-doped lower layers. The ridge

waveguide is defined by 800 nm ridge height and a 5 nm thick etch-stop. A detailed description of the laser material composition is shown in Table 2-3

Table 2-3. Epitaxial layer composition of the laser

Layer No.	Layer Name	Material	PL peak (nm)	Nominal Strain		Thickness (μm)	Doping Level (cm^{-3})
				(%)	T.S./C.S.		
12	p-Contact	InGaAs	1660	U.S.		0.050	Zn: $N_A = 2 \times 10^{19}$
11	Ridge 3	InGaAsP	1200	U.S.		0.010	Zn: $N_A = 8 \times 10^{18}$
10	Ridge 2	InGaAsP	1100	U.S.		0.010	Zn: $N_A = 2 \times 10^{18}$
9	Ridge 1	InP	919	U.S.		0.800	Zn: $N_A = 2 \times 10^{18}$
8	Etch stop	InGaAsP	1300	U.S.		0.005	Zn: $N_A = 7 \times 10^{17}$
7	SCH upper clad	InGaAsP	1100	U.S.		0.150	Zn: $N_A = 5 \times 10^{17}$
6		InGaAsP (b)	1200	0	U.S.	0.060	u.d.: $N_D < 3 \times 10^{15}$
5	6 \times MQW stack	InGaAsP (well)	$\frac{1541}{1550}$	-0.64	C.S.	0.005	u.d.: $N_D < 3 \times 10^{15}$
		InGaAsP (barrier)	1200	0	U.S.	0.008	u.d.: $N_D < 3 \times 10^{15}$
4		InGaAsP (b)	1200	0	U.S.	0.020	Si: $N_D = 5 \times 10^{17}$
3	SCH low clad 2	InGaAsP	1150	U.S.		0.100	Si: $N_D = 8 \times 10^{17}$
2	SCH low clad 1	InGaAsP	1050	U.S.		0.100	Si: $N_D = 8 \times 10^{17}$
1	Buffer	InP	919	U.S.		1.040	Si: $N_D = 3 \times 10^{18}$
0	Substrate	InP	919			50.000	Si: $N_D = 2 \times 10^{18}$

Where C.S is compressive strain, T.S is tensile strain, U.S is unstrained, PL is photoluminescence. SCH is separate confinement Heterostructure. u.d is undoped.

Assuming a known bandgap wavelength in μm as indicated in the table above, using equation 2-67 to convert to bandgap E_g in eV. Next using equation 2-65 to solve the second order equation for y_1 and then computing x using equation 2-66, we derive the x and y alloy compositions of the InGaAsP quaternary material layers, the table below summarizes the results.

Table 2-4. Composition of some InGaAsP material layers

Material	Bandgap (nm)	Bandgap E_g (eV)	Alloy composition		Refractive index
			x	y	
$\text{In}_{1-x}\text{Ga}_x\text{As}_y\text{P}_{1-y}$	1050	1.181	0.11	0.25	3.26
$\text{In}_{1-x}\text{Ga}_x\text{As}_y\text{P}_{1-y}$	1100	1.127	0.15	0.33	3.29
$\text{In}_{1-x}\text{Ga}_x\text{As}_y\text{P}_{1-y}$	1150	1.078	0.19	0.41	3.32
$\text{In}_{1-x}\text{Ga}_x\text{As}_y\text{P}_{1-y}$	1200	1.033	0.22	0.48	3.35
$\text{In}_{1-x}\text{Ga}_x\text{As}_y\text{P}_{1-y}$	1300	0.954	0.28	0.61	3.41
$\text{In}_{1-x}\text{Ga}_x\text{As}_y\text{P}_{1-y}$	1550	0.8	0.42	0.9	3.63

These results are then used to calculate the refractive indices for each material layer using the Adachi¹⁷ and Broberg¹⁸ well known methods. A more general interpolation of the refractive index for a wide variety of y values is shown in Figure 2-10 below

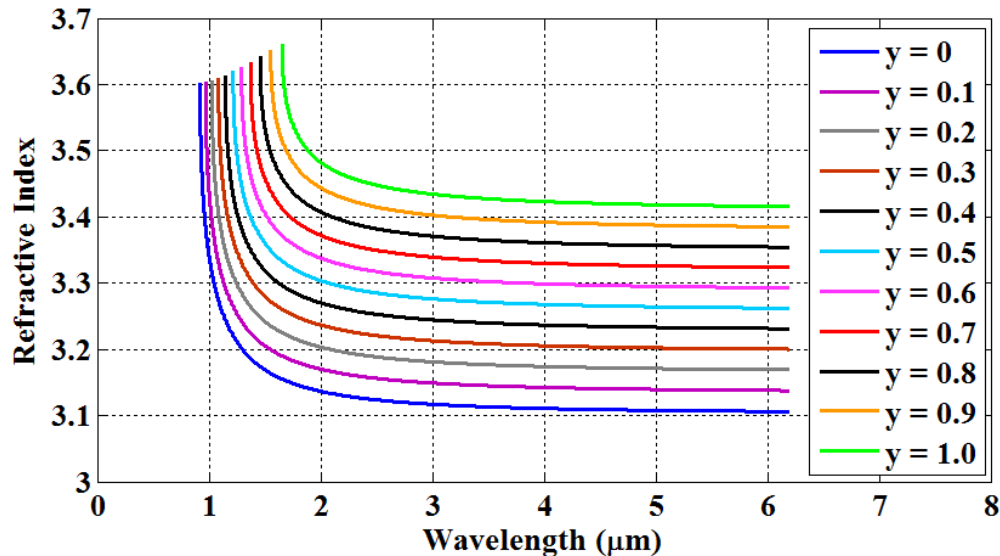


Figure 2-10 Refractive index variation of InGaAsP as a function of wavelength for different y values

2.7.1 Band structure and the quantum well wavefunction

The population inversion phenomenon in which more electrons are present in the conduction band than the valence band gives rise to stimulated emission. To maintain the energy inversion state, current has to be injected into the p-n junction. In Harold the

Poisson-Drift-Diffusion model is used to calculate the bands edges, quasi-Fermi levels and the carrier distribution (carrier and charge densities) at different applied bias.

When carriers are injected the laser is considered forward biased. Electrons are injected from the n-cladding layer and holes from p-cladding layer. These carriers then drift and diffuse across the separate confinement layers (which are generally employed to increase the optical field confinement in the QW region) before being captured by the QWs. The band structure is shown in Figure 2-11 and Figure 2-12

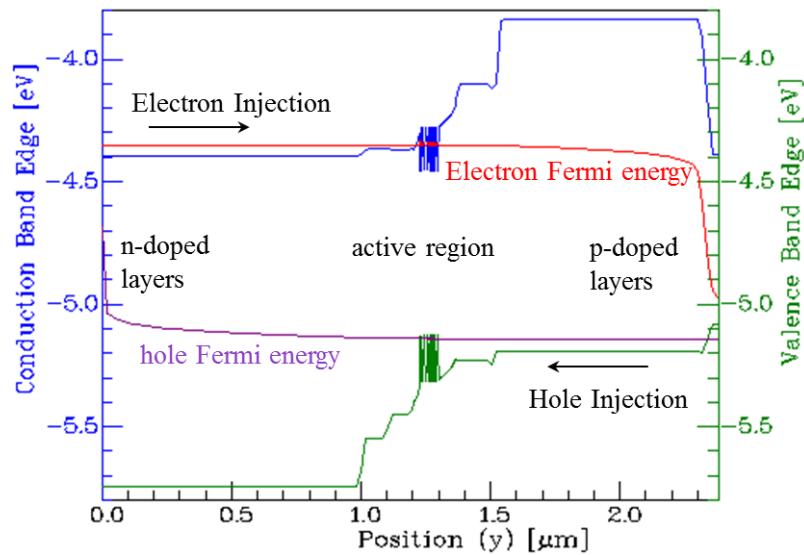


Figure 2-11 The conduction band, valence band and the Fermi levels at threshold.

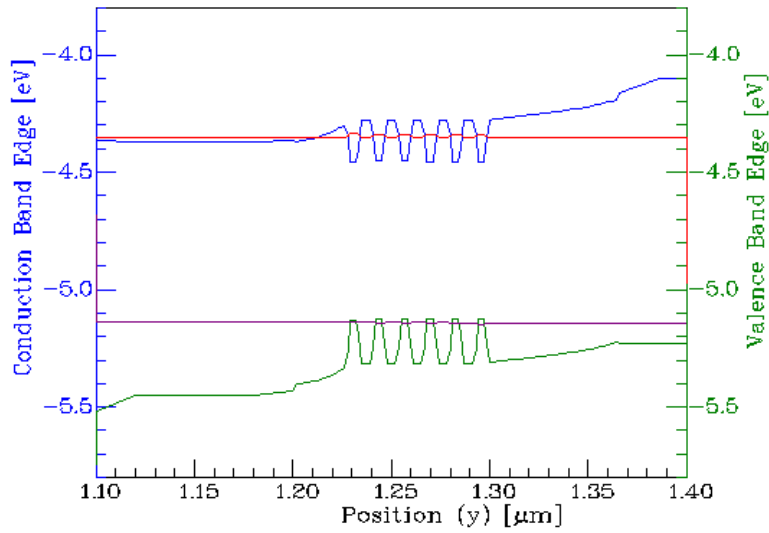


Figure 2-12 The conduction band, valence band and the Fermi levels within the quantum well region.

The electron, light-hole and heavy-hole eigenvalues and eigenfunctions are calculated from Schrödinger equations for the entire coupled quantum well region. The electron and hole wavefunctions and their energy levels in the QW structure are shown in Figure 2-13 and Figure 2-14

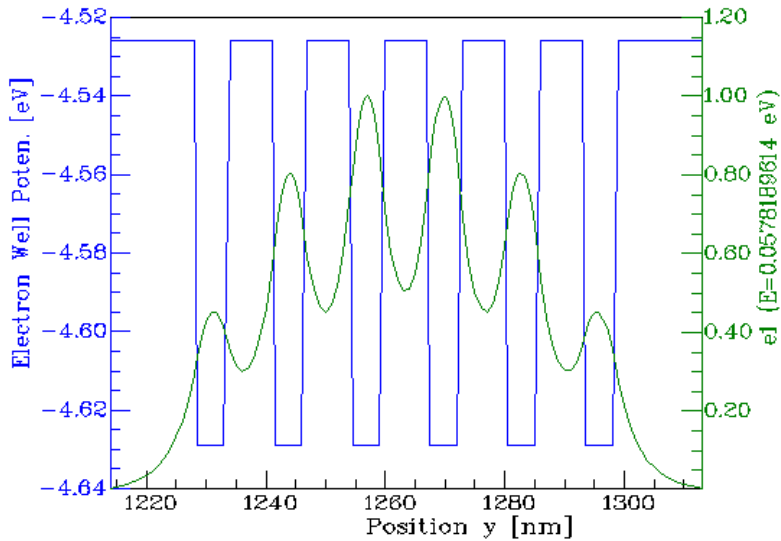


Figure 2-13 Electron well potential and the wavefunction of the lowest energy electron state in the 6 QWs

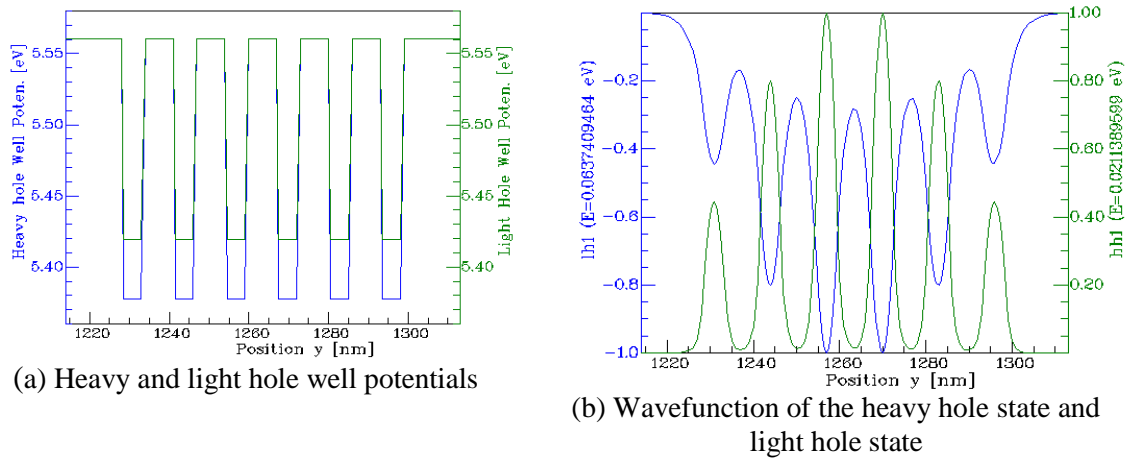


Figure 2-14 Heavy and light hole in the 6 QWs

2.7.2 Carrier densities

The threshold carrier density in diode lasers is affected by Shockley-Read-Hall (SRH) recombination, spontaneous emission and Auger recombination (shown in Figure 2-15), as well as the vertical leakage and lateral leakage makes up the net recombination rate.

Spontaneous emission and lateral leakage consume most of the injection carriers below threshold while SRH and Auger recombination are weak due to the high purity material and the relatively wide band gap hetero-junctions. Above threshold most of the carriers are recombined in the QW in the form of stimulated emission, the figure below shows non-uniform carrier injection within the quantum wells with QW1 (farthest right) having the greatest number of carriers, as it is the topmost quantum well and closest to the where current is injected.

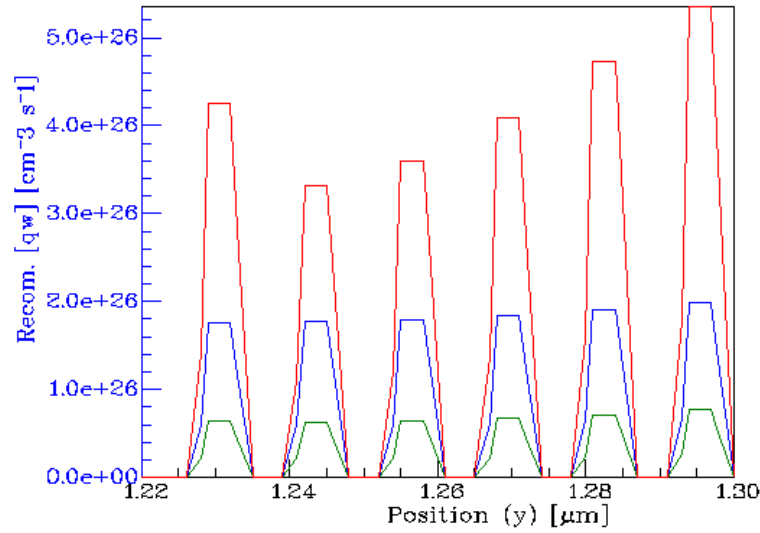


Figure 2-15 The net recombination rates for the 6 QWs at threshold. Stimulated (red), spontaneous (blue), Auger (green), SRH (very negligible).

Stimulated emission dominates the carrier density above threshold as shown in Figure 2-16.

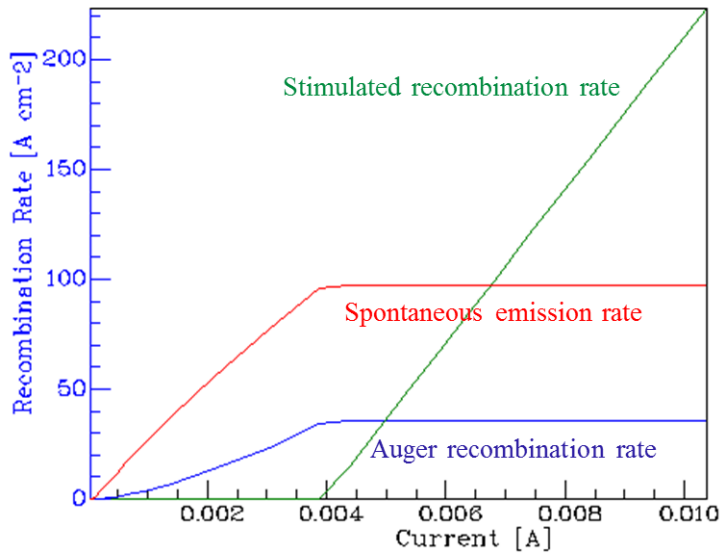


Figure 2-16 Comparison of the various recombination rates within the laser as a function of applied bias

Figure 2-17 shows the sum of the confined carrier densities for both the electron and holes in the quantum wells. The carrier density is normally concentrated in the quantum well region, the claddings and separate confinement layers (not shown) provides large potential steps to ensure carrier confinement in the QW region. The non-uniform carrier

density is due to the drift-diffusion whereby holes and electrons are injected from opposite sides as earlier indicated in the band structure of Figure 2-11. Figure 2-17 shows the carrier density in the 6 QWs, whereby the QW closest to the direction of injection has the greater electron or hole carrier density respectively.

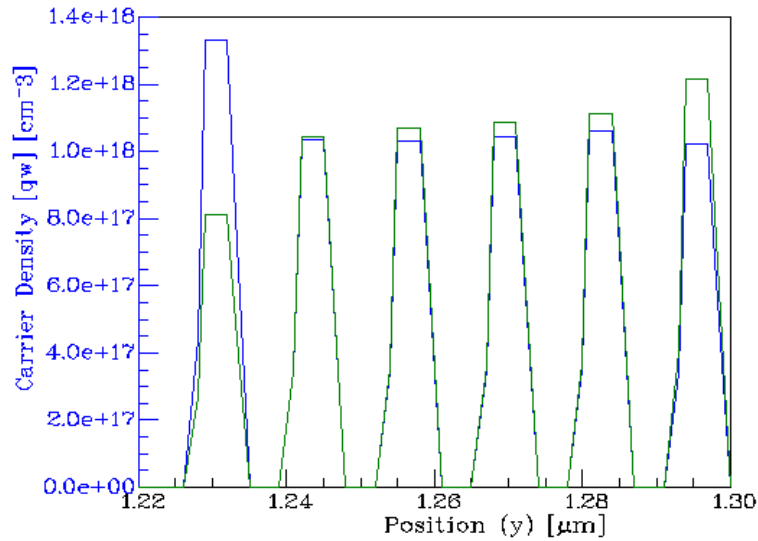


Figure 2-17 Electrons (blue) and holes (green) carrier density in the QWs

The electron and hole current densities for both the vertical and longitudinal directions are shown in Figure 2-18

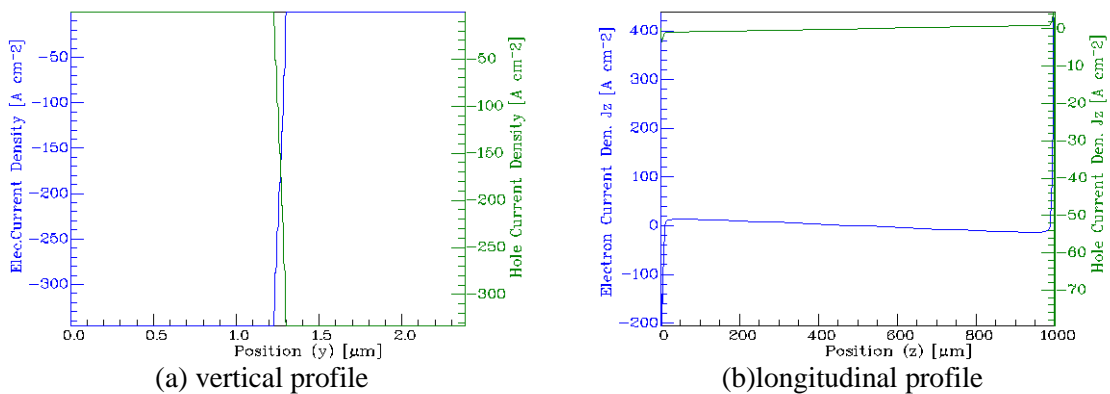


Figure 2-18 Electrons (blue) and holes (green) current density

2.7.3 Optical mode and photon density

The distribution of photons within the laser cavity is determined by the optical field laser eigenmode. Harold uses the passive vertical structure approximation to find the optical mode and with an imposed boundary conditions, the solution of the associated eigenvalue problem yields several cavity modes, the mode with the largest confinement factor is assigned the fundamental mode¹⁶. The fundamental optical mode is shown in Figure 2-19 with the highest intensity of the mode in the active region. The vertical refractive index profile and the doping concentration overlapping with the mode profile are shown in Figure 2-20

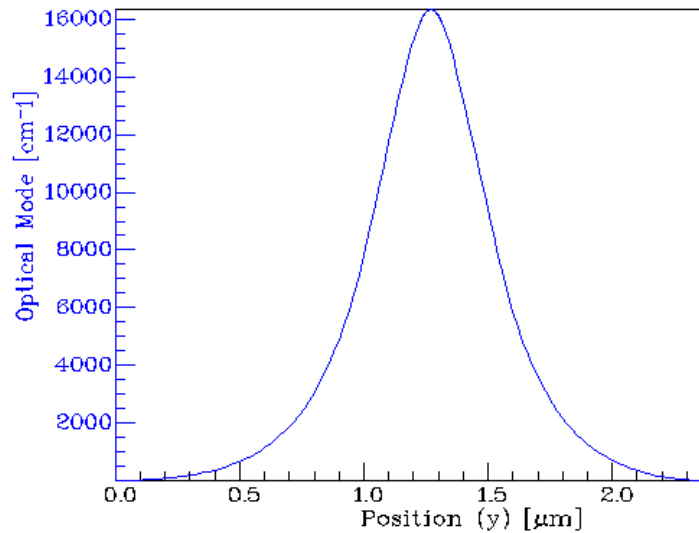


Figure 2-19 The vertical profile of the fundamental optical mode

The refractive index profile near the active region at the biasing carrier density determines the optical confinement factor which is the ratio of the optical volume in the active layer to the volume of the total optical mode in the QWs, the confinement factor is determined to be 0.048. The doping concentration shows an un-doped active region. With doped upper and lower layers.

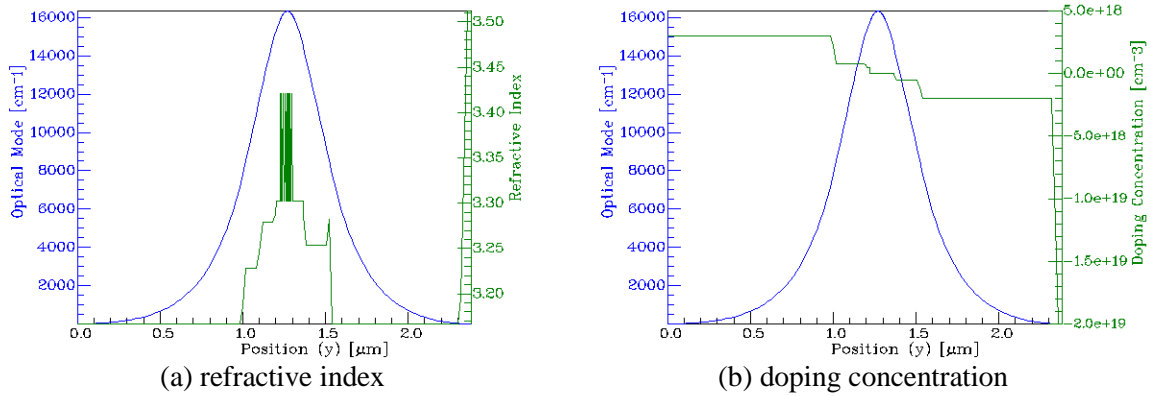


Figure 2-20 The vertical profile of the optical mode

The total photon density is determined by considering the gain and loss balance in the laser cavity. Non-uniformity of the photon density and carrier density can lead to longitudinal spatial hole burning. The longitudinal profiles of the photon density are shown in Figure 2-21

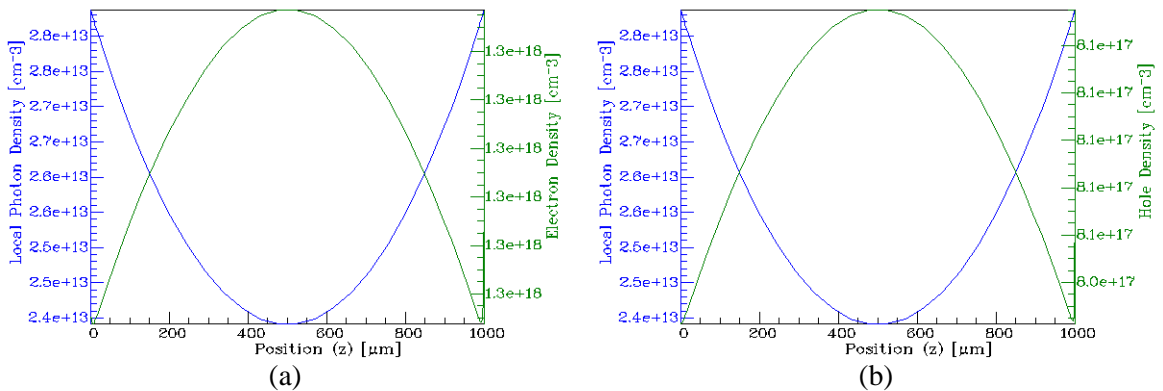


Figure 2-21 Longitudinal profiles photon density versus (a) electron density (b) hole density in the z-direction

2.7.4 Gain and loss

The gain is proportional to the probability that a given photon triggers an electron transition from a higher energy level to a low energy level. Therefore, the total optical gain will be the integral of all transitions to heavy and light holes, respectively, within the k-selection rule. The maximum gain is shown in and Figure 2-22(a). The modal gain

shown in Figure 2-22(b) is the maximum gain multiplied by the confinement factor. Gain saturation is observed above threshold.

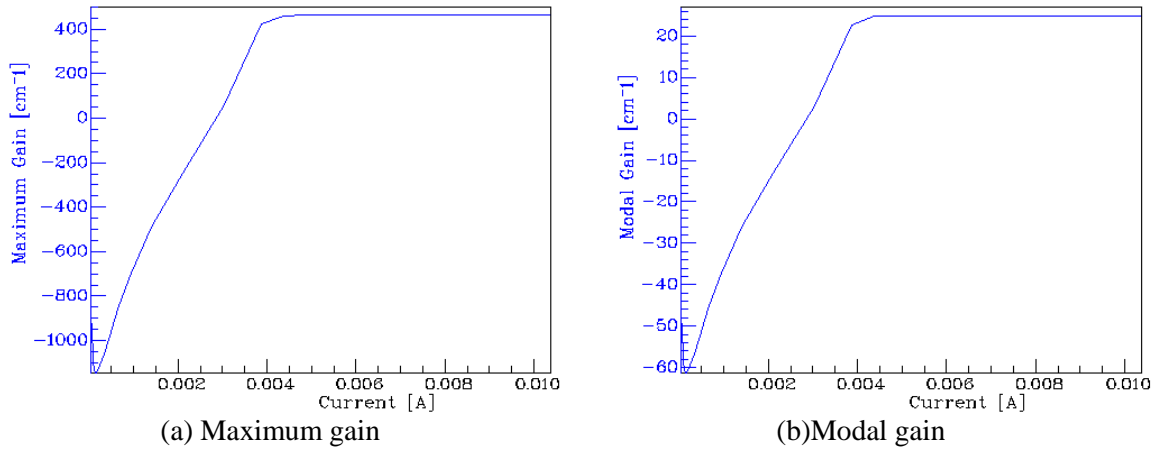


Figure 2-22 Gain as a function of bias current

The total losses in the laser cavity include scattering loss, mirror loss and free carrier absorption loss. Figure 2-23 shows the free carrier loss in the laser.

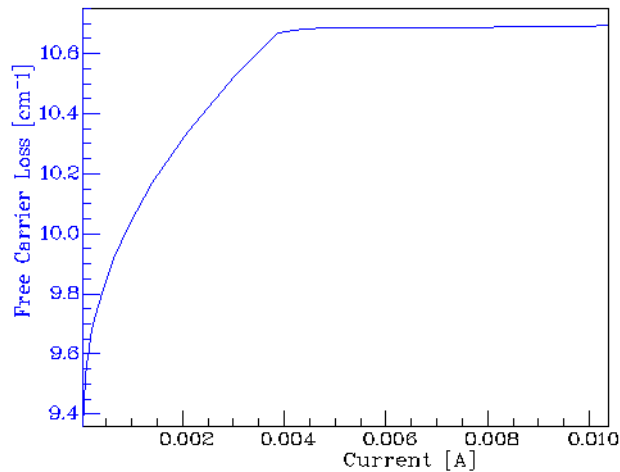


Figure 2-23 Free carrier loss as a function of bias current

The gain curve is generated at different carrier densities for the gain material as shown in Figure 2-24 (black arrow shows increasing carrier density). The gain peaks are shifted as a result of bandgap shrinkage at high carrier densities due to many-body interactions and temperature

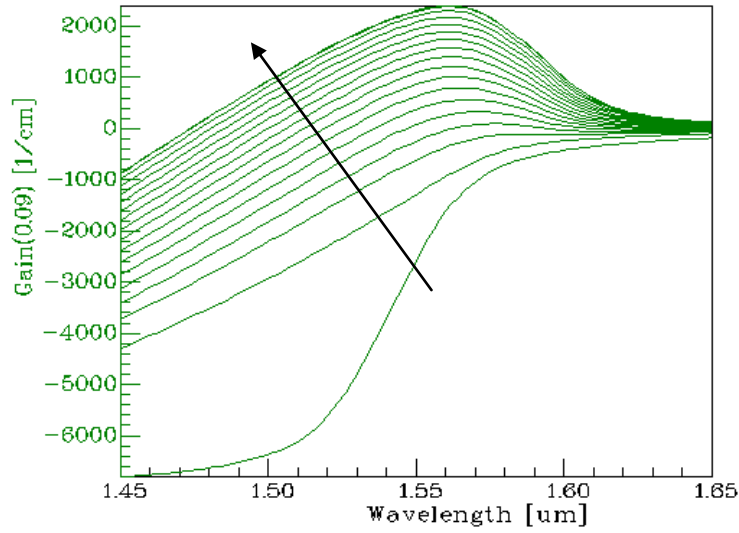


Figure 2-24 Gain spectra at different current densities

2.7.5 Optical power and heat flow

Gain broadening observed as a result of intra-band scattering is computed from the convolution of the optical gain with the Lorentzian line shape function.

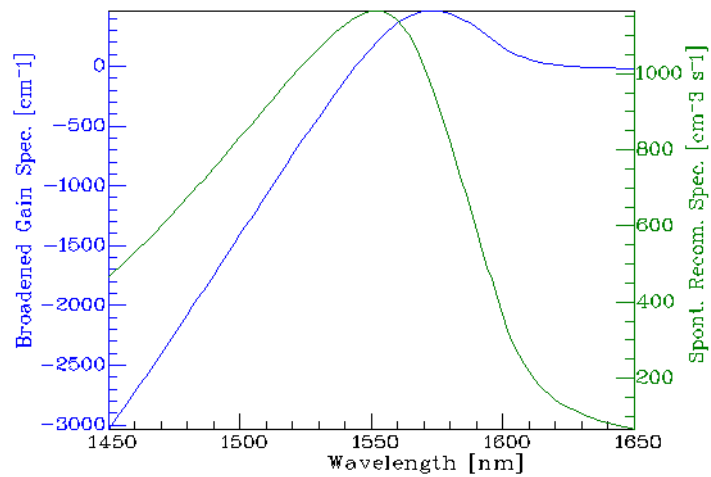


Figure 2-25 Broadened gain and Spontaneous recombination spectrum vs wavelength

Figure 2-25 shows the broadened gain and spontaneous spectrum with wavelength and Figure 2-26 shows the photon energy as a function of wavelength.

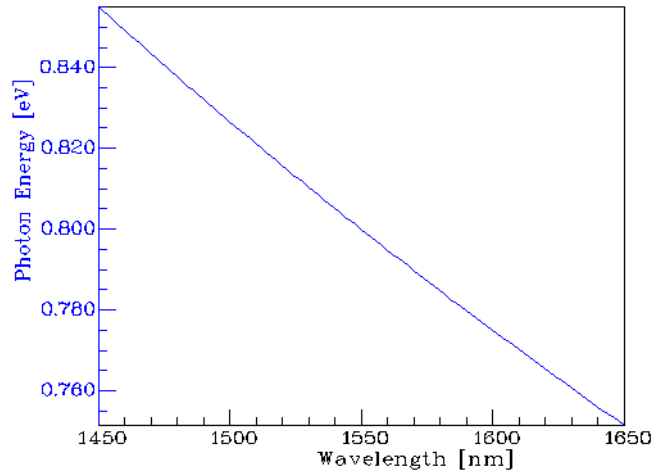


Figure 2-26 Photon Energy vs wavelength

Figure 2-27 shows the various power dissipation mechanisms in the laser. The excess power dissipation and free carrier absorption contributes to device heating and as such are the two largest power dissipation mechanisms as observed. The excess power dissipation arises mainly from spontaneous emission that is not coupled into the lasing mode as well as scattered stimulated simulation. These are all absorbed and dissipated as heat within the laser device.

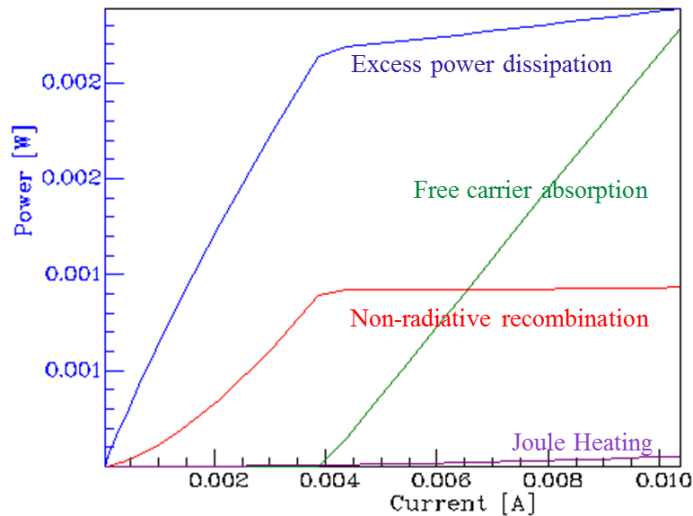


Figure 2-27 Comparison of the various power dissipation mechanisms

The local density of heat sources originates from the various power dissipation mechanisms in the laser device. The different sources of heat from Joule effect, non-radiative, excess power and free carrier photon absorption is shown in Figure 2-28.

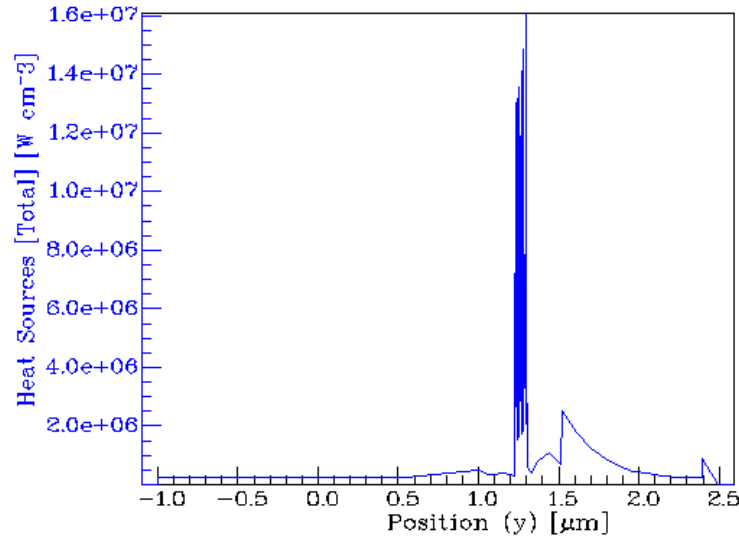


Figure 2-28 Heat sources from joule effect, non-radiative and free career absorption

The variation of the temperature distribution due to injection current is based on the heat flow from the heat sink of the laser device. Figure 2-29(a) shows the heat flow in the vertical direction

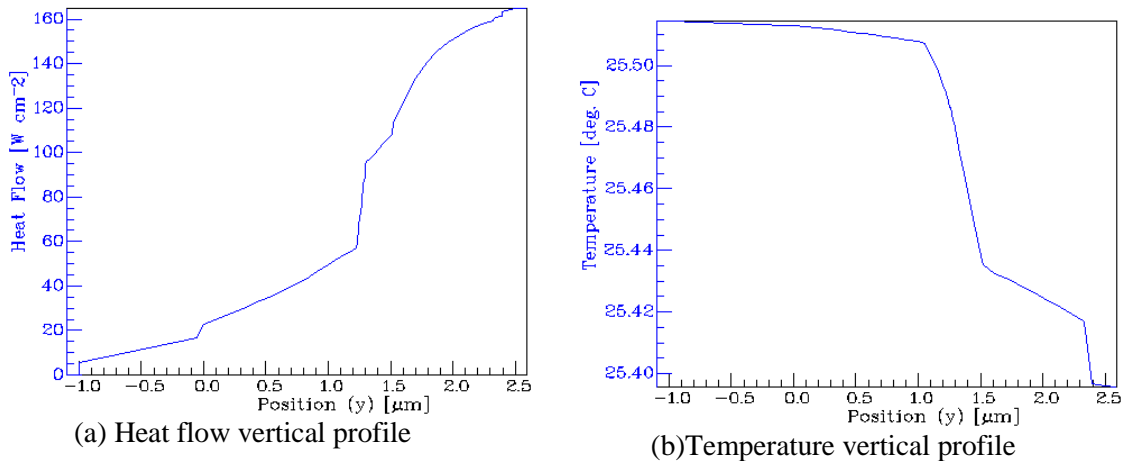


Figure 2-29 Thermal characteristics

Figure 2-29(b) shows the temperature profile whereby temperature increases laterally away from the top layer. The non-uniformity of the photon density leads to a small temperature variation along the length of device. Heating can cause thermal roll-offs in L-I curves, shift in gain peaks, reduction in gain and subsequent degradation of the laser device

2.8 Summary

This chapter reviews the different important properties of III-V semiconductor materials. Starting with the basic composition, it looked at the crystal lattice formation and energy bandgap while also illustrating the energy dispersion diagram from the **k.p** method. The carrier concentration and density of states was presented starting with the intrinsic carrier concentration that is obtainable in pure impurity-free semiconductors, the extrinsic carrier concentrations as a result using dopant (donor and acceptor) atoms which changes the electrical properties of the semiconductor, as well as the Fermi levels.

The mobility of carriers under carrier transport was presented; starting from the fundamental Maxwell's equation, from which the other semiconductor electronic equations (Poisson's and continuity) was derived, the drift and diffusion currents was also discussed. The different carrier generation and recombination mechanisms (Radiative, SRH, Auger) were presented. How semiconductor heterostructures are formed and confined in the different dimensions with its corresponding energy eigenvalues and density of states was discussed for bulk, QW, quantum wire and QDot structures. The quantum well structure and its transition energies was looked at further and the effect of strain on it was presented. The InGaAsP material system bandgap engineering was specifically discussed starting with the general interpolation formulas to derive the bandgap energy and the molar fractions. For the binary InP, ternary and quaternary material systems.

The chapter also presents the simulation results of the quaternary InGaAsP/InP laser structure used in the thesis, such as the bandstructure for the conduction band, valence

band and the Fermi energy levels. The carrier densities for electrons and holes, the recombination rates of which the stimulated emission dominates the carrier density above threshold. The fundamental optical mode is confined within the active region determined by the confinement factor. The total optical density is determined from the gain and loss balance in the laser cavity, the total loss in the cavity includes the scattering loss, mirror loss and free carrier absorption loss. Gain broadening is observed as a result of intra-band scattering. The various dissipation mechanisms in the laser shows the excess power dissipation and the free carrier absorption are the largest sources and contributes to device heating. Temperature distribution depends on the heat flow from the heat sink.

Chapter 3 Laterally-Coupled Distributed Feedback Laser

3.1 Introduction

The laterally-coupled (LC) otherwise called the corrugated-ridge waveguide distributed feedback (DFB) laser has many benefits. Compared to the buried grating (above active region) it has a single growth and processing sweep allowing for a lower cost and overall better yield. Because the gratings are on the ridge sidewalls, it limits the interaction between the carriers and the gratings which can result in a more stable laser device. Also the lithography technique employed uses stepper 5x i-line stepper which allows for better pattern resolution without the diffraction and scattering limits noticed with other conventional methods.

This chapter begins in section 3.2 with discussion about Bragg grating and the couple wave equations, Section 3.3 is focused on the simulations of the LC-DFB laser starting with the grating design, the grating simulation using FIMMPROP and the time-domain travelling wave modelling using PICWave. The success of the current multi-quantum well LC-DFB laser led us to consider further design variations, one of such is using the quantum dot (QD) active region, section 3.4 is therefore focused on adapting/changing our available epitaxy to fit a QD active region supplied by the National Research Council of Canada, this section also includes the development of the mask layout and the fabrication process. The chapter concludes with a summary in section 3.5

3.2 Bragg Grating and Couple Wave Equations

The distributed feedback effect is from the Bragg reflection which is as a result of the periodic perturbation of the waveguide. The reflection from alternating interfaces causes a wavelength-dependent feedback. The maximum reflection occurs when the Bragg

condition is satisfied and the dimensions of the gratings are determined by the condition given by equation below

$$\Lambda = \frac{m\lambda_B}{2n_{eff}} \quad 3-1$$

where Λ is the period of the perturbation (gratings), n_{eff} is the effective index of the unperturbed waveguide, m is the order of Bragg diffraction induced by the grating, λ_B is the wavelength of interest.

To achieve great spectral selectivity, thus single-mode output emission, this periodic perturbation can be incorporated in a laser structure. This periodic gratings act as a spectral filter in the laser. Assuming a laser device having periodic variations of the effective index, and consider a light wave incident on it, some of the incident wave will propagate forward through while some will be reflected backwards at every interface. When the periodicity (Λ) is half of the incident light wavelength, the backward reflected light will constructively interfere resulting in higher reflectivity. The periodic perturbation therefore provides feedback through Bragg scattering which couples the forward and backward propagating waves in the laser cavity.

The working of a distributed feedback (DFB) laser can be analyzed by considering wave propagation in periodic structures whereby grating induced perturbation results in coupling the forward and backward propagating waves. A detailed analysis of the coupling process whereby eigensolutions are obtained to solve the couple-mode equations relative to an infinitely long structure is given in Chapter 5 of John Carroll's book¹⁹. A simpler approach in analyzing the behaviour of DFB lasers is the coupled wave theory, whereby solutions to two coupled wave equations corresponding to the forward and backward propagating waves is derived from the wave equation.

Consider an axially varying optical field $E(z)$ consisting of right and left propagating field

$$E(z) = A(z) \exp(i\beta_0 z) + B(z) \exp(-i\beta_0 z) \quad 3-2$$

where the Bragg propagation constant β_0 is given by

$$\beta_0 = \frac{2\pi n_{eff}}{\lambda_B} = \frac{\pi m}{\Lambda}$$

where n_{eff} is the effective refractive index. Assuming the refractive index is dependent on the propagation direction z , and the refractive index perturbation, Δn present in the grating region is much smaller than the effective refractive index.

Under the ‘slowly varying envelope’ approximation, the following coupled wave equations can be derived

$$\frac{dA}{dz} = i\Delta\beta A + i\kappa B$$

3-3

$$\frac{dB}{dz} = -i\Delta\beta B - i\kappa A$$

Where $\Delta\beta$ is the deviation of the propagation constant from the Bragg condition and κ is the coupling coefficient given as

$$\kappa = \frac{\pi\Delta n}{\lambda}$$

3-4

The general solution to the coupled wave equations can be expressed as

$$A(z) = A_1 \exp(i\gamma z) + A_2 \exp(-i\gamma z)$$

3-5

$$B(z) = B_1 \exp(i\gamma z) + B_2 \exp(-i\gamma z)$$

where γ is the wave number, substituting equation 3-5 in 3-3 and equating the coefficients of the terms $\exp(\pm i\gamma z)$ results in nonzero solutions if the following dispersion relationship is satisfied

$$\gamma^2 = \Delta\beta^2 - \kappa^2 \quad 3-6$$

where γ is complex because $\Delta\beta$ is complex. By considering a set of boundary conditions, and because of the symmetry of the structure, we assume symmetric and antisymmetric field solutions so that $B_1 = \pm A_2$ and $A_1 = \pm B_2$, substituting these conditions into equation 3-5 and the result substituted into equation 3-3 while taking into consideration the dispersion relation of equation 3-6 we obtain the transcendental characteristic equation

$$\kappa \sin \gamma L = \pm i\gamma \quad 3-7$$

This eigenvalue equation describes the longitudinal field distribution of the modes of the DFB structure for a particular value of the coupling coefficient κ (coupling parameter κL can be used which is independent of the cavity length, L of the structure). This discrete set of modes corresponds to discrete set of eigenvalues, γ which can be determined by substituting the above equation in the coupled wave equations. Kogelnik and Skank thoroughly analyzed the couple wave theory in distributed feedback lasers²⁰

3.3 LC-DFB Laser Simulations

3.3.1 Grating design

Laterally coupled distributed feedback laser are edge-emitting lasers having a periodic variation of the effective refractive index along the direction of light propagation (longitudinal). This periodic structure is also commonly known as ‘grating’, while the ‘distributed feedback’ name is derived from the fact that the feedback is distributed along the grating. The longitudinal variation of the effective refractive index is achieved by etching a corrugation on the surface of the ridge while keeping in mind that it should provide a good overlap and coupling to the optical field in the active region hence the name laterally-coupled. The grating used in this design is a simple rectangular shape to allow for fabrication tolerances which is limited by the resolution of the stepper lithography used in the Canadian Photonics Fabrication Centre (CPFC). This limits us to

3rd order rectangular gratings with period ~ 720 nm. In previous designs and fabrication run in our group, Ron Millett had designed other grating shapes such as trapezoidal, sinusoidal and triangular gratings but these were all ‘washed out’ during etching in the fabrication process. Also other researchers such Streiffer *et al.*^{21,22}, Cho *et al.*²³ and P. Correc *et al.*²⁴ had all concluded that rectangular gratings provided the best coupling coefficient which is expected since the sharp and abrupt interfaces of rectangular gratings can reflect light directly backwards.

The duty cycle is an important geometrical grating design parameter which is defined as the ratio of the length of the wide ridge (a) over the grating period (Λ) as indicated in the schematic of Figure 3-1 below, where W_N and W_W is the narrow and wide ridge widths respectively. The duty cycle and refractive index contrast of the grating determines the Fourier coefficients of the gratings, and as the duty cycle increases, the average refractive index of the grating region tend to increase which affects the optical confinement. As the duty cycle approaches 1, the grating begins to disappear, as well as the coupling.

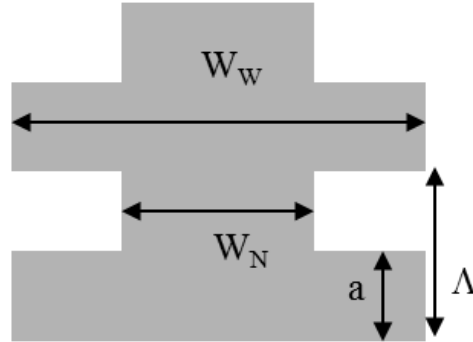


Figure 3-1. Schematic representation of the grating parameters

The grating order used in this design is third order being limited by the ~ 360 nm minimum feature size of the 5x i-line stepper used for fabrication, with this feature size it limits us to a minimum grating period of 720 nm for the target wavelength of 1550 nm, thereby placing the laser design in the third order regime, these numbers can be deduced from equation 3-1 [period = 3^{rd} order \times Bragg $\lambda / (2n_{\text{eff}})$] from this, the minimum number of grating periods needed which equates to the minimum cavity length for optical performance is determined from the transmission and reflection coefficients as shown in

Figure 3-2. As seen in the evolution of the transmission spectrum when the period is varied, the different number of periods shows 1024 periods to be the best but with some consideration for 512 periods being the minimum number of gratings required. As shown in the 1024 periods, the laser structure with that many periodic grating has the strongest reflection at 1550 nm wavelength range.

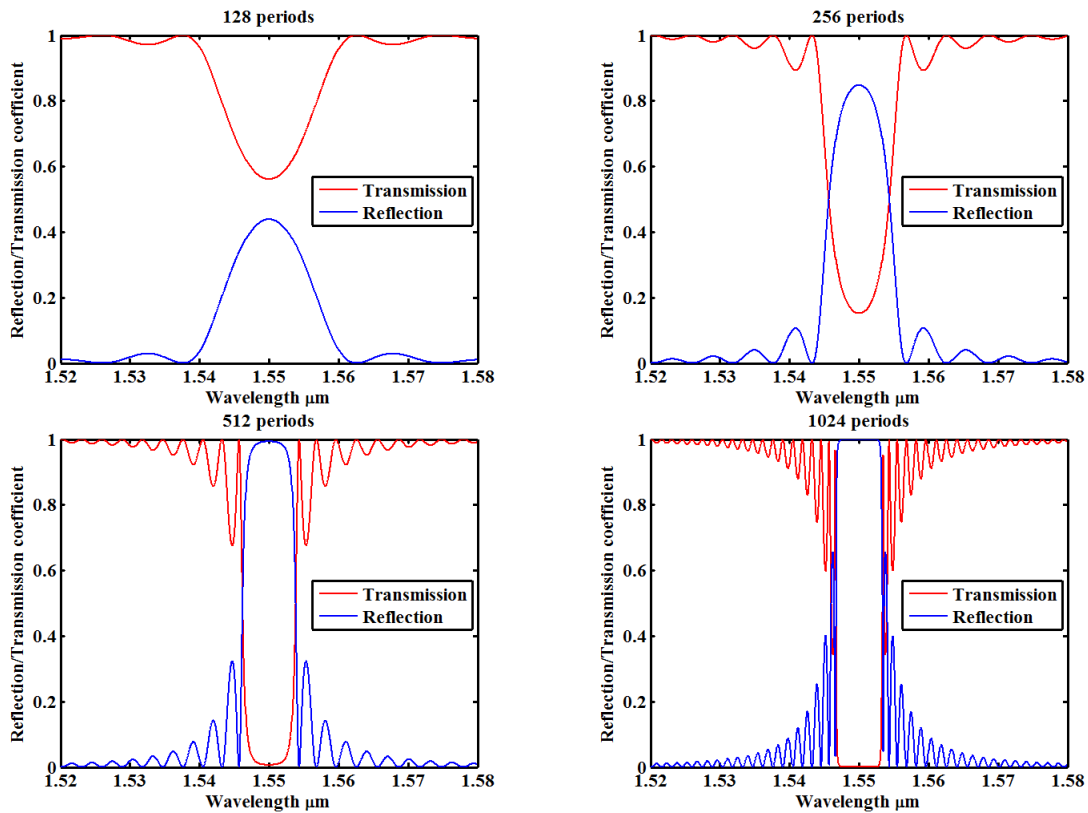


Figure 3-2. Reflection and transmission spectrum for different number of grating periods in the laser longitudinal direction

The choice of the grating height otherwise known as the ridge height corresponding to the use of the word laterally-coupled grating is important because it is desirable to have smooth and vertical sidewalls. Shallower etching is desirable but small ridge height will make the metal contact too close to the active region thereby affecting the optical mode, however greater ridge height will increase electrical resistance, also cause undercutting during fabrication and consequently reduce the coupling strength, 1000 nm ridge height is used for this design

The rectangular gratings implies having two ridge widths as shown in Figure 3-1, the narrow (W_N) and the wide ridge (W_W) widths, the values of the ridge widths are limited by some factors such as, the narrow ridge width must be wide enough to allow for dielectric via to be etched above the ridge for the p-contact, a dielectric minimum of $1\ \mu\text{m}$ is desirable therefore our narrow ridge width has a minimum value of $1.5\ \mu\text{m}$, on the other hand larger values will lead to higher electrical resistance which will cause less hot carriers to be captured in the active region. Very large values of the wide ridge widths will be detrimental in few ways, such as widening the mode profile which will result in coupling losses during testing, thus causing lateral carrier leakage. Large variance between the wide and narrow ridges, will cause uneven carrier distribution and large ridge widths will lead to multi-mode operation.

Analysis of the grating design and its effect on the coupling coefficient was presented by a former member of the group, Ron Millett in his PhD thesis²⁵. The schematic illustrating the final design of the QW LC-DFB laser structure is shown in Figure 3-3.

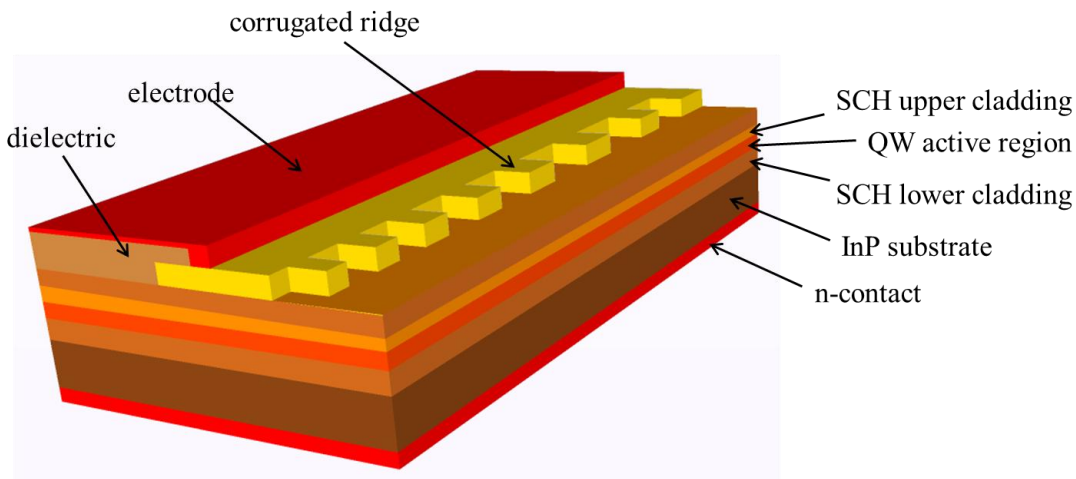


Figure 3-3. Schematic of the QW LC-DFB laser

3.3.2 Grating Simulation

The grating was simulated using FIMMPROP module of the FIMMWAVE simulator which is part of the Photon Design Photonics software suite²⁶. FIMMPROP is ideal for

modelling of optical propagation in structures with high refractive-index contrast using the rigorous eigenmode expansion method (EME) or the rigorous coupled mode theory (RCMT). These methods allow the study of the evolution of the mode power and mode properties along the laser structure during transmission. Although RCMT allows one to model many grating geometries more quickly and accurately than EME, it is limited to low order gratings and cannot fully model the partial wave radiation loss that occurs in 3rd order gratings. Our laser has 3rd order grating and because of this, it is a radiative structure, thus the EME method was used. Although the EME method is very effective it cannot still fully account for the radiating diffraction orders of this higher order grating.

EME is a fully bi-directional and fully vectorial propagation algorithm that offers a rigorous resolution of Maxwell's equation. Whereby the electromagnetic field is decomposed to the sum of local eigenmodes, however, to allow for stability of the algorithm, this method approximates the finite number of modes in each section of the laser structure. For a radiative structure whereby light is coupled to radiation modes of which these radiated light can then couple back into guided modes, a solution is proposed whereby the 3D structure is simplified to a 1D+Z(quasi-2D) problem. Using an effective index approximation which is done by replacing each slice with a uniform layer in which the refractive index is set to the effective index of the fundamental 1D mode of that slice.

The LC-DFB laser has a periodic grating, and to achieve this in FIMMPROP, a wide and narrow ridge width structure is modelled whereby a combination of these 2 structures make up a periodic unit of the laser device. FIMMPROP allows you to design these periodic sections in an automated way, when a given period is defined, you can assign how many number of periods you want to simulate, FIMMPROP simulates just this one period then quasi-instantaneously calculates the remaining using the scattering matrix approach whereby the scattering matrix of one period is multiplied by itself. The derivation of scattering matrix is a well known problem in microwave circuits. The way the scattering matrix works is such that the LC-DFB laser structure is divided into a series of discrete sections with alternating low and high impedances whereby each section spans a half-period of the LC-DFB. Within each section, the S matrices are used

to calculate the incident and reflected forward-traveling and backward-traveling fields from the first section to the n^{th} section.

The fundamental mode profile of the laser cross-section for the wide ridge width of $3\ \mu\text{m}$ and narrow ridge width of $1.5\ \mu\text{m}$ are shown in Figure 3-4 and Figure 3-5 respectively.

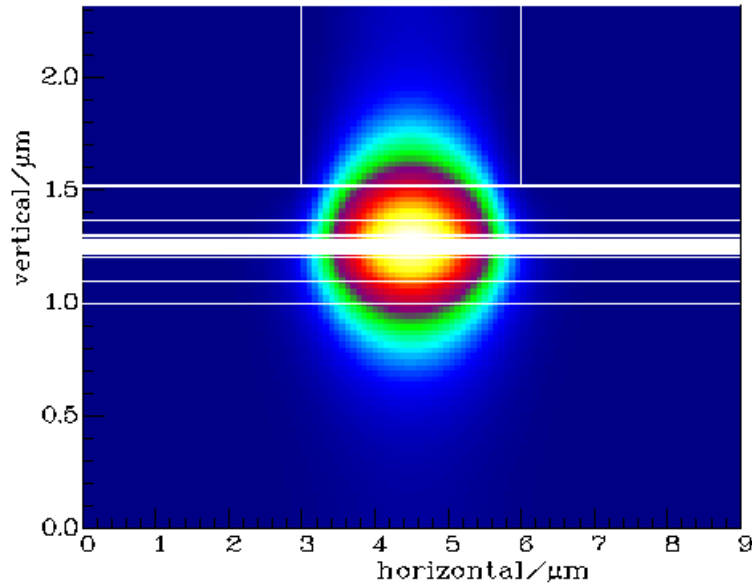


Figure 3-4. Mode profile of the transverse cross-section for the wide ridge

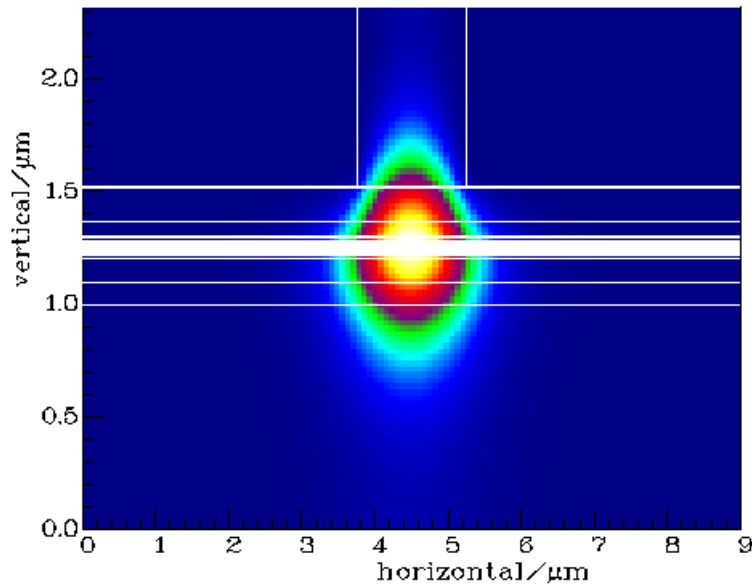


Figure 3-5. Mode profile of the transverse cross-section for the narrow ridge

As observed the mode profile is different for the larger ridge width, it covers a larger area as expected, both mode profiles show good coupling strength between the grating region and the active region. The table below lists the mode properties of these fundamental optical modes

Table 3-1. Mode properties of the fundamental mode

	Wide ridge	Narrow ridge
Propagation constant	12.9247295/ μm	12.87824133
Effective index of the fundamental mode	3.208974	3.197431794
Confinement factor	0.04761554	0.04814516
Fill factor	0.04465727	0.04498891
Effective Area	2.810825 μm^2	2.14639
Mode loss	2.017937/cm	2.02145
Group index	3.270587	3.278177

Whereby, the mode loss is the overlap integral between the material loss profile and the mode intensity. The far field profile of these fundamental modes was plotted on a planar projection as shown in Figure 3-6 and Figure 3-7 for the wide and narrow ridge width structures respectively.

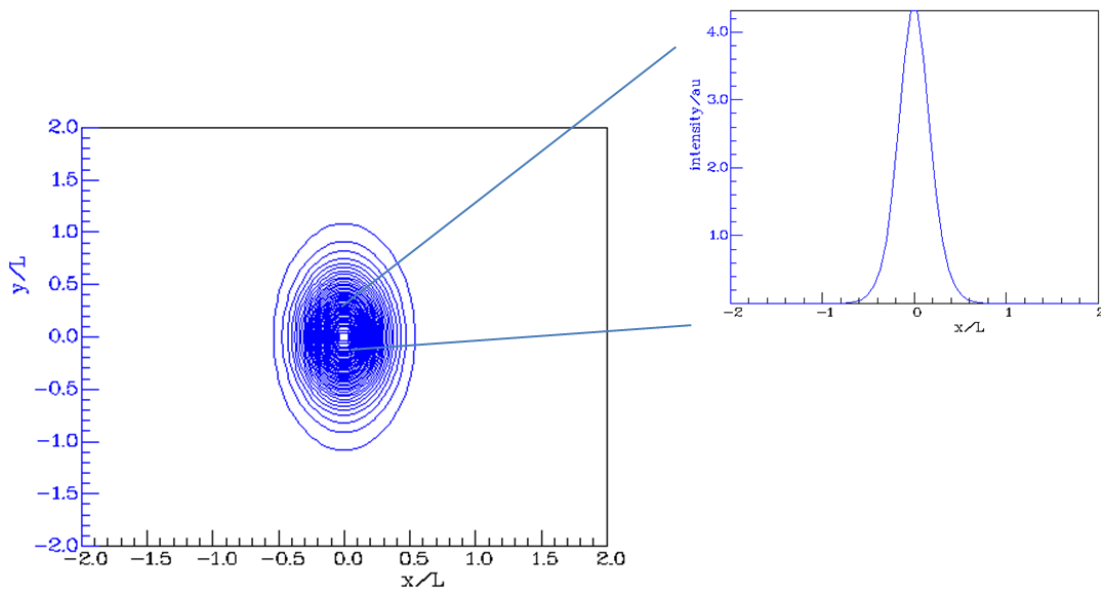


Figure 3-6. Farfield mode profile of the 3 μm ridge width laser structure

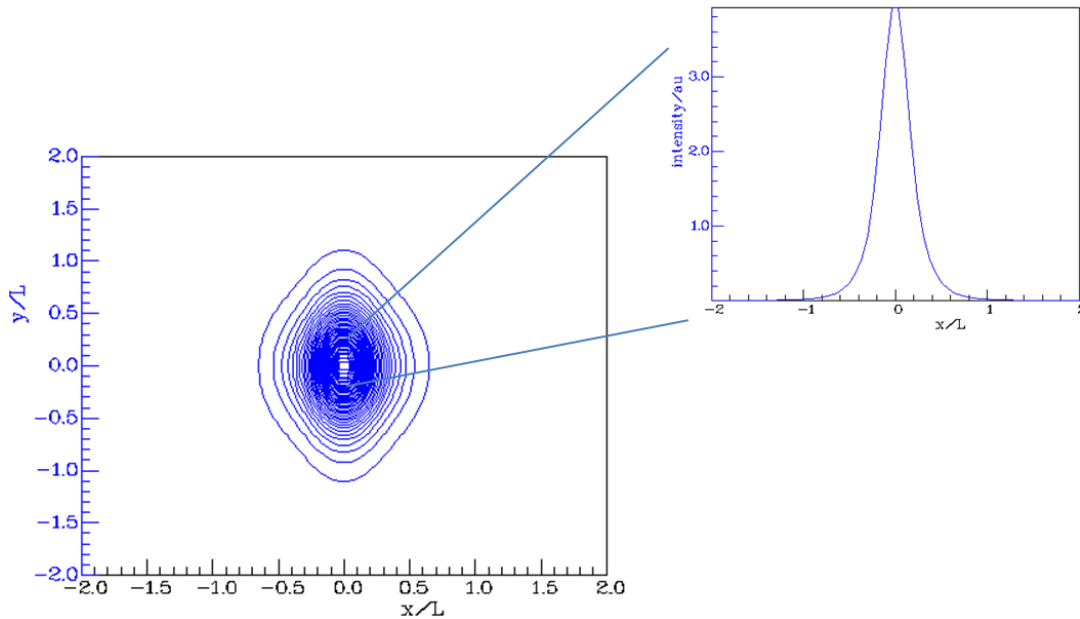


Figure 3-7. Farfield mode profile of the 1.5 μm ridge width laser structure

The wider 3 μm structure has a full wave at half maximum (FWHM) horizontal width of 0.399214 and a vertical width of 0.710889. While the narrower 1.5 μm ridge width structure has a FWHM horizontal width of 0.379984 and a vertical width of 0.73204 (this number is evident in the figure as having a wider vertical extension). Further far field analysis can give information on how much light will be incident on a given area of a photodiode of specific size as an example.

As mentioned earlier, the wide and narrow ridge width structures then form the fundamental periodic unit for the LC-DFB laser device. The laser was simulated and the top view of the propagating wave is shown in Figure 3-8 for different variation from a single period which is just a periodic unit to full but short devices of 10 periods and 100period. These are just for pictorial purposes because for a complete lasing device that has very many periods such as 1000 above, the fimmprop window is too narrow to display all such periods rather it displays a black screen.

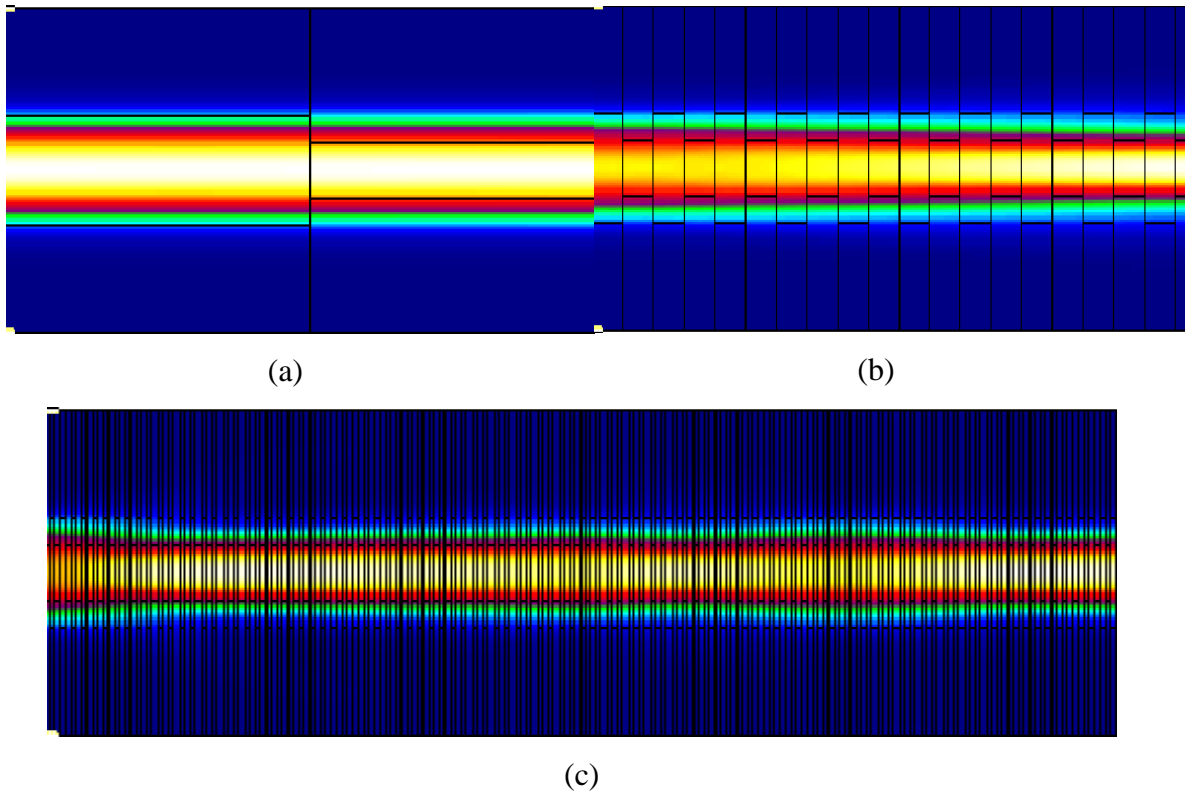


Figure 3-8. Top view of the light propagation through the grating for (a) one period, (b) 10 periods, and (c) 100 periods

In this, FIMMPROP uses the transfer S matrix method such that the laser cavity is divided into subsections in the longitudinal direction and waves then propagate from one subsection to another. The two bi-directionally propagating waves are considered i.e., the inward (backward) and outward (forward) propagating waves whereby the outward wave becomes the inward wave of the next subsection etc.

The evolution of the power in the fundamental mode along the laser for a 1000 μm laser device is shown in Figure 3-9

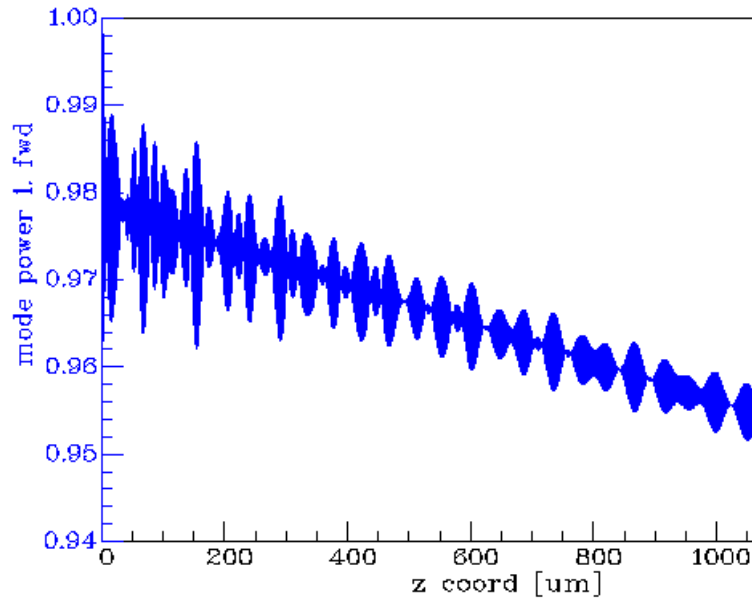


Figure 3-9. Forward mode power in the longitudinal direction of the laser device

It shows a strong forward propagating mode with slight decrease in the power at increasing step this is due to the light being coupled to higher-order modes as it propagates along the device. And the total energy density along the device which is mostly contributed by the forward propagating mode is shown in Figure 3-10 below.

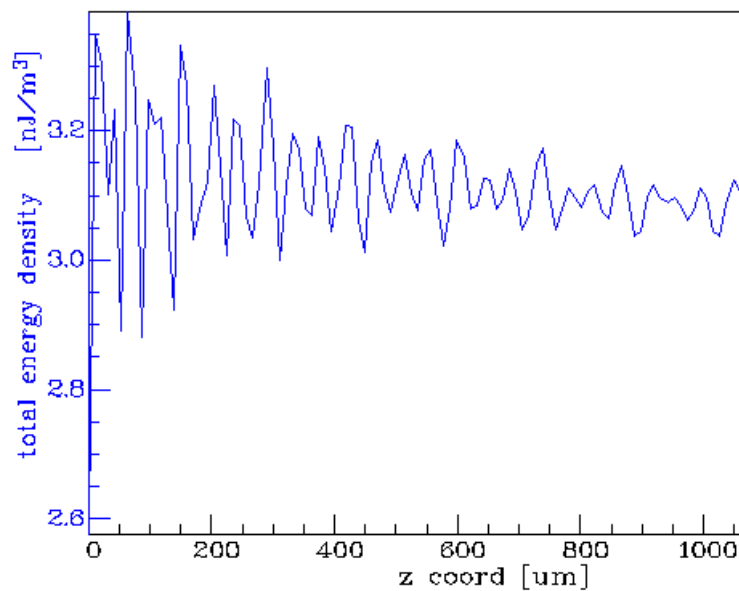


Figure 3-10. Total energy density along the laser device

From all indications it seems there is not much power being lost to radiation modes, so a calculation diagnostic to identify where power is lost from the simulation is shown in Figure 3-11 below. Power coupled to these non-included radiation modes appear as power loss which seems acceptable and low in this simulation at a maximum of 4% in the longitudinal direction. The forward power is shown in green and the backward power is shown in red, the backward power has no scale on the below plot and has an insignificant effect in the overall power when all plotted on the same axis.

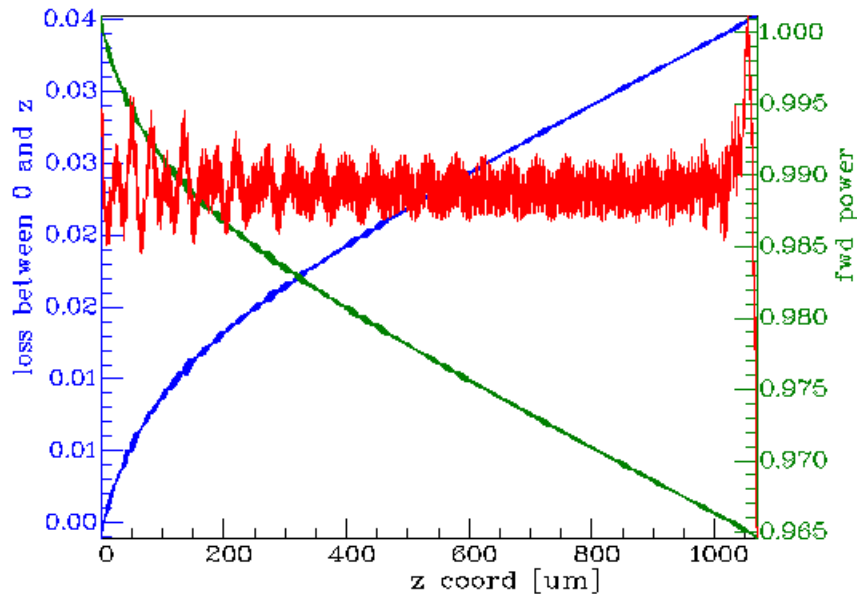


Figure 3-11. Loss and power diagnostics in the laser cavity

The reason why we notice low radiation loss even though this is a 3rd order grating is because the device was simplified to a quasi-2D (1D+Z) structure whereby only dozens of modes were required for the simulation. And also perfectly matched layers (PML) were used at the boundaries of the LC-DFB laser device to absorb radiations from the 3rd order gratings to avoid light being coupled back into the gratings and thereby perturb the simulation. For a 2D+Z simulation then we would require a very large number of modes as well as a very time consuming simulation of which at the end it still would not model the actual 3D DFB structure. This is the limitation of the available Photonics software tools available in the market. There is always an on-going improvement of these tools. The accuracy of the simulation and especially where the most error occurs in the device

can be assessed, the magnitude of error generally increases in the longitudinal direction of the device and including a larger number of modes will result in better simulation accuracy.

3.3.3 Time-Domain Travelling Wave Model

The time-domain travelling wave (TDTW) model is used to describe laser dynamics in a very small characteristic time scale by applying the discrete Fourier transform to the time-dependent envelope functions of the forward and backward travelling waves^{27,28,29}. TDTW models include stochastic spontaneous emission sources and take into account realistically the effects of spontaneous emission and quantum noise on the laser characteristics.

The design of the transverse structure of DFB lasers is such that only the fundamental solutions of transverse electric (TE) and transverse magnetic (TM) modes exist implying a single transverse mode operation. And because the optical feedback and confinement of TM modes are generally smaller than TE modes³⁰, it can be assumed that the fundamental TE mode starts to lase first, and the fundamental TM is suppressed, particularly in compressively strained QW structures like the LC-DFB laser so we consider only the quasi-TE mode. The two-dimensional transverse problem provides the transverse field distribution $u(x,y)$ of the fundamental TE mode. The operation along the longitudinal structure of the laser is explained by a pair of travelling wave equations. The derivation of the travelling wave equations used in this work is based on the assumption that the electric field amplitude can be written as

$$\psi(\mathbf{r}, t) = u(x, y) \sum (F(z, t)e^{\omega_0 t + \beta_0 z} + B(z, t)e^{\omega_0 t - \beta_0 z}) \quad 3-8$$

where β_0 is the characteristic propagation constant and ω_0 is the Bragg frequency otherwise the central frequency. And the forward and backward fields $F(z,t)$ and $B(z,t)$ are spatially and temporally slowly varying envelop functions. Taking into account the periodic variation in the longitudinal direction and assuming that the time variations of

the refractive index are slow compared to the optical frequencies, two travelling wave equations are obtained for the counter-propagating envelope functions³¹

$$\frac{1}{v_g} \frac{\partial F(z,t)}{\partial t} + \frac{\partial F(z,t)}{\partial z} - [\Gamma g - \alpha_i - j\delta]F(z,t) = j\kappa B(z,t) + i_{spon,f} \quad 3-9$$

$$\frac{1}{v_g} \frac{\partial B(z,t)}{\partial t} + \frac{\partial B(z,t)}{\partial z} - [\Gamma g - \alpha_i - j\delta]B(z,t) = j\kappa F(z,t) + i_{spon,f} \quad 3-10$$

where v_g is the group velocity, g is the material gain per unit distance, Γ is the confinement factor, and α_i is the loss factor from absorption, radiation and scattering within the laser cavity, κ is the coupling coefficient between the contra-directionally propagating waves due to the gratings and δ is the dynamic detuning factor whereby it describes the deviation from the Bragg condition due to variation of refractive index otherwise deviation from the propagation constant.

In the TDTW model the counter-propagating envelope functions are solved directly in time-domain and they carry information about the amplitude and phase of the spectral components which is essential in order to characterize the behavior of classical waves in gratings and interfaces. However, photons are not classical particles, therefore, the envelope functions and photon density must be somehow tied to each other. As both the photon flux and the square of the classical electric field are proportional to the light intensity, the envelope functions are normalized according to a semi-classical interpretation³²

$$S = |F(z,t)|^2 + |B(z,t)|^2 \quad 3-11$$

The photon density is related to the optical power of the laser by

$$P = hf v_g SA \quad 3-12$$

where A is the area of the guiding region.

Travelling wave equations are not solely sufficient to describe the behavior of DFB lasers that can exhibit highly non-uniform photon and carrier densities along the length of the laser device. In order to complete the picture of the energy exchange between carriers and photons in DFB lasers, the optical model must be coupled with the electrical transport process. Carrier rate equation is used to model the carrier density space and time dynamics along the laser cavity as described by John Carroll³³.

The time-domain traveling wave calculator of the PICWave³⁴ circuit simulator which is part of the Photon Design suite of photonics software tools was used. PICWave has an active module that can simulate the effect of charge carriers in active devices like lasers. It has an integrated 2D(+z) full vectorial waveguide solver and a grating model that has an integrated ‘Kappa’ calculator that models the gratings using the couple mode theory. It can therefore model advanced physical effects such as carrier diffusion, current spreading, longitudinal and lateral hole burning, as well as time domain response and spectral characteristics. PICWave has ability to import generated gain models from Harold simulator and then uses its wide-band gain fitting algorithm to accurately fit the gain over a broad range of wavelengths. In the TDTW simulation, the grating section is discretized into z-elements such that the algorithm approximates the grating by constant-pitch gratings within each z-element. In PICWave, the TDTW calculator first solves the optical mode and calculates the grating Kappa (coupling coefficient), then goes ahead to solve the current flows, heat flows, lateral diffusion/carrier recombination and optical propagation and stimulated emission.

Gain and peak wavelength

The imported stacked gain spectra at increasing carrier densities (green colour) are shown in Figure 3-12 below with the time domain model wide-band fitting (blue colour) from picwave.

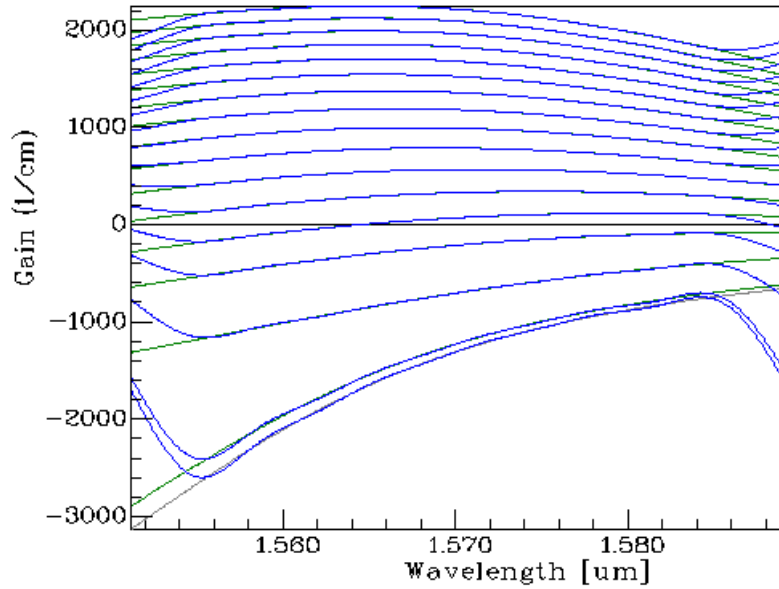


Figure 3-12. Gain spectra (imported data is green and fitted is blue)

The stacked gain spectra shows the sampled portion of the imported spectra which is after smoothing, scaling, extrapolation, interpolation have been applied within the simulation free spectral range. As observed the gain is well fitted in the central portion of the free spectral range and peaks at 1566 nm, however it deviates from the imported spectra at the outer edges of the free spectral range, this is due to the time domain filter used to model the gain. The maximum gain fitting is shown in Figure 3-13 below

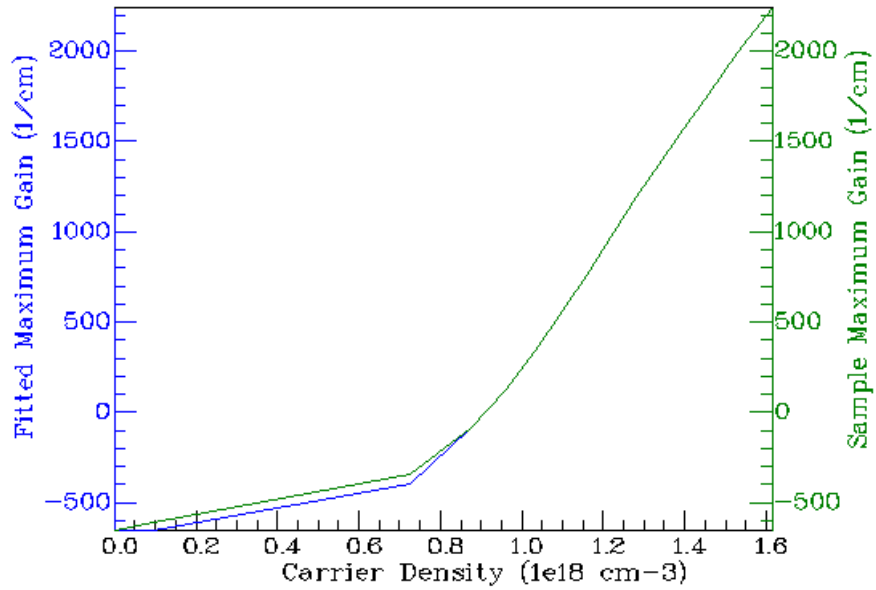


Figure 3-13. Maximum gain vs carrier density. Imported (green) and fitted (blue)

The wavelength peak is fixed at the band edge which is the wavelength corresponding to the transparent carrier density (carrier density below transparency). This fitting is shown in Figure 3-14

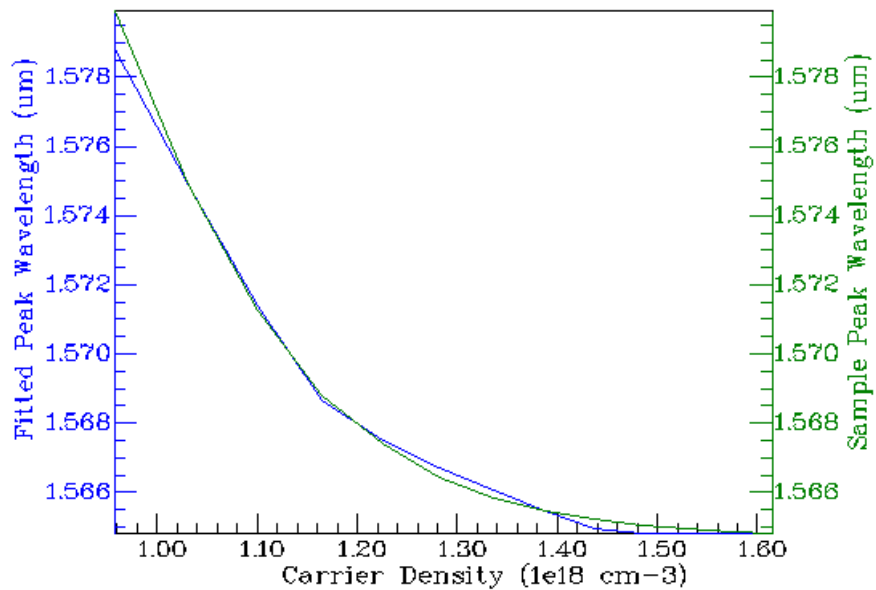


Figure 3-14. Peak wavelength vs carrier density. Imported (green) and fitted (blue)

Light-Current

The light-current characteristic with uniformly distributed injection current of 0-100 mA is shown in Figure 3-15. The threshold current is at 35mA, the turn-on transient settles down around 7ns which characterises delay in onset of lasing above threshold, this delay is evident in the L-I curve kink. The simulation time of the simulation is chosen to be 20 ns in order to guarantee that the continuous wave operation is reached. A threshold current of 35 mA is measured with a differential quantum efficiency of 0.52W/A, the non-linearity of the curve due to gain saturation and heating is very negligible.

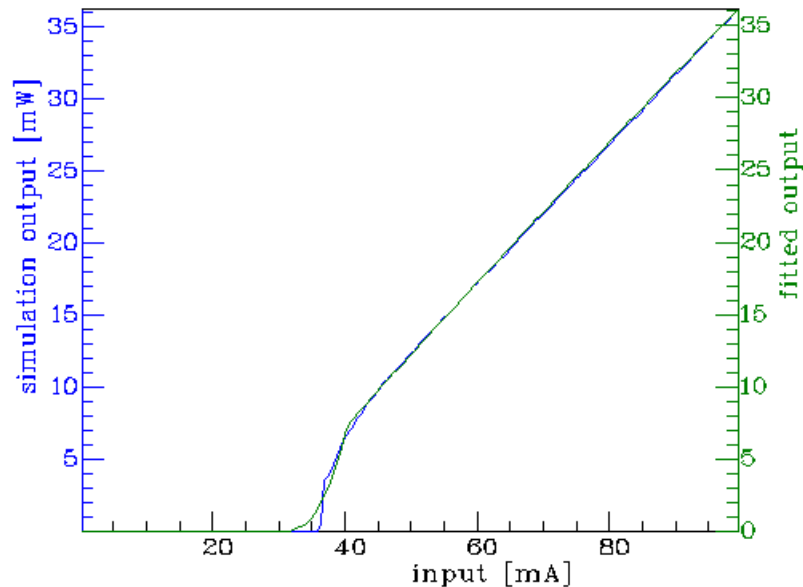


Figure 3-15 Light-current characteristic

A phase shift placed within the grating introduces a reflectivity dip in the stopband. This dip in the reflectivity enables single longitudinal mode emission for the quarter-wave shifted laser. An integer multiple of a quarter of the Bragg wavelength is usually chosen as a phase-shift section for the grating because it guarantees the widest band gap and attenuates the other longitudinal modes near to the Bragg wavelength¹⁹. Although the original LC-DFB laser design has no phase shift but for simulation purposes a phase shift was introduced in the middle of the grating for comparison and future recommendation.

Output power in time domain

The evolution of the output power with time at constant drive current of 50mA is shown in Figure 3-16 for both the no-phase shift and the phase shifted LC-DFB laser

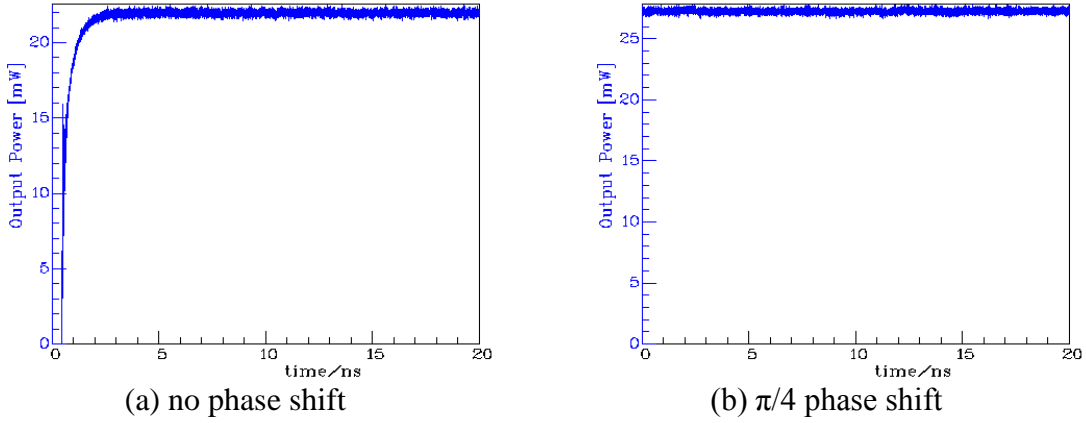


Figure 3-16 Output power in the time domain at constant current injection of 50mA

Spectrum

The spectrum of the laser is shown below around the center wavelength of 1560nm. The side modes are strongly suppressed with a side mode suppression ratio of 57 dB and the laser emits as single mode as shown in Figure 3-17

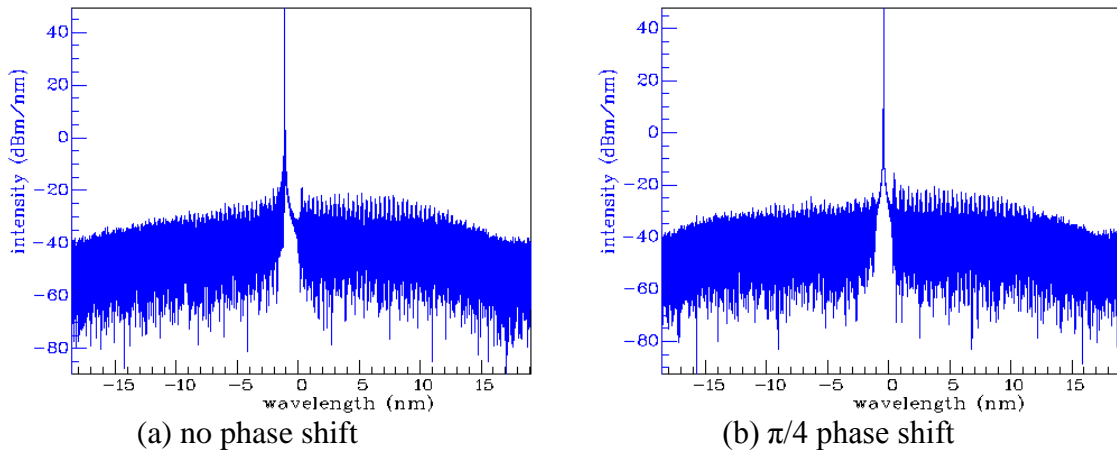


Figure 3-17 Intensity spectra of the laser

Time evolving spectrum

The spectrum is further analyzed in the time evolving spectrum as shown of Figure 3-18 comparing both the laser and its phase shifted counterpart. Each of this spectrum consist of a set of spectra taken at successive time intervals with the 20ns. The no phase shift laser shows a small time delay in pico seconds before emission and a much wider spectrum than the $\pi/4$ wavelength shifted laser.

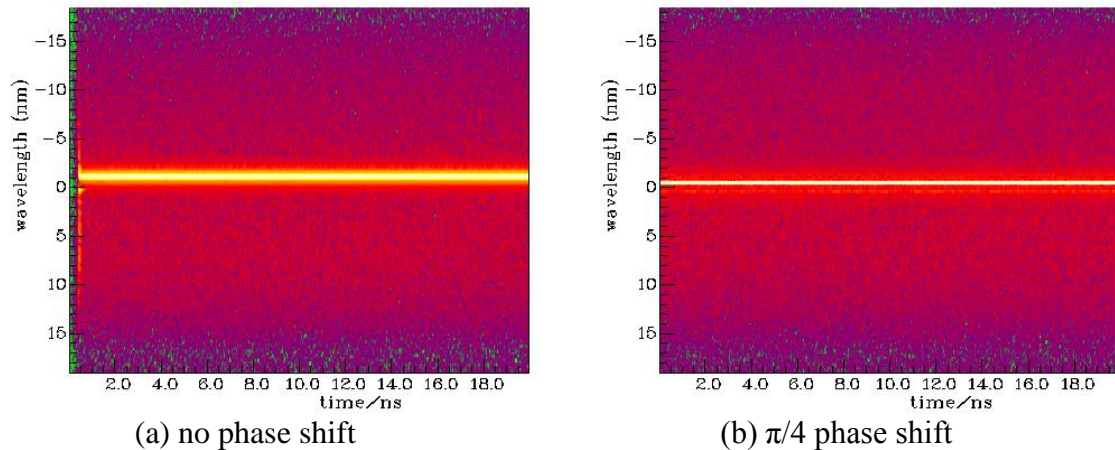


Figure 3-18 Time evolving spectra of the laser

Longitudinal and lateral spatial profile

Longitudinal spatial hole burning is as a result of the stimulated recombination as well as non-uniformity in the carriers and photon densities along the cavity longitudinal direction³⁵. The effects of spatial hole-burning (both longitudinal and lateral) is of great importance in DFB lasers because of the variation in the refractive indices, carrier densities and gain affects the magnitude of the phase and feedback from each section of the grating. The longitudinal non-uniformity in the effective refractive index and gain of the mode arises if the longitudinal mode intensity distribution is non-uniform, whereby as the photon density rises, the injected carrier density hole burns. This is what causes the mode intensity to change and as a consequence changes the gain suppression of the side modes relative to the lasing mode. If the side modes are not sufficiently suppressed, with increasing output power, it can lead to multi-mode operation. And the lasing mode will exhibit a non-linear light-current characteristic³⁶. Single mode operation and high side mode suppression ratio is highly desirable.

The intensity of the TE fundamental mode power in the longitudinal direction is shown in Figure 3-19. The mode power has a stronger peak in the phase shifted laser and at the location of the phase shift which is the middle of the grating

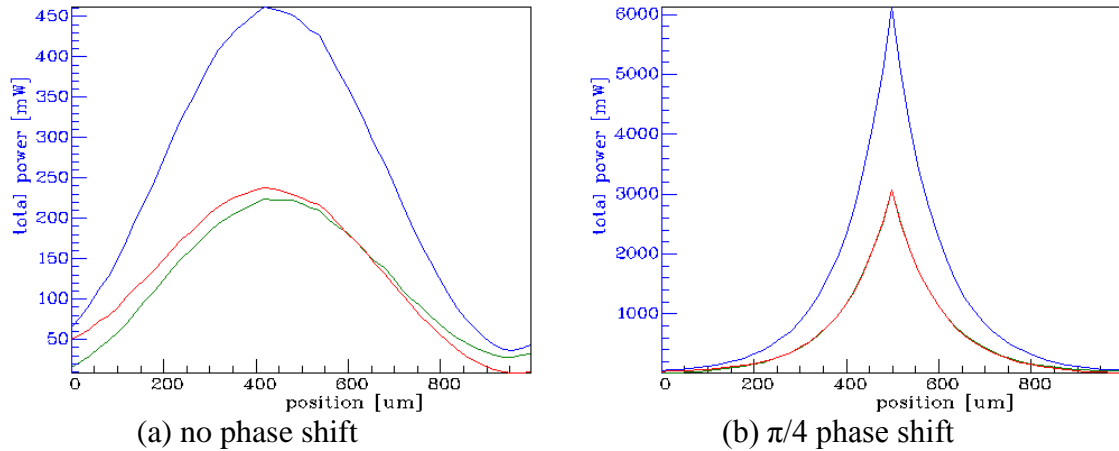


Figure 3-19 Longitudinal profile of the total optical power (blue), forward (red) and backward (green).

The longitudinal z-profile of the carrier and current densities are shown in Figure 3-20 and Figure 3-21. The strong intensity peak had caused longitudinal hole burning with a dip in the carrier density

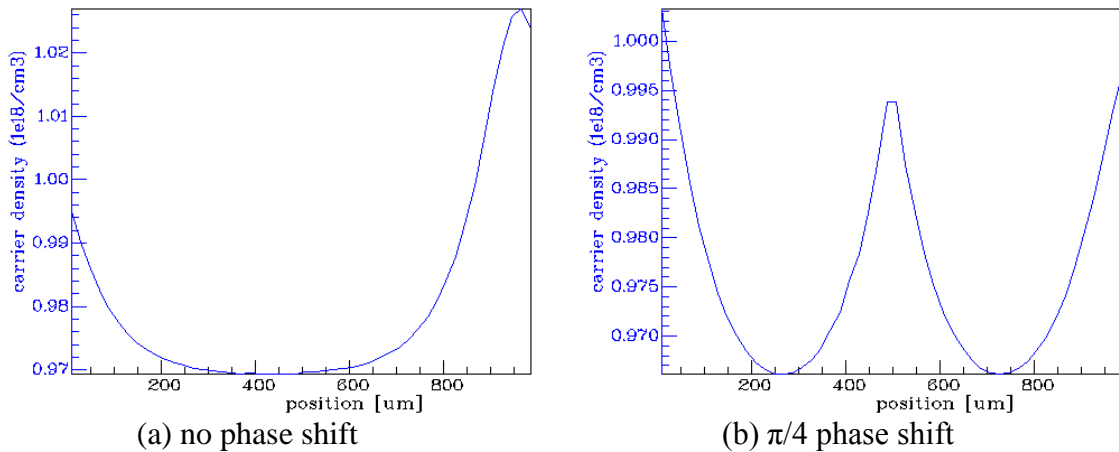


Figure 3-20 Longitudinal spatial profile of the carrier density

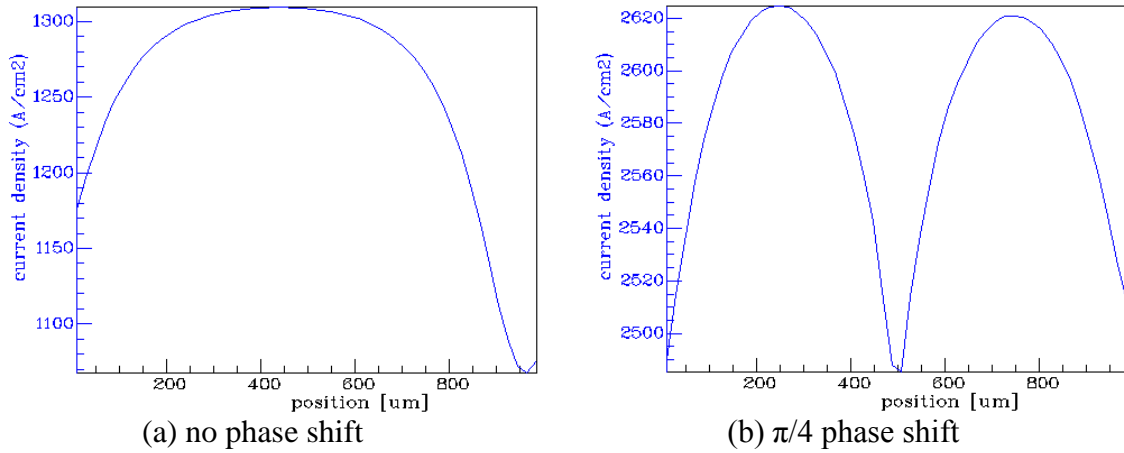


Figure 3-21 Longitudinal spatial profile of the current density

Figure 3-22 shows the material gain profile of the laser

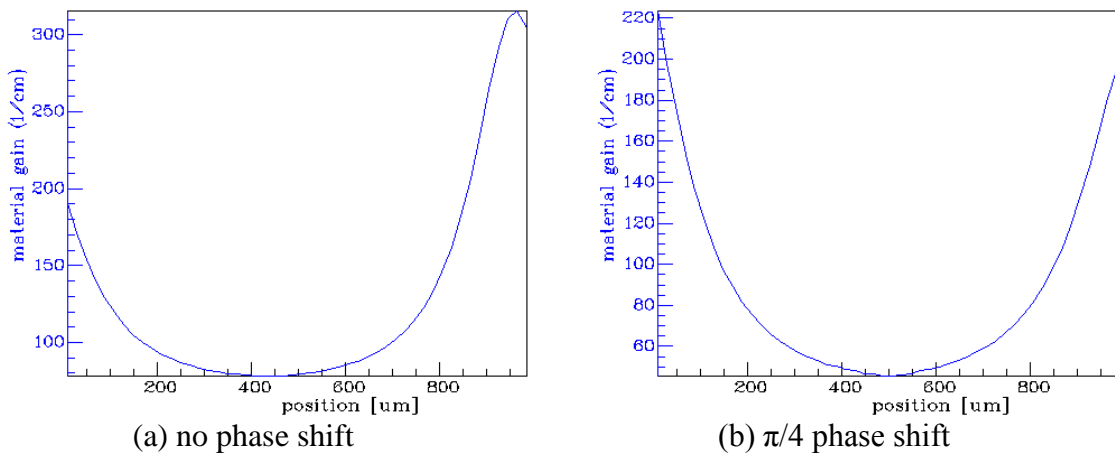


Figure 3-22 Longitudinal profile of the material gain

The lateral spatial profile of the carrier and current densities is shown in Figure 3-23 and Figure 3-24, the lateral profile is very similar between the two lasers.

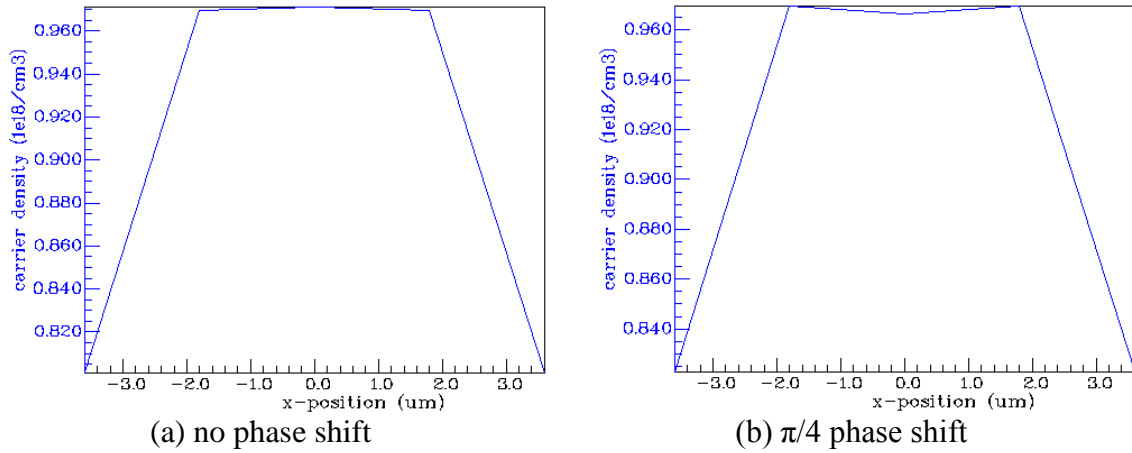


Figure 3-23 Lateral profile of the carrier density

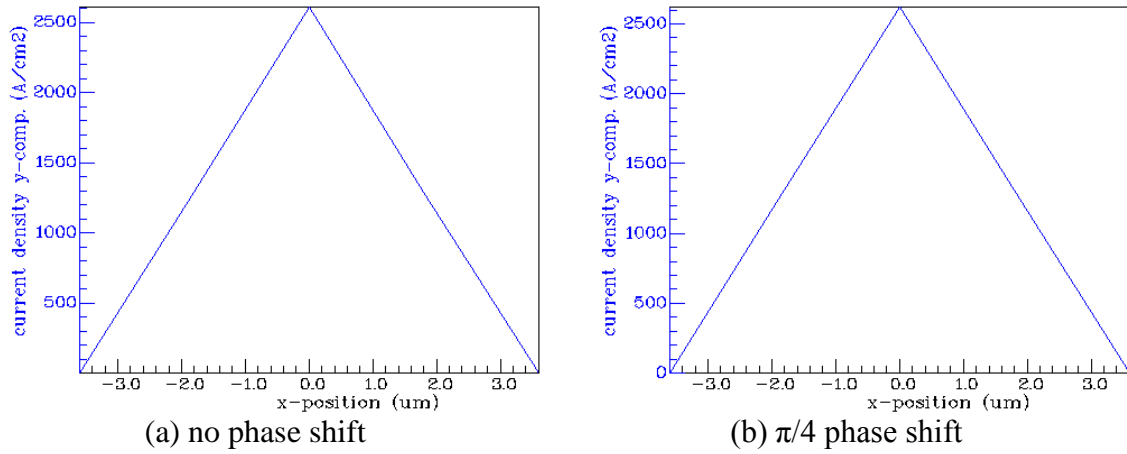


Figure 3-24 Lateral profile of the current density

3.4 Design Considerations for the Quantum Dot LC-DFB laser

The functionality of the quantum confinement of carriers in semiconductors has fostered many new designs and the trend is to provide more stringent carrier confinement through these designs. We have seen this from the homojunction to heterojunction, from bulk to quantum well and now to quantum dot (QD) lasers³⁷. QD lasers provide the size quantization concept to semiconductor lasers whereby carriers are spatially restricted to the smallest possible dimension. The QD lasers have been highly studied and reviewed over the past two decades^{38,39,40,41,42}. Increasing carrier confinement in all three

dimensions can provide several key advantages to the laser, some of the benefits reported are lower threshold current and superior temperature stability⁴³, reduced linewidth enhancement factor⁴⁴, reduced leakage due to the suppressed diffusion of non-equilibrium carriers increase material and differential gain⁴⁵ as well as increased flexibility to adjust the wavelength and large modulation bandwidth.

Miller *et al.* presented work on laterally-coupled distributed feedback lasers using e-beam lithography⁴⁶. e-beam is an established fabrication technique and therefore a fabrication of choice for many researchers^{47,48,49,50,51,52}. Reid *et al.* published work on third order gratings fabricated using stepper lithography⁵³. They published good results for a good threshold current, high side mode suppression ratio (SMSR), high power but not narrow linewidth. They noticed partial hole burning at higher power and concluded that it must be related to their grating design. Laakso *et al.* has demonstrated LC-DFB lasers with higher order gratings using nano-imprint technique⁵⁴, they have presented low threshold currents and good SMSR but these lasers do not operate in the telecommunication band of interest rather 980 nm. Zanola *et al.* presented work on $\lambda/4$ phase shift distributed feedback laser operating in the 1550 nm but made from InAlGaAs/InP quaternary material system, low threshold currents and high SMSR values were obtained as well⁵⁵.

In our PTLab group, we have published some good results for InGaAsP/InP LC-DFB lasers operating in the 1310 and 1560 nm wavelengths and fabricated using the 5x stepper lithography^{56,57}. The 1550nm wavelength LC-DFB lasers have been optimized with multi-electrode contacts and some published results have centered around the design, as well as the narrow linewidth obtained for these lasers^{58,59,60,61}. Additional interesting results have been discovered such as the benefits of the multi-electrode configurations, using the optical feedback experimental techniques to further reduce the linewidth⁶², as well as flat frequency modulation (FM) response. It is necessary to explore other design options to make the LC-DFB lasers even better^{63,64}. The QD design we believe will further reduce the threshold current and make the laser more temperature stable when compared with the previous designs.

3.4.1 Epitaxial Design

The epitaxy of the QD LC-DFB laser structure is designed to provide gain around 1550 nm wavelength, to efficiently inject carriers into the active region. The active region constitutes a large number of quantum dots grown on a wetting layer that acts as a reservoir. Few layers of quantum dots are ideal as shown in Figure 3-25. In actual case, the dot sizes are as uniform in size and shape as portrayed in the figure

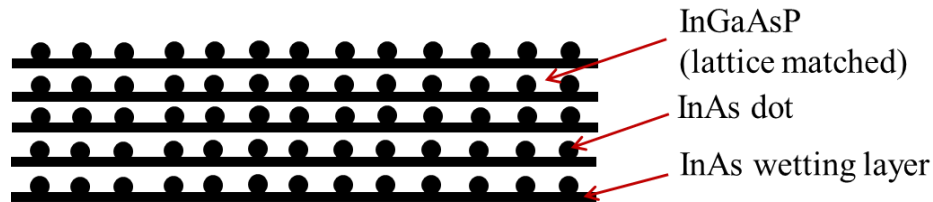


Figure 3-25. Schematic of 5 layers of InAs QDs

This core is a 1.15Q 250 nm thick with an average refractive index of 3.364⁶⁵, the active region is made up of the 5 stacked InAs/InP quantum dot layers with equal wetting layers, each QD layer has an average density of dots 5×10^{10} dots/cm² (5×10^{-4} dots/nm²) for a mean dot size of 30nm (D) x 4nm (H). This core region is a ‘third party recipe’ from the National Research Council, Canada. They have developed world class quantum dot lasers designed by Z. G. Lu et al^{66,67} and grown by Philip J. Poole et al⁶⁸. A typical photoluminescence (PL) map of a QD laser provided by Phillip J. Poole is shown in Figure 3-26. The colour map shows a circular symmetry due to the rotation of the substrate from long wavelength at the center to shorter wavelengths at the edges with variation in the wavelength from 1498 - 1562 nm. These variations in the PL map can be detected during testing of same laser devices cleaved from different sections of the same wafer.

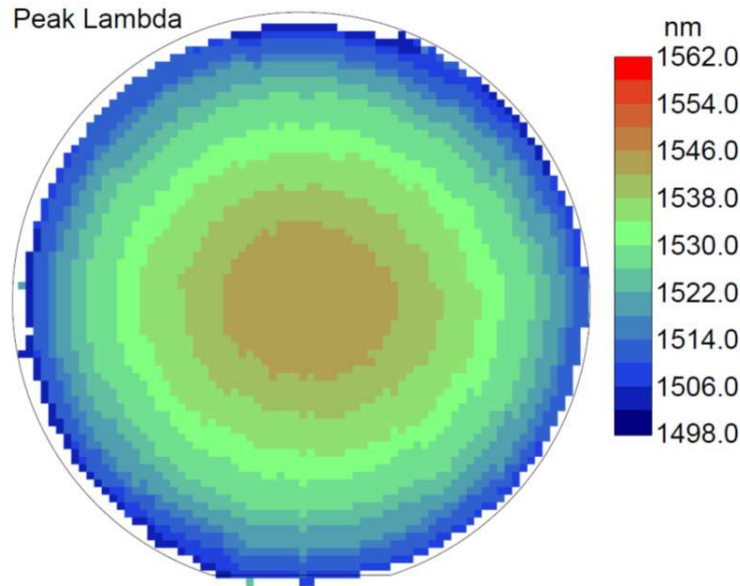


Figure 3-26. Typical quantum dot laser wafer PL map⁶⁵

The surrounding separate confinement heterostructure sandwiching this QD active region is designed to provide optical mode confinement to the active region, as well as but not limited to, low threshold current, low electrical resistance and high efficiency. The third order rectangular gratings are then patterned on the ridge sidewalls of the QD LC-DFB laser, or otherwise not for the QD Fabry-Perot laser.

The design of a laser heterostructure is complicated and needs many interacting considerations to arrive at the above epitaxial design. The following design considerations were implemented. Each epitaxial layer is made of different parameters such as the material composition, thickness, bandgap, dopants/doping level etc., as well as dimensional parameters such as ridge width and depth, cavity length etc., although these parameters can be individually optimized for each layer, any change can affect all other layers in the structure. However, not all layers are critical to the overall performance of a laser, therefore emphasis is placed on the most important layers and parameters.

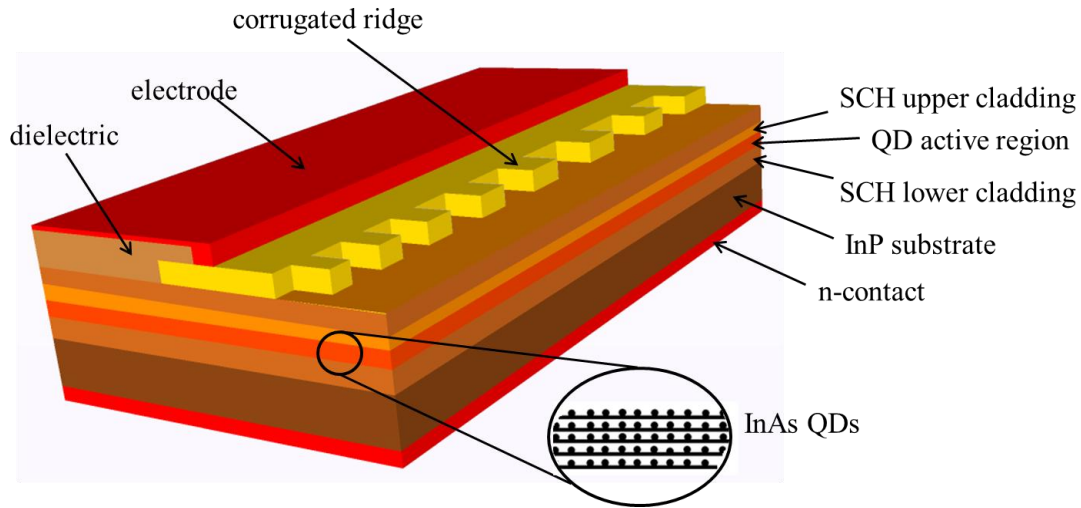


Figure 3-27. Schematic of the QD LC-DFB laser

As shown in Figure 3-27, starting with the QD active region, it is made up of the most critical layers, the composition and thickness of these layers is based on the target wavelength of the laser. This region as stated above has been provided. This core region will generally be undoped although during growth of the layers some p-dopant (Zn) might diffuse into it. The next important layers are those closest to the active region and sandwiching it. They are called the separate confinement heterostructure (SCH) layers, the p-doped above and the n-doped below. They are important because they influence the carrier concentration and optical confinement. For the upper p-doped SCH layer, simulations were done for different thicknesses and composition and their dependence on the characteristic performance of the laser such as threshold and efficiency. The threshold and efficiencies seem to reduce as thickness reduces, however if too thin the mode profile changes, asymmetric mode profile can result in coupling losses, thick layers also caused the mode profile to change. The thickness of the upper SCH layer was set to 150 nm, and the doping set to $5 \times 10^{17} \text{ cm}^{-3}$. To influence the bandgap, the material composition was chosen such that the bandgap of the material is large enough to allow flow of carriers into the active region but also adequate enough such that the ridge layer sees a drop in the bandgap. There is a thin etch stop layer above the SCH layer, to allow tolerance of the ridge definition during the etching process.

A highly p-doped InGaAs layer is used at the top as an ohmic p-contact. The right material composition of this layer is needed to avoid the mode profile being pulled too upwards away from the active region and sometimes producing a local maximum in this layer, such situation happens if the refractive index is much higher than that of the active region but can be mitigated by increasing the size of the ridge or reducing the size of the InGaAs layer, but a thin InGaAs layer will cause the contact to be less ohmic. The thickness of this layer is set at 100 nm and the refractive calculated for this layer is 3.78 while that of the active region is 3.364, even this is a big difference, it did not affect the position of the mode profile because of the thickness of the ridge set at 1000 nm. However, etching of the ridge can be difficult, it is important to have smooth and vertical sidewalls especially because the gratings are etched on the ridge sidewalls, in order words this defines the gratings and its performance. Etching depth is optimized to ensure adequate coupling between the grating and the active region. The choice of metal contact combination of Au/Pt/Ti (gold/platinum/titanium) is used. Using only a gold contact, although it has low losses tend to have poor adhesion to semiconductor materials and during annealing has rapid diffusion of the Au into the semiconductor material⁶⁹. To mitigate this, platinum is used right below it to prevent adhesion and titanium is used to improve metal adhesion to the semiconductor material^{70,71}.

Table 3-2. Material composition of the laser

Layer Name	Material (composition)	Band gap (nm)	Thickness (nm)	Dopant/ Type	Doping Level (cm ⁻³)
p-contact	InGaAs	1660	100	Zn /p	$N_A = 1.5 \times 10^{19}$
Ridge	InP	919	1000	Zn /p	$N_A = 1 \times 10^{18}$
Etch stop	InGaAsP	1300	10	Zn /p	$N_A = 5 \times 10^{17}$
SCH upper cladding	InP	919	150	Zn /p	$N_A = 5 \times 10^{17}$
Quantum dot active region '3 rd party recipe'	InAs	1550	250	Undoped	Undoped
SCH lower cladding	InP	919	200	Si /n	$N_D = 5 \times 10^{17}$
Buffer	InP	919	400	Si /n	$N_D = 5 \times 10^{18}$
Substrate	InP				

The final growth structure is therefore made up of the active region and the surrounding heterostructure layers. The epitaxial structure is shown in Table 3-2 with the active region highlighted in yellow. Appendix A shows a table for the laser design variations in more details.

The fundamental mode profile of the laser cross-section for the narrow ridge is shown in the Figure 3-28 below. As observed it shows good coupling strength between the grating region and the active region.

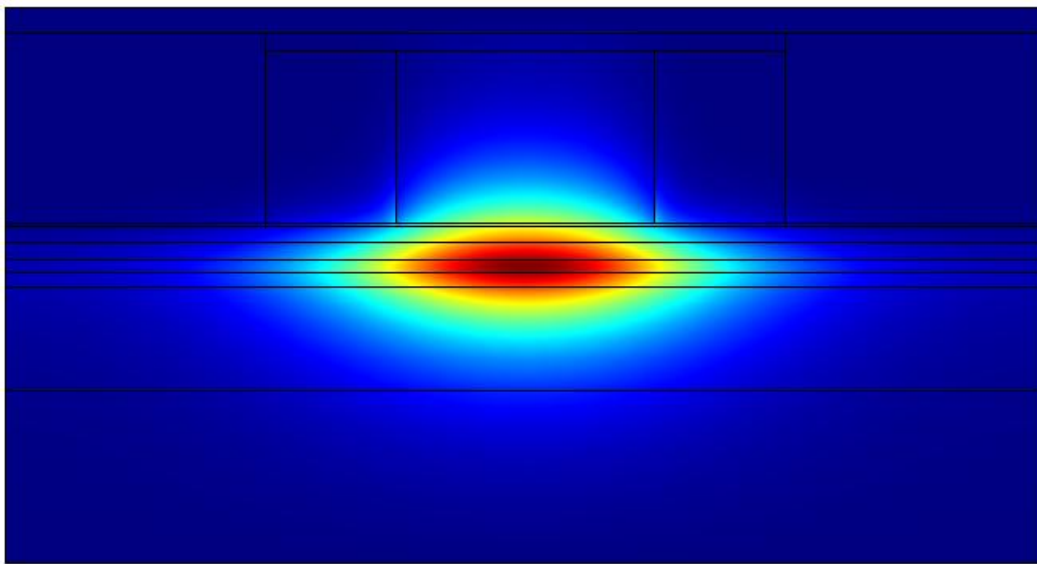


Figure 3-28. Mode profile of the transverse cross-section of the laser

3.4.2 Mask Layout

The LC-DFB laser devices were laid out on a mask using commercially available mask layout software called DW-2000 v8.6 (dw-2000TM) by Design Workshop Technologies made available through CMC Microsystems, Canada. It uses a Graphics Programming Environment (GPE) for data generation procedure. Scripts can be written to automate repetitive and batch tasks, which saves time and reduces the amount of code writing. DW-2000 then implements a technique called parametric cells (PCells) which allows elements (laser structure) to be created automatically on the layout. This is made possible by assigning arbitrary input parameters such as in a QD DFB laser device, one-word

parameters can be defined each with default values to represent the period of the grating, cavity length, narrow ridge width, wide ridge width, duty cycle, trench width etc. The mask layout created had different types of PCells to represent the QD laser design variations such as for the standard DFB, multi-electrode DFB, Fabry-Perot laser, Multi-electrode Fabry-Perot. The PCell definition allows dimensions of similar laser devices in the layout to be changed quite easily such as if for instance after laying out the mask, you realize you need to adjust any of the input parameters for all or some of the laser devices, these can be changed. The script that lays out the entire mask creates an instance of each of these PCells for each of the design variations.

Table 3-3. QD LC-DFB laser design variations with laser device labels

L21	L41	L61	L81	L101	L121
L22	L42	L62	L82	L102	L122
L23	L43	L63	L83	L103	L123
L24	L44	L64	L84	L104	L124
L25	L45	L65	L85	L105	L125
L26	L46	L66	L86	L106	L126
L27	L47	L67	L87	L107	L127
L28	L48	L68	L88	L108	L128
L29	L49	L69	L89	L109	L129
L30	L50	L70	L90	L110	L130
L31	L51	L71	L91	L111	L131
L32	L52	L72	L92	L112	L132
L33	L53	L73	L93	L113	L133
L34	L54	L74	L94	L114	L134
L35	L55	L75	L95	L115	L135
L36	L56	L76	L96	L116	L136
L37	L57	L77	L97	L117	L137
L38	L58	L78	L98	L118	L138
L39	L59	L79	L99	L119	L139
L40	L60	L80	L100	L120	L140

MultiElectrodeDFB

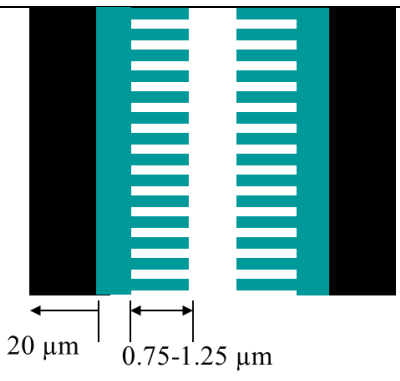
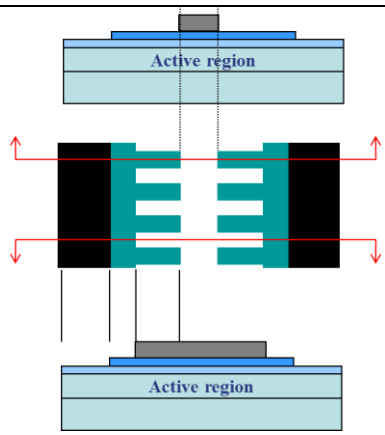
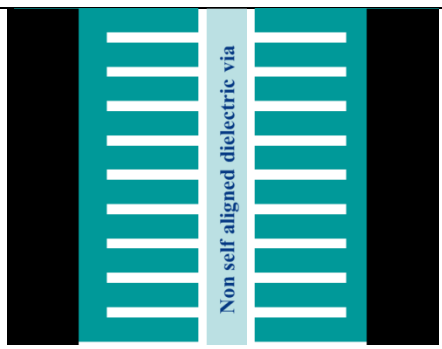
FabryPerot

MultiElectrodeFP

StandardDFB

Table 3-3 shows the laser design variations (colour coded) with device labels to differentiate each laser device. L21-L81 are all multi-electrode laser devices with the blue colour for the LC-DFB while yellow colour for Fabry-Perot. L81-L140 are all single electrode laser devices with green colour for Fabry-Perot and red colour for LC-DFB lasers. More details of these variations and the grating parameters are shown in AppendixA.

Table 3-4. Some mask layer definitions for the lithography process of the QD LC-DFB laser

	Layer	Schematic
Grating definition	Lithography + dry etching	 <p>20 μm 0.75-1.25 μm</p>
Ridge definition	<ul style="list-style-type: none"> - Dry etch (for small features) - Dry etch + wet etch (for large features) - Dry etch + wet etch de-risk (large features + 0.1μm bias on both sides) 	 <p>Top and side view</p>
Dielectric via	<p>Non self-aligned, via will be used with sloped sidewall. - 0.25 μm bias from the ridge edge</p>	 <p>Non self aligned dielectric via</p>

The mask of the LC-DFB laser layout was designed to be compatible with a stepper lithography process, whereby a single stepper tile is continuously exposed along the wafer during the lithography processing. The size of the stepper tile is 7500 μm x 9250 μm . The mask includes seven layers: three dry/or wet etching layers for the ridge definition, an evaporated metal layer that includes the device labels shown in the table

above, a dielectric via layer, an InGaAs removal layer, and an evaporated metal layer for p-contact. The layer definition is shown in Table 3-4 and Figure 3-29. The three dry-etching layers include one layer for the detailed etching around the ridge, another layer for the coarser etching of the trench around the ridge, and a de-risk layer to create a bias on both sides. The dielectric via is made narrower than the ridge layer and have sloped sidewalls to permit better coverage of the evaporated metal material.

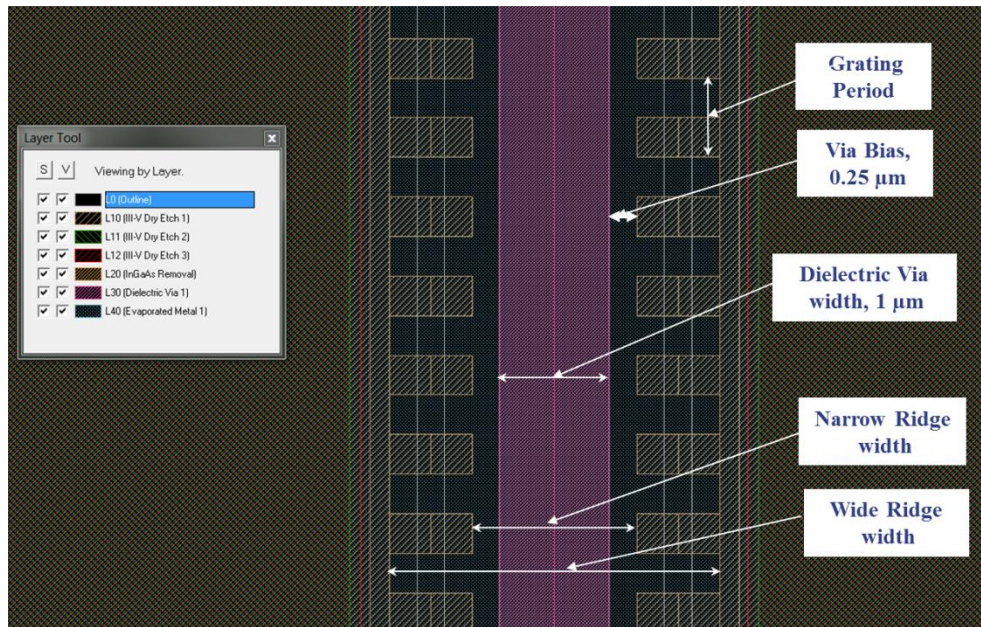


Figure 3-29. DFB laser PCell with the rectangular grating indicating details for the lithography process

The mask also includes an InGaAs removal layer that defines regions where InGaAs is to be etched away. This is done for the multi-electrode configurations for less crosstalk to reduce the amount of lateral current spreading between the electrodes. The evaporated metal layer is for the p-contact and also to create the device labels and cleaving marks.

The whole area of the mask layout stepper tile from DW-2000 is shown in Figure 3-30, it shows colour coded areas to indicate the four different design variations, as well as the cleaving channels, that will cleave the laser devices into bars of specific cavity lengths indicated in mm above the figure such lengths are 500, 750, 1000, 1250, 1500 μm , A zoom in of the 750 μm L62 (2-electrode) and L63(3-electrode) laser devices are

indicated. The final mask layout is shown in Figure 3-30, this is related to Table 3-3 that showed the laser design variations.

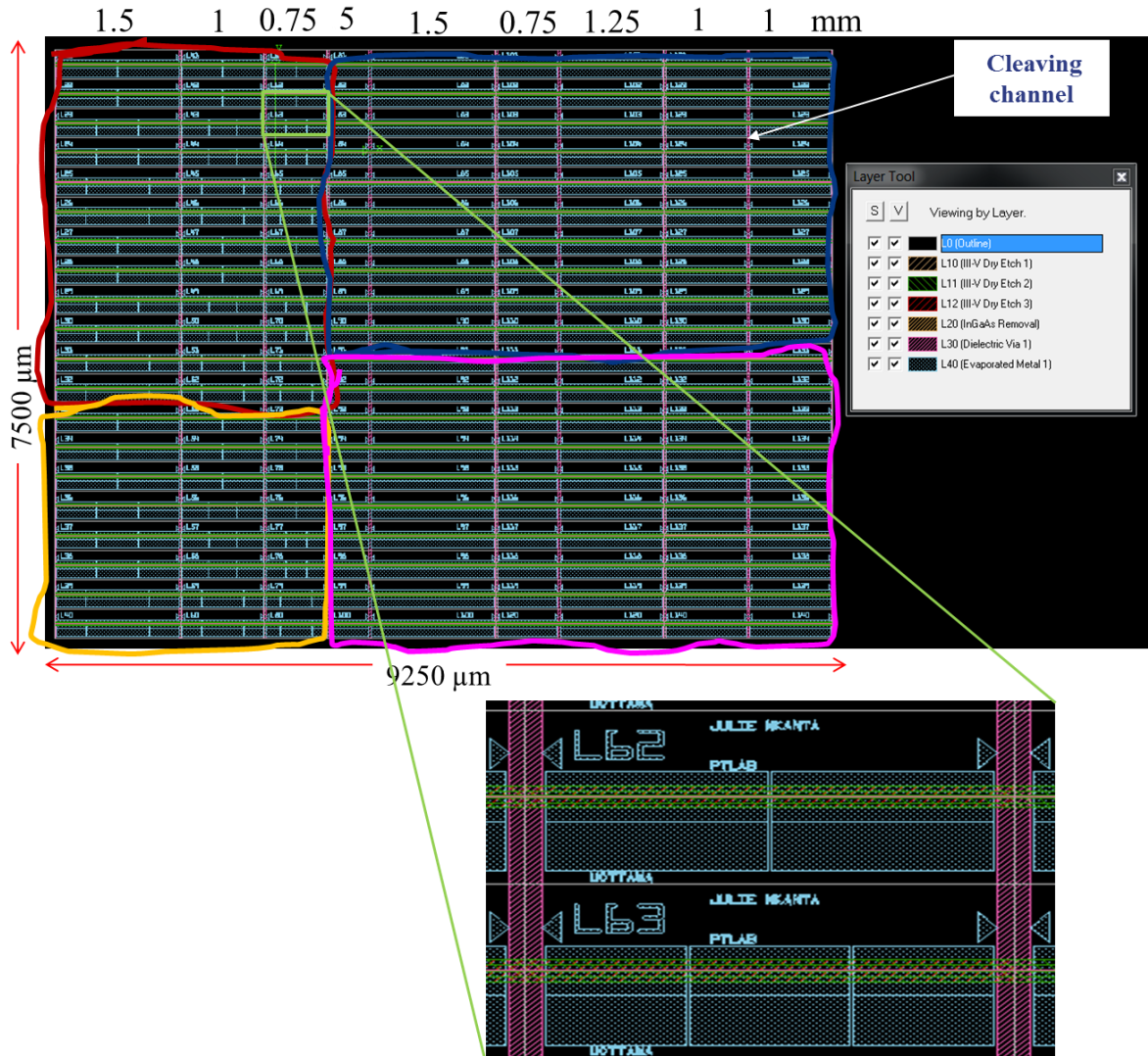


Figure 3-30. Layout of the mask on DW-2000 with colour coded regions to indicate the 4 different design variations

3.4.3 Fabrication

The fabrication steps for the LC-DFB laser is simpler than that of the conventional DFB lasers where the gratings are embedded thereby re-growth steps. In the most basic form, conventional DFB requires growing the epitaxial layers from the substrate up to the active region, then pause the growing, to start the lithography process whereby the

grating layer is patterned, then continue the growing (re-growth) of the remaining epitaxial layers, then patterning the ridge. The LC-DFB on the other hand requires only one growing process for all the epitaxial layers, and the lithography process for patterning the gratings defines the ridge at the same time. Carroll *et al*⁷² described a conventional DFB manufacturing process in details, however that will not be discussed here rather focus will be on the fabrication process of the LC-DFB laser used in this work. Although it is good to point out again that there is fabrication inefficiency due to the regrowth process, it will reduce manufacturing yield and might be an avenue for damage to the wafer during multiple handling. A more detailed description and the schematic are presented below for the fabrication of the corrugated-ridge (LC-DFB) laser.

The LC-DFB lasers are fabricated at the Canadian Photonic Fabrication Centre (CPFC) in Ottawa, Canada with support from CMC Microsystems. The gratings are defined using i-line 5x stepper lithography, and etched using an inductively-coupled reactive ion etch (RIE) process⁷³ for the fine grating features and a wet chemical etch for coarser features such as the trench surrounding the grating. A high-quality crystalline semiconductor wafer is chosen, it is mostly pre-made and commercially available, this is also known as the substrate. The following steps are involved in the fabrication process, (1) The epitaxial layers are grown on the substrate using a technique called metal organic chemical vapour-deposition (MOCVD) or the molecular-beam epitaxy (MBE), the different layers were discussed earlier and shown in Table 3-2. For the active region the quantum dot layers are grown for a QD LC-DFB laser or otherwise the QW layers are grown for the QW LC-DFB laser. (2) After all the layers are grown the grating is patterned out of the upper layers of the epitaxial structure, this also defines the ridge such that it looks like the gratings is patterned on the sidewall of the ridge, this is done with optical lithography called stepper lithography⁷⁴ is used by exposing a photoresist to a periodic standing wave pattern generated by an ultraviolet laser source. Another method is using e-beam lithography with high resolution for smaller feature sizes of gratings suitable for first order gratings but e-beam is an expensive and slow process. (3) The next step is growing the insulating dielectric layers with vias (openings) etched for electrical injection, in multi-electrode devices, there is an InGaAs removal before the dielectric as

explained in previous section. (4) Ohmic contact (p-contact) is formed at the top, the substrate is reduced in size before applying another ohmic contact (n-contact) at the bottom, contact formation is done using evaporation.

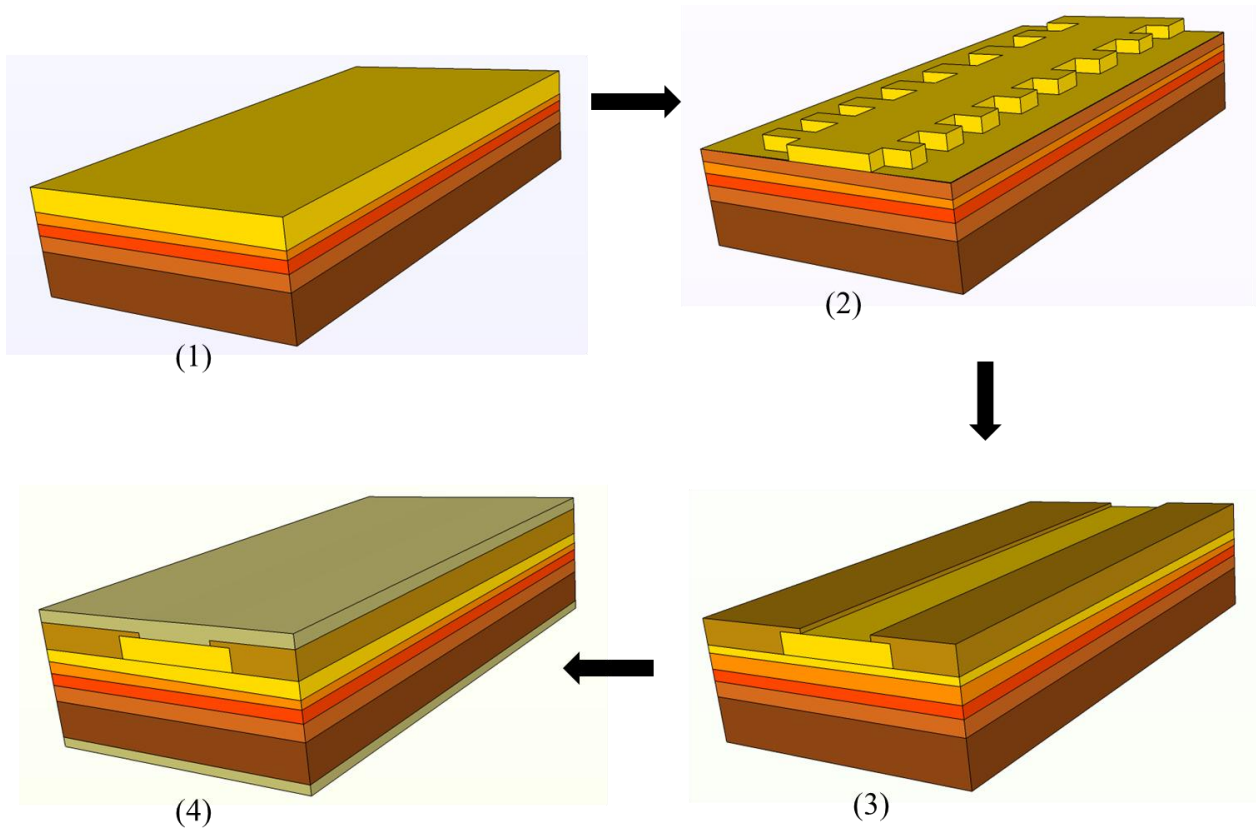


Figure 3-31. LC-DFB laser fabrication process: (1) Growth of epitaxial layers, (2) patterning of the gratings, (3) dielectric deposition and via etching, and (4) top and bottom metal contact deposition.

3.5 Summary

The modelling of the grating design, the time-domain travelling wave simulation and adapting the LC-DFB laser to fit a QD active region was presented in this chapter. Careful design considerations are required for any successful laser design, the epitaxial composition is really important especially for the active region and the layers closest to it, for LC-DFB laser the grating that will selectively filter the emission wavelength. The

geometry such as the grating height, period/number, duty cycle of the grating is instrumental to the performance of an LC-DFB laser since the dimensions will determine the coupling strength and the wavelength. High duty cycles are undesirable because it increases waveguide losses, and in our design it is not fabrication tolerant. Too high grating height (ridge depth) can cause problems during etching such as undercutting. Increasing the narrow ridge width while the large ridge width remains constant decreases the coupling strength and eventually leads to no coupling, on the other hand increasing the width ridge width while keeping the narrow ridge with constant increases the coupling strength, large ridge increases lateral current spreading and can lead to multi-mode operation.

A confined mode profile of the fundamental mode shows good coupling strength between the grating regions and the active region. The evolution of the power shows a slight decrease in the power as it propagates along the laser device with low power loss. The power diagnostics shows the power is mostly contributed by the forward propagating mode. The evolution of the output power with time shows a small time delay in picoseconds before lasing. The spectrum of the laser reveals a single mode emission with center wavelength at 1560 nm. The side modes of are highly suppressed with a SMSR of 57 dB. The longitudinal and lateral spatial profiles reveal non-uniformity in the laser carrier and photon densities.

Careful laying out the mask is very important for the definition of the ridge and the grating region. In LC-DFB lasers, a grating is etched directly out of the waveguide ridge thus eliminating regrowth steps. The stepper lithography for LC-DFB laser fabrication is a technique more suitable for high-volume manufacture than traditional approaches, such as electron-beam lithography and thus reduces cost for manufacturing. However, fabrication process and techniques can be a limiting factor in exploring many design variations and can also be prone to human imperfections. For any design and fabrication, there is always room for tolerance and room for future optimization.

Chapter 4 Quantum Well Distributed Feedback Laser Characterization

4.1 Introduction

Tunable spectrally pure semiconductor laser sources for coherent optical communication systems are in high demand. The lasers are required to be cost effective with stable single mode operation, having low threshold current, high emission power with high side mode suppression ratio. Narrow linewidth and low noise and flat frequency modulation response are also desirable. This chapter is on the quest to realize these optimal performance characteristics. The characterization of the InGaAsP/InP multi-quantum well multi-electrode laterally-coupled distributed feedback laser operating in the 1560 nm wavelength is hereby presented. These lasers have 1-, 2- and 3- partitioned electrodes from which each individual electrode section can be selectively bias controlled. This can lead to ability to ‘tune’ the performance characteristics of a laser to desired requirements.

In this chapter, section 4.2 is the description of the laser device under test, with details of surface grating dimensions, the SEM pictures, and the PL mapping of the wafer. Section 4.3 describes the experimental set-up used. Sections 4.4 and beyond presents results of the tests carried out to analysis the different characterization parameters of the laser devices. Section 4.4 discusses the L-I-V characteristics of these lasers under symmetric and asymmetric bias control at various operating temperatures. The emission spectra and its red-shift behaviour under different driving current and temperature is presented in section 4.5 and the subsequent side mode suppression ration in section 4.6, section 4.7 discusses the linewidth analysis of these laser devices using the delayed self-heterodyne interferometer method in the free-running and under optical feedback operation. Section 4.8 discusses the frequency modulation response and the relative intensity noise of these lasers. The chapter concludes with a summary of the results analyzed.

4.2 Laser Device

Material composition

The InGaAsP/InP LC-DFB laser consists of a multi-quantum well active region made up of six lightly compressively-strained (-0.64 %) 5 nm thick InGaAsP quantum wells and equally six lattice matched 8 nm thick InGaAsP barriers. This active region is sandwiched between two 200nm thick separate confinement heterostructure (SCH) layers. The ridge waveguide is defined by 800 nm ridge height and a 5 nm thick etch-stop. The third-order rectangular grating uniformly etched along the laser cavity on the ridge sidewalls is 800 nm deep with an average period of ~720 nm and a duty cycle of 50 %. The gratings were etched by a 5× i-line stepper lithography process. After the etching process, the wafer is passivated with an insulated dielectric SiO₂ layer. Then follows etching of the via areas where electrical injection will be provided, multi-electrode devices are segmented into 2 and 3 lengths with electrically isolated regions separated by a few microns, ohmic contacts are formed, n-contact below the device and heavily doped p-contact above the device. Schematic to illustrate the different electrode configurations of LC-DFB laser is shown in Figure 4-1 below.

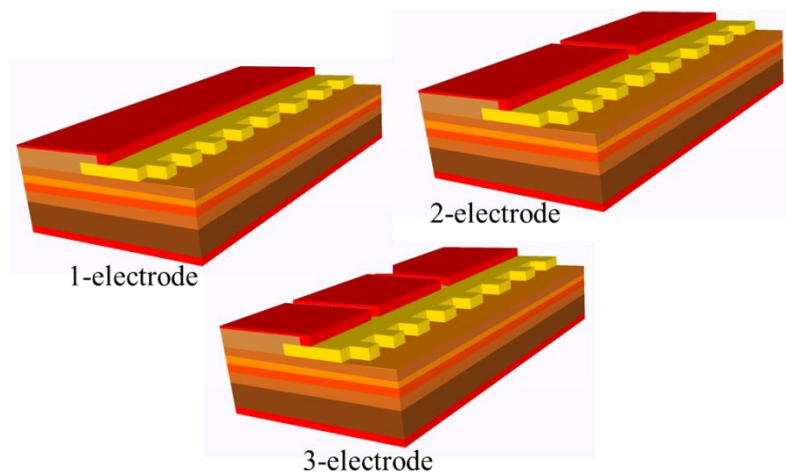


Figure 4-1. Schematic of the LC-DFB laser in different electrode configurations

These lasers are then cleaved into bare die bars for characterization, some laser devices are further diced and their electrodes wire bonded to interfacing printing circuit boards

for frequency modulation injection. A detailed description of the laser composition is shown in Table 4-1, where layers 4 to 6 is the undoped active region

Table 4-1. Material composition of the laser

Layer No.	Layer Name	Material	PL peak (nm)	Nominal Strain		Thickness (μm)	Doping Level (cm^{-3})
				(%)	T.S./C.S.		
12	p-Contact	InGaAs	1660	U.S.		0.050	Zn: $N_A = 2 \times 10^{19}$
11	Ridge 3	InGaAsP	1200	U.S.		0.010	Zn: $N_A = 8 \times 10^{18}$
10	Ridge 2	InGaAsP	1100	U.S.		0.010	Zn: $N_A = 2 \times 10^{18}$
9	Ridge 1	InP	919	U.S.		0.800	Zn: $N_A = 2 \times 10^{18}$
8	Etch stop	InGaAsP	1300	U.S.		0.005	Zn: $N_A = 7 \times 10^{17}$
7	SCH upper clad	InGaAsP	1100	U.S.		0.150	Zn: $N_A = 5 \times 10^{17}$
6		InGaAsP (b)	1200	0	U.S.	0.060	u.d.: $N_D < 3 \times 10^{15}$
5	6 \times MQW stack	InGaAsP (well)	$\frac{1541}{1550}$	-0.64	C.S.	0.005	u.d.: $N_D < 3 \times 10^{15}$
		InGaAsP (barrier)	1200	0	U.S.	0.008	u.d.: $N_D < 3 \times 10^{15}$
4		InGaAsP (b)	1200	0	U.S.	0.020	Si: $N_D = 5 \times 10^{17}$
3	SCH low clad 2	InGaAsP	1150	U.S.		0.100	Si: $N_D = 8 \times 10^{17}$
2	SCH low clad 1	InGaAsP	1050	U.S.		0.100	Si: $N_D = 8 \times 10^{17}$
1	Buffer	InP	919	U.S.		1.040	Si: $N_D = 3 \times 10^{18}$
0	Substrate	InP	919			50.000	Si: $N_D = 2 \times 10^{18}$

Where C.S is compressive strain, T.S is tensile strain, U.S is unstrained, PL is photoluminescence, **u.d** is undoped.

Details of the grating design dimensions are listed in Table 4-2 below for some of the laser devices, there were many repeated laser devices on different bars and these laser devices were tested for repeatability. In the table each row is dedicated to each laser device for the different grating dimensions as indicated by the column titles, where W_N and W_W are the narrow ridge width and wide ridge widths respectively, grating periods Λ_1 and Λ_2 represents the periods for each side of the grating teeth (all equal for the laser devices). Sections 1, 2, and 3 represents the different partitioned electrodes, a dash (-) is used where additional electrodes are not available, implying if all 3 sections are indicated then it is a 3-electrode device, the spacing between the electrodes are also indicated in the

table. The cumulative number gives the device length. The devices were cleaved into various lengths such as 500, 750, 1000, 1250, 1500 μm .

Table 4-2. LC-DFB grating design variations

Ridge Width (μm)		Grating Periods (nm)	Duty Cycle	Partitioned electrode, section lengths and spacing (μm)			
W_N	W_W			Λ	Section 1	Section 2	Section 3
1.5	3.0	720	0.50	745	745	-	10
1.5	3.0	720	0.50	745	745	-	10
1.5	3.0	720	0.50	747	747	-	6
1.5	3.0	720	0.50	494	494	494	9
1.5	3.0	720	0.50	496	496	496	6
1.75	3.5	720	0.50	1500	-	-	-
1.5	4.0	720	0.50	1500	-	-	-
1.5	3.0	720	0.50	373	373	-	6
1.5	3.0	720	0.50	370	370	-	10

Photoluminescence mapping

The photoluminescence (PL) taken at the center of the wafer is shown in Figure 4-2 below with a PL peak at 1552.8 nm

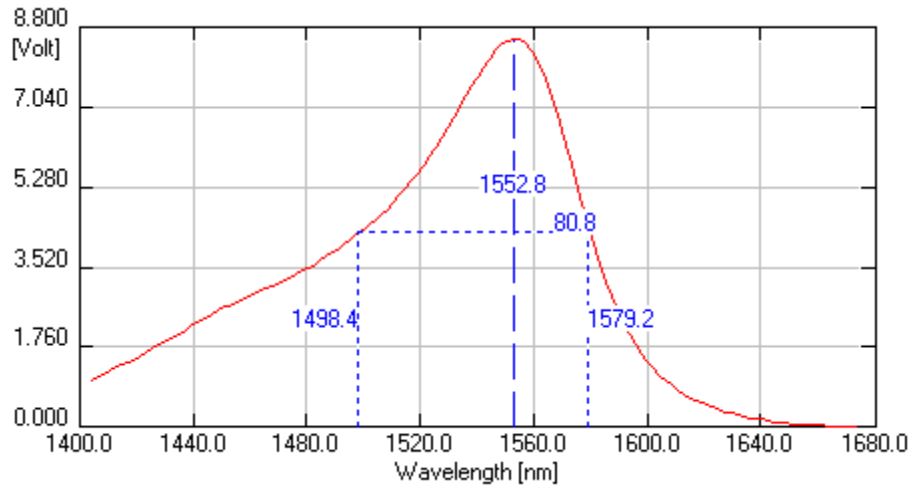


Figure 4-2. Single point PL at the center of a wafer⁷⁵

A more descriptive PL mapping of the wafers is shown in the six figures of Figure 4-3 below, with a colour map showing the peak wavelength (λ). We observe a somewhat circular symmetry due to the rotation of the substrate from long wavelength at the center to shorter wavelengths at the edges. The PL mapping varies from 1534 - 1566 nm in wavelength. The PL colour mapping reveals some information about our fabricated devices. It shows that devices at the center bottom of the wafer tend to have their photoluminescence at the peak and those farther out especially at the top part of the wafer has photoluminescence in the lowest wavelength ranges. And depending on where the laser devices are cleaved from the wafer, one can expect to have varying photoluminescence that can cause slight differences between fabricated devices. Although these devices had the same epitaxial composition we notice slight to obvious differences between the PL mappings of the wafers, these differences can be fabrication related.

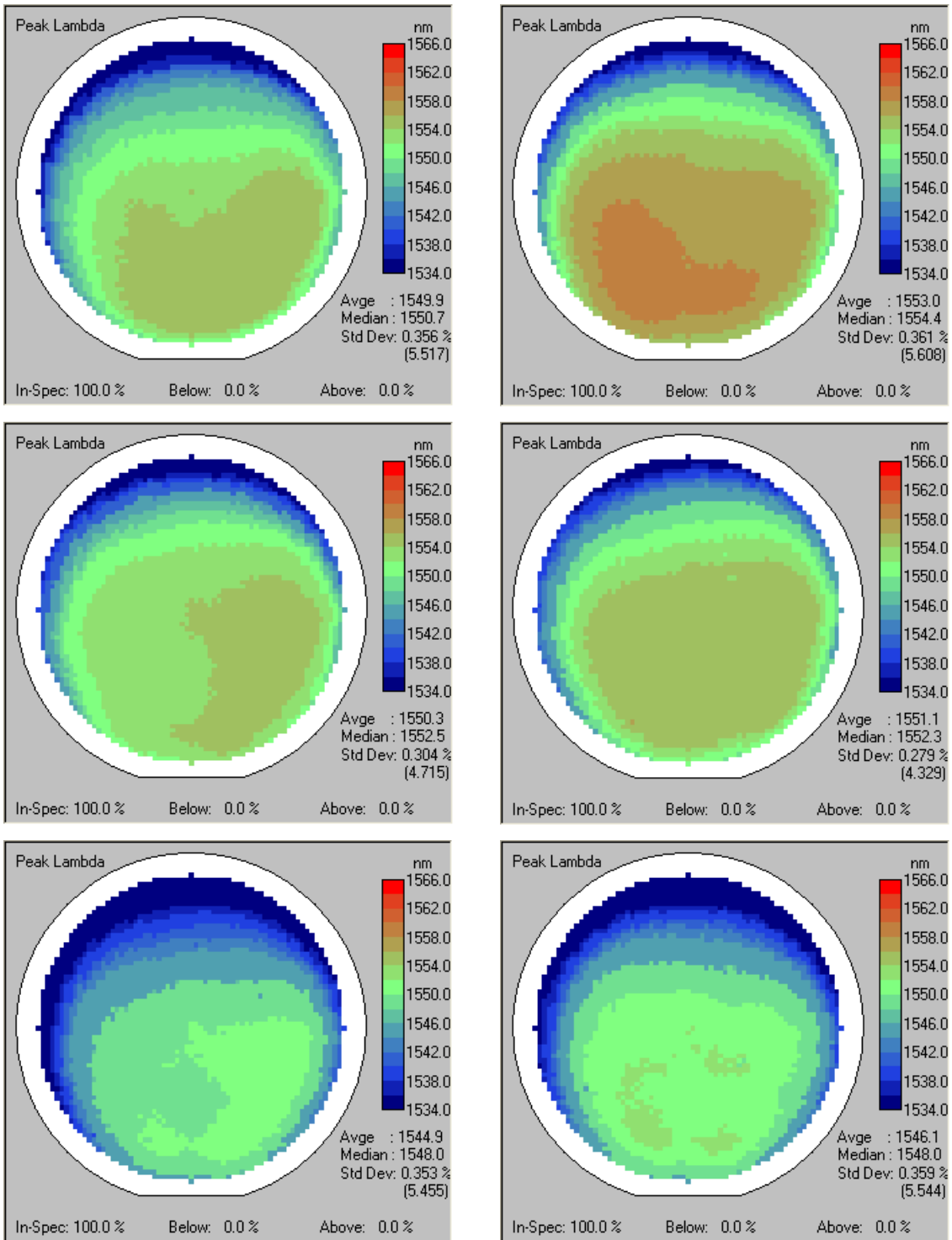


Figure 4-3. Photoluminescence mapping of the six fabricated wafers⁷⁵

Microscope images

The scanning electron microscope (SEM) slanted top view images were taken by CPFC staff after fabrication of the laser (see Figure 4-4). The different images show the smooth well defined rectangular gratings under different magnifications. The grating shape is uniform and extends over the length of the laser with no missing or deformed grating.

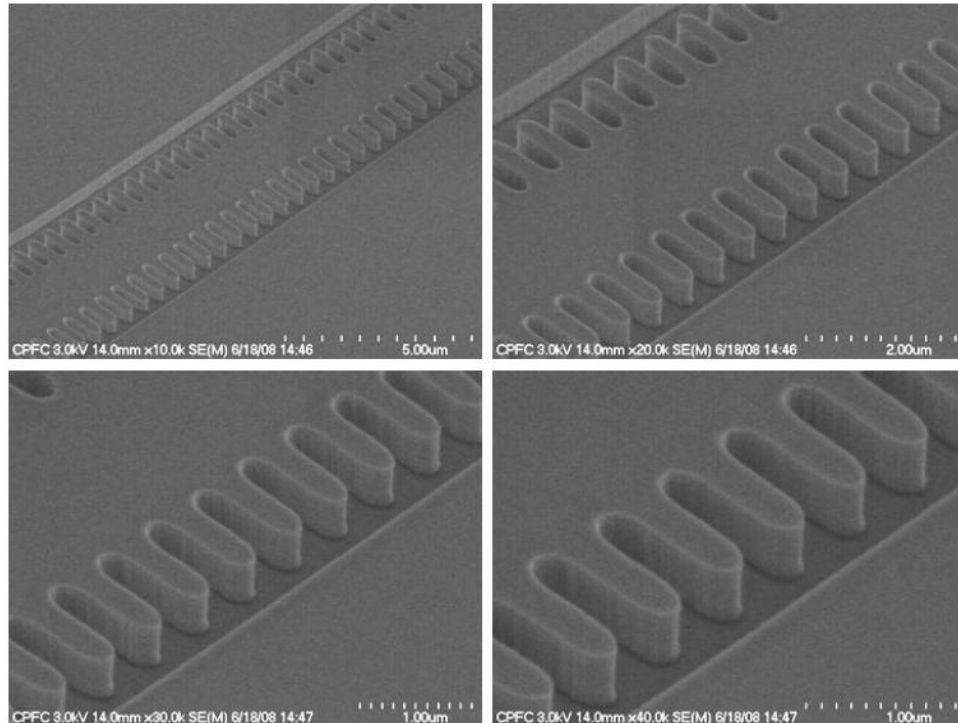


Figure 4-4. SEM slanted view images of the 3rd order rectangular gratings showing the shape of the grating

Several SEM images were taken of laser devices from the different wafers fabricated, the gratings looked similar/uniform and measurements of the grating teeth across the different regions of the wafers (center, top, bottom, left and right) showed a cross-wafer uniformity of ± 30 nm of the specified grating period. This indicates a good and consistent lithography process within allowable tolerance. However, as observed in the SEM images, the grating teeth are somewhat rounded, these rounding are due to the resolution limitations of the etching process as defined by the stepper lithography. As should be predicted, fine grating features below the stated resolution of the stepper lithography process will completely be washed-out during the etching process, thus for grating features above but close to the stated resolution as our lasers were, we expect

washing-out resulting in rounded edges of the gratings. One can suggest why not choose grating features farther away from the resolution limit, but we can argue that we are constrained by the fact that the Bragg condition must be satisfied as explained in equation 3-1 of chapter 3, and any larger grating features will move us into much higher order gratings and more complications.

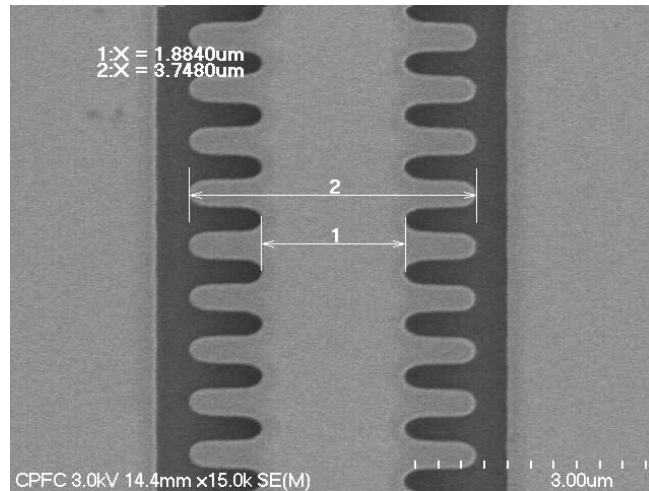


Figure 4-5. SEM top view images of the rectangular gratings showing the 1(narrow), 2 (wide) ridge widths dimensions

SEM measurements of the ridge width variations is shown in Figure 4-5 indicating the narrow and wide ridge widths dimensions of the fabricated L34 device. The figure indicates $W_N = 1.884 \mu\text{m}$ and $W_W = 3.748 \mu\text{m}$, these numbers deviate from the target W_N of $1.75 \mu\text{m}$ and W_W of $3.5 \mu\text{m}$. These widening and/or shortening of the ridge widths were observed for some of the laser devices and will likely be observed across the whole wafer if more SEM images were taken. These are all fabrication related and in combination with the rounding of the gratings reduces the effective coupling coefficient. In future fabrication of these devices, we used a de-risk layer in the mask design to offset this effect. In other images (not indicated) some bowing in the sidewalls of the gratings was observed, between the top and bottom spacing of the gratings $\sim 10\%$ bowing was measured. And the top and bottom surfaces of the gratings were mostly flat with a very small tilt $\sim 1\%$ observed (see Figure 4-6). These are all fabrication induced imperfections that can be avoidable by compensating for it or unavoidable.

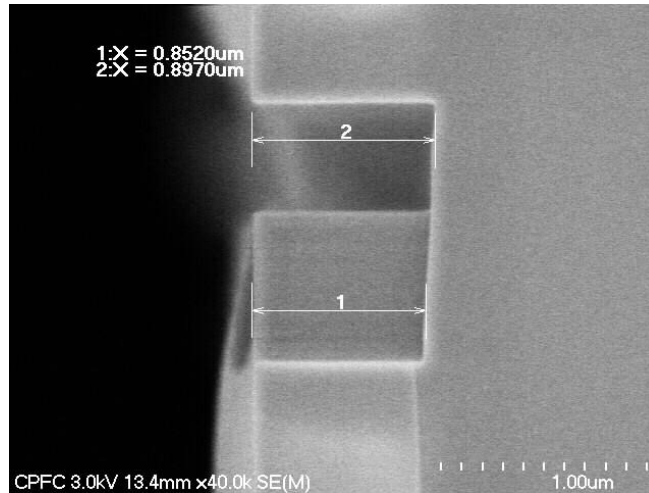


Figure 4-6. Side view of the rectangular gratings showing the surface tilt

Figure 4-7 shows the top view of the 1500 and 1250 μm devices on bars. The top bar image indicates L21-L40 devices and the bottom image indicated L41-L60 devices. The metal contacts show no noticeable lift-off except some scratches and probe pins marks, the facet cleave were not inspected on an SEM, but in some cases, when we ruled out other issues, we safely assumed that some non-optical performance were due to facet imperfections. On closer observations of the microscope images, one can differentiate between the 1-,2- and 3- electrode laser devices.



Figure 4-7 Microscope top view images of the fabricated laser devices on 2 bars, from the top L21-L40 (1500 μm), L41-L60 (1250 μm)

The multi-electrode laser devices also known as the multi-section or multi-segment have their top electrodes segmented into 2 or 3 electrically isolated sections of few microns

apart, this is to allow control of the carrier injection within each segment otherwise the carrier density distribution within the laser cavity. In this thesis, the first electrode is considered to be the one closest to the output facet (far right), for example in a 3-electrode laser device the electrode1 is far right closest to the output facet, electrode2 is the middle electrode and electrode3 is the far left electrode. This ability to control the driving conditions can lead to ability to suppress the longitudinal spatial hole-burning, improve frequency modulation response, spectral linewidth, wavelength tunability and other desirable outcomes as will be seen in later sections.

4.3 Experimental Set-up

An experimental set-up for the laser measurement is given below. Further experimental description will be provided for subsequent sections when needed. The experimental setup is composed of a laser stage, optical spectrum analyzer, photo detector/power meter, taper fiber, thermoelectric cooler (TEC)/controller, rotational stages/positioners, source meter, piezoelectric controller, infra-red viewer, microscope, and a computer/LABVIEW for data acquisition. The laser stage is a combination of 6-positioner stages, heat sink, probes and a microscope. The heat sink stage is composed of a XYZ stage, copper plate, brass sample holder and thermoelectric cooler. A thermo epoxy resin was used to bond the copper plate and the TEC cooler. The stage is built such that there is a uniform distribution of heat on the copper plates where the brass sample holder is placed. The lasers were injected with currents using source meter through tungsten needle probes directly applied to the contact above and grounded through alligator clips to the brass sample holder. Light from the laser device is focused into a single mode taper fiber connected to an optical spectrum analyzer (OSA) for spectral measurement, or connected to a photodetector for light-current-voltage measurements. The taper fiber is used to optimize maximum coupling of light, as loss due to coupling of light through the fiber is a drawback in the setup. Care was taken to optimize the alignment of the setup. Piezo-electric controllers were used to control the nano-positioning and alignment of the experimental setup. Measurements were taken for varying temperatures. Figure 4-8 shows a picture of the experimental setup, where the

laser bar is sitting on a temperature controlled laser stage, there are 3 pins probing and injecting current into the three different electrodes of a 3-electrode laser device.

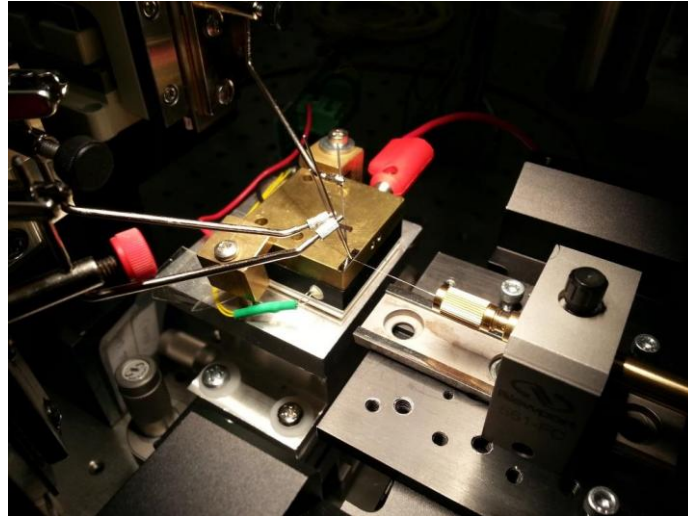


Figure 4-8. Experimental stage set up showing the laser device with probe pins for current injection

And Figure 4-9 shows the schematic of the experimental setup where OSA is the optical spectrum analyzer, and GPIB is the general purpose interface bus. Symmetric and asymmetric bias control is used throughout the experiment. As observed in the below picture, a taper fiber is used at the output facet for light collection.

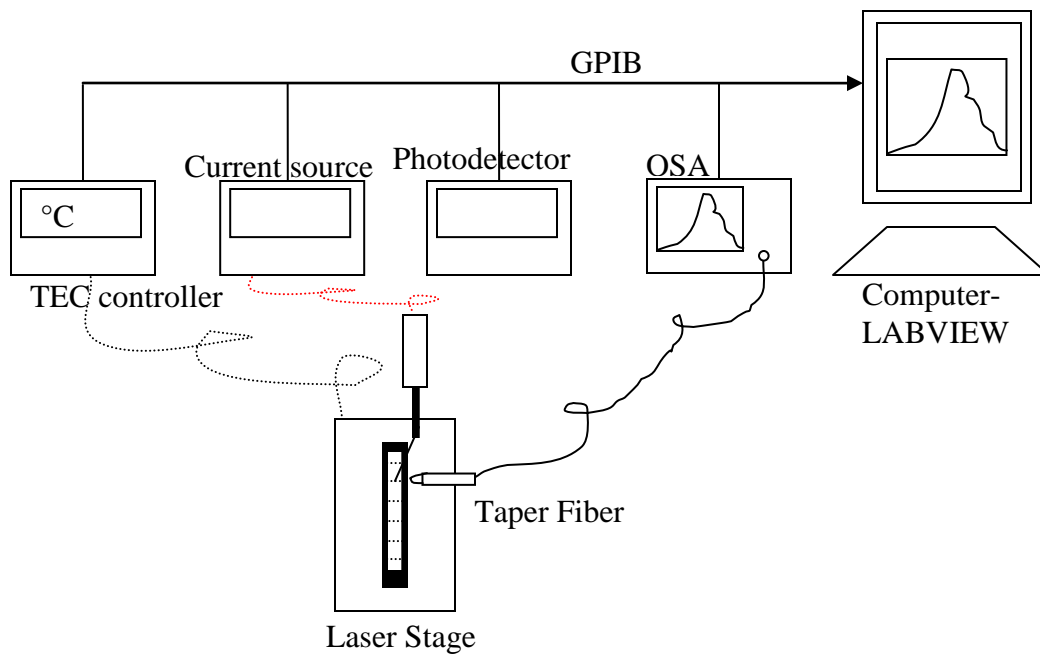


Figure 4-9. Schematic of the experimental setup

Further experimental set-up and measurement techniques are discussed under the linewidth and frequency modulation sections. Precautions were taken to reduce vibrations and other noise sources due to the sensitive nature of the experimental setup such as fixing (taping) all fiber patch cords and connectors on the optical table, decluttering the optical table, and placing all instruments/measurement sources on the overhead rail and movable racks.

4.4 Light-Current

The light-current (L-I) curve is an important parameter in laser characterization. It is a plot of the light power emitted as a function of the injection current for a specific laser device at a specific temperature. The L-I measurements are obtained by varying the injection current and simultaneously measuring the light output power using a photodetector. At very low current, the spontaneous emission dominates and the output power stays at very low levels. When the current passes threshold, the stimulated

emission dominates and there is an abrupt increase in the light output power. Several laser parameters can be derived from the L-I plot such as the maximum power, threshold current, threshold current density, slope efficiency, external quantum efficiencies etc of the laser device.

Figure 4-10 (a) shows the combined L-I and I-V plots of the single electrode 1500 μm LC-DFB laser device with a threshold current of 110 mA and maximum power of 1.6 mW. This device is one of the lowest output power and largest threshold current laser devices tested as will be seen in later sections, its overall performance is not as optimal as the multi-electrode devices or shorter cavity length devices. This comparison is shown in Figure 4-10 (b) whereby the two laser devices are same cavity length of 1500 μm but one is a single electrode and the other is a 2-electrode device with 6 μm spacing in between the electrodes.

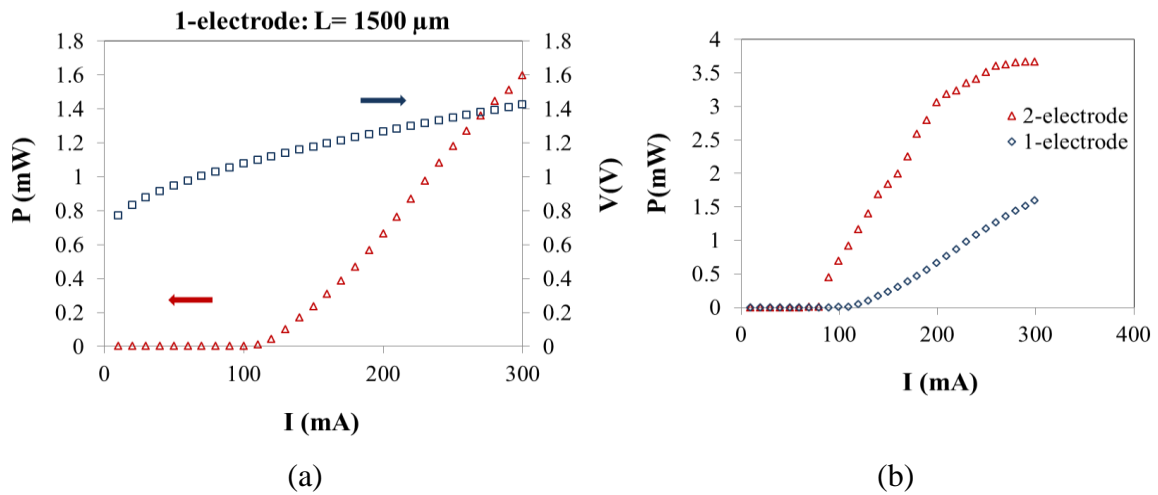


Figure 4-10. L-I-V characteristic of (a) Single electrode 1500 μm LC-DFB laser device (b) 1-, and 2-electrode 1500 μm LC-DFB laser device

The threshold current can be determined by the x -intercept of the L-I curve. As it is observed the 2-electrode device has smaller threshold current (80 mA compared to 110 mA) and a much higher maximum power (3.7 mW compared to 1.6 mW).

When both electrodes are not equally biased, we notice some differences in their L-I characteristic. The bias currents are I_1 for electrode1, I_2 for electrode2 and I_3 for electrode3.

2-electrode laser device: The 2-electrode laser device first electrode is biased at varying current from 0 to 250 mA while its second electrode is fixed at 100 mA, the reverse whereby the first electrode is fixed and the second electrode is varied is shown in Figure 4-11. A higher maximum power is observed when electrode 1 is varied compared to when electrode2 is varied.

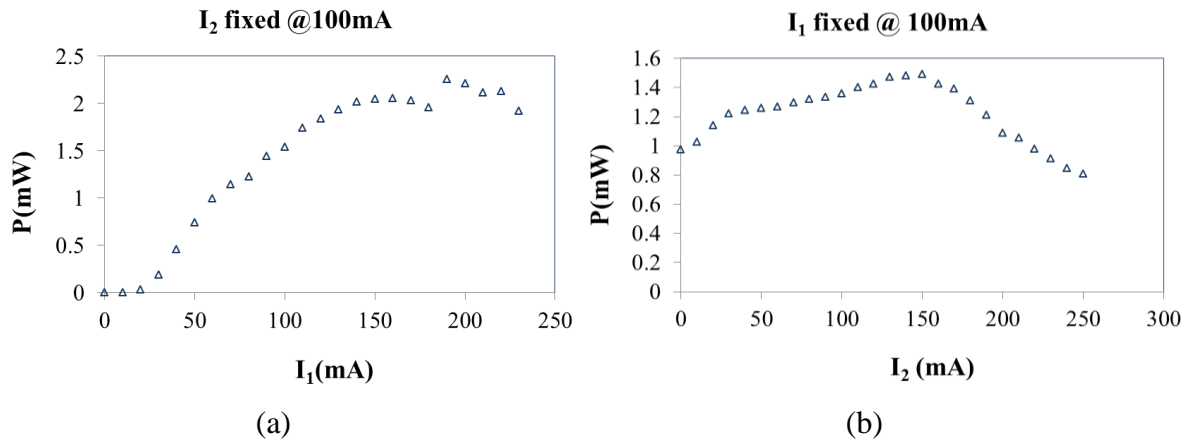


Figure 4-11. L-I characteristic for 2-electrode 1500 μm LC-DFB laser device. (a) varying electrode1, and electrode2 fixed at 100 mA
(b) varying electrode2, and electrode1 fixed at 100 mA

In Figure 4-11(a) it is observed that even though electrode2 has been biased at a high 100mA, lasing has yet to occur until electrode1 is 20 mA, this is because the gain and stimulated emission due to higher carrier density is dominating mostly in the second half of the laser farther away from the output facet. Also for this plot, saturation starts to occur after 100/200 mA bias. In Figure 4-11(b) electrode1 is biased at 100 mA and as observed even at 0 mA current injection into electrode2, lasing had already occurred being that electrode1 is closer to the output facet, saturation starts to occur at 100/150 mA bias.

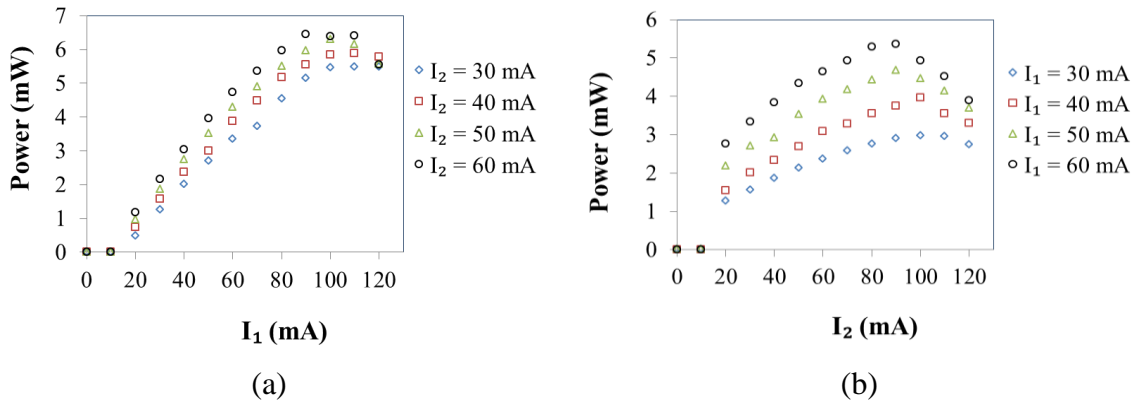
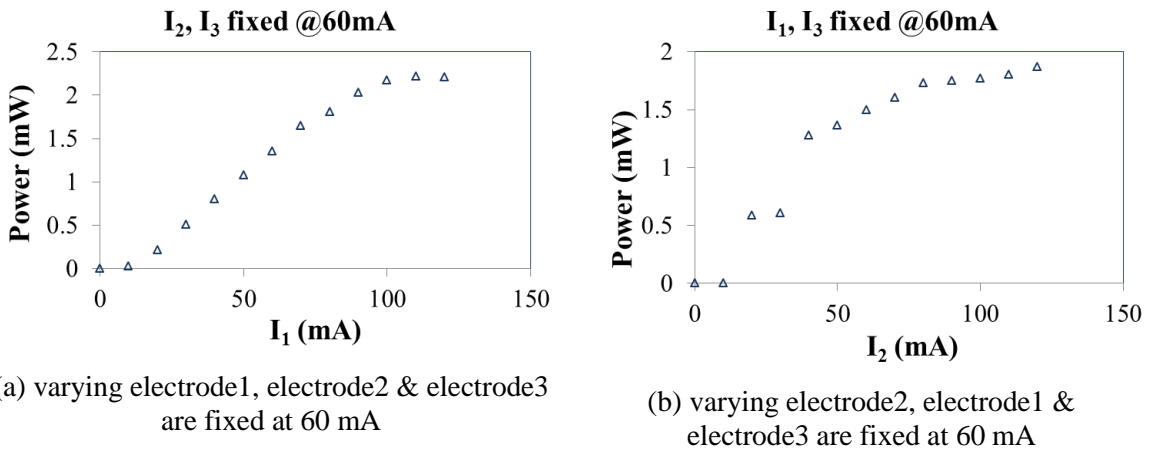


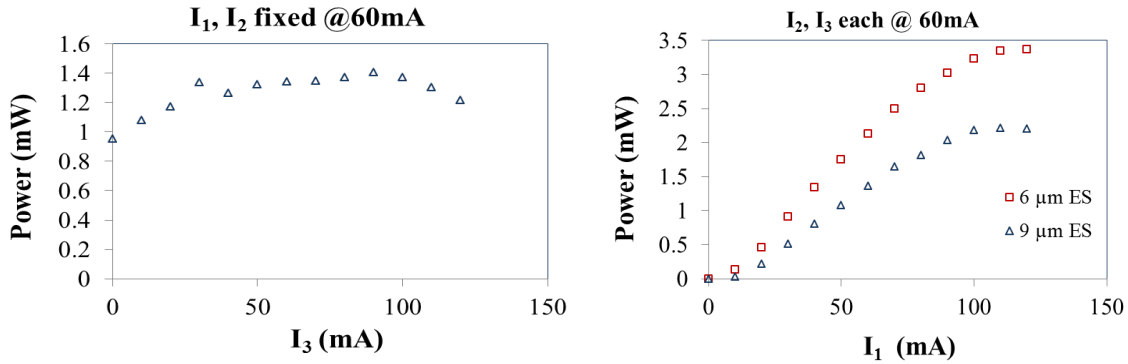
Figure 4-12. L-I characteristic for 2-electrode 750 μm LC-DFB laser device (a) varying electrode1, electrode2 is fixed at 30 mA, 40 mA, 50 mA and 60 mA (b) varying electrode2, electrode1 is fixed at 30 mA, 40 mA, 50 mA and 60 mA

Figure 4-12(a) shows the L-I characteristic of the 750 μm laser device where electrode1 is varied and electrode2 is fixed at 30 mA, 40 mA, 50 mA and 60 mA. The output power is plotted against the current through electrode1. At the above fixed currents lasing occurs when the electrode1 current just passes 10 mA. The maximum power peaks at ~7 mW. Figure 4-12(b) is the reverse here output power is plotted against the current through electrode2 while current through electrode1 is fixed at different currents. The L-I characteristic is a bit different, after threshold the output power seems to rapidly increase at a rate faster than in Figure 4-12(b), but its peak output power is limited at ~5.5 mW.



(a) varying electrode1, electrode2 & electrode3 are fixed at 60 mA

(b) varying electrode2, electrode1 & electrode3 are fixed at 60 mA



(c) varying electrode3, electrode1 and electrode2 are fixed at 60 mA

(d) Comparison for 3-electrode 1500 μm LC-DFB laser devices. Electrode spacing (ES) 6 μm & 9 μm

Figure 4-13. L-I characteristic for 3-electrode 1500 μm LC-DFB laser device

3-electrode laser device: asymmetric current injection is more difficult to achieve in a 3-electrode device because it requires 3 degrees of freedom, considering that the devices are very small and on a bare die (not mounted on a carrier), the probe needles need very careful placement/adjustment on the metal contacts.

Figure 4-13 shows the different L-I characteristics of the 3-electrode 1500 μm laser device when the current injection on the three electrodes are either fixed at 60 mA or varied from 0 to 120 mA. Figure 4-13(a) shows where the output power is plotted against the current through electrode1 while electrode2&3 are each biased at 60 mA, lasing starts to occur after electrode1 current reaches 10 mA, and peak power of ~2.5 mW was measured before saturation. Figure 4-13(b) is a plot of the output power vs the current through electrode2 while electrode1/3 are each biased at 60 mA, the L-I curve is not kink-free and maximum power occurs at 2 mW. Figure 4-13(c) shows current through electrode3 is varied while electrode1/2 are each biased at 60 mA, it is observed that even while there has been no current through the third electrode yet (0 mA), lasing had already occurred since there is higher carrier density in the first two electrodes with enough gain and stimulated emission, the plot also shows that as the current is increased past 30 mA in this third and last electrode, there is not much increase in output power rather it is almost flat and peaks at 1.4 mW before saturation.

Considering that these multi-electrode some of the laser devices have slight differences in their electrode spacing that electrically isolates each other, it is imperative that we compare this difference in order to know which separation gives more optimal performance based on their L-I curve. Figure 4-13(d) shows the output power versus current through electrode1 when it is varied from 0 – 120 mA while electrode2/3 are each biased at 60 mA. In this plot the first laser device has a 6 μm separation between its electrode one and two, with another 6 μm separation between electrodes two and three. The other laser device has a 9 μm separation each between its electrodes. From observation, there seem to be a slight different in the lasing threshold, the 6 μm ES lasing occurs just before 10 mA current injection in electrode1, while in 9 μm ES lasing occurs just after 10 mA current injection. Their difference does not stop there, 6 μm ES has a much steeper L-I slope with a maximum output power of ~ 3.5 mW. While the 9 μm ES laser device maximum output power is 2 mW. Based on electrode spacing the smaller 6 μm inter-electrode spacing in the makes it a better performance and efficient laser, it can be deduced from here that for even larger inter-electrode spacing past the 9 μm the performance of the laser will keep deteriorating further confirming that large isolations between electrodes are not optimal, also when the isolation are too small in the order of 1 μm or less the laser starts to behave like a single electrode device.

Light-current for varying temperatures

The ability of the laser to perform well at elevated temperatures is of great interest because heat generated in the test environment can cause the laser device temperature to rise significantly thus degrading the device if it does not have a good characteristic temperature. In order to understand the stability of laser performance when subjected to temperature it is necessary to determine the characteristic temperature of the laser. The characteristic temperature (T_0) is a measure of the temperature sensitivity of the laser device. It is a parameter that relates laser operating temperature (laser local temperature) to its threshold current defined by the Arrhenius relationship of diode laser:

$$I_{th} = I_0 e^{T/T_0} \quad \text{or} \quad J_{th} = J_0 e^{T/T_0} \quad 4-1$$

where T_0 can be obtained by the linear regression of the natural log of the threshold current over the temperature. T_0 is largely determined by the dominant recombination mechanism, which varies greatly with temperature. The temperature range of the measurement must be specified for a meaningful T_0 value.

$$T_0 = \frac{\Delta T}{\Delta \ln(I_{th})} \quad \text{or} \quad T_0 = \frac{\Delta T}{\Delta \ln(J_{th})} \quad 4-2$$

where I_{th} is the threshold current, J_{th} is the threshold current density, T is its operating temperature in Kelvin (K), and T_0 is its characteristic temperature in K.

Equation 4-2 shows that the threshold current is highly dependent on both its operating and characteristic temperatures. It is therefore preferable for a laser to have a high characteristic temperature so that its threshold current does not increase much even with a large increase in its operating temperature. This exponential relationship is related to the temperature effect on gain and loss within a laser. Temperature sensitivity of the threshold current is dominated by Auger recombination at lower temperatures and by vertical leakage at higher temperatures. Carrier losses increase at higher temperatures due to higher carrier density which is mainly as a result of gain reduction.

Higher values of T_0 imply that the threshold current density and the differential quantum efficiency of the device increase less rapidly with increasing temperatures. This translates into the laser being more thermally stable. The wavelength of a laser diode is directly proportional to its operating temperature. There is a linear relationship in which the temperature increases with wavelength. This is a red-shift characteristic which is useful in spectroscopic applications, where the wavelength of emission of the laser diode can be accurately temperature tuned to the specific properties of the material with which the laser diode is interacting⁷⁶.

Figure 4-14 shows the L-I plot of the 2-electrode device at varying temperatures from 0 to 250 mA bias currents. The non-linearity of the curve due to gain saturation and heating is very obvious in this plot. The threshold current can be determined by the x -intercept of

the linear regression of the L-I curve just above threshold. As the injection current increases, the carrier density increases thus resulting in greater spatial hole burning as well as increase in the local temperature of the laser device. Thermal roll-off starts to occur while the slope of the L-I curve decreases until saturation is reached at maximum output power (P_{max}), after which the P_{max} starts to decrease gradually with increasing bias current.

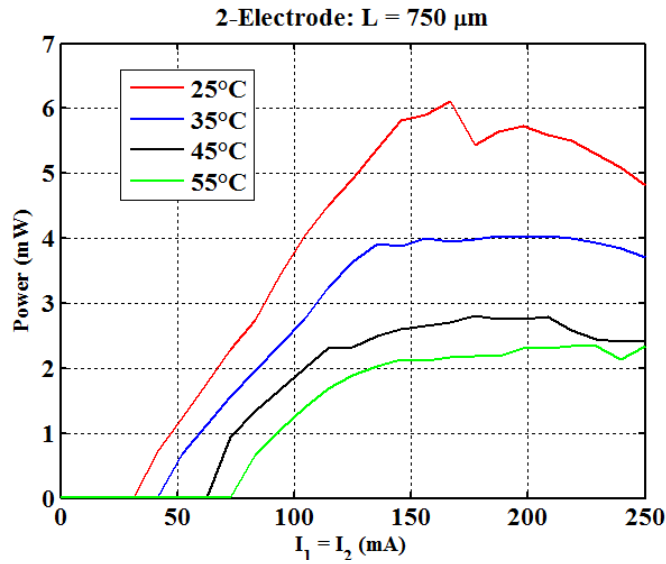


Figure 4-14. L-I characteristic plot for varying temperature for the 2-electrode LC-DFB laser device

Figure 4-15 shows the different threshold current deduced from the L-I curve at different temperatures. It clearly shows the increase in threshold current from 40 mA to 80 mA with increasing temperature.

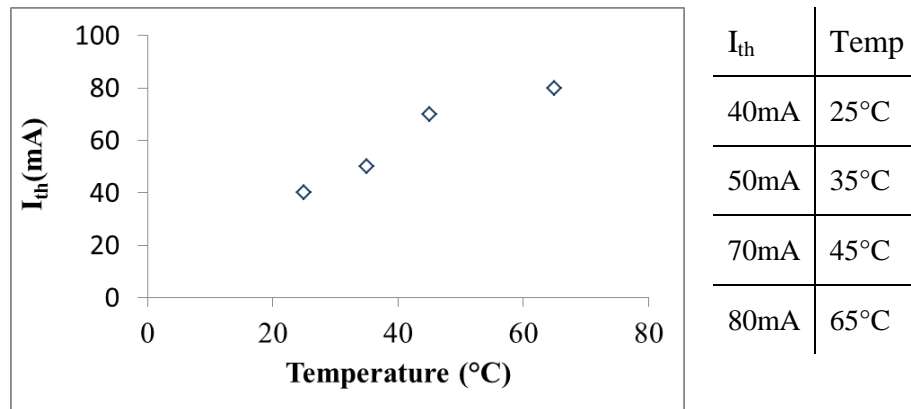


Figure 4-15. Threshold current as a function of temperature

The current-voltage (IV) characteristic of a laser diode informs of the electrical quality of the metal contacts and the p-i-n junction. In order to contribute to optical gain in the active region, it is necessary that most of the electrical carriers injected through the probe pins on the metal contacts collect in the active region. It is understandable that some carriers will spread laterally into regions where it will not contribute to optical gain. The IV characteristic therefore informs how efficiently carriers are injected into the laser structure.

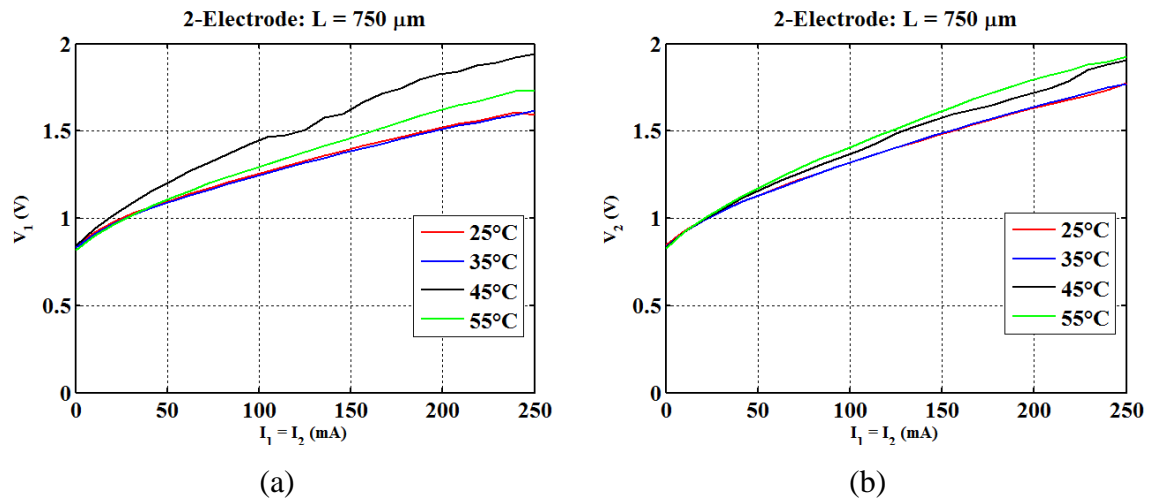


Figure 4-16. IV plot as a function of (a) first electrode (b) second electrode

The IV characteristics of the 2-electrode device for varying temperatures are shown in Figure 4-16. The current flowing through the p-i-n junction is negligible until the forward-biased turn-on voltage is reached, in both figures it is approximately 0.85 V, above the turn-on voltage the current increases. To assess the quality of the metallic ohmic contacts on the laser device, the dynamic series resistance can be determined from the IV plots where $R = \Delta V / \Delta I$. The dynamic resistance varies from $\sim 3\Omega$ (@ 25/35°C) to 4.5Ω (@55°C) The dynamic resistance as to be expected increases with temperature due to self-heating of the laser devices. High resistance is not desirable in a laser diode rather a low dynamic resistance because it will have less heating, and more carriers injected into the active region, thereby resulting in a lower threshold current and better overall efficiency

4.5 Optical Spectra

The optical spectrum of a DFB laser is unique because it has a spectrally pure and sharp peak (see Figure 4-17), this is because an ideal DFB spectrum filters out all but a single longitudinal mode. Also DFB laser exhibits stable single-mode operation over temperature ranges⁷⁷ this is because the temperature dependence of the wavelength is dominated by the change in the Bragg wavelength, λ_0 due to a change of refractive index with temperature², $\sim d\lambda_0/dT = 0.1 \text{ nm}$. Some important parameters can be extracted from the optical spectrum such as the side-mode suppression ratio (SMSR) and the peak lasing wavelength.

The optical spectrum analyser used has a minimum 0.08 nm resolution, the sensitivity was set to -64 dBm, and the wavelength span was set to 20 nm (centered at 1560 nm wavelength). Figure 4-17 shows an optical spectrum of the 2-electrode 750 μm laser device with a peak emission wavelength at 1559.5 nm when electrode1 and electrode2 are each biased at 30 mA.

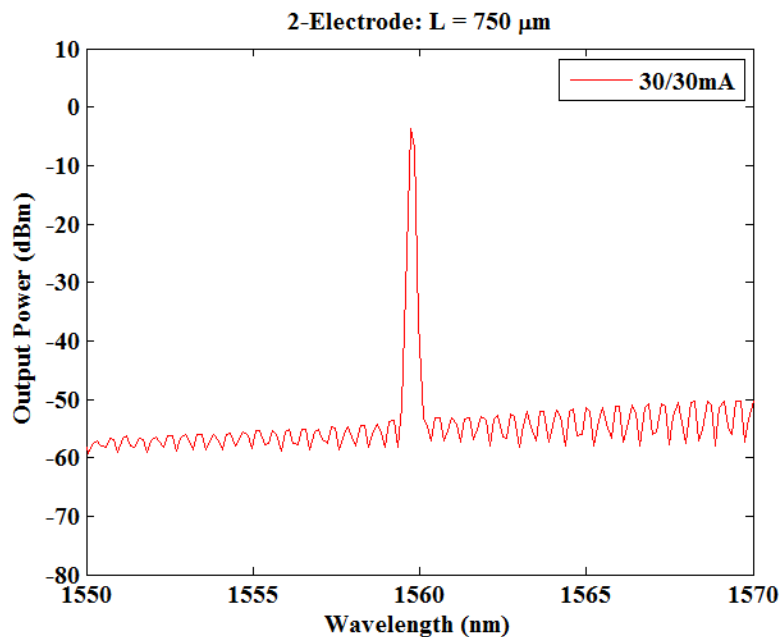


Figure 4-17. Output spectra of the 2-electrode 750 μm laser device at 30/30 mA bias

Spectra for varying current

The optical spectra shown in Figure 4-18 exhibits a stable DFB lasing at different bias points, a red-shift in the peak wavelength is observed as current increases, this plot gives information on the current dependent stability of the DFB lasers. This red-shift in the emission wavelength will be analyzed further in the next few sections.

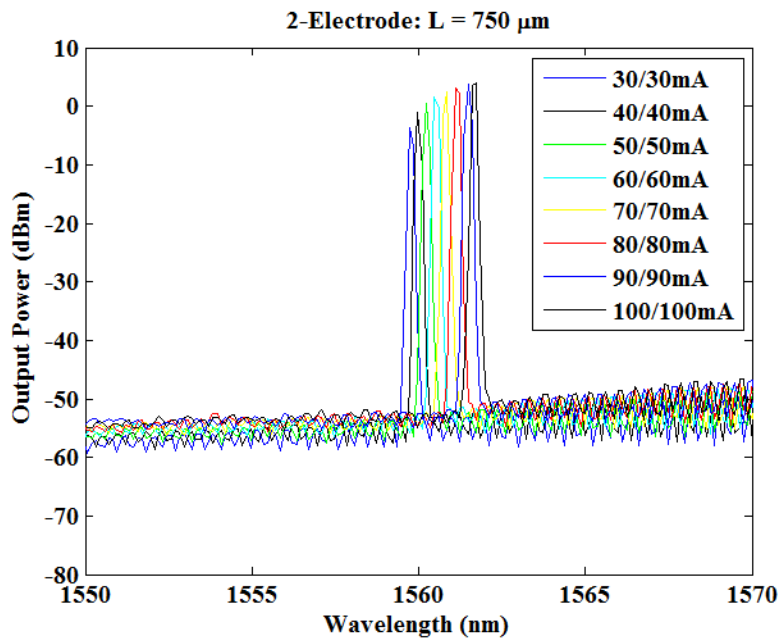


Figure 4-18. Output spectra of the 2-electrode 750 μm laser device at various uniform current injection

Spectra for varying temperature

Temperature change in a laser structure induces a red-shift of its center wavelength due to the temperature dependence of the refractive indices of the laser material composition. The temperature dependent stability of the laser is shown in Figure 4-19 where each electrode is injected with 50 mA current. A red-shift of the peak wavelength of emission from 1560 nm at 25°C to 1563 nm at 55°C is observed, the numerical amount of these shifts will be further analyzed. The plot also shows a decrease in peak output power with increasing temperature.

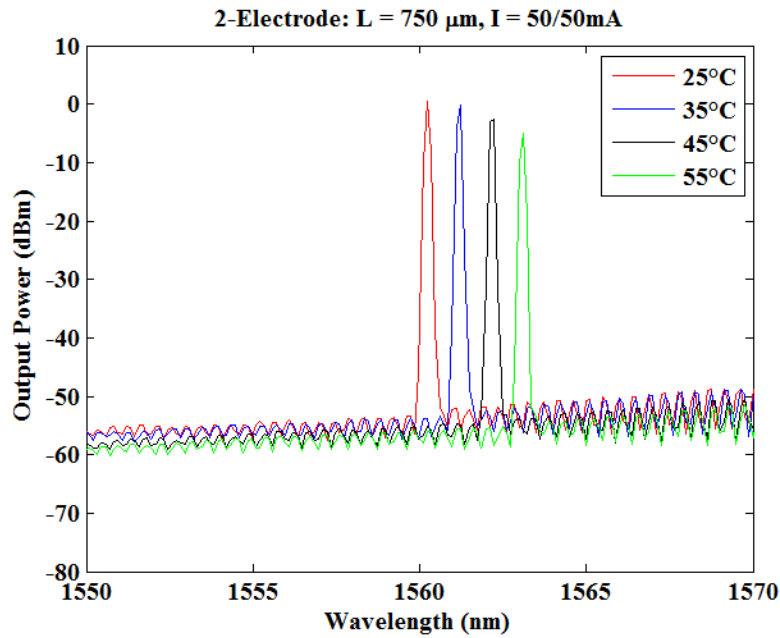


Figure 4-19. Output spectra of the 2-electrode 750 μm laser device at 50/50 mA bias at different temperatures

Wavelength tuneability

The spectral red-shift in peak emission wavelength of the 2-electrode laser device is further analyzed in this section, this occurs with current and temperature increase as shown in Figure 4-20 and in a more detailed analysis in Table 4-3.

As observed the tuning range and rate is dependent on both the bias conditions and the temperature conditions. Analyzing the spectra at 25°C (see Figure 4-20 and Table 4-3), the emission wavelength peaks at 1559.55 nm just after threshold (40 mA) and is tuned to 1561.8 nm at 200 mA (tuning of 2.25 nm), implying a tuning rate ($d\lambda/dI$) of approximately 0.014 nm/mA (14 pm/mA), at 65°C the tuning rate increases to 0.0162 nm/mA (16.2 pm/mA). At 100 – 200 mA a consistent temperature tuning of 3.38 nm at a rate ($d\lambda/dT$) of 0.097 nm/°C (97 pm/°C) is measured.

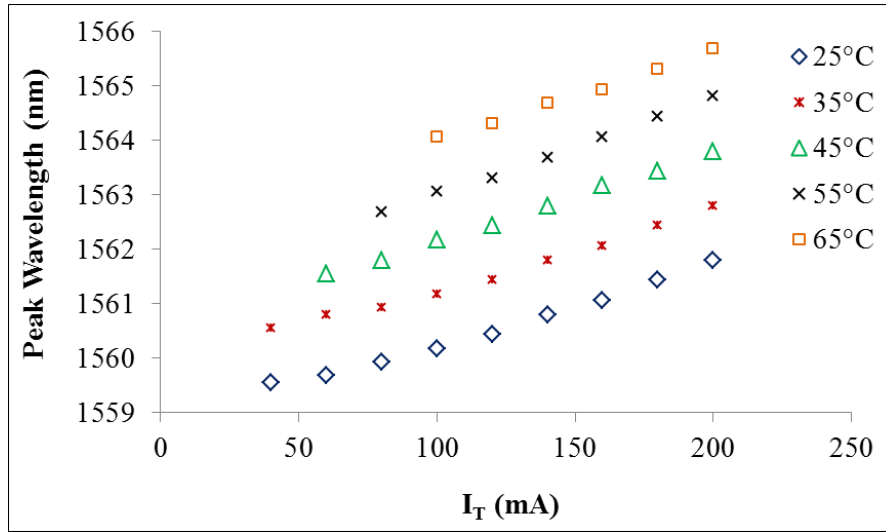


Figure 4-20. Peak wavelength as a function of uniform current injection

Table 4-3. Wavelength and temperature tuning as a function of bias current

I (mA)	25°C	35°C	45°C	55°C	65°C	Remarks
40	1559.55	1560.55				
60	1559.68	1560.8	1561.55			
80	1559.93	1560.93	1561.8	1562.68		
100	1560.18	1561.18	1562.18	1563.05	1564.06	~3.88nm/40°C
120	1560.43	1561.43	1562.43	1563.3	1564.31	~3.88nm/40°C
140	1560.8	1561.8	1562.8	1563.68	1564.68	~3.88nm/40°C
160	1561.05	1562.05	1563.18	1564.06	1564.93	~3.88nm/40°C
180	1561.43	1562.43	1563.43	1564.43	1565.31	~3.88nm/40°C
200	1561.8	1562.8	1563.8	1564.81	1565.68	~3.88nm/40°C
	~2.25nm per 160mA	2.25nm per 160mA	2.25nm per 140mA	2.33nm per 120mA	1.62nm per 100nm	Summary: 0.014 - 0.0162nm per 1mA 0.097nm per 1°C

4.6 Side Mode Suppression Ratio

The side-mode suppression ratio (SMSR) is the difference between the power at the peak lasing wavelength (peak mode) and the next highest peak in the spectrum (side mode). High SMSR values of greater than 50 dB are desirable in DFB lasers because even when under continuous (CW) regime, the side modes can significantly increase under high

speed modulation. Smaller values often indicate poor longitudinal mode discrimination, resulting in mode instability.

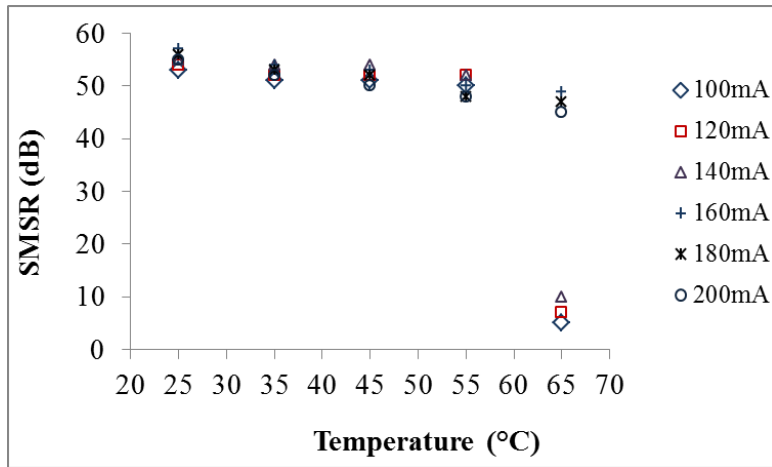


Figure 4-21. SMSR as a function of temperature for the 2-electrode 750 μm laser device for various bias currents

Figure 4-21 shows the SMSR versus temperature for various bias currents. The maximum SMSR value of 58 dB as expected is observed at 25°C and starts to degrade gradually as temperature increases. The low SMSR values of around 10 dB observed at 65°C for the 100 – 140 mA range of bias is due to the lower output power as well as mode instability observed for these current ranges.

Figure 4-22 shows the SMSR plotted against bias current at various operating temperatures. The higher SMSR of greater than 50 dB is observed for most currents at 25°C. Higher SMSR is observed for higher currents for most temperatures peaking at 150 mA.

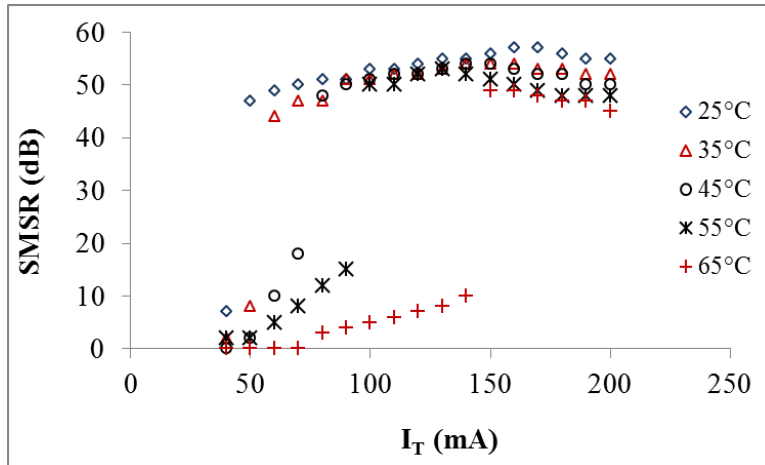


Figure 4-22. SMSR as a function of current for the 2-electrode 750 μm laser device at various operating temperatures.

4.7 Linewidth Characterization

The interest to develop very highly coherent DFB lasers lies in several applications one being the need to minimize the effects of chromatic dispersion in optical fibers in long-haul telecommunication transmission systems, these coherent systems require DFB laser devices with the narrowest possible linewidth. In this application, the coherence length (propagation distance over which the coherence significantly decays) which is directly related to the linewidth of the laser is of utmost importance, this coherence length is limited by the phase noise of the laser. Spectral linewidth refers to the optical phase fluctuation of the lasing longitudinal modes, the phase noise is as a result of the spontaneous emission from laser cavity gain medium.

To extract the linewidth, a Voigt fitting is applied to the measured beat spectrum^{78,79} from the electrical spectrum analyzer (ESA). The Voigt profile is the convolution between the Lorentzian and the Gaussian lineshapes which is necessary because the broadening (due to the $1/f$ frequency noise) of the RF spectrum is observed at the center⁷⁸. The Voigt profile therefore allows simultaneous quantification of the effect of extrinsic noise which is mapped by the Gaussian part and the intrinsic linewidth mapped by the Lorentzian part.

The delayed self-heterodyne interferometer signal was recorded in logarithmic scale but converted to linear scale in order to simplify the fitting process. The equations for Voight, Gaussian and Lorentzian functions were integrated into Matlab[®] codes to use for the fitting. These were fitted to the obtained experimental data while adjusting the Lorentzian gamma (γ) parameter and the Gaussian FWHM parameter, the derived Voight FWHM is computed at the end of the fitting process as

$$F_V = 0.5346F_L + \sqrt{0.2166F_L^2 + F_G^2} \quad 4-3$$

where F_V is the Voight FWHM, F_L is the Lorentzian FWHM equal to 2γ and F_G is the Gaussian FWHM is equal to 2.355σ .

4.7.1 Measurement Technique

The spectral linewidth, $\Delta\nu$ is defined by the full wave at half-maximum (FWHM) of the Lorentzian distribution of the optical field power spectrum. There are several techniques employed to determine the linewidth of a laser, a well-known method is called delayed self-heterodyne interferometer (DSHI) method⁸⁰ which is based on the delayed self-heterodyning of the optical signal. This method compared to the heterodyne method eliminates the need for the use of a stable narrow line-width reference laser (local oscillator), rather it uses a 20 km of optical fiber to create an optical delay⁸¹.

The schematic in Figure 4-23 below shows the experimental set up of the delayed self-hetrodyne technique in the free-running operation. The optical beam goes through an optical isolator (to minimize the back-reflections from the optical fiber into the laser under test) into the Mach-Zehnder interferometer and is split into 2 paths, one arm has a single mode fiber delay of 20 km and the other arm is frequency shifted to the center frequency (110 MHz) of the acousto-optic modulator (AOM), then both arms are combined and the beating signal is detected by the photodetector. The beat tone produced is shifted from 0 Hz by the frequency shift, and is shown on an electrical spectrum

analyzer (ESA) with a low resolution of 3-10kHz required for these measurements⁸¹. The spectrum shown is as a convolution of the individual power spectrums. The spectral linewidth is then extracted and analyzed.

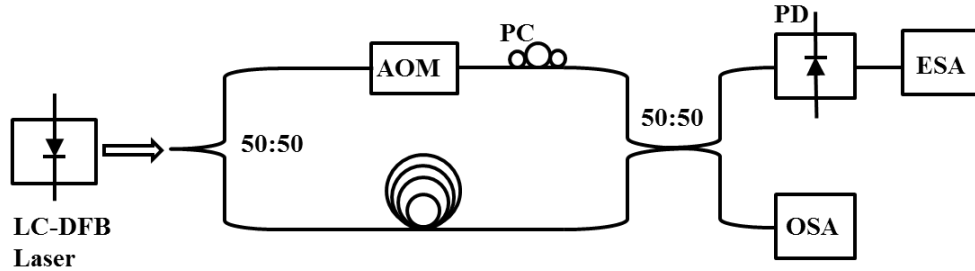


Figure 4-23. Schematic of the experimental setup for delayed Self-heterodyne interferometric technique for measuring the linewidth. AOM: acoustic-optic modulator, PC: polarization controller, PD: photodiode, ESA: electrical spectrum analyzer, OSA: optical spectrum analyzer

To further improve (narrow) the spectral linewidth of the laser external optical feedback is used. Although external optical perturbations can often produce undesired instabilities in the laser, if well controlled, it can result in improved spectral stability. Thus the experimental setup above is modified to an optical feedback operation, first the isolator is removed in order not to impede the feedback power. The schematic of the experimental setup in feedback operation is shown in Figure 4-24. An optical circulator is used whereby the output light from the laser passes through port 2 of the optical circulator and the output at port 3 is divided into two arms. The feedback light is measured by an optical power monitor and variable optical attenuator (VOA). The polarization of the signal is aligned to the principal axis of the LC-DFB waveguide by a polarization controller (PC) and injected to the laser through port 1 of the circulator. The second arm (50%) of the signal is sent to the self-heterodyne configuration similar to the free-running. Another VOA can be used before the PC to monitor the emitted power and hence the butt-coupling alignment, also an erbium doped fiber amplifier could have been used before the VOA to amplify the feedback light in order to provide a wider range of feedback power.

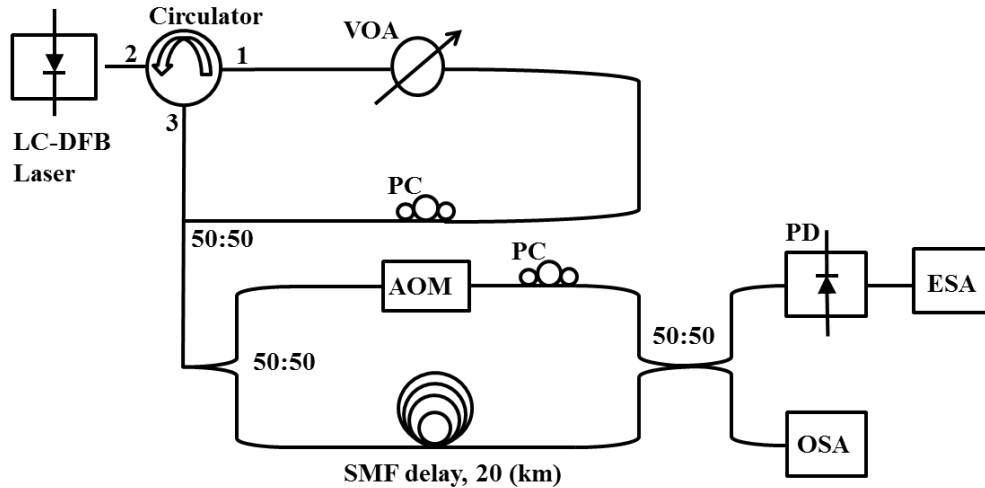


Figure 4-24: Schematic of the experimental setup for optical feedback operation. VOA: variable optical attenuator, AOM: acousto-optic modulator, PC: polarization controller, PD: photodiode, ESA: electrical spectrum analyzer, OSA: optical spectrum analyzer

For the linewidth experiment, the ESA is set to the following, a span of 2-20 MHz with a center frequency of 110 MHz, resolution bandwidth (rbw) and video bandwidth (vbw) of 3kHz for the feedback experiment and 10kHz for the free running experiments.

4.7.2 Linewidth in free-running

Voigt fitting is applied to the measured RF beat spectrum under uniform current injection of each electrode at 50 mA for a total of 100 mA shown in Figure 4-25. The Voigt fitting gives FWHM of 0.637 MHz, from which the extracted Lorentzian and Gaussian FWHMs are 0.420 MHz and 0.380 MHz, respectively. The intrinsic linewidth $\Delta\nu$ is half of the Lorentzian FWHM which is 0.210 MHz.

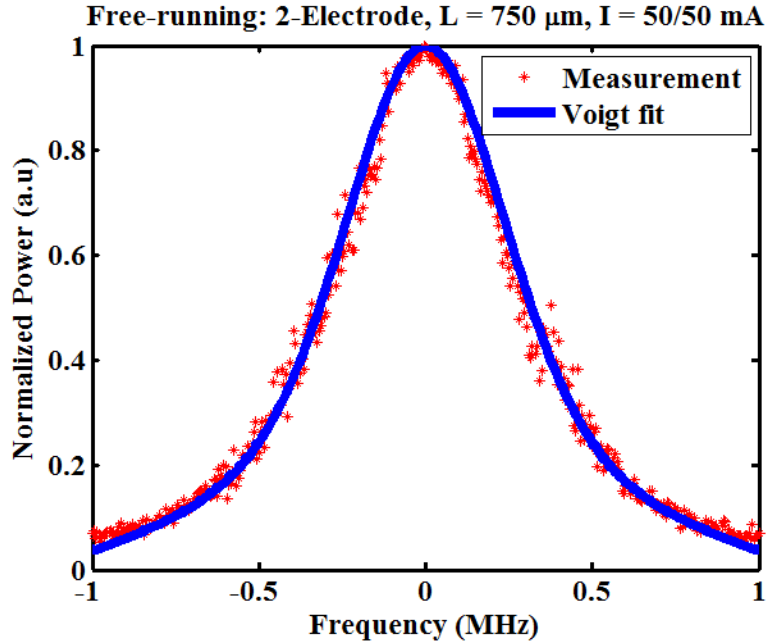


Figure 4-25. Measured RF beat note spectrum of the 2-electrode 750 μm laser device at 50/50 mA bias under free-running

The linewidth variation as a function of the bias current range of 50 mA (corresponding to 25/25 mA) to 250 mA (corresponding to 125/125 mA) under several operating temperatures is shown in Figure 4-26. As observed the linewidth increases with increasing temperatures. For all temperatures the linewidth variation shows a trend where by starting at 50 mA, the linewidth is highest, it then lowers as current is increased and starts to increase again at higher current. The smallest linewidths are measured in the range of 70-140 mA with a minimum of 210 kHz at 25°C. The average linewidth is above 250 kHz.

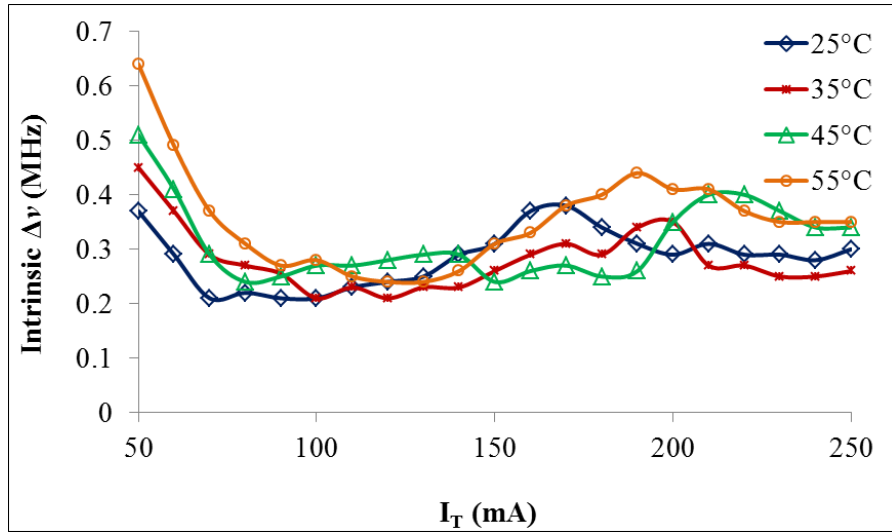


Figure 4-26. Linewidth variation at symmetric bias control under free-running for various operating temperatures 25°C, 35°C, 45°C, and 55°C. I_T is the total current

4.7.3 Linewidth in optical feedback

Optical feedback is a technique used to further reduce the linewidth in semiconductor lasers. The reduction of the spectral linewidth due to optical feedback is based on the amount of power fed back to the laser from strong to very weak feedback power levels. A plot showing the effect of the different feedback power levels on the linewidth is shown in Figure 4-27 for feedback powers of -20, -15, -10 and -5 dBm. The higher the feedback power the narrower the linewidth and varies with bias current. Compared to the free running the linewidth is reduced depending on feedback power. The lowest linewidth measured under feedback is 96 kHz. The average linewidth in feedback operation is 100 – 200 kHz

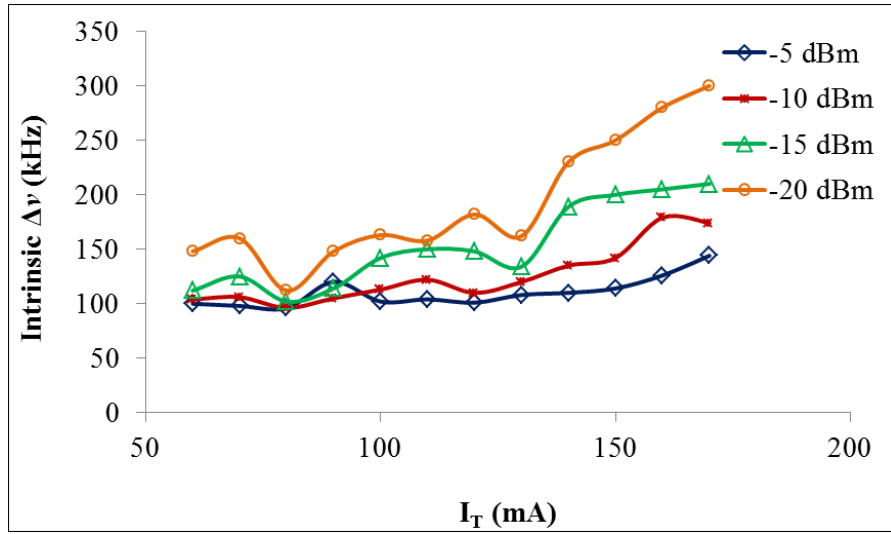


Figure 4-27. Linewidth variations at symmetric bias control under optical feedback for various feedback powers -5, -10, -15 and -20 dB. I_T is the total current

4.8 Frequency Modulation Response and Relative Intensity

Noise

The viability of a laser source to be used in a coherent optical system is partly determined by the laser output spectrum after modulation. The laser spectrum is a contribution from the intensity modulation, laser chirp as well as the phase and intensity noise⁸¹. The dynamics of a laser device can therefore be characterized from its response to stimulus, as a function of frequency. Suitable laser sources exhibiting a frequency response (FM) response that remains flat for high frequencies of hundreds of MHz and beyond are highly desirable for optical phase-locked loops^{82,83,84}. In a standard DFB laser, current injection leads to a red shift of the laser wavelength at low frequency due to the thermal effect, whereas it causes a blue shift at high frequency due to the carrier induced refractive index change, this phase shift of the FM response between low and high frequencies limits the loop bandwidth⁸⁵.

There has been an interesting progress towards miniaturised optical phase locking systems based on silicon photonics chips by Teraxion Inc⁸⁵. There has been a positive

and collaborative interest between our laboratory PTLab and Teraxion Inc on these LC-DFB lasers. The experimental work presented in this section was carried out in their state-of-the-art facility in Quebec City, Canada.

4.8.1 Measurement Technique

The laser devices on bare die bars are cleaved into individual devices and its electrodes are wire bonded to interfacing printing circuit boards (PCB) to allow for frequency modulation injection greater than 300 MHz. Figure 4-28 shows an image of a 3-electrode laser device mounted on a PCB.

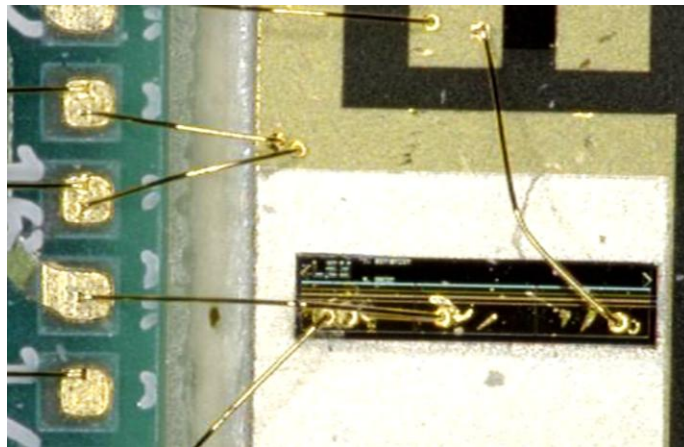


Figure 4-28. A 3-electrode laser device mounted on a printing circuit board with 3 wire bonded electrodes

The coherent interferometric technique consisting of a stimulus-response measurement⁸⁶ is used to measure the phase and frequency modulation response of the LC-DFB laser signal as shown in Figure 4-29.

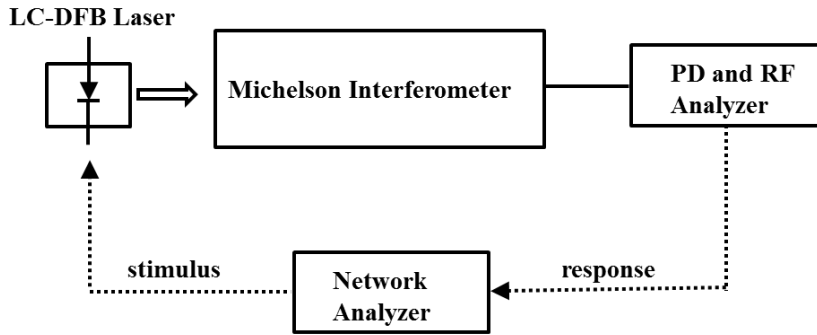


Figure 4-29. Schematic of the experimental setup

The setup consist of a single-mode fiber-based Michelson interferometer operating in quadrature whereby a phase modulator and feedback biasing is used to hold the interferometer in quadrature position, and to compensate for slow drifts in the average optical frequency and in the fiber lengths of the interferometer. The interferometer also acts as a frequency discriminator (to convert optical carrier fluctuations into intensity variations). The input to the interferometer comes from the LC-DFB laser under test in a free space scheme with an isolator to eliminate back reflections. The output of the interferometer is impinging on a high speed DC-coupled photo detector. Laser frequency noise converted into intensity noise is analysed by a FFT-based signal analyser to allow for spectral density (PSD) of the frequency noise measurement from DC to ~100 kHz, whilst an RF spectrum analyser is used for higher frequencies. An electrical network analyzer is used to provide sinusoidal stimulus to the laser and to measure the frequency and phase modulation response of the laser.

The FM response, PSD of the frequency noise, and relative intensity noise are measured by varying the total bias current in the single electrode laser, or varying the current in one electrode of the 2- and 3-electrode lasers while keeping the electrodes at fixed current.

4.8.2 Frequency Modulation Response

The flat FM-response versus bias current results is shown below in Figure 4-30 for the 1-electrode, Figure 4-31 for the 2-electrode, and Figure 4-32 for the 3-electrode laser

devices. In Figure 4-30 of the single-electrode LC-DFB, the flat FM response is observed only near threshold which is ~ 120 mA to 140 mA @ 25°C and 150 mA to 180 mA @ 35°C . At this narrow range of injection current, the limitations encountered are the low output power under 1 mW measured, a high relative intensity noise (to be discussed later), and a small wavelength tuning of only 0.2 nm centered around 1553.5 nm (see insert).

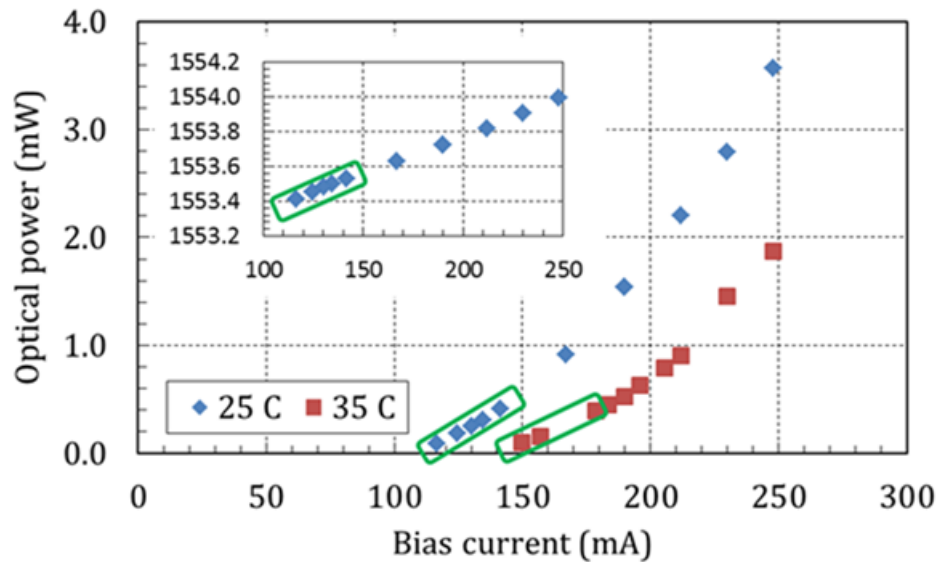


Figure 4-30. Light-current in the single electrode 1500 μm LC-DFB laser. Green-color rectangular boxes indicate regions with flat FM response. Inset plot shows the wavelength tuning range.

For the two-electrode laser in Figure 4-31, a flat FM-response is observed above the laser threshold in areas where electrode1 is supplied with currents under ~ 210 mA and electrode2 under ~ 150 mA.

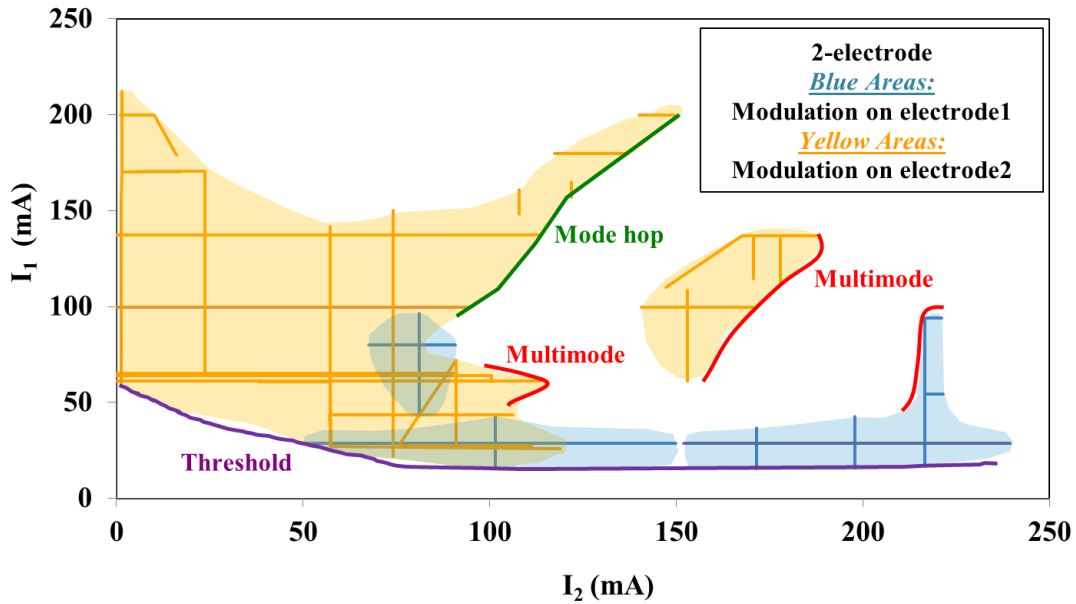


Figure 4-31. Flat FM response map for the 2-electrode 1500 μm laser device with varying current injection.

Areas with non-flat FM-response (white regions), mode-hopping and multi-mode are also identified (properly designed anti reflection coatings may prevent multi-mode emission in the tested lasers). Within the flat FM-response areas, the lasing mode can be tuned up to 2 nm for the range of bias currents analyzed and when the laser is controlled at 25°C, this tuning reduces to 1.7 nm when at 35°C operation temperature (not shown). In this temperature range, the laser maintains a single mode operation and a good Lorentzian linewidth.

Results for the three-electrode laser are shown in Figure 4-32 at 25°C, 35°C and 45°C. To simplify the analysis, electrodes 1 and 3 (the extreme electrodes) are injected with the same amount of current while the middle electrode is varied at relatively low bias currents. For the three temperatures analyzed, flat FM response is observed for currents in electrodes 1&3 ranging from ~30 mA to 132 mA and electrode 2 ranging from ~3 mA to 36 mA.

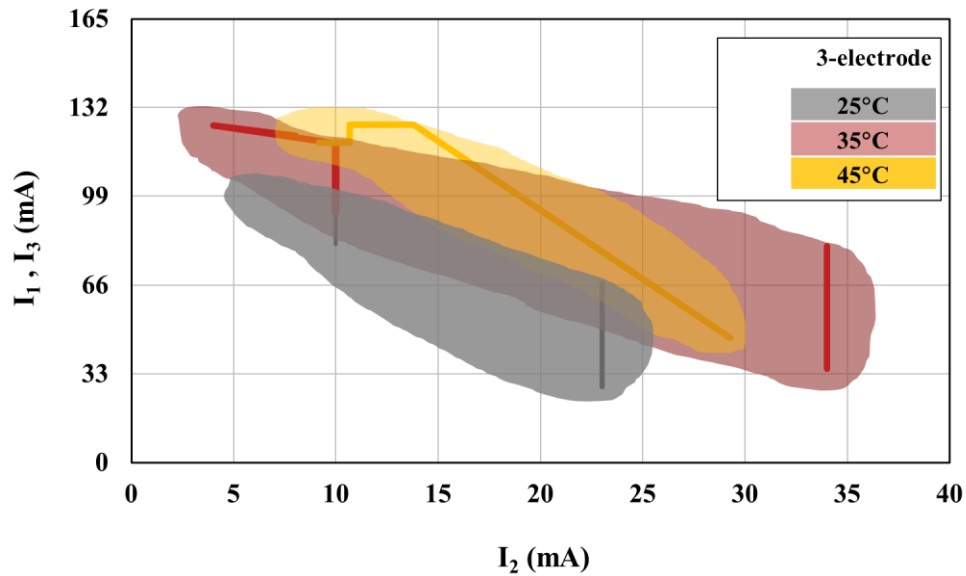


Figure 4-32. Flat FM response map for the 3-electrode L29 1500 μm laser device with varying current injection and under different operation temperatures.

For comparison, the performance of the three-electrode device reduces to almost that of the single electrode device when each electrode is supplied with the same current level and with the total current matching the single electrode device. These observations are maintained while the three-electrode laser device is temperature controlled from 25 to 45°C. As observed from the figures above, the flat FM response is further optimized by taking advantage of the different combinations of injections currents possible in a multi-electrode laser device.

Table 4-4. Current injection for a achieving a flat FM response in the laser devices

Device label	Number of electrodes	Cavity Length (μm)	Current (mA)		
			#1	#2	#3
L35	1	1500	135	-	-
L62	2	750	208	171	-
L28	2	1500	189	134	-
L29	3	1500	101	10	97

Specific bias conditions and operation temperature are selected – listed current in Table 4-4. Characterization was focused on laser operation for flat FM and phase response ($\Delta\phi < 90^\circ$) while maintaining the laser in a single mode operation with reasonably good Lorentzian linewidth and a large current tuning range.

As shown in Figure 4-33 and Figure 4-34, a flat profile of the frequency response for both amplitude and phase is measured for the 1-, 2-, and 3-electrode laser devices for frequencies from 1 kHz to over 300 MHz at certain bias conditions.

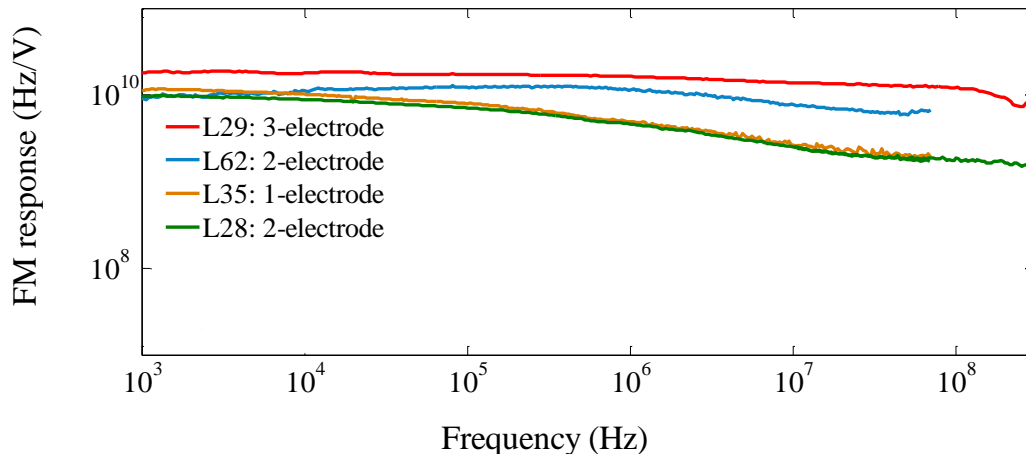


Figure 4-33. Frequency modulation response measured in the four tested multi-electrode MQW LC-DFB lasers.

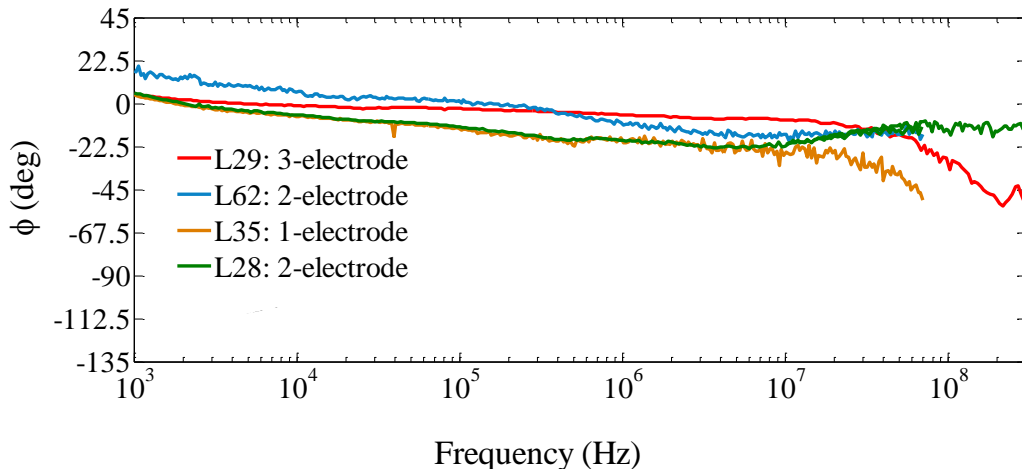


Figure 4-34. Phase modulation response measured in the four tested multi-electrode MQW LC-DFB lasers.

4.8.3 Relative Intensity Noise

Small fluctuations in the carrier and photon densities caused by spontaneous emission results in fluctuations in the laser output power, this is known as relative intensity noise (RIN) given as

$$RIN = \frac{\langle \Delta P(t)^2 \rangle}{P_0^2} \quad 4-4$$

Where P_0 is the average optical power and $\Delta P(t)$ is the fluctuations in the optical power. These fluctuations in the laser output power is transformed to electrical power fluctuations during detection, and the RIN can be expressed as

$$RIN(\omega) = \frac{\langle |\Delta P(\omega)|^2 \rangle}{\langle P_0^2 \rangle}$$

Where $\langle |\Delta P(\omega)|^2 \rangle$ is the power spectral density of the frequency noise and measures the overall noise made up of the thermal noise, shot noise, and laser intensity noise. The power spectral density (PSD) of the frequency noise shown in Figure 4-35

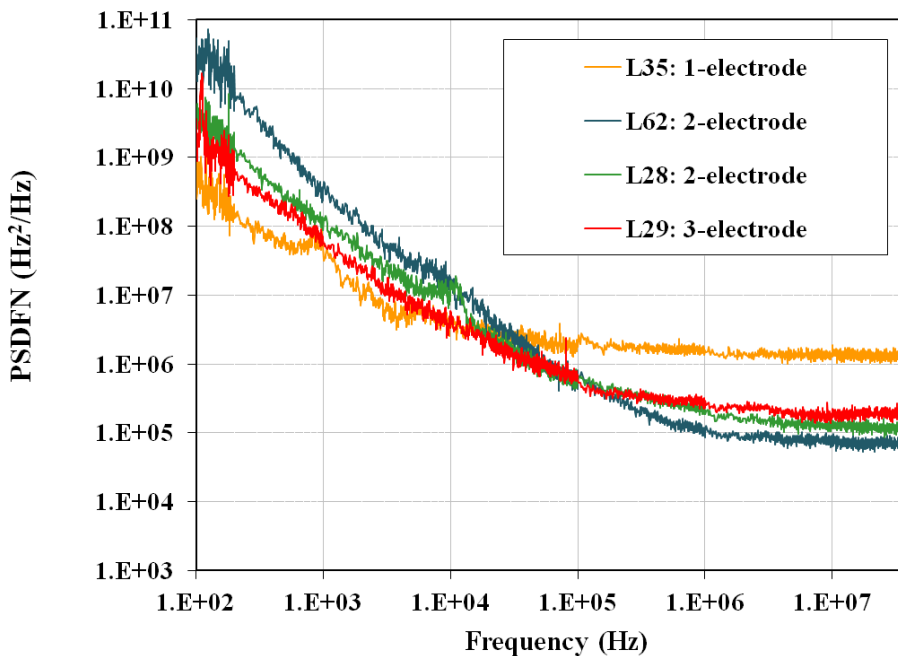


Figure 4-35. PSD of the frequency noise measured in the 1-, 2- and 3-electrode laser devices of same 1500 μm cavity lengths and 750 μm (L62)

Similar $1/f$ frequency noise profile below 100 kHz followed by a white noise plateau is observed in the two- and three-electrode lasers. Relative to the single-electrode device, the start of the white noise plateau and the level of noise is extended by one order of frequency and reduced by 10 dB, respectively. The PSDFN is less than $10^6 \text{ Hz}^2/\text{Hz}$ except the 1-electrode laser device.

The relative intensity noise (RIN) is analysed for only the 1500 μm multi-electrode laser devices as shown in Figure 4-36 for the 2-, and 3-electrode. The RIN is limited by shot noise in the detection system at -148 dB/Hz for 3-electrode and -155 dB/Hz for 2-electrode.

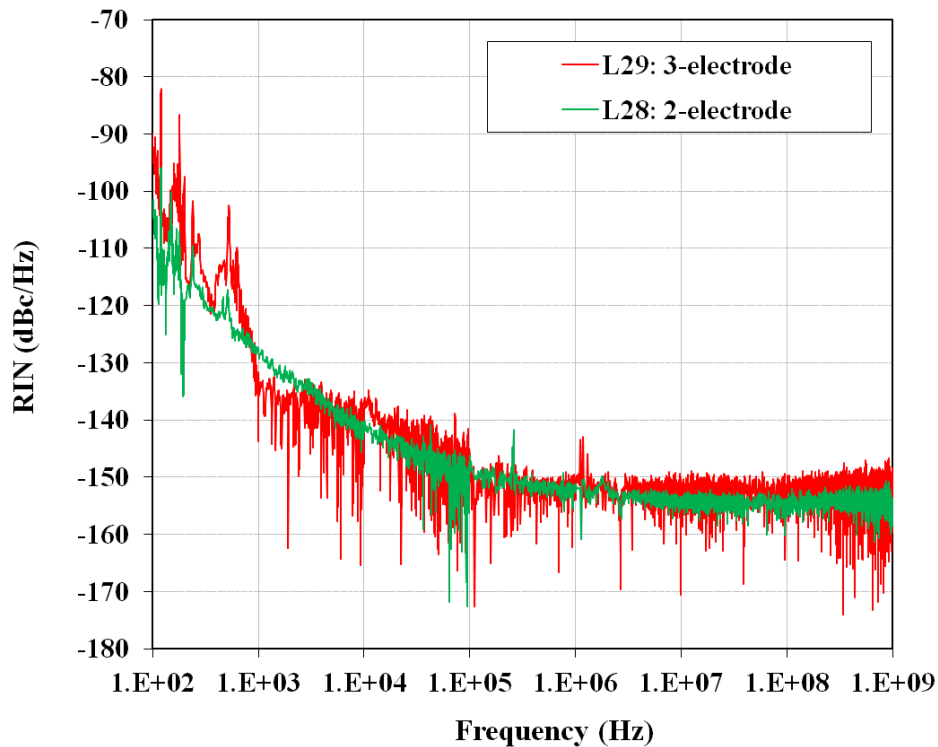


Figure 4-36. RIN measured in the 2- and 3-electrode MQW LC-DFB lasers devices of same 1500 μm cavity length

4.9 Summary

The performance characteristics of the InGaAsP/InP multi-quantum well multi-electrode laterally-coupled distributed feedback laser operating in the 1560 nm wavelength was presented. The lasers active region consist of six compressively strained 5 nm thick QWs and equally six but 8 nm barriers. It has an approximate 800 nm ridge height. A third-order rectangular grating with a period of ~720 nm and a duty cycle of 50% is etched on the ridge sidewalls thus creating alternate ridge widths (narrow and width). The lasers have 1-, 2- and 3- electrically isolated partitioned electrodes from which each individual electrode section were selectively biased either uniformly or non-uniformly. Scanning electron microscopy revealed some minor and not so minor fabrication imperfections which can affect laser performance. The laser devices were an as-cleaved on bare die bars of varying lengths, some of the laser devices were cleaved into individual chips and its electrodes were wire bonded on interfacing printing circuit boards. Several laser parameter characteristic experiments were carried out to ascertain the performance of these laser devices. A comparison was made but not limited to the symmetric/asymmetric bias conditions, for the different number of electrodes, the driving currents, the various operating temperatures, the laser device dimensions etc. These LC-DFB laser devices have shown repeatable performance without hysteresis. They are hereby summarized below based on the laser characteristic parameter.

Laser device microscopy and PL mapping

The SEM images shows rounding of the rectangular grating teeth, this rounding can affect the coupling between the grating and the active region. Microscope measurements also showed the overall dimensions deviated from target such as the period of the gratings by tens of nanometers, the narrow and wide ridge widths also deviated by some nanometers. All these are fabrication related. A good thing of note is that the gratings revealed smooth and vertical sidewalls. The PL mapping of the wafer revealed cross-wafer non-uniformities, we observe a somewhat circular symmetry due to the rotation of the substrate from long wavelength at the center to shorter wavelengths at the edges ranging from 1566 to 1534 nm.

Light-Current

A smooth linear L-I curve is observed with saturation occurring at higher injection currents. Threshold currents determined from the x-intercept of the linear regression varies based on the operating conditions or laser dimension. Under symmetric current injection threshold current determined from the L-I curve showed the 2-electrode laser device with a lower threshold current of 80 mA in comparison with a 1-electrode device at 110 mA for the same cavity length of 1500 μm , while also revealing a higher maximum power for the 2-electrode laser. Under asymmetric current injection for the same 2-electrode laser device, a higher maximum power is observed when electrode1 is biased (or varied) at a higher current ratio than electrode2 due to the higher current density dominated in this first electrode being closest to the laser output facet. Comparing the 2-electrode laser device with its counterpart but having a shorter laser cavity of 750 μm reveals a smaller threshold of 40 mA for the shorter cavity length laser device. At different operating temperatures (25°C – 65°C), the threshold current increases linearly. A dynamic resistance of $\sim 3 - 4.5 \Omega$ was estimated from the I-V curve at different operating temperatures with the higher resistance observed at higher temperatures.

Optical spectra

A stable single longitudinal mode was observed in the laser spectrum peaking at ~ 1560 nm and analyzed using an optical spectrum analyzer. It showed a red-shift in peak emission wavelength as current increases and the same phenomena as temperature increases. It showed an increase in emission output power with increasing current but a decrease in emission power with increasing temperatures for a particular current injection. A current tuning rate of 14 pm/mA (at 25°C) and 16.2 pm/mA at (65°C) was measured reaching a tuning of 2.25 nm in the analyzed bias range. A temperature tuning of 3.38 nm at a rate of 97 pm/°C was measured.

Side mode suppression ratio

In general, the laser devices exhibit good longitudinal mode discrimination. A maximum SMSR of 58 dB was observed at 25°C while biased at 160 mA. At this temperature the

SMSR was >50 dB for most currents. However the SMSR gradually degrades with increasing temperatures with the lowest observed at 65°C . A higher SMSR was observed for the multi-electrode devices compared with the single electrode.

Linewidth

In all cases analyzed, the linewidth varies with bias current in free running operation. The linewidth when the laser is under optical feedback operation was reduced compared to when the laser was in free-running. For individual bias, the amount of linewidth reduction depends on the feedback power level. For all cases, the linewidth increases with increase in operating temperatures. For applications where ultra-narrow linewidths are required to increase the laser coherence, optical feedback operation can be used, whereby if the feedback power is well controlled, it might result in spectral stability and ultra-narrow linewidths and it will also improve the modulation characteristics of the laser. The multi-electrode lasers are useful whereby under appropriate and selected driving conditions, a linewidth of interest can be achieved. In general the laser exhibited a Lorentzian linewidth the lowest linewidth of 210 kHz and varied based on the current/temperature while in free-running. A linewidth reduction to as low as 96 kHz was measured while under optical feedback operation.

Intensity modulation and relative intensity noise

The tested multi-electrode LC-DFB laser devices under appropriate and selective driving conditions were able to exhibit a flat FM-response from DC to above 300 MHz. The flat FM response was optimized by taking advantage of the different combinations of bias conditions that is available to the multi-electrode laser device thus providing a mechanism to improve its FM response relative to its single electrode counterpart. The RIN was limited by shot noise in the detection system. The FM response of these tested LC-DFB lasers when compared with the best commercially-off-the-shelf (COTS) DFB lasers performs better in terms of the flatness and the frequency range, this will facilitate its use in miniaturised OPLLs for further laser line width reduction or optical phase-locking for high spectral purity RF generation applications

In general, the multi-electrode laterally-coupled distributed feedback laser characterized and reported exhibits a stable single mode emission with a good tuneability, it has narrow spectral linewidth and high side mode suppression ratio. In addition, a flat frequency modulation response is observed in the low frequency range. Therefore this laser has potential of being used in a coherent optical system.

Chapter 5 Semiconductor Optical Amplifier and Fabry-Perot Laser

5.1 Introduction

This chapter is on the semiconductor optical amplifier (SOA) operating in the E-band wavelength region, it begins with an overview of the advantages of SOAs, due to its versatility it has become a key enabling component in the fast growing optical communication system. This chapter presents the device structure for the asymmetric multi-quantum well SOA. Fabry-Perot lasers of same material compositions as the SOA were included on the same wafer as test structures for the SOA. Detailed characterizations such as light-currents, threshold current density, slope efficiency, internal and external quantum efficiencies, optical spectra, gain/loss are presented. The result analysis helped to narrow down the SOA devices based on the geometry that will give the best performance. Overall performance analysis of this ‘best performance’ SOA was carried out and presented in a later section, parameter extraction of its characteristics such as its amplified spontaneous emission and spectrum, gain, broad bandwidth, output saturation power, polarization sensitivity and noise figure. A summary of the results is presented in the last section. The non-uniformity in some of the data plots could be an indication of fabrication variations and imperfections across the wafer, spontaneous emission noise, vibration of the test setup, noise in the instruments, coupling inefficiencies and human error.

5.2 SOA vs other Optical Amplifiers

There are different kinds of optical amplification technologies used in communication network system. The choice of which amplifier to use is dependent upon application of interest. In recent times, the use of SOAs as in-line amplifiers in optical networks has become commonplace, however, their use has yet to match that of Erbium doped fiber

amplifier (EDFA), which seems to be the amplifier technology of choice for optical networks in the C-band regime⁸⁷. An EDFA is made up of a length of optical fiber that is doped with Er^{+3} ions. EDFAs exhibit high optical gain in the 1550 nm wavelength region which makes it widely used in amplification in Dense Wavelength Division Multiplexed (DWDM) transmission schemes^{88,89,90}. For in-line amplification, EDFA is advantages over SOAs because it has been demonstrated to have lower noise figure, higher output saturation power and slow gain dynamics, which essentially allows multiple input signals amplification with no crosstalk effects. The drawback is that it requires optical pumping which makes it large and expensive therefore not a good candidate for integration with other photonic devices. Their long lived gain dynamics compared with SOAs implies they cannot be used for certain functional applications. SOA on the other hand is electrically pumped and is capable of amplification outside the C-band, its active region can be engineered to provide gain in a broader band.

Another amplification technology is Raman amplification. Raman amplifiers use stimulated Raman scattering (SRS) to amplify signals. An intense pump beam propagates in an optical fiber, and through SRS gives up its energy to create another photon at a lower frequency by inelastic scattering. By selectively choosing the pump beam energy can be transferred between the pump beam and a signal beam, achieving optical gain. Raman amplifier is demonstrated to have a wide gain bandwidth and operates in windows that EDFA is limited⁹¹. However, it also requires optical pumping thus increasing the cost and complexity.

The advantages of SOA therefore lie in its versatility, it is electrically pumped and has a broader bandwidth, it is compact and capable of being monolithically integrated with other optical components such as couples and passive waveguides. In addition, because of its fast dynamics and nonlinearities, it can perform all-optical signal processing⁹¹.

5.3 Motivation of Research

Optical access networks are currently the best solution to provide the ever increasing broadband services demanded by the end users^{92,93}. Standardized broadband services at

2.5 Gbits/s and beyond in the form of passive optical networks (PON) have been implemented in many countries and are under deployment worldwide. Although PONs provide a significantly larger bandwidth relative to copper and wireless based access networks, an exhausted capacity has been anticipated as bandwidth-hungry applications such as HDTV and 3-D video become available^{94,95,96}. Variations of the existing networks to enhance their performance have been proposed, thus emerging the so-called next generation optical access networks^{97,98,99,100}. Figure 5-1 and Figure 5-2 below shows the typical structure of an optical access network implementing optical amplifier.

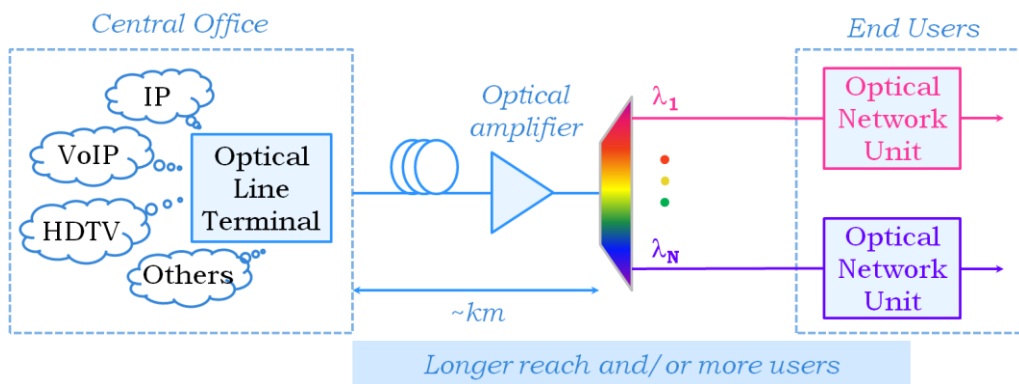


Figure 5-1. Optical amplifier to extend reach of a network and/or add more users

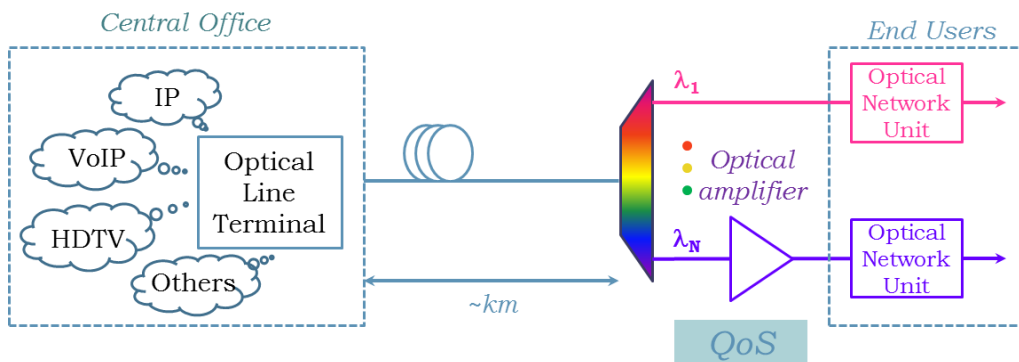


Figure 5-2. Optical amplifier to improve quality of service (QoS)

The low-water peak fiber being manufactured by Corning¹⁰¹. has made feasible the use of optical carriers allocated at wavelengths within the E-band, spanning from 1360 to 1460 nm see Figure 5-3 below. Similarly to the traditional PONs, increasing the number

of users in the next generation optical access architectures through the physical extension of the network is crucial to reduce its cost, and to allow the consolidation between access and core networks. At such wavelength range of operation, choices for low cost in-line or boost optical amplifiers, with compact size, low energy consumption and feasibility for integration with other optoelectronic components are rather limited, making the semiconductor optical amplifiers (SOA) a realistic solution.

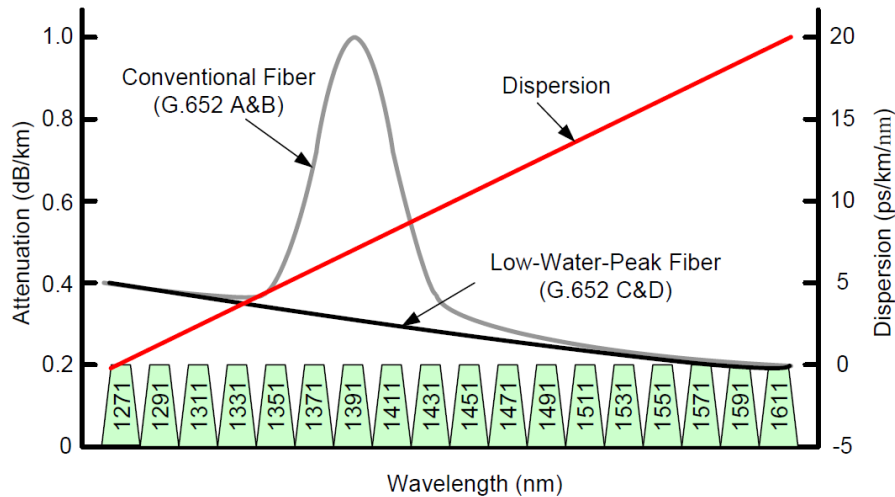


Figure 5-3. Attenuation/Dispersion in low water peak fiber in E-band wavelength regime¹⁰¹

A combination of broadband amplification, polarization insensitivity and high gain are desirable characteristics in an optical amplifier. SOAs based on multi quantum wells (MQW) structures have been proposed to obtain high gain and low polarization sensitivity. A chip gain of 15 dB and polarization insensitivity under 3 dB for a 30 nm bandwidth at 1300 nm was reported for a 4-tensile strained MQW InGaAsP/InP material system¹⁰². Polarization insensitivity as low as 0.3 dB for 30 nm bandwidth in C-band was reported with a gain of 19 dB¹⁰³.

Asymmetrical MQW (AMQW) structures have been investigated to improve the amplification bandwidth¹⁰⁴ and it has been demonstrated that AMQW SOAs provide a broader spectral range than their MQWs counterpart^{105,106}. The active region of these asymmetric structures consists of a collection of MQWs of varying thicknesses and/or

material composition. The broad bandwidth characteristics of these structures are due to the superposition of the gain of individual quantum wells, each of them providing optical gain in definite wavelength ranges. AMQW with varying material composition have advantages over the thickness differing designs due to improved contributions to the carrier densities at different energy transitions¹⁰⁷. Equal thickness of the QWs results in equal gain contributions, whereas thin wells produce less gain than thicker ones for the same carrier density¹⁰⁷.

5.4 SOA Device Structure

The SOA consists of nine 6 nm $\text{In}_{1-x}\text{Ga}_x\text{As}_y\text{P}_{1-y}$ 0.2% tensile strained MQW layers sandwiched between nine latticed matched 6 nm InGaAsP barriers as shown in Figure 5-4 below. The asymmetry of the active region is based on the difference of the molar concentrations equivalent to bandgap wavelengths of $\lambda_g=1.1 \mu\text{m}$ for the barriers and $\lambda_g = 1.23 - 1.44 \mu\text{m}$ for the QW layers. The active region is grown on an n-doped InP substrate and buried by p-doped InGaAsP layers. A detailed description of the different layers comprising the SOA device is illustrated in

Table 5-1 below.

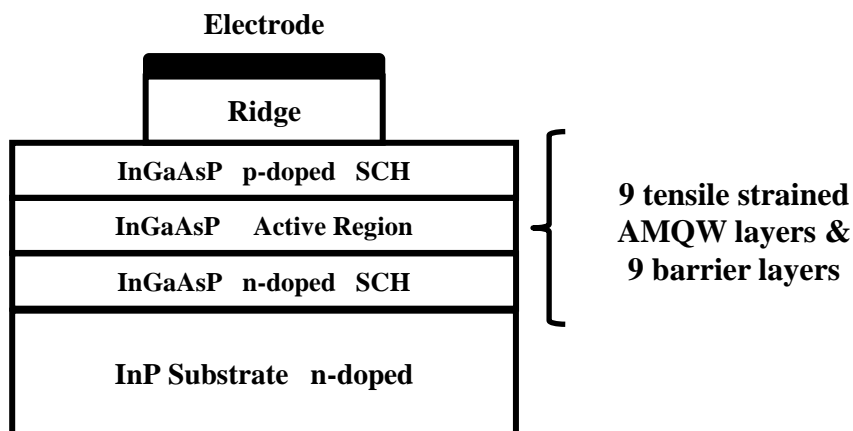


Figure 5-4. Cross-section diagram of the asymmetric MQW SOA. SCH is the separate confinement heterostructure

Table 5-1. Description of the SOA composition

Layer Description	λ_g (μm)	Material System	Thickness (nm)	Doping Concentration (cm^{-3})
p-Contact		InGaAs	180	p, 2×10^{19}
Ridge 1	1.1	InGaAsP	20	p, 2×10^{18}
Ridge 2	0.919	InGaAsP	1000	p, 2×10^{18}
Etch Stop	1.3	InGaAsP	5	p, 7×10^{17}
Cladding 1	0.97	InGaAsP	100	p, 1×10^{16}
Cladding 2	1.0	InGaAsP	100	p, 5×10^{17}
Outer Barrier	1.1	InGaAsP	60	Undoped
9 Barriers	1.1	InGaAsP	6	Undoped
9 QWs	1.23 - 1.44	InGaAsP	6	Undoped
Outer Barrier	1.1	InGaAsP	20	Undoped
Cladding 1	1.0	InGaAsP	30	n, 8×10^{17}
Cladding 2	1.0	InGaAsP	30	n, 8×10^{17}
Cladding 3	0.95	InGaAsP	30	n, 8×10^{17}
Buffer	0.919	InP	1040	n, 2×10^{18}
Substrate	0.919	InP	5000	n, 4×10^{18}

Some of the devices have cleaved-cleaved facets and some are anti-reflection coated. The devices that have 7° tilt anti-reflected coated facets have facet reflectivity of 5×10^{-5} . The center wavelength is around 1360 nm. Fabry-Pérot (FP) lasers of similar dimensions but no tilted facets have also been fabricated on the same wafer. These devices were fabricated using digital alloy molecular beam epitaxy (MBE) and metalorganic chemical vapour deposition (MOCVD). The mask layout of the devices on the wafer is shown in Figure 5-5 where each section consists of 9 SOAs and 5 FP lasers.

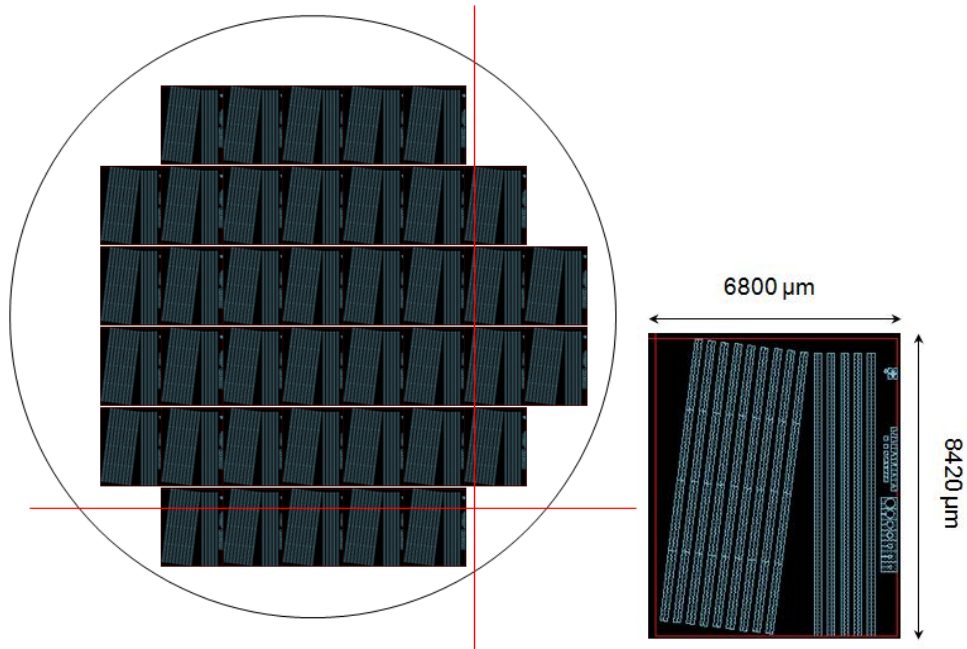


Figure 5-5. Mask layout of the SOAs and FP lasers

Figure 5-6 below shows the photoluminescence taken from the surface of the wafer provided by the fabrication foundry CPFC.

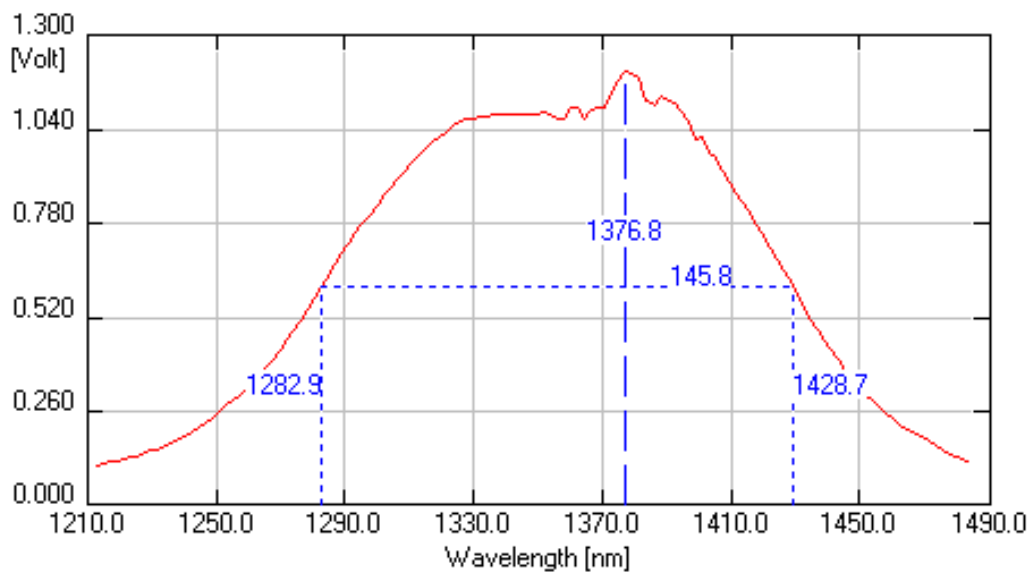


Figure 5-6. Photoluminescence for SOA from wafer surface⁷⁵

The SOAs were designed and characterized at the Photonics Technology Laboratory, Centre for Research in Photonics, and the fabrication was done at Canadian Photonics Fabrication Center, supported by CMC Microsystems, Canada. Table 5-2 shows the received devices on bars with cavity lengths (300, 600, 900, 1200, and 1500 μm) and ridge widths {2:0.25:4} μm for the SOA. The Fabry-Perot lasers have similar cavity dimensions but with ridge widths {2:2:10} μm .

Table 5-2. Cleaved SOA and FP laser devices on bars

No. of Bars	Length (μm)	Devices	Ridge width (μm)
4	1500	9 SOAs + 5 lasers + repeat	SOA = {2.0 : 0.25 : 4.0} Laser = {2 : 2 : 10}
4	1200	9 SOAs + 5 lasers + repeat	SOA = {2.0 : 0.25 : 4.0} Laser = {2 : 2 : 10}
4	900	9 SOAs + 5 lasers + repeat	SOA = {2.0 : 0.25 : 4.0} Laser = {2 : 2 : 10}
4	600	9 SOAs + 5 lasers + repeat	SOA = {2.0 : 0.25 : 4.0} Laser = {2 : 2 : 10}
4	300	9 SOAs + 5 lasers + repeat	SOA = {2.0 : 0.25 : 4.0} Laser = {2 : 2 : 10}

On reducing facet reflectivity

While light is propagating through the SOA, any reflections along the transmission path that is coupled back into the active region of the SOA causes spectral distortion since these reflections are amplified during the multiple passes within the gain medium¹⁰⁸. Large facet reflectivity therefore lower the carrier density, the gain bandwidth, and the output saturation power, as well as enhance the noise figure^{109,110}. It is therefore

necessary to reduce the reflectivity of the amplifier facets in order to provide a smooth gain spectrum¹¹¹. Low facet reflectivity in the range of 10^{-5} and lower is typical to reduce ripples in the gain spectrum

There are different ways to achieve low facet reflectivity such as applying anti-reflection coatings (ARCs) on the facets, this can lower reflectivity to about 10^{-3} ¹¹². Another method is using angled facets. Tilting the facets from the normal to the propagation direction reflects light at a greater angle than the waveguide can accept thus preventing it re-entering the active region of the SOA. Typical tilt values are in the range of 5 -10°. The angled facet is achieved by orienting the SOA device at an angle to the cleave plane of the wafer. A combination of these two will yield desirable facet reflectivity. Another method is tapering the waveguide such that the mode profile expands, this will allow only a small portion of the propagating optical field to reflect back into the active region of the SOA. Figure 5-7 below shows the calculated reflectance at the 7° tilted facet.

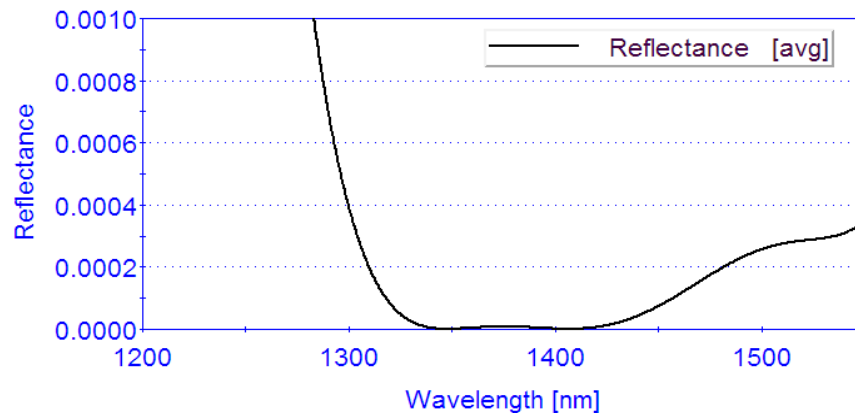


Figure 5-7. Calculated reflectance at the 7° incidence angle

5.5 Fabry-Perot Laser Characterization

As previously mentioned, The Fabry-Perot (FP) lasers have similar material composition as the SOA. It also same the same cavity lengths dimensions but with ridge widths {2:2:10} μm . For the experiment carried out, some of the devices were excluded from the

test for several reasons such as: The 300 μm devices had cavities too short and therefore no lasing occurred. Depending on the area (RW x CL) of the laser devices some the larger laser devices were yet to lase at high injection current, some that did, saturated immediately shortly after lasing. Notwithstanding, some of these non-optimal devices result are still presented for comparison purposes. Most of the ridge widths are too large for these lasers and an overall recommendation based on theory and experimental analysis will be provided at the end of the chapter.

5.5.1 Experimental Set-up

The experimental setup is composed of a laser stage, optical spectrum analyzer, photo detector/power meter, taper fiber, thermoelectric cooler (TEC)/controller, rotational stages/positioners, source meter, piezoelectric controller, infra-red viewer, microscope, and a computer/LABVIEW for data acquisition. The laser stage is a combination of 6-positioner stages, heat sink, probes and a microscope. The heat sink stage is composed of a XYZ stage, copper plate, brass sample holder and thermoelectric cooler. A thermo epoxy resin was used to bond the copper plate and the TEC cooler. The stage is built such that there is a uniform distribution of heat on the copper plates where the brass sample holder is placed. All measurement for the FP lasers were carried out at 25°C. The lasers were injected with currents using source meter through tungsten needle probes directly applied to the contact above and grounded through alligator clips to the brass sample holder

Light from the laser device is focused into a single mode taper fiber connected to an optical spectrum analyzer (OSA) for spectral measurement, or connected to a photodetector for light-current measurements. The taper fiber is used to optimize maximum coupling of light, as loss due to coupling of light through the fiber is a major drawback in the setup. Care was taken to optimize the alignment of the setup. Piezo-electric controllers were used to control the nano-positioning and alignment of the experimental setup. Figure 5-8 below shows a simple schematic of the experimental setup

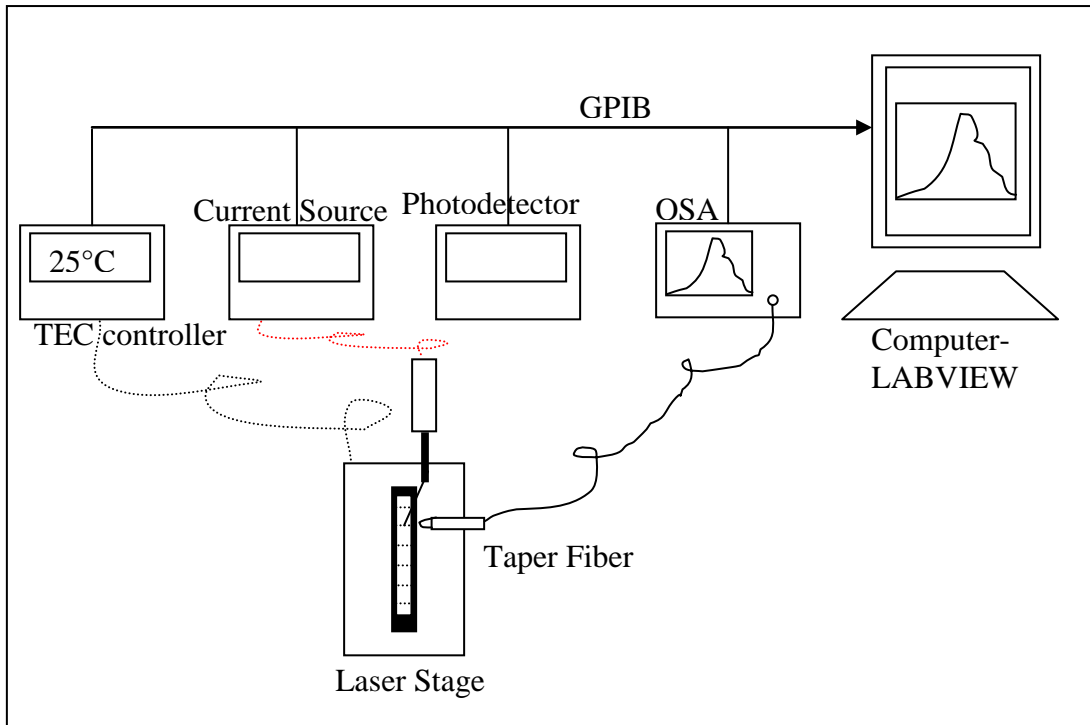


Figure 5-8. Schematic of the experimental setup

5.5.2 Light-Current

The light-current (L-I) curve is important in laser characterization. It is a plot of the light power emitted as a function of the injection current for a specific laser device at a specific temperature. The L-I measurements are obtained by varying the injection current and simultaneously measuring the light output power using a photodetector. Several laser parameters can be derived from the L-I graph such as the maximum power, threshold current, threshold current density, slope efficiency, external quantum efficiencies etc of the laser device. At very low current, the spontaneous emission dominates and the output power stays at very low levels. When the current passes threshold, the stimulated emission dominates and there is an abrupt increase in the light output power.

Threshold Condition

For lasing to occur, the injection current must reach a certain minimum value called the threshold current. At this current there are enough carriers to compensate for all the losses in the laser cavity, such as the leakage current and recombination processes.

Lasing threshold occurs when the gain in the active region overcomes the propagation and mirror losses. The electric field exactly replicates itself after one round-trip in the cavity. Increase in the gain occurs as a result of increase in the injection current density and subsequent increase in the carrier concentration. A threshold condition is thereby reached when the carrier concentration is at a threshold value. Since the lasing process is a steady-state phenomenon, gain should therefore clamp at the threshold gain even as current is increased¹¹³. This is illustrated by the linear behaviour that the graph exhibits after threshold. The value of the threshold current in the simplest form is the intercept of the x-axis (current axis), considering only the linear part of the graph.

Threshold current is therefore an important characteristic since it is the minimum current value at which a laser turns on. Low threshold currents are usually desirable because if a threshold current is low it minimizes the input power needed to operate a laser, low current implies low internal temperatures which means less expensive thermoelectric coolers needed in packaging the laser devices thereby lowering the cost, a high threshold current on the other hand can heat up the laser device which will degrade the device performance.

The light-current (LI) and voltage-current (VI) characteristic plots for the FP emission are shown in Figure 5-9 and Figure 5-10 for cavity lengths 600, 900, 1200, and 1500 μm and ridge widths of 2, 4, and 6, and 8 μm .

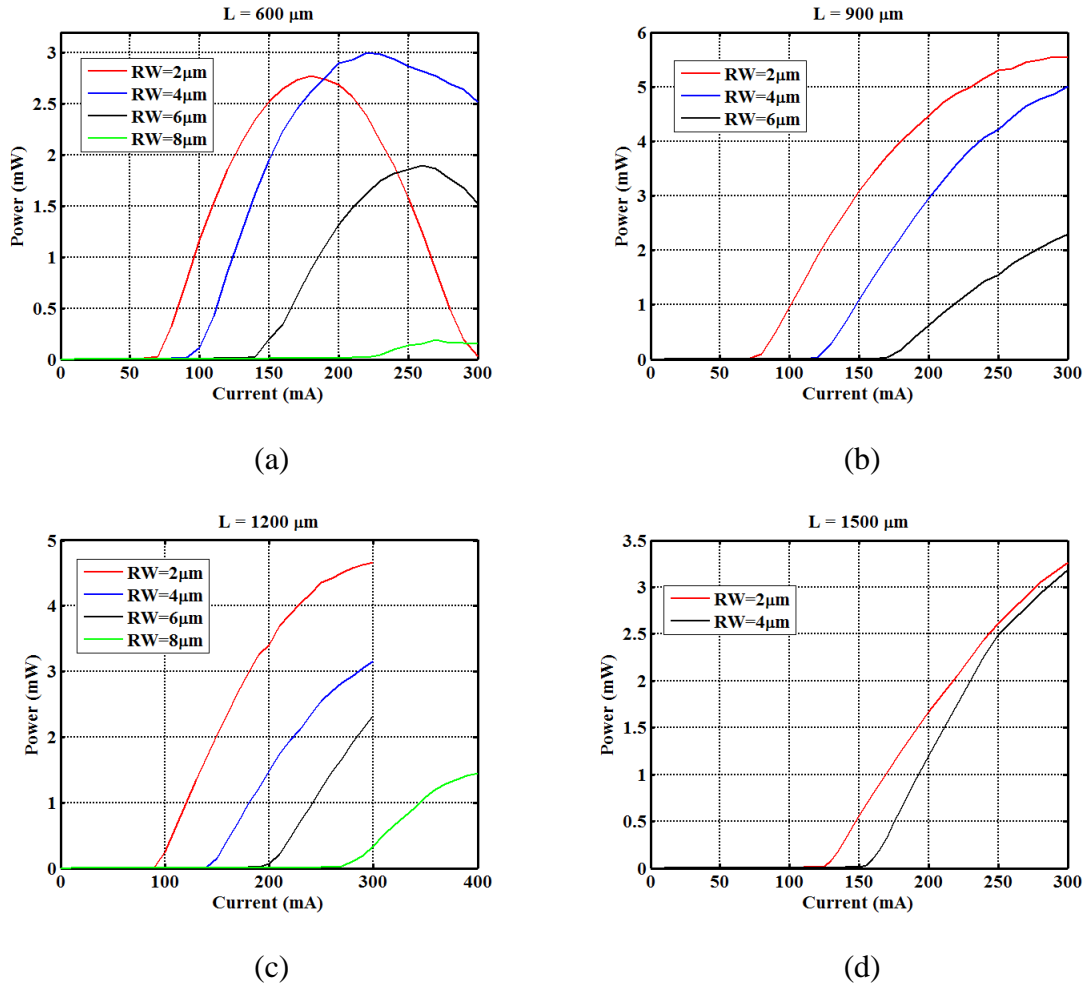
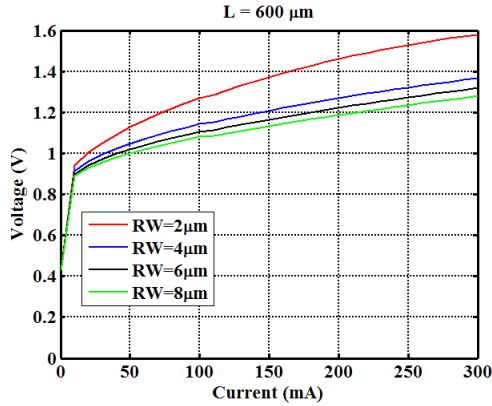
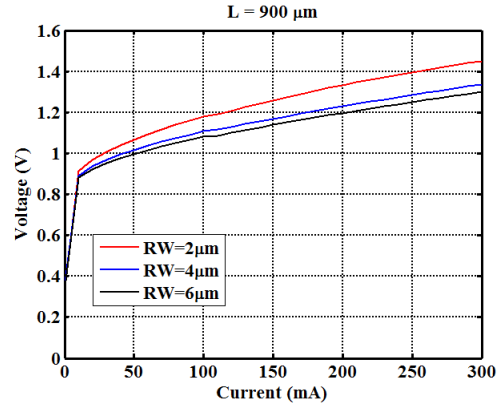


Figure 5-9. LI characteristic plots with varying ridge widths (RW) for (a) 600 μm (b) 900 μm (c) 1200 μm and (d) 1500 μm cavity lengths respectively

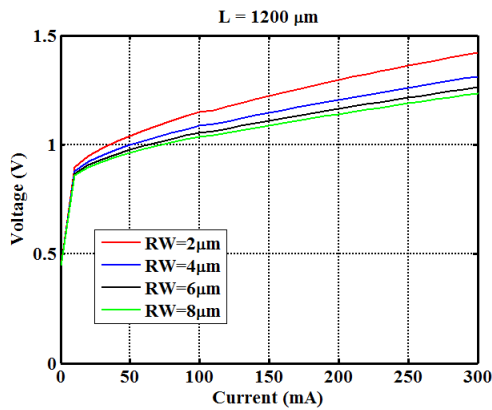
For each of the cavity lengths, threshold current (I_{th}) increases with ridge width from 70 mA up to 250 mA combined. The threshold current values for each device are indicated in Table 5-3. Due to their internal resistance, lasers heat up fast during operation such that when the laser reaches its maximum power at a particular current level, it fails to operate optimally, the power output starts to decrease as more current is injected. Thereby, saturation effect and thermal roll-over is observed for certain currents which is very obvious in the 600 μm plot. These geometry-dependent L-I analysis is used to extract other parameters such as the threshold current density, slope efficiency, external quantum efficiency etc.



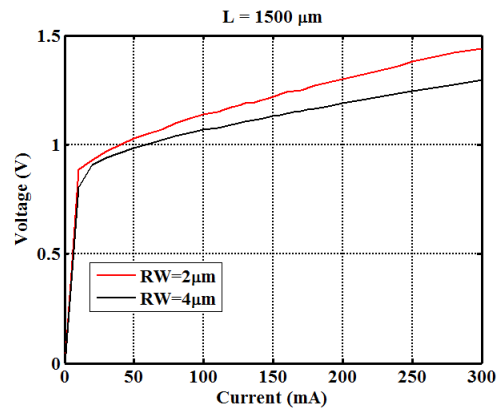
(a)



(b)



(c)



(d)

Figure 5-10. VI characteristic plots with varying ridge widths (RW) for (a) 600 μm (b) 900 μm (c) 1200 μm and (d) 1500 μm cavity lengths respectively

To assess the quality of the metallic ohmic contacts on the laser device, the dynamic series resistance is determined from the VI plots. High series resistances can be as a result of low quality material used. For the 2 μm devices, the dynamic resistance is 2.07 Ω for the 600 μm , 1.67 Ω for the 900 μm , 1.54 Ω for the 1200 μm , and 1.57 Ω 1500 μm devices.

A summary of the maximum output power and the current threshold are presented in Figure 5-11 and Figure 5-12 for all the cavity lengths and ridge widths tested.

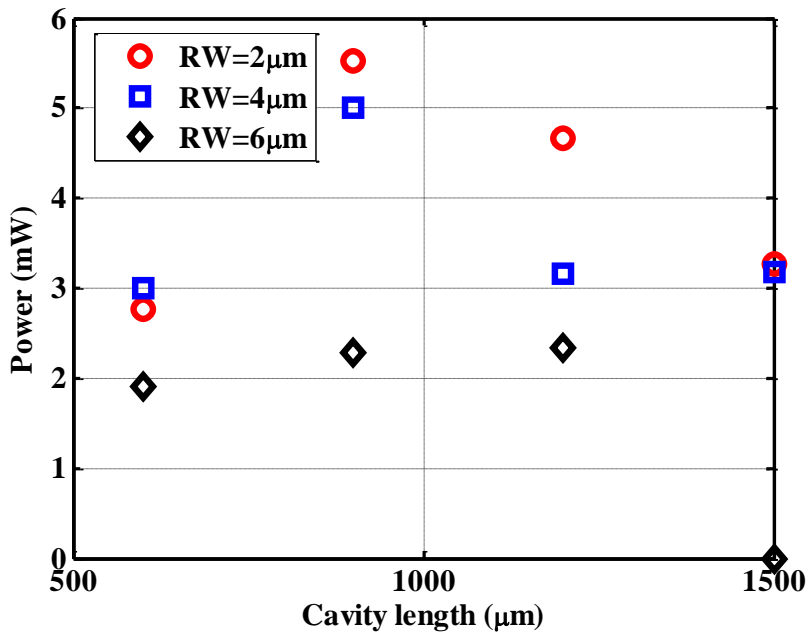


Figure 5-11. Maximum output power vs cavity length of the laser

The maximum power observed is in the 900 μm device at 5.5 mW per facet. These are cleaved-cleaved facets and it would also be appropriate to multiply these numbers by 2 since we assume equal amount of light is also exciting from the other facet. And the lowest power is observed in the 600 μm devices which is related to the early saturation observed in its L-I plots. The threshold current increases linearly with the cavity length. The increase in threshold current with cavity length agrees with theory because longer cavity lengths implies longer time for facet-to-facet reflection thus requiring higher injection current for gain to equal the losses. The 600 μm devices have the lowest threshold current with the 900 μm following closely behind. The exact numbers are shown in Table 5-3. Laser devices dimension with their corresponding threshold current/density. Table 5-3.

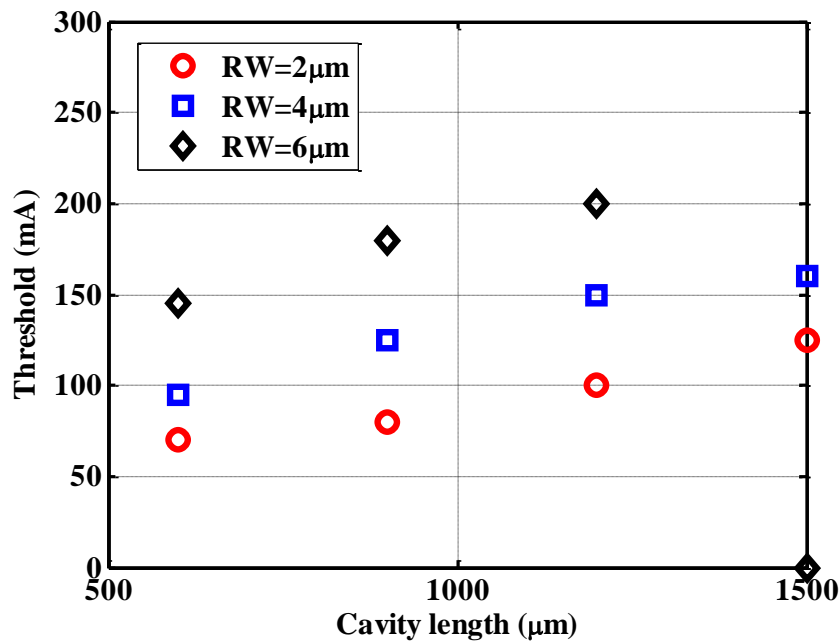


Figure 5-12. Threshold current vs cavity length of the laser devices.

Threshold current is dependent on the quality of the semiconductor material from which the device is fabricated and the geometry of the laser device. A wider and longer laser requires more injection current to start lasing. Therefore when comparing the threshold current values of different laser devices, it is more accurate to consider threshold current density rather than threshold current. Threshold current density is denoted by the symbol J_{th} , it is determined by dividing the experimentally obtained threshold current value, I_{th} by the area of the laser. In a ridge waveguide laser, the area of the laser device is the multiplication of the ridge width and cavity length i.e., $RW \times CL$, as a matter of simplicity and ease of understanding, this relation will be used to denote the dimension of the laser devices.

Table 5-3. Laser devices dimension with their corresponding threshold current/density.

RW (μm)	L (μm)	1/L (cm^{-1})	I _{th} (mA)			
				Area(cm^2)	J _{th} (A cm^{-2})	Ln(J _{th})
2	600	16.67	70	1.2×10^{-5}	5833.33	8.67
	900	11.11	80	1.8×10^{-5}	4444	8.4
	1200	8.33	100	2.4×10^{-5}	4166.67	8.33
	1500	6.67	125	3.0×10^{-5}	4166.67	8.33
4	600	16.67	95	2.4×10^{-5}	3958.33	8.28
	900	11.11	125	3.6×10^{-5}	3472.22	8.15
	1200	8.33	150	4.8×10^{-5}	3125	8.05
	1500	6.67	160	6.0×10^{-5}	2666.67	7.89
6	600	16.67	140	3.6×10^{-5}	3972.22	8.29
	900	11.11	180	5.4×10^{-5}	3333.33	8.11
	1200	8.33	200	7.2×10^{-5}	2777.78	7.93
	1500	6.67	-	9.0×10^{-5}	-	-

The result shows that threshold current density decreases with increasing cavity length for a specific ridge width and a similar observation of its natural log. For a specific cavity length it decreases as the ridge with widens.

The threshold current density as a function of the reciprocal cavity length is shown in Figure 5-13 . It increases with the inverse of the cavity length. The intercept of the linear regression gives the transparency threshold current density J_0 . The transparency threshold current density is independent of the geometry of the laser device and can be assumed to be the threshold current of a theoretically infinitely long cavity length laser with no losses

at its facets. It is a better way to compare quality of the different wafers these devices were fabricated on. As shown in Figure 5-13 below, the J_0 for the 2 μm is $2800\text{A}/\text{cm}^2$ and $2000\text{A}/\text{cm}^2$ for the 4 μm .

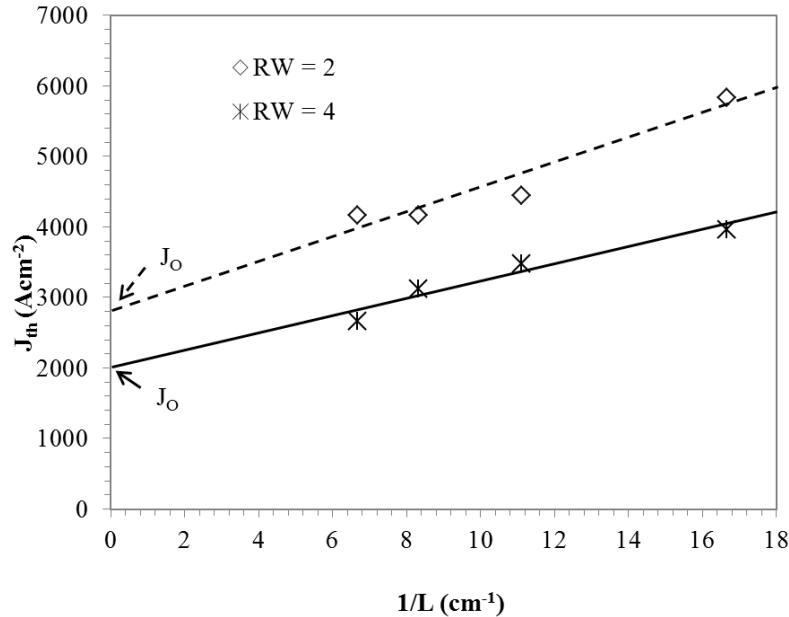


Figure 5-13. Threshold current density versus the reciprocal cavity length

5.5.3 Slope and Quantum Efficiencies

As it is desirable to have a low threshold current, it is also important to have rapid increase in output light emission for a small change in the input current above the threshold current. This measurement of the change in the output power versus injected current ($\Delta P/\Delta I$) above the threshold current is termed the slope efficiency; it is the slope of the linear portion of the L-I characteristic in units of mW/mA, the steeper the slope the better. The parameter indicates the device efficiency and shows how much more output power can be expected out of a laser device given a certain amount of increase in current above threshold. The slope efficiency is dependent on the cavity length; usually longer cavity length lasers have lower slope efficiency.

The external quantum efficiency, η_d (converted to a percentage) indicates the efficiency of laser device in converting the injected electron hole pairs into photons emitted from the device. Theoretically, the recombination of each electron-hole pair results in the generation of one photon and the photon survives its travel through the laser waveguide structure to be emitted from the device. In reality, not all electron-hole pair recombination results in the generation of photons, some result in the generation of other undesirable forms of energy, such as heat¹¹⁴. Also, not all photons are emitted from the device, as some of them are reabsorbed by the structure.

The value of the external quantum efficiency is calculated from the slope efficiency as in below. For cleaved-cleaved facets, the reflectivities of both facets are assumed to be identical and a factor of two is incorporated. The external quantum efficiency is equal to

$$\eta_d = 2 \frac{\Delta P}{\Delta I} \cdot \frac{\lambda q}{hc} \quad 5-1$$

where;

λ is the wavelength of the laser,

h is Planck's constant = $6.62606896 \times 10^{-34}$ Js,

q is the fundamental electronic charge = $1.602176487 \times 10^{-19}$ C,

c is the speed of light = 3×10^8 m/s.

The amount of current that generates carriers in the active region determines the internal quantum efficiency. Like η_d , the internal quantum efficiency (η_i) is a measure of the efficiency of a laser in converting electron-hole pairs (injected current) into photons within the laser structure. However, unlike the external quantum efficiency, the internal quantum efficiency is independent of the geometry of the laser device such as the cavity length or the ridge width. This parameter is used for the comparison of material properties of the laser devices.

Table 5-4. The calculated slope and external quantum efficiencies

Ridge Width, R(μm)	Cavity Length, L(μm)	Slope Efficiency, $2 \frac{\Delta P}{\Delta I}$ (W/A)	External Differential Quantum Efficiency, η_d (%)	$1/\eta_d$
2	600	0.06666	7.307	13.6855
	900	0.08518	9.337	10.0997
	1200	0.06951	7.619	13.1244
	1500	0.04548	4.983	20.0677
4	600	0.06702	7.3465	13.612
	900	0.07654	8.39	11.919
	1200	0.05134	5.628	17.769
	1500	0.04604	5.047	19.8148
6	600	0.04157	4.557	21.9455
	900	0.03974	4.356	22.9561
	1200	0.04566	5.005	19.9798
	1500	-	-	-

The 2 μm ridge width 900 μm long device exhibits a better slope efficiency as well as the best external quantum efficiency than its counterparts in

Table 5-4 above. This is also evident in Figure 5-14 below. Comparing the 4 μm of the different cavity lengths also shows that the 900 μm device performs better (see Figure 5-15 below). For both plots, the 900 μm device has better slope efficiency showing that for small increase in the injection current it exhibits rapid increase in the output light emission in order words it has a good conversion rate of input electric power to output light power.

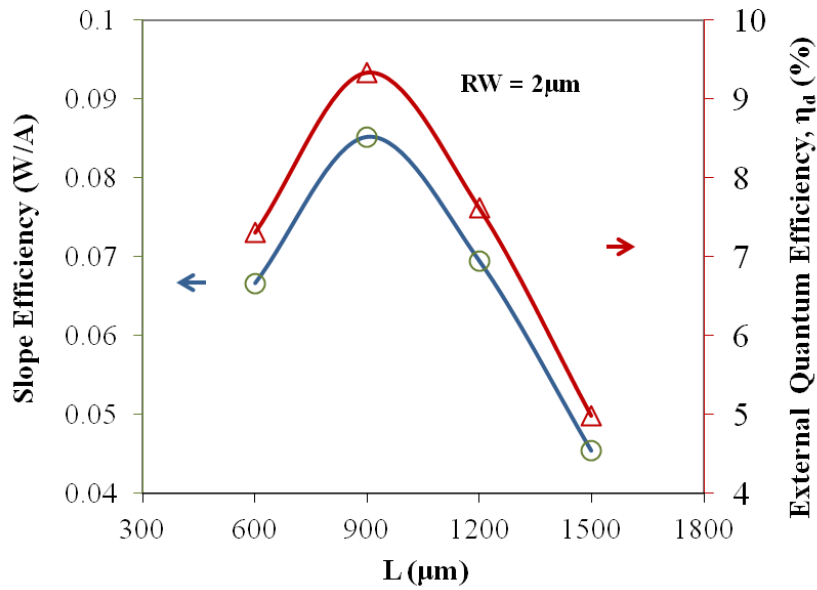


Figure 5-14. The slope efficiency and external quantum vs of cavity length for the $2\mu\text{m}$ ridge width laser devices

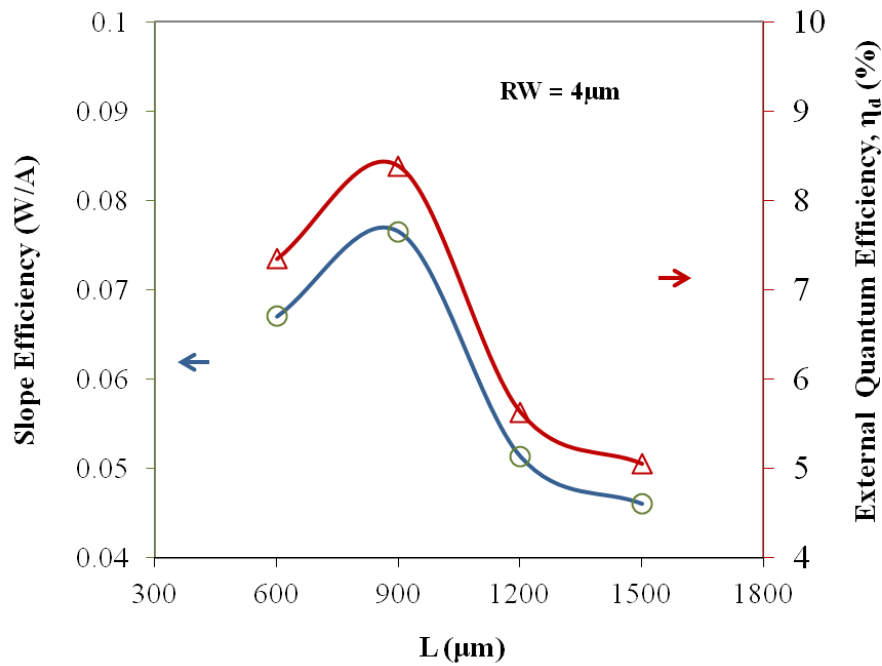


Figure 5-15. The slope efficiency and external quantum vs of cavity length for the $4\mu\text{m}$ ridge width laser devices

The external quantum efficiencies are quite low due to losses within the cavity and improper cleaved facets. This efficiency is geometry dependent as observed, because the wider ridge widths (corresponding to the larger overall device area) have lower external quantum efficiencies. The cleaved-cleaved facet is put into consideration when calculating both the slope and external quantum efficiencies.

The reciprocal of the external quantum efficiency, the internal quantum efficiency and optical loss can be extracted by doing measurements on identical devices of different cavity lengths and fitting the measurement data into the following equation:

$$\frac{1}{\eta_d} = \frac{1}{\eta_i} \left[1 + \frac{\alpha_i}{\ln(1/R)} L \right] \quad 5-2$$

where

α_i is the net internal optical loss,

η_d is the external quantum efficiency,

η_i is the internal quantum efficiency,

R is the reflectivity,

and L is the cavity length.

A straight line can be obtained by plotting the reciprocal of the measured device efficiency (η_d) versus cavity length (L). The y-intercept of the straight line gives the inverse of the internal quantum efficiency and then used in the equation above to obtain the net optical loss. The value of η_d is less than the value of η_i . And the ratio of η_d/η_i gives the ratio of the number of photons emitted from the laser to the number of photons generated within the laser.

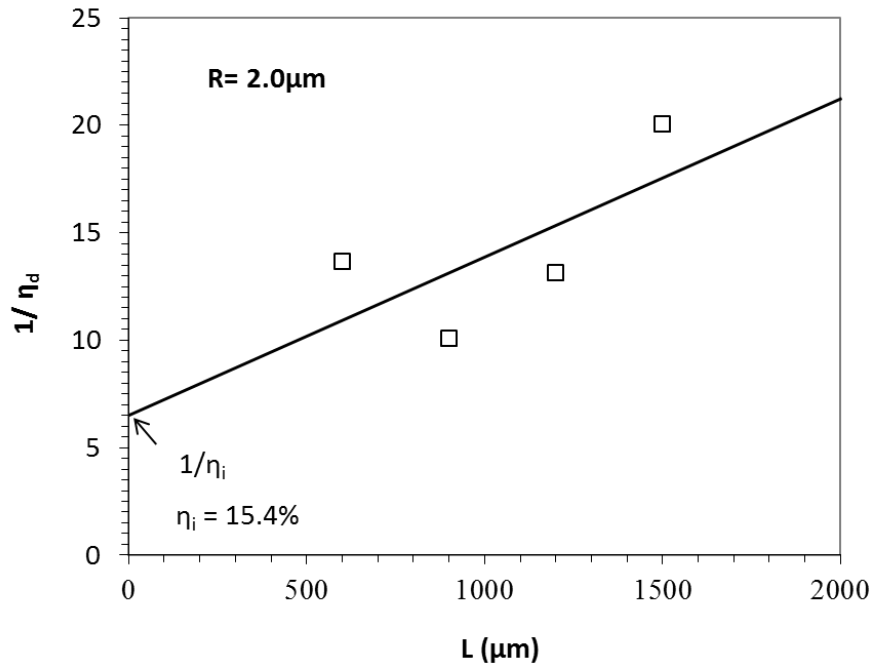


Figure 5-16. The reciprocal of external quantum efficiency as a function of cavity length for the 2.0 μm ridge width laser devices

The linearly increasing line plot in Figure 5-16 shows that the device efficiency decreases with increasing cavity length. Except of course the outlier 600 μm device with a higher value than the 900 and 1200 μm devices.

A true measure of the efficiency of the laser is in its internal quantum efficiency which shows its ability to convert the current (electron-hole pairs) into light (photons). This parameter is not geometry dependent and therefore a good test of efficiency which is based on the wafer and material composition quality. Above it shows that we only have 15.4% conversion which is quite low but expected for these kinds of lasers. This percentage is open to interpretation because if the 600 μm device were to be eliminated from this plot, we would have a much better fit and lower intercept ($1/\eta_i$) resulting in a larger percentage of the internal quantum efficiency. Also, the low % is an indication that most of the electron-hole pair recombination did not result in the generation of photons but other unwanted forms of energy such as heat, some of the generated photons were re-absorbed due to various internal loss mechanisms and maybe due to fabrication imperfections some of the photons are being re-absorbed by the laser structure. However,

the percentage of the internal quantum efficiency is higher than the external quantum efficiency which should be expected and agrees with theory as the external differential quantum efficiency is the measure of efficiency after the photons exit the laser.

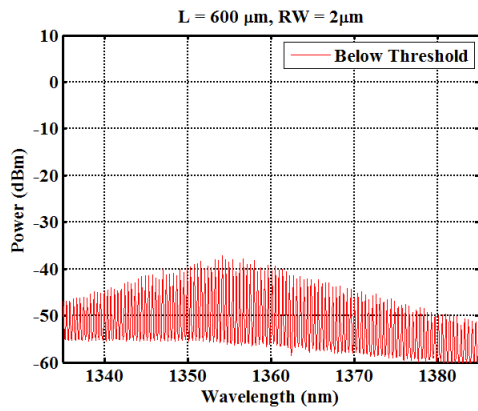
The optical loss is a coefficient that relates the number of existing photons to the number of photons that will remain inside the cavity after having propagated a certain distance¹¹³. The losses could be caused by lateral spreading of carriers, carrier escape from the active region, and by recombination losses within the active layers. All these loss mechanisms contribute to the internal quantum efficiency.

The internal loss, α_i is calculated to be 12.38 cm^{-1} . Which is the slope of the linear fit of Figure 5-16 multiplied by $(\eta_i) \ln(1/R)$. Higher internal quantum efficiency and lower internal loss are desirable and show a better performance laser

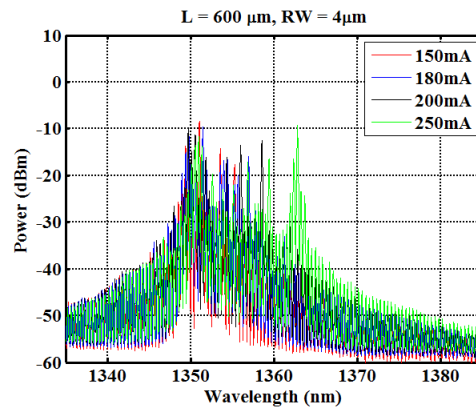
5.5.4 Optical Spectra

The laser optical cavity characteristics affect its optical spectrum. The cavity structure therefore defines the number of spectral lines it can support at a particular injection current. In FP lasers, the output spectra is multi-mode, each of these longitudinal mode in the laser cavity resonate at distinct wavelength thus exhibiting multiple peaks. As mentioned earlier all laser devices have maximum power at certain current level in which they can operate before saturation, and most times the power output then starts to decrease even if the injection current keeps increasing.

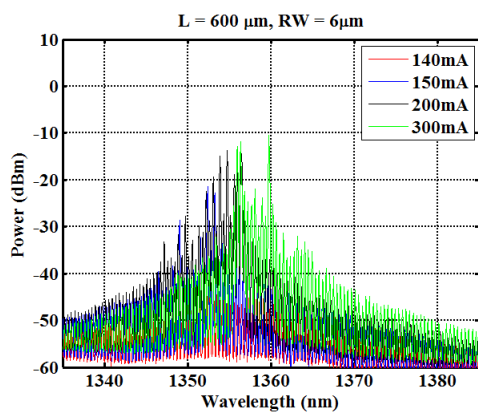
Recorded optical spectra from the FP lasers for selected various injection currents for each tested laser device are shown in Figures 5-18 to 5-21 below. A small increment in the bandwidth of the emitted spectrum with bias current is observed. In addition, a reduction of the optical spectra's bandwidth with ridge width is observed, going from a typical FP spectral emission to a more elaborate emitted spectrum comprising sets of adjacent longitudinal modes rather than an homogeneous FP profile.



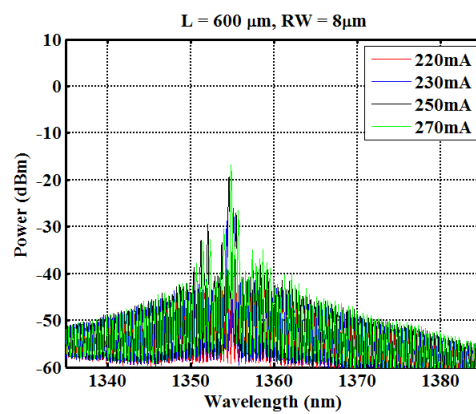
(a)



(b)



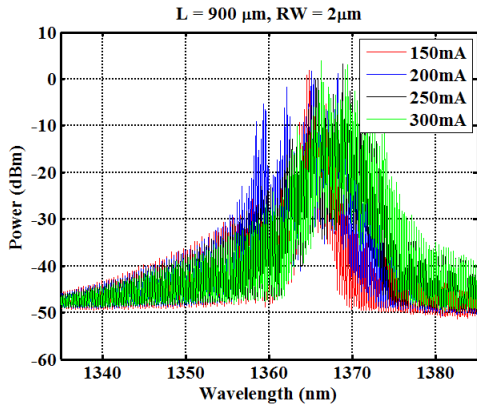
(c)



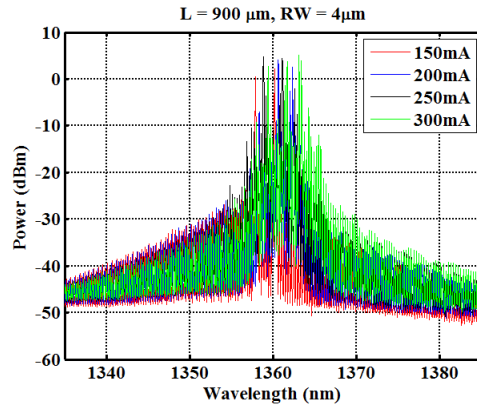
(d)

Figure 5-17. Optical emission spectra for the 600 μm long laser with (a) 2 μm (b) 4 μm (c) 6 μm and (d) 8 μm ridge widths respectively

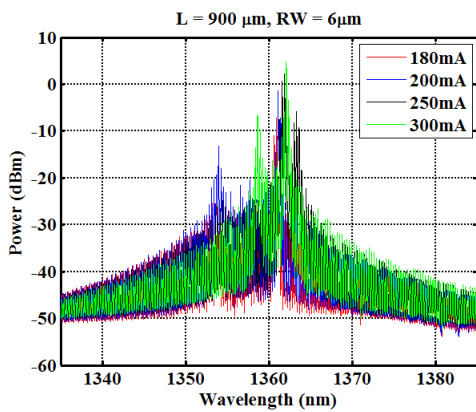
There seem to have been an error during the experiment, the spectra I recorded for the 2 x 600 μm device for various injection currents only showed a spectrum below threshold. Am assuming I deleted the file(s) by mistake or I just did not save them, however am showing the plot I have which is the sub-threshold spontaneous emission spectrum.



(a)

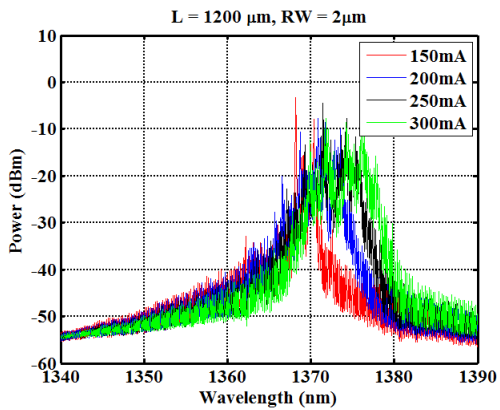


(b)

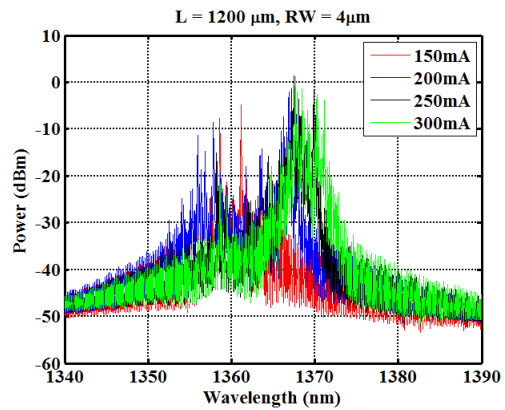


(c)

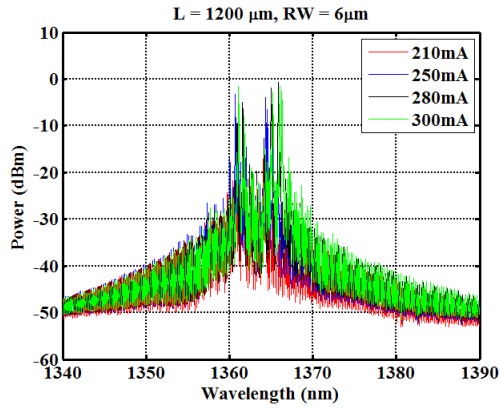
Figure 5-18. Optical emission spectra for the 900 μm long laser with (a) 2 μm (b) 4 μm and (c) 6 μm ridge widths respectively



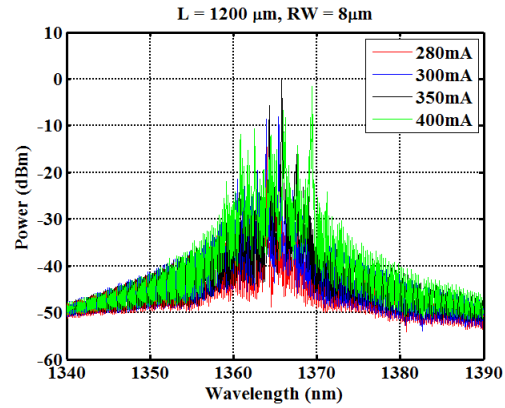
(a)



(b)

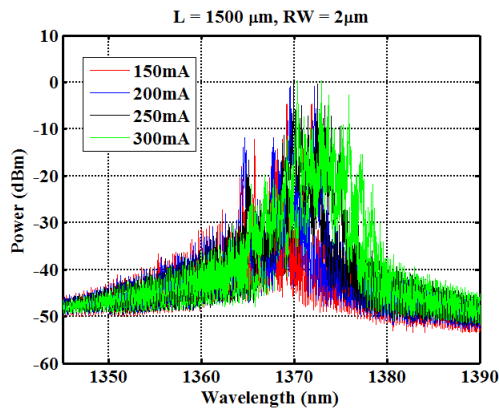


(c)

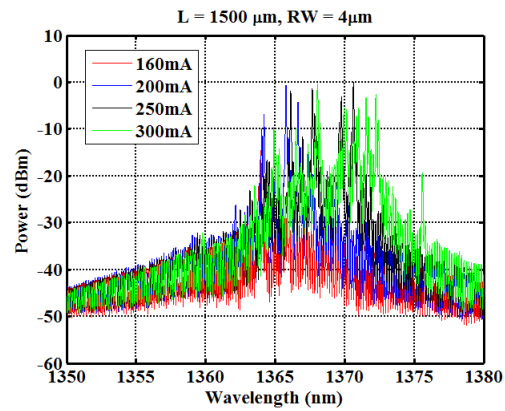


(d)

Figure 5-19. Optical emission spectra for the 1200 μm long laser with (a) 2 μm (b) 4 μm (c) 6 μm and (d) 8 μm ridge widths respectively



(a)



(b)

Figure 5-20. Optical emission spectra for the 1500 μm long laser with (a) 2 μm and (b) 4 μm ridge widths

Broadening of the spectrum is observed as more current is injected due to thermal effect and as the energy levels are filled up. Mode hopping occurs with bias current changes, increasing the bias current cause red-shift in the centre wavelength which is as a result of the shift in gain spectra caused by reduction in the band gap. This hopping of peak wavelength over discrete wavelength bands is shown in Table 5-5 and Figure 5-22 for the 2 x 900 μm laser device. It shows the increase of peak emission wavelength from 1361

nm @70mA current to 1371 nm @ 300 mA current. This is a 10 nm shift for a 230 mA change implying a tuning of 0.043 nm/mA

Table 5-5. Peak Wavelength and peak intensity with varying current for the 2 x 900 μm laser device

I(mA)	Peak wavelength (nm)	Peak Intensity (dBm)
70	1361	-45.48
80	1362	-22.51
100	1364	-8.72
150	1367	-3.77
200	1369	-3.23
250	1370	-4.70
300	1371	-6.62

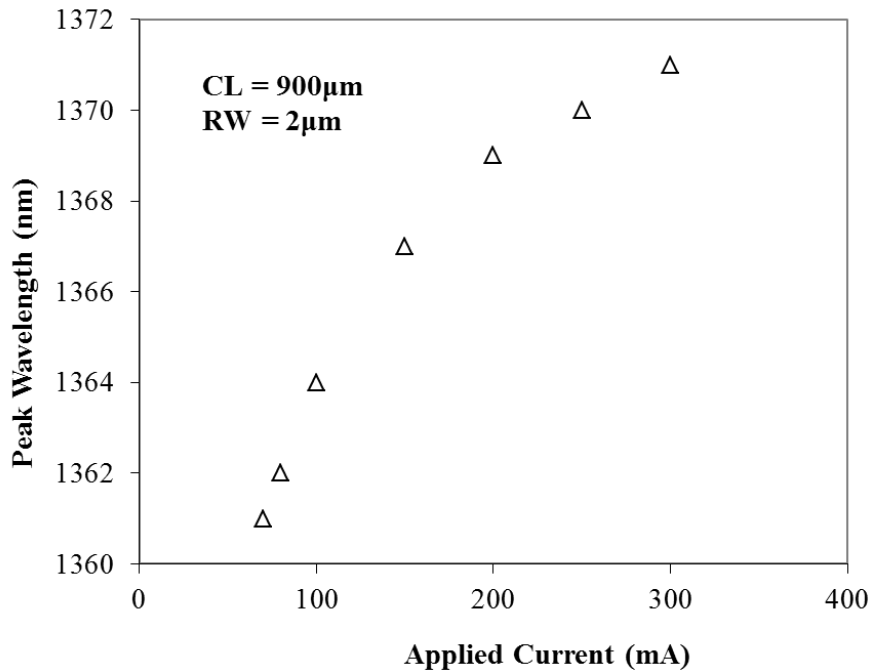


Figure 5-21. Peak wavelength as a function of the injection current for the 2 x 900 μm laser device

The net peak gain is shown in Figure 5-22 below

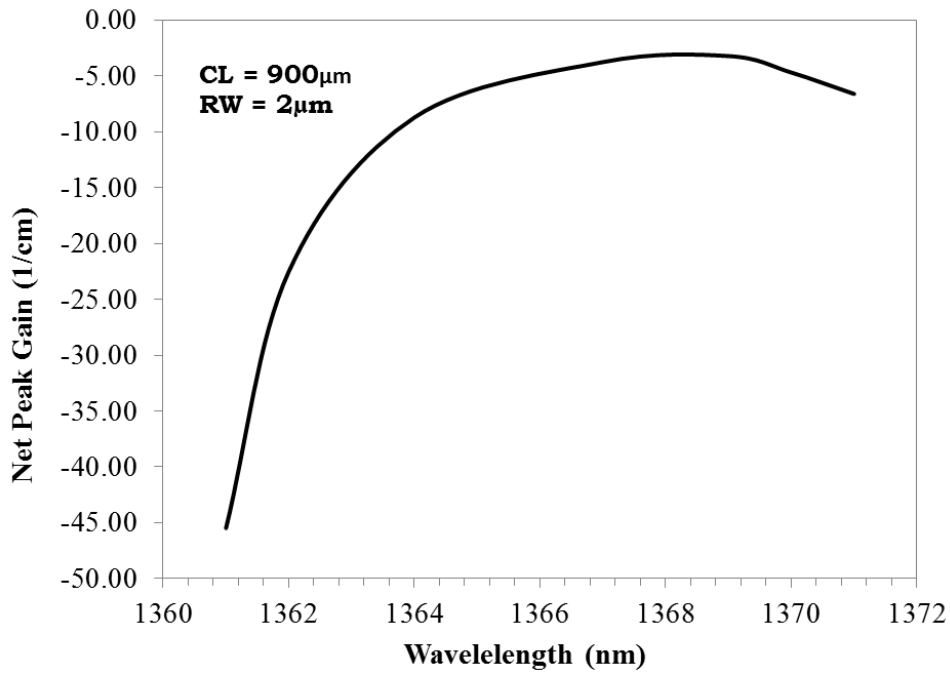


Figure 5-22. Net peak gain vs wavelength for the 2 x 900 μm laser device

5.5.5 Optical Gain and Loss

As the photon density propagates along the laser cavity, the material gain grows proportionally and the maximum gain is determined by the density of states of the material. Optical gain can be determined by considering the multiple reflections of a photon in a laser cavity at a sub-threshold current. Assuming that only the fundamental mode is excited in a laser cavity, the electric field at facet one is F_1 , where F_1 is the fundamental mode field. When the reflected $\sqrt{R_1}F_1$ field propagates back along the cavity, it gets reflected at the second facet and when it returns back to the first facet, the electrical field will change to $\sqrt{R_1R_2}F_1 \exp(-2\alpha(\lambda)L)$, where $\alpha(\lambda)$ is the mode propagation gain or loss in the cavity. Considering multiple reflections occurring at the two facets, the total field of the constructive wave at the first facet is ¹¹⁵:

$$F_1^+ = F_1 \sum_{n=0}^{\infty} \left(\sqrt{R_1 R_2} \right)^n \exp(-n\alpha L) = \frac{F_1}{1 - \sqrt{R_1 R_2} \exp(-\alpha L)} \quad 5-3$$

the total field of the destructive wave at the same facet is:

$$F_1^- = \frac{F_1}{1 + \sqrt{R_1 R_2} \exp(-\alpha L)}$$

The constructive and destructive waves can be measured outside the laser cavity by intensity variation. The ratio of the maximum and minimum intensity is:

$$r(\lambda) = \frac{P^+}{P^-} = \left(\frac{1 + \sqrt{R_1 R_2} \exp(-\alpha(\lambda)L)}{1 - \sqrt{R_1 R_2} \exp(-\alpha(\lambda)L)} \right)^2 \quad 5-4$$

Therefore, the modal gain or loss can be calculated as:

$$\alpha(\lambda) = \frac{1}{L} \ln \left(\frac{\sqrt{r(\lambda)} + 1}{\sqrt{r(\lambda)} - 1} \right) + \frac{1}{2L} \ln R_1 R_2 \quad 5-5$$

and the material gain $G(\lambda)$ is related to $\alpha(\lambda)$ and the confinement factor Γ by:

$$\Gamma G(\lambda) = \alpha(\lambda) \quad 5-6$$

The laser internal loss can be measured based on the principles of Fabry-Perot cavity resonance. In a F-P resonant cavity, the steady-state output intensity at the end of a laser can be approximated as ¹¹⁶:

$$I^{\pm}(\nu) = \frac{B(1 + R_{\mp}G_s)(1 - R_{\pm})}{(1 + RG_s)^2 - 4RG_s \sin^2(\theta)} \quad 5-7$$

where R^{\pm} are the reflectivities of the mirrors, G_s is the single-pass intensity gain, and B is the total amount of spontaneous light at frequency ν coupled into the laser mode.

For a symmetrical laser cavity, $\theta = 2\pi L\nu/c$, where $c/2L$ is the free spectral range of the resonator. At $\theta = 0$ and $\theta = \pi/2$, the intensity of the output reaches its minimum and maximum, respectively. The intensity ratio between the adjacent peak, I_p , and valley, I_v , can be calculated as:

$$r = \frac{I_p}{I_v} = \left(\frac{1 - G_s R}{1 + G_s R} \right)^2 \quad 5-8$$

At transparency, a single pass gain relates to the internal loss by

$$G_s = e^{-\alpha_i L} \quad 5-9$$

where L is the cavity length. The internal loss α_i can be found using Equations 5-8 and 5-9 once the intensity ratio r is determined.

The facet reflectivity can be calculated using the effective index of reflection, n_{eff} , and the Fresnel's reflectivity formula

$$R = \left(\frac{n_{eff} - 1}{n_{eff} + 1} \right)^2 \quad 5-10$$

n_{eff} is estimated by:

$$\Delta\lambda = \frac{\lambda^2}{2Ln_{eff}}$$

5-11

where λ is the lasing wavelength and $\Delta\lambda$ is the mode spacing in the F-P cavity.

The carrier distribution in the active layer therefore strongly depends on the injection current below threshold. The sub-threshold spectrum is useful because the broad spectrum of spontaneous emission clearly shows the FP-modes of the cavity better than the spectrum after threshold which is predominantly stimulated emission.

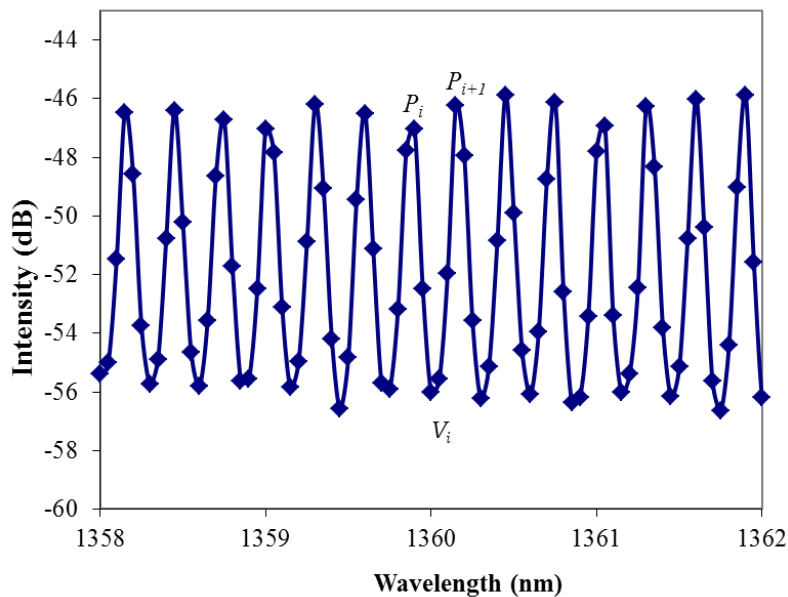


Figure 5-23. The Fabry-Perot resonance of the spontaneous emission from the 2 x 900 μm laser device. Biased at 50mA

Figure 5-23 displays the spontaneous emission spectrum below threshold biased at 50 mA and zoomed in to show the F-P resonance mode. The intensity peaks (maximum) and valleys (minimums) are determined in order to calculate the gain and loss. To increase the accuracy of gain extraction, algorithms such as the mode sum minimum method ¹¹⁷ and the nonlinear least-squares fitting method ¹¹⁸ have been introduced. An averaging

method that computed the intensity contrast, $r(\lambda)$ at any wavelength is used by first averaging the intensities of adjacent peak, $\frac{1}{2}(P_i + P_{i+1})$, and then dividing by the intensity of the intermediate valley, V_i ¹¹⁹ :

$$r_i = \frac{P_i + P_{i+1}}{2V_i} \quad 5-12$$

From the $2 \times 900 \mu\text{m}$ devices and as shown in Figure 5-23 the mode spacing $\Delta\lambda$ is 0.3 nm. At the lasing wavelength of 1361 nm and using Equation 5-11 the calculated effective index n_{eff} is 3.43, the mirror reflectivity calculated using Fresnel's equation is 0.3 for the 900 μm devices. The intensity contrast is determined to be 0.8323.

For the 900 μm device the internal loss, α_i is about 12.38 cm^{-1} . The mirror loss is given by $\alpha_m = \frac{1}{2L} \ln \frac{1}{R_1 R_2}$ and it is calculated for the cavity length 900 μm with $R = 0.3$, $\alpha_m = 13.38 \text{ cm}^{-1}$. The optical loss is a sum of the cavity internal loss and the mirror loss. Therefore the optical loss is 25.76 cm^{-1} .

Final Note

Based on all the analysis presented above, out of all the Fabry-Perot laser devices tested the $2 \times 900 \mu\text{m}$ laser device shows the better performance. And therefore the SOA devices with similar dimension have been selected and will be the focus for further analysis of the SOA in the next section.

5.6 SOA Characterization Parameters

Semiconductor optical amplifiers can be characterized by a number of measurable parameters that determine its suitability for use in optical networks. It is therefore necessary to analyse the overall performance of the SOA based on these parameter characterization such as gain (G), saturation output power (P_{sat}), bandwidth, polarization sensitivity and noise figure (NF). Based on the conclusions from the previous laser

section, the SOA device with dimension $2 \times 900 \mu\text{m}$ is used for all the parameter characterizations in this section. Initial test and analysis were carried out for the cleaved-cleaved SOA devices, but to further improve its performance, anti-reflection (AR) coatings were applied to the 7° tilted facets having a reflectivity of 5×10^{-5} . Few of the parameter extractions such as the gain and saturation output power are presented for both devices, but due to better performance, focus is on the AR coated devices. To show polarization insensitivity characteristic linear state of polarization of the injected beam in coincidence with the transverse electric (TE), and transverse magnetic (TM) are considered.

5.6.1 Experimental Set-up

A continuous wave laser with wavelength tuneable from 1340 to 1440 nm is used as the light source. A polarization controller followed by a linear polarizer is used to set linear horizontal and vertical states of polarization of the injected beam along the TE and TM propagation modes of the SOA. Tapered fibers are used for injection and collection of light at the amplifier input and output facets. The SOA under test is DC-biased and temperature controlled at 25°C . An optical spectrum analyzer set at a resolution bandwidth of 0.06 nm and a power meter are used for data collection and further analysis. Figures 5-25 to 5-27 shows the experimental setup and the SOA device under test.

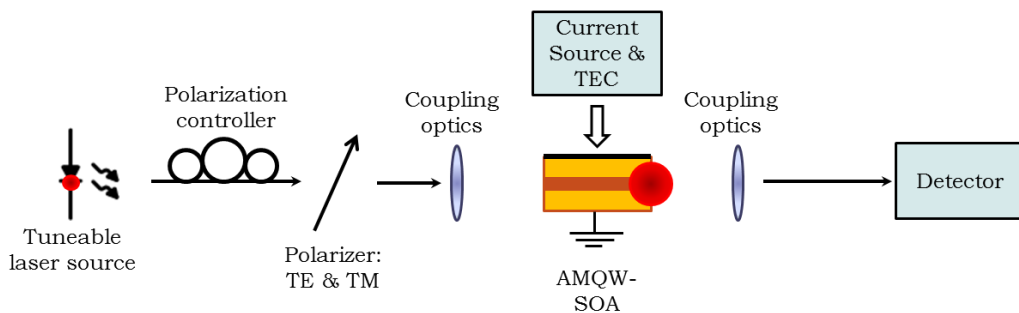


Figure 5-24. Schematic representation of the experimental setup.

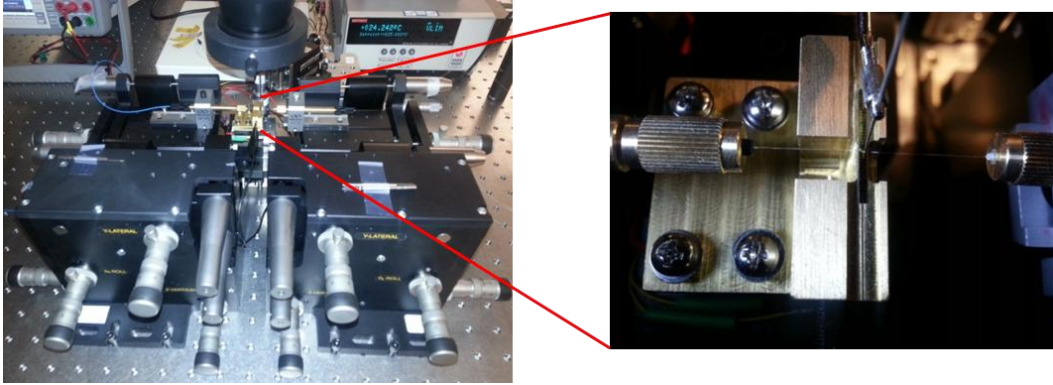


Figure 5-25. Experimental setup

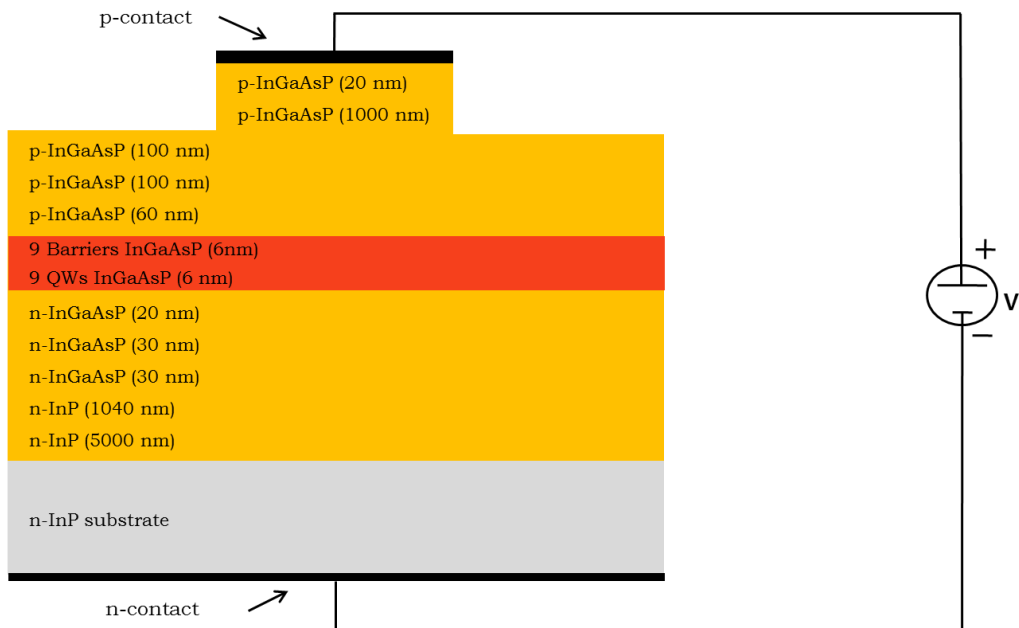


Figure 5-26. Epitaxial structure of the $\text{In}_{1-x}\text{Ga}_x\text{As}_y\text{P}_{1-y}/\text{InP}$ SOA device

5.6.2 Amplified Spontaneous Emission

The amplified spontaneous emission (ASE) is usually the first and easiest characteristic parameter to be measured in an SOA. It provides valuable information on SOA parameters such as the gain peak location, optical bandwidth, optical gain, facet reflectivity. Many photons are generated by spontaneous emission due to the large carrier density present in the conduction band. However, only a fraction of these photons are

coupled into the fundamental mode of the active region and are amplified. The ASE is a combination of the spontaneous and stimulated emission which is evident in the ASE output, the wide optical spectrum comes from the spontaneous emission and the high intensity comes from optical amplification by the stimulated emission. During operation of the SOA, the ASE can be detrimental because it depletes carriers and limits the maximum small signal gain, and it degrades signals by adding noise to amplified signals resulting in non-desirable signal-to-noise ratio (SNR)

The amplified spontaneous emission (ASE) spectra for bias currents from 70 to 300 mA are shown in Figure 5-27. An increase of the output power and blue shift (shorter wavelength) with increasing bias current is observed from 70 to 200 mA, this is primarily due to band filling with injected electrons/holes, the gain of the SOA is not the same for all frequencies of the input signal. The ASE power peaks around 1360 nm and exhibits a saturation effect above 200 mA (after which point the gain cannot be increased by further increasing the bias). When the drive current is increased to 300mA the SOA begins to leak current and the electrical confinement begins to break down thus reducing efficiency.

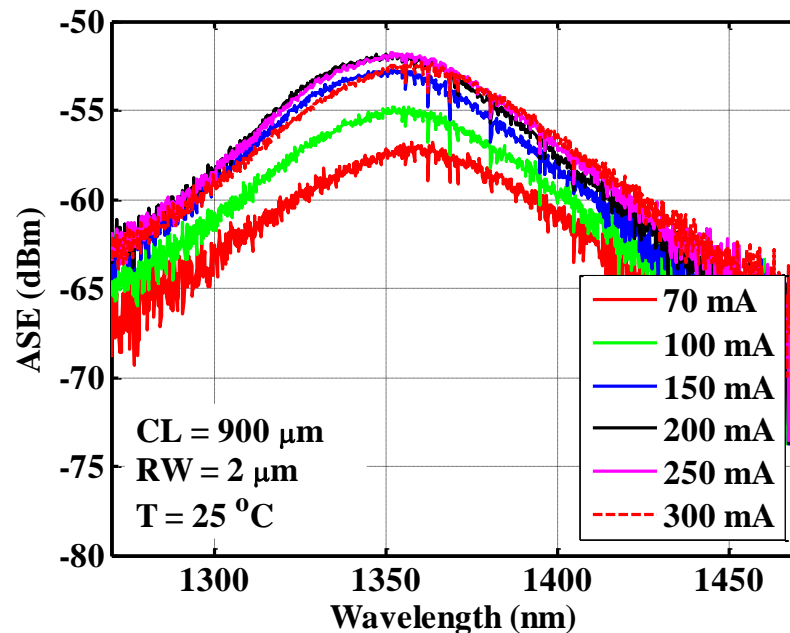


Figure 5-27. Amplified spontaneous emission collected at the output facet of the SOA for various bias currents

5.6.3 Optical Spectrum

The optical power and spectrum collected at the output facet of the SOA were recorded for different powers and wavelengths of the input laser. The room temperature photoluminescence spectrum of the SOA is centered at 1360 nm for the amplified output spectra for input powers of -20 dBm and -10dBm and at the linear vertical and horizontal polarizations whilst the SOA is DC-bias at 150mA and 200 mA. Figure 5-28 below shows the optical power spectrum collected at the output facet of the SOA are recorded for different powers and wavelengths of the input laser for the -10dBm power at 150mA.

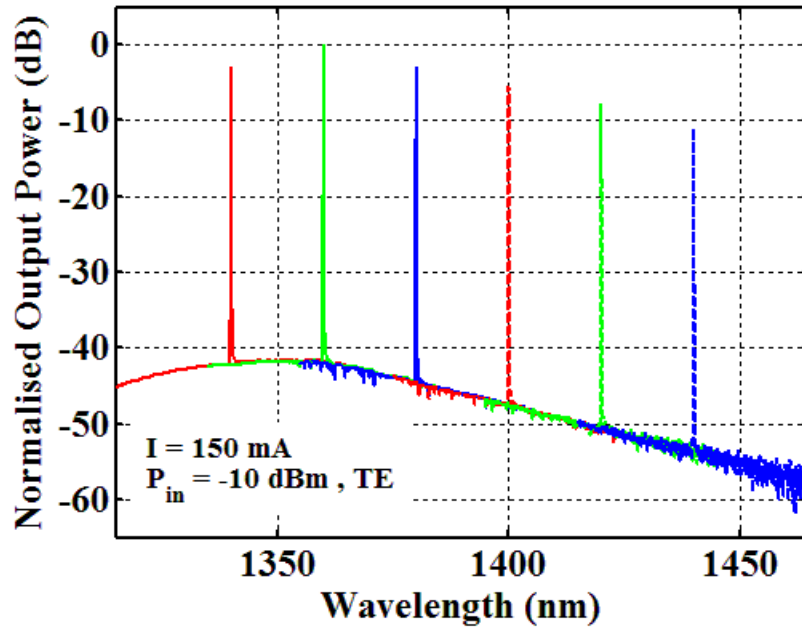


Figure 5-28. Output spectra for different input wavelengths with a linear vertical polarization and power of -10 dBm

5.6.4 Gain and Polarization Insensitivity

The SOA device exhibits optical gain when a population inversion is achieved in the SOA active region which is when the output power exiting the SOA greater than the input power entering it. The gain of an SOA is dependent on both the input optical power

level and the input signal wavelength. The gain G can be expressed as a function of signal power P simply as:

$$G = \exp[(\Gamma g_m - \alpha)L] \quad 5-13$$

where Γ is the confinement factor, g_m is the material gain, α is the total internal loss, and L is the cavity length.

Polarization insensitivity is addressed by the optical gain of a beam propagating through the SOA as expressed earlier in the gain Equation 5-13. However, the confinement factors Γ^{TE} and Γ^{TM} for the transverse electric (TE) and transverse magnetic (TM) propagation modes are not equal. Due to the anisotropy of the material system, g_m and α in both TE and TM modes are different. Therefore, polarization independency of the SOA gain can be realized by satisfying:

$$\Gamma^{TE} g_m^{TE} - \alpha_{TE} = \Gamma^{TM} g_m^{TM} - \alpha_{TM} \quad 5-14$$

where the modal gain (Γg_m) is much larger than the internal loss, then the loss term can be ignored.

Tensile QW and lattice matched barrier balances the modal gain difference between the transverse electric (TE) and transverse magnetic TM modes. By introducing a tensile strain, the light-hole band edge is closer to the conduction band edge than the heavy-hole band. This enhances the TM mode gain at the expense of the TE mode gain. In this way the overall optical gain of the modes is balanced. Also, the anti-reflection coatings used to suppress cavity resonance can also exhibit polarisation sensitivity, as shown in the experimental results comparing cleaved-cleaved facets and those with AR coatings.

Linear states of polarization of the injected beam in conjunction with the TE and TM propagation modes are considered for assessing the polarization sensitivity of the tested SOA.

For the as-cleaved facets, setting a bias current of 150 mA in the asymmetric MQW SOA, a peak single pass gain of 13.5 dB is measured for an input beam with a polarization in TM and input power of -20dBm. As shown in Figure 5-29, a flat 3 dB bandwidth of 60 nm centered at 1380 nm is obtained for a polarization in TE and a 3 dB bandwidth of 50 nm centered at 1370 nm is obtained for a polarization in TM. A polarization sensitivity of less than 0.5 dB is observed for wavelengths around 1350 nm, whereas it increases with wavelength for the range from 1370 to 1440 nm.

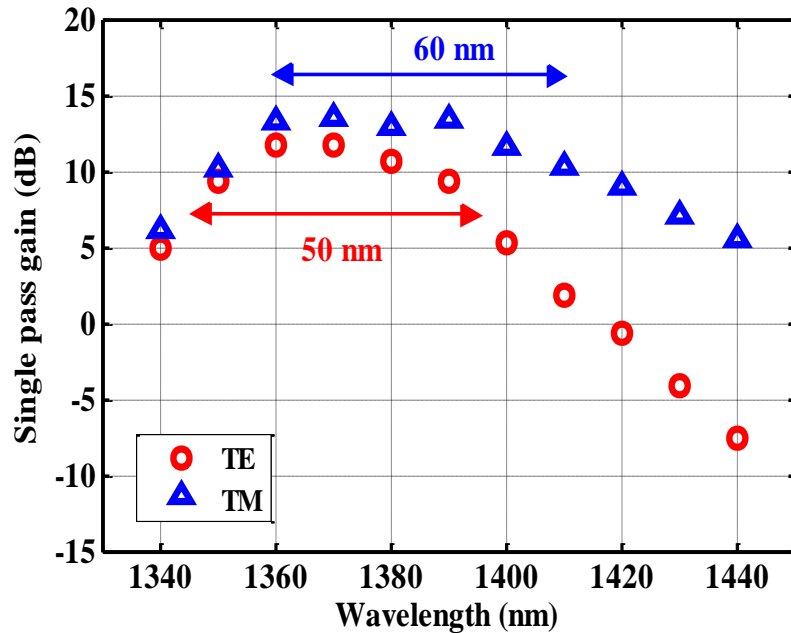


Figure 5-29. Single-pass (chip) gain versus wavelength for an input power of -20 dBm @ 150mA. For as-cleaved facets

For the AR coated devices, the obtained single-pass (chip) gain versus wavelength is shown in Figure 5-30 and Figure 5-31 for input powers of -20 and -10 dBm, respectively. The maximum gain of 20 dB is obtained at injection current of 200 mA (black-colour top trace in Figure 5-30 for an input power of -20 dBm and linear horizontal polarization). At these operation conditions, a 3 dB bandwidth of around 50 nm is obtained. A gain peak of 21 dB for a 3 dB bandwidth of 45 nm is measured for an input power of -10 dBm at injection current of 200 mA (see Figure 5-31). As observed in these plots, larger bandwidths are obtained for lower chip gains.

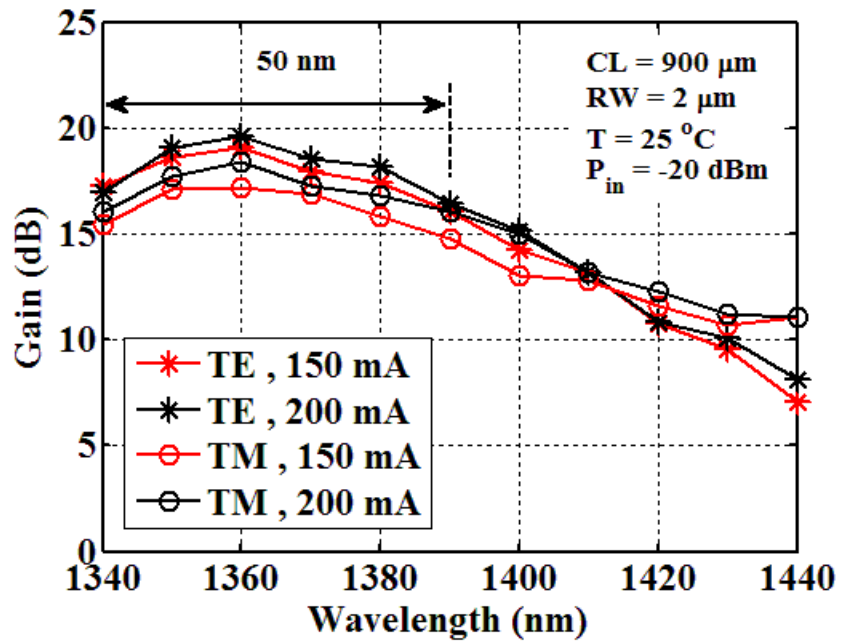


Figure 5-30. Chip gain versus wavelength for an input power of -20 dBm. For AR coated facets

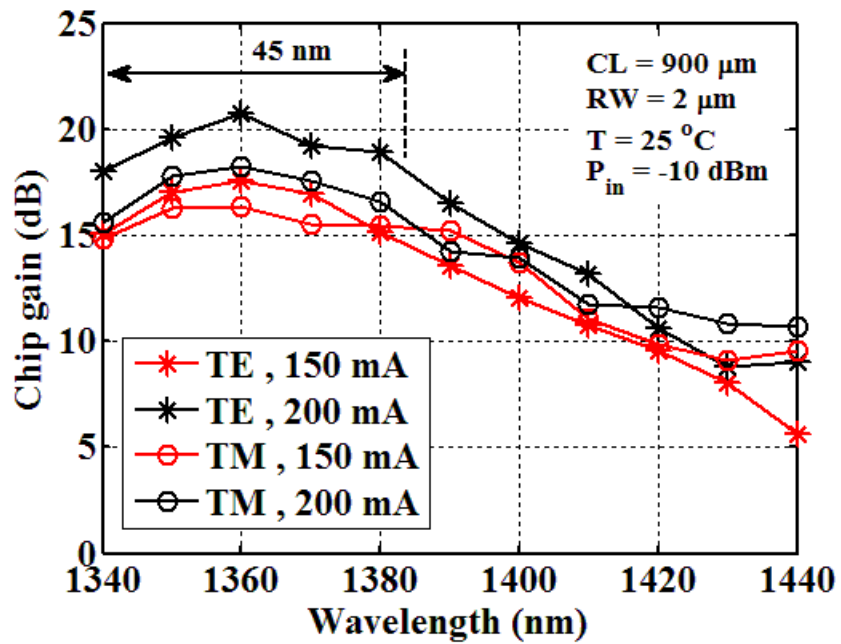


Figure 5-31. Chip gain and noise figure versus wavelength for an input power of -10 dBm. For AR coated facets

As observed in the plots whilst comparing the as-cleaved vs the AR coated devices, the gain and the polarization sensitivity is very improved in the AR coated SOA devices. The polarization insensitivity is further analyzed in Figure 5-32 below and the polarization insensitivity for 1 dB and 3 dB bandwidth for the conditions in Figure 5-30 and Figure 5-31 is summarized in Table 5-6.

The polarization sensitivity of the chip gain, defined as the difference of the chip gains for the linear horizontal and vertical states of polarization, and extracted from the previous two figures (AR coated SOA devices), is shown in Figure 5-32 below. A maximum polarization sensitivity of around 3 dB is measured from 1340 to 1440 nm which spans a range of 100 nm.

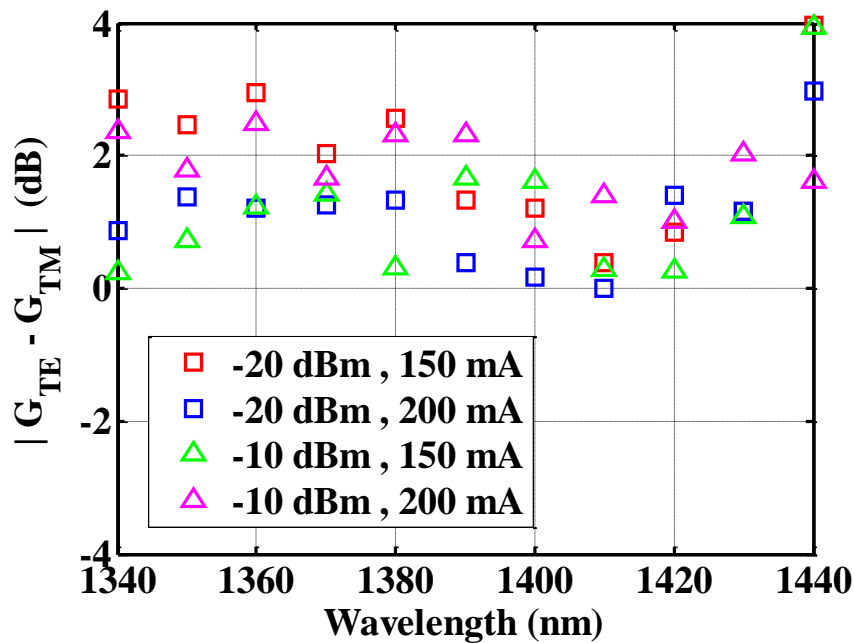


Figure 5-32. Polarization sensitivity of the chip gain for input powers of -10 and -20 dBm at bias currents of 150 and 200 mA.

The largest bandwidth with the low (< 1dB) polarization sensitivity of the chip gain is obtained at the input power of -20 dBm and an injection current of 200 mA as indicated in Table 5-6. Polarization sensitivity of less than 0.5 dB is observed for some wavelengths.

Table 5-6. Polarization sensitivity bandwidth

Input power = -20 dBm		
	< 1 dB	< 3 dB
150 mA	30 nm	90 nm
200 mA	50 nm	100 nm
Input power = -10 dBm		
	< 1 dB	< 3 dB
150 mA	20 nm	90 nm
200 mA	20 nm	100 nm

5.6.5 Saturation Output Power

Saturation is the limitation of the maximum achievable gain in the SOA¹²⁰. It is as a result of the stimulated emission process removing the carriers from high energy states faster than they can be replenished by the injected current, depleting the population inversion thus impeding the gain. Saturation of the gain will occur when the total spontaneous emission power approaches saturation output power (P_{sat}) which is the point where the device gain is reduced by 3dB. Since gain saturation implies reduction of the carrier density at a specific injection current, it therefore causes a shift of the gain maximum towards longer wavelengths.

Taking into account the wavelength at the maximum gain, which is located around 1360 nm. Shown in Figure 5-33, output saturation powers of 12 and 15 dB are obtained for TE and TM, respectively for the cleaved-cleaved SOA device. A minimum polarization sensitivity of around 1.5 dB is obtained for injection current of 150 mA at 1360 nm wavelength.

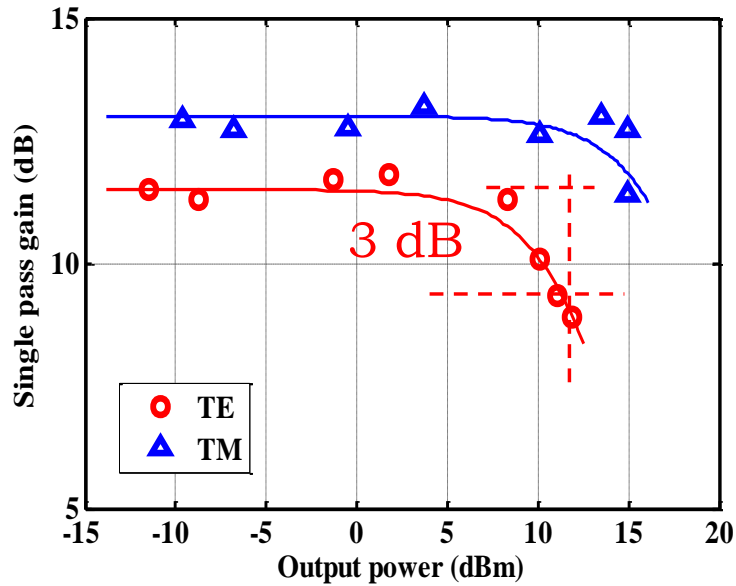


Figure 5-33. Single pass (chip) gain versus optical input power at 1360 nm. Bias current is set at 150 mA. For as-cleaved facets

For the AR coated SOA device, the chip gain versus output power is shown in Figure 5-34. At 1360 nm wavelength, saturation output powers of 18 dBm for TE and 22 dBm for TM are obtained. Comparing this plot at 150 mA injection with the previous plot, these powers are higher than those obtained for the as-cleaved facets.

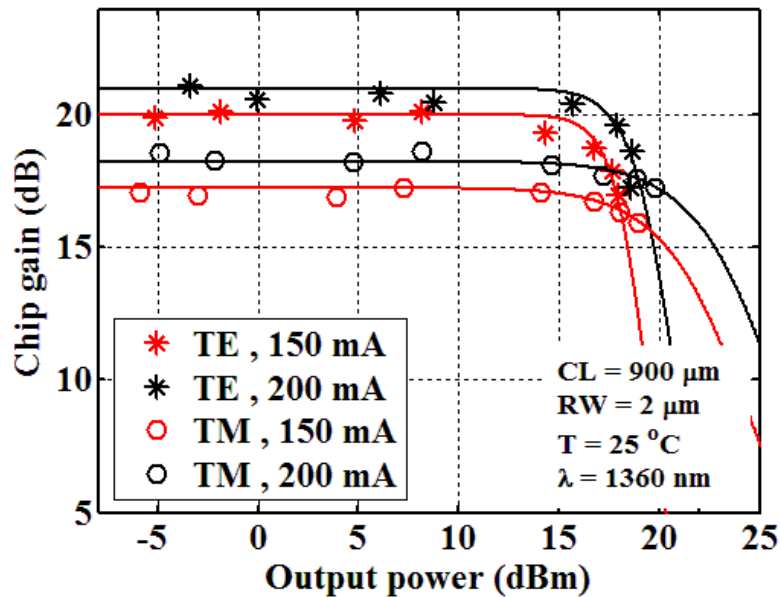


Figure 5-34. Chip gain versus output power for TE and TM polarizations at 1360 nm. Bias currents set at 150 and 200 mA. For AR coated facets

5.6.6 Signal-to-Noise ratio and Noise Figure

The signal-to-noise ratio(SNR) refers to the SNR of the electrical power generated when the signal is converted to current by a photodetector.

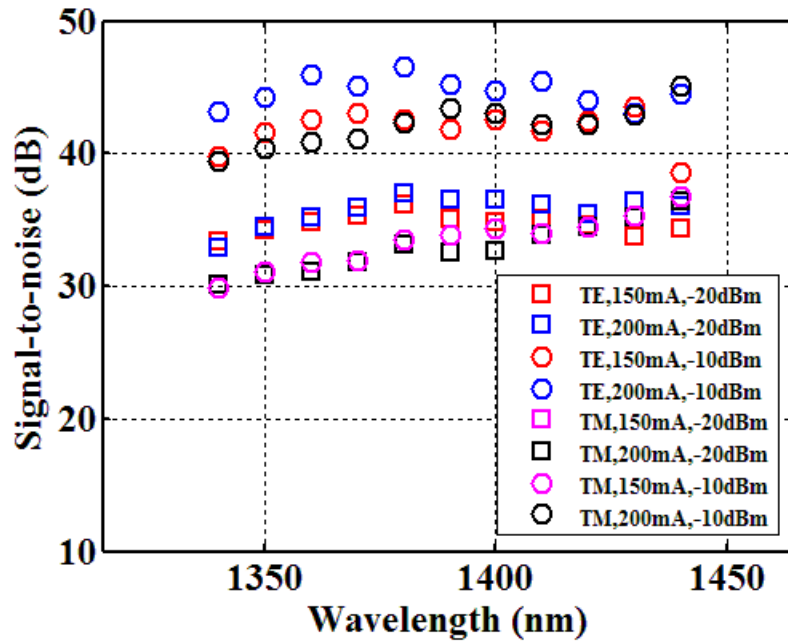


Figure 5-35. Signal-to-noise ratio vs wavelength for the different currents and input powers combinations for TE and TM polarizations

As mentioned earlier, the ASE affects the SNR, the spontaneous emission mixes coherently with the signal of the photodetector and produces fluctuating photocurrent within the bandwidth ¹²¹. Figure 5-35 shows the signal-to-noise ratio for varying currents and input powers. The SNR is higher for input power of -10dBm

The degradation of the signal-to-noise ratio (SNR) as the signal is amplified is quantified by the noise figure (NF) which is due to ASE, this is a major cause of low power in-line amplification and the limiting factor for SOAs in low power transmission. The noise figure (NF) spectra obtained at the same conditions of operation as those for the chip gain are shown in Figure 5-36 and Figure 5-37 below. Obtained results show a minimum NF

of 8 dB and a polarization dependence of 3 dB for wavelengths between 1340 and 1400 nm.

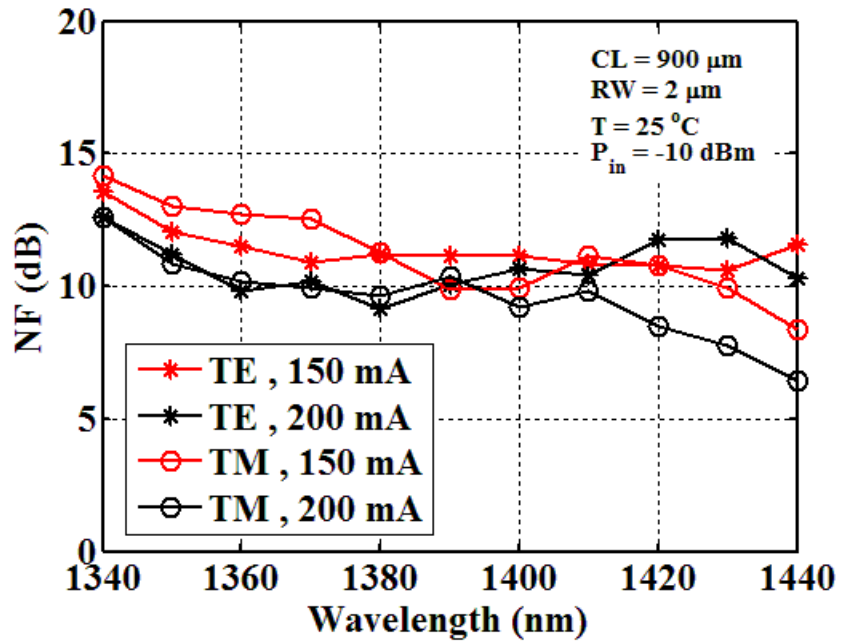


Figure 5-36. Noise figure versus wavelength for input power of -10 dBm.

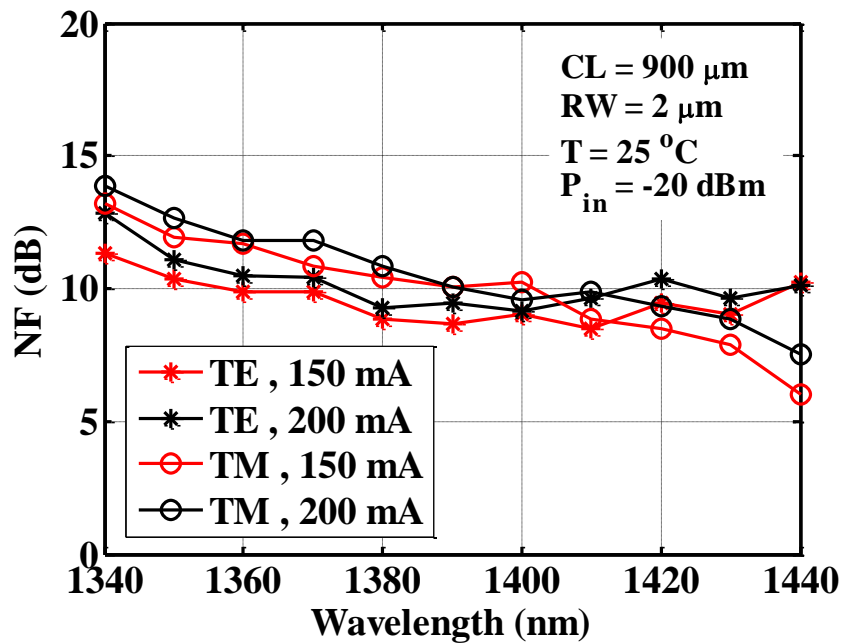


Figure 5-37. Noise figure versus wavelength for input power of -20 dBm

In this case, the reported NF accounts for the signal-spontaneous beat noise density, which depends on the product of the ASE spectral density in the same polarization state of the signal and the amplified optical signal. NF has been calculated using experimentally obtained quantities by the following formula ¹²²:

$$NF(\lambda) = 10 \log_{10} \left(\frac{2\rho_{ASE}(\lambda)}{G(\lambda)hc/\lambda} \right) \quad 5-15$$

where ρ_{ASE} is the ASE power spectral density that is co-polarized with the input signal, $G(\lambda)$ is the single-pass gain, h is Planck's constant, and λ is the signal wavelength.

Noise figure definition can also be based on the detection of electrical signal-to-noise ratio at the input divided by that of the output ports:

$$NF = \frac{SNR_{input}}{SNR_{output}} \quad 5-16$$

5.7 Summary

In this chapter, the lasing and SOA properties of the E-band (1360 - 1440 nm) wavelength regime was investigated. These devices are made from the InGaAsP on InP quaternary material system, they are composed of asymmetric multiple (9) quantum wells. The asymmetry is based on the varying emission wavelengths within the quantum well region. And to realize polarization insensitivity, tensile-strained quantum wells was used. To reduce facet reflectivity, a 7 ° tilt facet and anti-reflection coatings at the facets of the SOA devices was used. The Fabry-Perot devices were as-cleaved facets only. The devices structure was presented in details.

A major motivation in this SOA/FP research is due to the ever increasing broadband services demanded by end users for their bandwidth-hungry applications such as HGTV, 3D/4D etc. An exhaustive capacity has been anticipated, and people have come up with variations of the existing networks such as using optical carriers allocated at wavelengths within the E-band. We know in the popular available fibers, this wavelength regime is

plagued by water absorption. However, Corning Inc has made this feasible by manufacturing fibers with low water peak in this E-band. This research is therefore new and understudied and has generated a lot of interest. For the reason it is a novel area of interest, we therefore seek semiconductor optical amplifiers at such wavelength range of operation, SOAs that are low cost for both in-line or boost applications, compact size, low energy consumption and feasibility for integration with other optoelectronic components. In terms of performance, we need broadband (covering most of the E-band) polarization insensitive SOAs with low noise and high gain. We also need tunable highly efficient laser sources for this wavelength region.

Therefore, the lasing properties and the SOA parameter characterization were studied and analyzed. Even though the devices had a broad geometry designs, based on the results obtained, it was narrowed down to a few better designs and further analysis was done for these groups of devices.

Different properties of the lasers were studied, their dependence on the various cavity lengths and ridge widths were analyzed. The L-I plots showed that the wider/ longer corresponding to large area laser devices had large threshold currents. L-I characteristics thereby showed a linear increase in threshold current with the cavity lengths and ridge widths. The smallest devices either did not lase or saturated early after lasing. Also the largest devices lased at such high threshold currents and also saturated shortly after lasing. The threshold current range was 70 mA for the 2 x 600 μm up to 250 mA for the 8 x 1200 μm devices. Other properties, such as the threshold current density and the threshold transparency current was analyzed.

The slope and external differential quantum efficiencies were analyzed, it showed a decrease with increase in cavity length with the highest efficiency for the 2 x 900 μm devices. The slope efficiencies were low which could already be deduced from the less steep slopes of the L-I plots, the low external quantum efficiency is also likened to the less than perfect cleaved-cleaved facets as well as other less than stellar occurrences within the laser cavity. The internal quantum efficiencies and internal loss were extracted

as well. Internal quantum efficiency of only 15.4% was realized, this low percentage of the electron-hole pairs recombination that did not result in the generation of photons within the cavity can be attributed to high re-absorption and loss mechanisms within the laser cavity, and also to wafer/fabrication imperfections. The optical loss which is a combination of the internal loss and the mirror losses was approximately 26 cm^{-1}

The spectral properties of the laser shows a small increment in the bandwidth of the emitted spectrum with bias current, going from a typical FP spectral emission to a more elaborate emitted spectrum comprising sets of adjacent longitudinal modes rather than an homogeneous FP profile. An increase and red-shift of peak emission wavelength from 1361 nm @70mA current to 1371 nm @ 300 mA current is observed. This is a 10 nm shift for a 230 mA change implying a tuning of 0.043 nm/mA. The red-shift of emission wavelength is due to gain shift which occurs because of band gap reduction with increasing carrier injection

Overall, the $2 \times 900 \mu\text{m}$ laser devices showed the best performance based on all these analysis. Thus SOA devices with similar dimension were the focus of the SOA parameter characterization.

For the SOA, based on the fact that the polarization sensitivity was an important analysis, the linear vertical and horizontal states of polarization corresponding to the TE and TM modes were fully considered. The input power of -20 dBm and -10dBm were used, as well as injection current of 150 mA and 200 mA.

The first parameter to be analyzed was the amplified spontaneous emission spectrum, which showed saturation after 200 mA current with a peak at 1360 nm. This same peak was observed (and in line) with the output spectra tuned for different wavelengths of a specific input power. Because 2 sets of SOA devices were characterized - the as-cleaved facets and AR coated facets - their gain peak/bandwidth, polarization sensitivity/bandwidth, and saturation output powers were analyzed separately. Overall,

the AR coated SOA devices showed better performances in all the characterizations. As expected because the AR coatings reduced reflections at the surface, the output power was larger, higher peak gain and bandwidth was observed as well a higher saturation output power. The AR coating which suppresses cavity resonance had a huge impact on polarization sensitivity, it showed much lower polarization sensitivity in comparison to the as-cleaved facets. In summary, a 3-dB gain bandwidth of 50 nm was presented for each TE and TM polarizations and a gain peak of 21 dBm at 1360 nm was observed. Similarly, a polarization sensitivity of under 3 dB was obtained for the entire wavelength range analyzed from 1340 to 1440 nm with polarization sensitivity lower than 0.5 dBm for some wavelength range. Saturation output powers were observed around 20 dBm. The noise figure and signal-to-noise ratios were also analyzed.

These broad bandwidth and low polarization sensitive SOA devices, with high gain are very promising and has potential of being used in the next generation optical access networks.

Chapter 6 Conclusions and Future Work

6.1 Introduction

In this thesis, modelling and experimental analysis has been presented for the multi-quantum well LC-DFB lasers, multi-quantum well Fabry-Perot lasers, as well as low polarization sensitive semiconductor optical amplifier (SOA). The motivation and applications of these photonics devices have been presented as well. The research provided fundamental experimental and design insights of the LC-DFB lasers devices which lead to improving existing LC-DFB designs based on the available fabrication and material constraints by adopting a third party quantum dot active region into our designs, this QD LC-DFB lasers are currently being fabricated. The multi-electrode laterally-coupled distributed feedback laser characterized and reported exhibits a stable single mode emission with a good tuneability, it has narrow spectral linewidth and high side mode suppression ratio. Also, flat frequency modulation response is observed in the low frequency range. The SOA devices exhibited broad bandwidth and low polarization sensitivity and high gain. The results presented show mostly good outcomes and a growing interest in them from industry partners. These LC-DFB lasers and SOAs have commercial potential and wide applications especially as they have a small form factor and are designed to be easily monolithically integrated with other opto-electronics devices.

6.2 Summary

The InGaAsP/InP multi-quantum well multi-electrode laterally-coupled distributed feedback laser operating in the 1560 nm wavelength has a third-order rectangular grating etched on the ridge sidewalls thus eliminating regrowth steps obtainable with conventional DFB lasers. This in turn reduces associated manufacturing cost thus making it more suitable for high-volume manufacture. The modelling and simulation of the semiconductor band structure, carrier densities, recombination, gain, thermal and optical

characteristics as well as the modelling of the grating dimensions and coupling strength with the time-domain travelling wave characteristics shows a good LC-DFB laser. The lasers have 1-, 2- and 3- electrically isolated partitioned electrodes from which each individual electrode section were selectively biased. The scanning electron microscopy images photos shows rounding of the rectangular grating teeth, this rounding can affect the coupling between the grating and the active region. Microscope measurements also showed fabrication imperfections, the overall dimensions deviated from target such as the period of the gratings by tens of nanometers, the narrow and wide ridge widths also deviated by some nanometers. All these are fabrication related. A good thing of note is that the gratings revealed smooth and vertical sidewalls. The photoluminescence mapping of the wafer revealed cross-wafer non-uniformities, we observed an almost circular symmetry due to substrate rotation going from the longer wavelength at the center towards shorter wavelengths at the edges. Several laser parameter characteristic experiments have been carried out to ascertain the performance of these laser devices. A comparison was made but not limited to the symmetric/asymmetric bias conditions, for the different number of electrodes, the driving currents, the various operating temperatures, the laser device dimensions etc. These LC-DFB laser devices have shown repeatable performance.

The L-I characteristic shows power saturation occurring at higher injection currents. Threshold currents determined from the x-intercept of the linear regression varies based on the operating conditions or laser dimension. Under same current injection threshold current determined from the L-I curve showed the 2-electrode laser device with a lower threshold current of 80 mA in comparison with a 1-electrode device at 110 mA for the same cavity length of 1500 μm , while also revealing a higher maximum power for the 2-electrode laser. For the 2-electrode laser device, a higher maximum power is observed when electrode1 is biased (or varied) at a higher current ratio than electrode2 due to the higher current density dominated in this first electrode being closest to the laser output facet. Comparing the 2-electrode laser device with its counterpart but having a shorter laser cavity of 750 μm reveals a smaller threshold of 40 mA for the shorter cavity length laser device. At different operating temperatures (25°C – 65°C), the threshold current

increases linearly. A dynamic resistance of $\sim 3 - 4.5 \Omega$ was estimated from the I-V curve at different operating temperatures with the higher resistance observed at higher temperatures. A stable single longitudinal mode was observed in the laser spectrum peaking at ~ 1560 nm and analyzed using an optical spectrum analyzer. It showed a red-shift in peak emission wavelength as current increases and the same phenomena as temperature increases. It showed an increase in emission output power with increasing current but a decrease in emission power with increasing temperatures for a particular current injection. A current tuning rate of 14 pm/mA (at 25°C) and 16.2 pm/mA at (65°C) was measured reaching a tuning of 2.25 nm in the analyzed bias range. A temperature tuning of 3.38 nm at a rate of 97 pm/°C was measured. The laser devices exhibit good longitudinal mode discrimination. A maximum SMSR of 58 dB was observed at 25°C while biased at 160 mA. At this temperature the SMSR was >50 dB for most currents. However the SMSR gradually degrades with increasing temperatures with the lowest observed at 65°C. A higher SMSR was observed for the multi-electrode devices compared with the single electrode.

The linewidth analyzed shows variation with bias current in free running operation. The linewidth when the laser is under optical feedback operation was reduced compared to when the laser was in free-running. For individual bias, the amount of linewidth reduction depends on the feedback power level. For all cases, the linewidth increases with increase in operating temperatures. For applications where ultra-narrow linewidths are required to increase the laser coherence, optical feedback operation can be used, whereby if the feedback power is well controlled, it might result in spectral stability and ultra-narrow linewidths and it will also improve the modulation characteristics of the laser. The multi-electrode lasers are useful whereby under appropriate and selected driving conditions, a linewidth of interest can be achieved. In general the laser exhibited a Lorentzian linewidth the lowest linewidth of 210 kHz and varied based on the current/temperature while in free-running. A linewidth reduction to as low as 96 kHz was measured while under optical feedback operation.

The tested multi-electrode LC-DFB laser devices under appropriate and selective driving conditions were able to exhibit a flat FM-response from DC to above 300 MHz. The flat FM response was optimized by taking advantage of the different combinations of bias conditions that is available to the multi-electrode laser device thus providing a mechanism to improve its FM response relative to its single electrode counterpart. The RIN was limited by shot noise in the detection system. The FM response of these tested LC-DFB lasers when compared with the best commercially-off-the-shelf (COTS) DFB lasers performs better in terms of the flatness and the frequency range, this will facilitate its use in miniaturised OPLLs for further laser line width reduction or optical phase-locking for high spectral purity RF generation applications.

These good results have contributed to us seeking further optimization of these laser devices, such as changing the LC-DFB structure to fit a QD active region which is a third part recipe from the National Research Council, Canada. There was a lot that went into the design such as careful epitaxial composition analysis as well as the geometry considerations of the rectangular grating since it needs to selectively filter the emission wavelength. The geometry such as the grating height, period/number, duty cycle of the grating were investigated for their coupling strength. High duty cycles are undesirable because it increases waveguide losses, and in our design it is not fabrication tolerant, too high grating height (ridge depth) can cause problems during etching such as undercutting. Increasing the narrow ridge width while the large ridge width remains constant decreases the coupling strength and eventually leads to no coupling, on the other hand increasing the width ridge width while keeping the narrow ridge with constant increases the coupling strength, large ridge increases lateral current spreading and can lead to multi-mode operation. Careful laying out the mask was very important for the definition of the ridge and the grating region since for the LC-DFB lasers the grating is etched directly out of the waveguide ridge thus eliminating regrowth steps. Fabrication process for the growth of the epitaxial layers and the lithography, however fabrication process and techniques can be a limiting factor in exploring many design variations and can also be prone to human imperfections, the 5x i-line stepper lithography is limited by an approximately 360 nm

resolution thus confining us to the 3rd order rectangular gratings. For any design and fabrication, there is always room for tolerance and room for future optimization.

Fabry-Perot (FP) laser and semiconductor optical amplifier were designed and fabricated on the same wafer. These devices operate in E-band (1360 - 1440 nm) wavelength regime which is unconventional to the telecommunication C and L bands. We know in the popular available fibers, this wavelength regime is plagued by water absorption. However, Corning Inc has made this feasible by manufacturing fibers with low water peak in this E-band. And due to the exhaustive capacity anticipated it is necessary to use optical carriers allocated at wavelengths within the E-band, this research is therefore new and understudied and has generated a lot of interest from researchers worldwide. These devices are made from the InGaAsP on InP quaternary material system, they are composed of asymmetric multiple (9) quantum wells. The asymmetry is based on the varying emission wavelengths within the quantum well region. And to realize polarization insensitivity, tensile-strained quantum wells was used. To reduce facet reflectivity, a 7 ° tilt facet and anti-reflection coatings at the facets of the SOA devices was used. The Fabry-Perot devices were as-cleaved facets only.

In this thesis, the FP laser SOA characterization parameters studied and analyzed through experimentation. Even though the devices had a broad geometry designs, based on the results obtained, it was narrowed down to a few better designs and further analysis was done for these groups of devices. First different properties of the lasers were studied, their dependence on the various cavity lengths and ridge widths were analyzed. The L-I plots showed that the wider/ longer corresponding to large area laser devices had large threshold currents. L-I characteristics thereby showed a linear increase in threshold current with the cavity lengths and ridge widths. The smallest devices either did not lase or saturated early after lasing. Also the largest devices lased at such high threshold currents and also saturated shortly after lasing. The threshold current range was 70 mA for the 2 x 600 μm up to 250 mA for the 8 x 1200 μm devices. Other properties, such as the threshold current density and the threshold transparency current were analyzed. The slope and external differential quantum efficiencies were analyzed, it showed a decrease

with increase in cavity length with the highest efficiency for the 2 x 900 μm devices. The slope efficiencies were low which could already be deduced from the less steep slopes of the L-I plots, the low external quantum efficiency is also likened to the less than perfect cleaved-cleaved facets as well as other less than stellar occurrences within the laser cavity. The internal quantum efficiencies and internal loss were extracted as well. Internal quantum efficiency of only 15.4% was realized, this low percentage of the electron-hole pairs recombination that did not result in the generation of photons within the cavity can be attributed to high re-absorption and loss mechanisms within the laser cavity, and also to wafer/fabrication imperfections. The optical loss which is a combination of the internal loss and the mirror losses was approximately 26 cm^{-1} . The spectral properties of the laser shows a small increment in the bandwidth of the emitted spectrum with bias current, going from a typical FP spectral emission to a more elaborate emitted spectrum comprising sets of adjacent longitudinal modes rather than an homogeneous FP profile. An increase and red-shift of peak emission wavelength from 1361 nm @70mA current to 1371 nm @ 300 mA current is observed. This is a 10 nm shift for a 230 mA change implying a tuning of 0.043 nm/mA. The red-shift of emission wavelength is due to gain shift which occurs because of band gap reduction with increasing carrier injection. Overall, the 2 x 900 μm laser devices showed the best performance based on all these analysis.

Thus SOA devices with similar dimension were the focus of the SOA parameter characterization. Based on the fact that the polarization sensitivity was an important analysis, the linear vertical and horizontal states of polarization corresponding to the TE and TM modes were fully considered. The input power of -20 dBm and -10dBm were used, as well as injection current of 150 mA and 200 mA. The first parameter to be analyzed was the amplified spontaneous emission spectrum, which showed saturation after 200 mA current with a peak at 1360 nm. This same peak was observed (and in line) with the output spectra tuned for different wavelengths of a specific input power. Because 2 sets of SOA devices were characterized (as-cleaved facets and AR coated facets) their gain peak/bandwidth, polarization sensitivity/bandwidth, and saturation output powers were analyzed separately. Overall, the AR coated SOA devices showed better

performances in all the characterizations. As expected because the AR coatings reduced reflections at the surface, the output power was larger, higher peak gain and bandwidth was observed as well a higher saturation output power. The AR coating which suppresses cavity resonance had a huge impact on polarization sensitivity, it showed much lower polarization sensitivity in comparison to the as-cleaved facets. In summary, a 3-dB gain bandwidth of 50 nm was presented for each TE and TM polarizations and a gain peak of 21 dBm at 1360 nm was observed. Similarly, a polarization sensitivity of under 3 dB was obtained for the entire wavelength range analyzed from 1340 to 1440 nm with polarization sensitivity lower than 0.5 dBm for some wavelength range. Saturation output powers were observed around 20 dBm. The noise figure and signal-to-noise ratios were also analyzed.

6.3 Recommendation and Future Work

Although a lot of analysis and results has been presented in this thesis, there are still several resource limitations such as equipment/facilities, software tools and fabrication. Nonetheless, based on the analysis enclosed in this thesis, I recommend the following:

- Due to the limitation of the fabrication process available here in Ottawa, it might be good to explore other fabrication centers such as III-V Lab in France, their fabrication techniques allow for lower resolution such that we can design first order gratings devices that some research groups have presented lower threshold currents. This will also enable us compare experimental laser parameters between our first order and higher order gratings beyond theoretical work. Being limited to 3rd order gratings seems rather unfortunate since first order is not plagued by radiation problem of the higher order gratings whereby some light from the fundamental mode couples into radiating diffraction orders. Also it is shown that DFB lasers made with higher orders will have higher threshold current and lower overall efficiency.

- In the next work, it will be good to include other grating designs such as using $\lambda/4$ phase shifts in the middle of the gratings as I presented earlier in chapter 3. Also using apodized sampled gratings as shown in the simulation of Figure 6-1 below

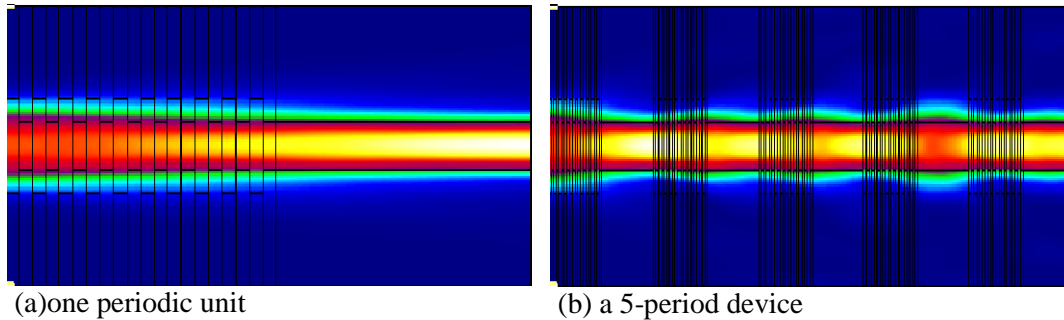


Figure 6-1 Light propagation through an apodized sampled grating

The sampled grating consist of different grating sections of 10 periods length each which are periodically interrupted with non-grating (Fabry-Perot like) regions of equal length along the longitudinal direction. The sampled grating will generate a series of reflection filters, the difference in the non-grating regions will correspond to the difference in the mode spacings of each of its reflection spectrum. Based on the mode spacings, wavelength peaks corresponding to emission wavelengths can be obtained. These can then be filtered by comb reflections to generate only 2 modes, this target of two modes can be used in applications whereby 60 GHz dual mode lasing is needed. This option can be further explored in the research group

- There has been great interest in hybridization amongst researchers in recent years^{123,124,125}. Distributed feedback lasers are attractive for this application due to their single longitudinal mode emission. I recommend for further research a laterally-coupled distributed feedback III-V/Si laser.

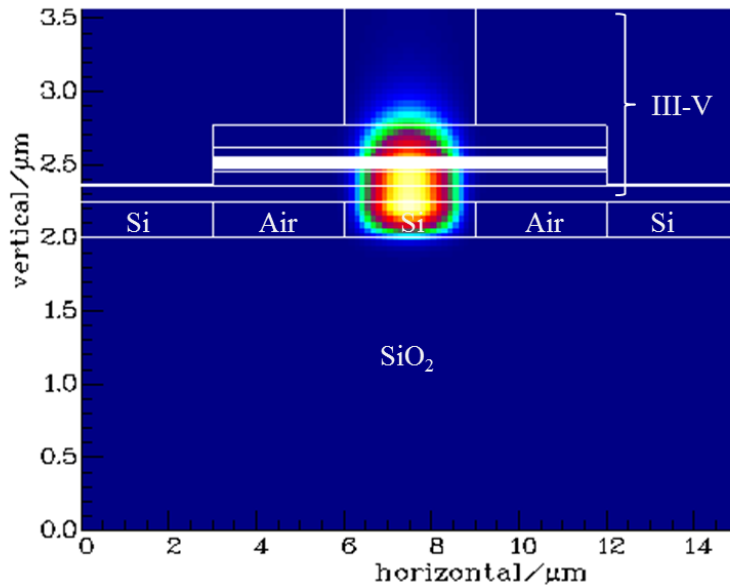


Figure 6-2 Mode profile of a potential hybrid III-V/ silicon laser

Figure 6-2 is a simulated mode profile of a viable hybrid laser consisting of a III-V gain region and a corrugated silicon on insulator waveguide and Table 6-1 shows the mode properties of the fundamental mode.

Table 6-1: Mode properties

	Hybrid III-V/Silicon
Propagation constant	13.055266/ μm
Effective index of the fundamental mode	3.2413838
Confinement factor	0.043409
Fill factor	0.0411163
Effective Area	2.810825 μm^2
Mode loss	1.46441/cm
Group index	3.40966

The upper part of the laser structure is made up of III-V layers, the bottom part has a silicon (Si) rib with air channels on each side. Although it is not very clear in the picture, the mode shape is actually a mushroom shape, whereby the bottom of the mode lies in the silicon (Si) rib and the upper part of the mode lies in the active region. The mode will adiabatically be transformed from the active gain region to the passive silicon waveguide through further adjustment - by carefully

narrowing the III-V region directly above the silicon rib. This option can be further explored in the research group.

- In terms of experimental work, we recently acquired a new test analyzer instrument that might be able to directly measure the phase noise of these laser devices. I was not able to make use of this opportunity because it arrived while I was writing up my results. Another student will be able to carry on this work and include in his/her thesis.
- Re-designing the LC-DFB laser as dual wavelength source for microwave signal is something of interest in our research group, work on it was started by a previous student and was included in a previous fabrication run but they did not yield good results. There has been little successful research done on the dual-wavelength and is still generating a big interest worldwide. This is an area we should look into for the next design/fabrication.
- For the SOA devices, if we intend to continue in this research, I will recommend, we use less number of quantum wells, the design here was for 9 quantum wells and equal number of barriers, a smaller number like 6 will be sufficient, more quantum well tend to reduce the overall gain. Also adjusting the amount of the tensile strain in the quantum wells improves the polarization insensitivity. Another major optimization will be shifting the emission wavelength to the center of the e-band, that way the broad bandwidth measured covers most of the e-band.
- And finally, for all devices tested, further system testing is necessary to ascertain their performance in an optical communication system. This can be done after packaging. Therefore a push for packaging is very much recommended with a view of commercialization. In my opinion, these devices meet the requirement for packaging and potential implementation in the next-generation optical access networks.

Appendix A: Laser Design Variation Table

This appendix presents in more details the laser design gratings variations for the QD LC-DFB and QD Fabry-Perot (FP) lasers. These design variations were carefully chosen to allow for Bragg grating tuned to 1550 nm and for a third order (fabrication limited) rectangular gratings. The different laser devices are identified by the device label beginning with letter L, this is given in the first column. The next column is for the duty cycle, some cells for this column is empty indicating a Fabry-Perot laser device as indicated by the last column called Notes.

The next two columns are for the narrow and wide ridge widths, in microns. The narrow ridge (W_N) widths have variations between 1.5 and 2.0 μm , and the wide ridge widths (W_W) between 2.5 and 4 μm for LC-DFB lasers, the Fabry-Perot laser devices have only one ridge width ranging between 1.5 and 4 μm , the same values for the narrow and wide ridge widths is an indication of a Fabry-Perot laser .

The next four columns are for the partitioned electrode lengths and the spacing in between them. L21-L80 laser devices are all multi-electrode for either QD LC-DFB or QD Fabry-Perot. Section1,2&3 is an indication of a 3-electrode device, while section1&2 is an indication of a 2-electrode laser device. L81-L140 are all single electrode laser devices. The electrode spacing is between 4 and 10 μm . The next column is for the third order grating period ($\Lambda^{(3)}$) in nanometers. And the last column (Notes) indicates the type of laser device and its configuration. These labels were used in the mask layout for easy reference and understanding. Config.1 is an indication of a 2-electrode laser device of equal partitioned electrode lengths, config.2 is an indication of an equal partitioned 3-electrode laser device. Config.3 indicates another 3-electrode device but the middle electrode is double the length of the other two.

InGaAsP/InP 1550 nm QD LC-DFB and QD Fabry-Perot Laser; Grating Order = 3; Ridge Height = Etch depth = 1.0 μm

Device label	Duty cycle	Ridge Widths (μm)		Partitioned electrode section lengths and spacing (μm)				Grating Periods (nm) $\Lambda^{(3)}$	Notes
		W_N	W_W	Section 1	Section 2	Section 3	Spacing		
L21	0.50	1.50	3.0	745	745	-	10	723.6	DFB Config. 1
L22	0.50	1.50	3.0	747	747	-	6	723.6	DFB Config. 1
L23	0.50	1.50	3.0	494	494	494	9	723.6	DFB Config. 2
L24	0.50	1.50	3.0	496	496	496	6	723.6	DFB Config. 2
L25	0.50	1.50	3.0	370	740	370	10	723.6	DFB Config. 3
L26	0.50	1.50	3.0	373	746	373	4	723.6	DFB Config. 3
L27	0.55	1.50	4.0	745	745	-	10	723.6	DFB Config. 1
L28	0.55	2.00	4.0	747	747	-	6	723.6	DFB Config. 1
L29	0.55	1.50	4.0	494	494	494	9	723.6	DFB Config. 2
L30	0.55	2.00	4.0	496	496	496	6	723.6	DFB Config. 2
L31	0.55	1.50	4.0	370	740	370	10	723.6	DFB Config. 3
L32	0.55	2.0	4.0	373	746	373	4	723.6	DFB Config. 3
L33		2.0	2.0	747	747	-	6		FP config 1
L34		2.5	2.5	745	745	-	9		FP config 1
L35		3.0	3.0	745	745	-	10		FP config 1
L36		2.0	2.0	496	496	496	6		FP config 2
L37		2.5	2.5	494	494	494	9		FP config 2
L38		3.0	3.0	493	493	493	10		FP config 2
L39		2.0	2.0	372	744	372	6		FP config 3
L40		3.0	3.0	370	740	370	9		FP config 3
L41	0.50	1.50	3.0	495	495	-	10	723.6	DFB Config. 1
L42	0.50	1.50	3.0	497	497	-	6	723.6	DFB Config. 1
L43	0.50	1.50	3.0	327	327	327	10	723.6	DFB Config. 2
L44	0.50	1.50	3.0	331	331	331	4	723.6	DFB Config. 2
L45	0.50	1.50	3.0	247	494	247	5	723.6	DFB Config. 3
L46	0.50	1.50	3.0	245	490	245	9	723.6	DFB Config. 3
L47	0.55	1.50	4.0	495	495	-	10	723.6	DFB Config. 1
L48	0.55	2.00	4.0	497	497	-	6	723.6	DFB Config. 1
L49	0.55	1.50	4.0	327	327	327	10	723.6	DFB Config. 2
L50	0.55	2.00	4.0	331	331	331	4	723.6	DFB Config. 2
L51	0.55	1.50	4.0	247	494	247	5	723.6	DFB Config. 3
L52	0.55	2.0	4.0	248	496	248	3	723.6	DFB Config. 3
L53		2.0	2.0	497	497	-	6		FP config 1
L54		2.5	2.5	496	496	-	9		FP config 1
L55		3.0	3.0	495	495	-	10		FP config 1
L56		2.0	2.0	247	494	247	6		FP config 2
L57		2.5	2.5	245	490	245	9		FP config 2
L58		3.0	3.0	245	490	245	10		FP config 2
L59		2.0	2.0	249	497	249	6		FP config 3
L60		3.0	3.0	245	490	245	9		FP config 3
L61	0.50	1.50	3.0	370	370	-	10	723.6	DFB Config. 1
L62	0.50	1.50	3.0	373	373	-	6	723.6	DFB Config. 1
L63	0.50	1.50	3.0	246	246	246	6	723.6	DFB Config. 2
L64	0.50	1.50	3.0	244	244	244	9	723.6	DFB Config. 2
L65	0.50	1.50	3.0	185	370	185	5	723.6	DFB Config. 3

L66	0.50	1.50	3.0	182	364	182	11	723.6	DFB Config. 3
L67	0.55	1.50	4.0	370	370	-	10	723.6	DFB Config. 1
L68	0.55	2.00	4.0	373	373	-	6	723.6	DFB Config. 1
L69	0.55	1.50	4.0	246	246	246	6	723.6	DFB Config. 2
L70	0.55	2.00	4.0	244	244	244	9	723.6	DFB Config. 2
L71	0.55	1.50	4.0	185	370	185	5	723.6	DFB Config. 3
L72	0.55	2.0	4.0	182	364	182	11	723.6	DFB Config. 3
L73		2.0	2.0	372	372	-	6		FP config 1
L74		2.5	2.5	370	370	-	9		FP config 1
L75		3.0	3.0	370	370	-	10		FP config 1
L76		2.0	2.0	246	246	246	6		FP config 2
L77		2.5	2.5	244	244	244	9		FP config 2
L78		3.0	3.0	244	244	244	10		FP config 2
L79		2.0	2.0	185	370	185	6		FP config 3
L80		3.0	3.0	183	366	183	9		FP config 3
L81		1.5	1.5						Fabry-Perot
L82		2.0	2.0						Fabry-Perot
L83		2.0	2.0						Fabry-Perot
L84		2.5	2.5						Fabry-Perot
L85		3.0	3.0						Fabry-Perot
L86		3.0	3.0						Fabry-Perot
L87		3.0	3.0						Fabry-Perot
L88		3.5	3.5						Fabry-Perot
L89		4.0	4.0						Fabry-Perot
L90		4.0	4.0						Fabry-Perot
L91	0.55	1.50	3.5					720.2	DFB
L92	0.55	1.75	3.5					720.2	DFB
L93	0.50	1.50	3.0					720.2	DFB
L94	0.50	1.75	3.0					720.2	DFB
L95	0.50	1.50	4.0					720.2	DFB
L96	0.50	2.0	4.0					720.2	DFB
L97	0.50	1.50	3.0					720.2	DFB
L98	0.50	1.75	3.0					720.2	DFB
L99	0.50	1.50	4.0					720.2	DFB
L100	0.50	1.75	4.0					720.2	DFB
L101		1.5	1.5						Fabry-Perot
L102		2.0	2.0						Fabry-Perot
L103		2.0	2.0						Fabry-Perot
L104		2.5	2.5						Fabry-Perot
L105		3.0	3.0						Fabry-Perot
L106		3.0	3.0						Fabry-Perot
L107		3.0	3.0						Fabry-Perot
L108		3.5	3.5						Fabry-Perot
L109		4.0	4.0						Fabry-Perot
L110		4.0	4.0						Fabry-Perot
L111	0.55	1.50	4.0					720.2	DFB
L112	0.50	1.50	3.0					720.2	DFB
L113	0.50	1.75	3.0					720.2	DFB
L114	0.50	1.50	4.0					720.2	DFB
L115	0.50	1.75	4.0					720.2	DFB
L116	0.55	1.50	3.0					720.2	DFB
L117	0.55	1.75	3.0					720.2	DFB
L118	0.55	1.50	4.0					720.2	DFB

L119	0.55	2.0	4.0					720.2	DFB
L120	0.55	1.50	3.0					720.2	DFB
L121		1.5	1.5						Fabry-Perot
L122		2.0	2.0						Fabry-Perot
L123		2.0	2.0						Fabry-Perot
L124		2.5	2.5						Fabry-Perot
L125		3.0	3.0						Fabry-Perot
L126		3.0	3.0						Fabry-Perot
L127		3.0	3.0						Fabry-Perot
L128		3.5	3.5						Fabry-Perot
L129		4.0	4.0						Fabry-Perot
L130		4.0	4.0						Fabry-Perot
L131	0.55	1.75	4.0					720.2	DFB
L132	0.55	1.75	3.0					720.2	DFB
L133	0.55	1.50	4.0					720.2	DFB
L134	0.55	2.0	4.0					720.2	DFB
L135	0.55	1.50	3.0					720.2	DFB
L136	0.55	1.75	3.0					720.2	DFB
L137	0.55	1.50	4.0					720.2	DFB
L138	0.55	1.75	4.0					720.2	DFB
L139	0.50	1.50	3.0					720.2	DFB
L140	0.50	1.75	3.0					720.2	DFB

References

- ¹ N. W. Ashcroft and N. D. Mermin. (1976) “Solid State Physics” Dumfries, NC, USA: Hold, Rinehart and Winston. Chapter 4; chapter 10.
- ² S. L. Chuang. (1995) “Physics of Optoelectronic Devices” Hoboken, NJ, USA: John Wiley & Sons.
- ³ J. Bardeen, “An improved calculation of the energies of the metallic Li and Na,” J. Chem. Phys. 6, 367-371 (1938)
- ⁴ F. Seitz, “The Modern Theory of Solids” McGraw Hill, New York, 1940, p.352
- ⁵ E. O. Kane, “The $\mathbf{k} \cdot \mathbf{p}$ method” Chapter 3 in R. K. Willardson and A. C. Beer, Eds., Semiconductors and semimetals, Vol. 1, Academic, New York, 1966
- ⁶ J. M. Luttinger and W. Kohn, “Motion of Electrons and Holes in perturbed periodic fields” Phys. Rev. 97, 869-883 (1955)
- ⁷ S. L. Chuang. (2009) “Physics of Photonics Devices” Hoboken, NJ, USA: John Wiley & Sons
- ⁸ M. Sotoodeh, A.H. Khalid, and A.A. Rezazadeh, “Empirical low-field mobility model for III-V compounds applicable in device simulation codes”, J. Appl. Phys., Vol.87, pp. 2890-2900, 2000.
- ⁹ P. Bhattacharya, “Semiconductor Optoelectronic Devices,” Prentice hall, Second Edition, 1997
- ¹⁰ N. Tessler, and G. Eisenstein “On Carrier Injection and Gain Dynamics in Quantum Well lasers,” IEEE J. Quantum Electron. vol. 29, pp. 1586-1596. Jun. 1993
- ¹¹ W. Rideout, W. F. Sharfin, E. S. Koteles, M. O. Vassell, and B. Elman. “Well barrier hole burning in quantum well lasers.” IEEE Photon. Technol. Lett., vol. 3, pp. 784-786, Sept. 1991
- ¹² S. C. Kan, D. Vassilovski. T. C. Wu, and K. Y. Lau. “On the effects of carrier diffusion and quantum capture in high speed modulation of quantum well lasers,” Appl. Phys. Lett., vol. 61, pp. 752-754, 1992
- ¹³ S. L. Chuang, “Physics of Optoelectronics devices”, John Wiley & Sons Inc., New York, 1995.
- ¹⁴ M. L. Cohen and J. R. Chelikowsky, Electronic Structure and Optical Properties of Semiconductors, Springer Series in Solid-State Sciences, Springer, Berlin, 1998
- ¹⁵ I. Vurgaftman,, J. R. Meyer and L. R. Ram-Mohan “Band parameters of III-V compound semiconductors and their alloys” Journal of Applied Physics 89, 5815 (2001)
- ¹⁶ Photon Design Ltd, Oxford, United Kingdom www.photond.com/products/harold.htm

-
- ¹⁷ S. Adachi “Material parameters of $\text{In}_{1-x}\text{Ga}_x\text{As}_y\text{P}_{1-y}$ and related binaries” J. Appl. Phys. 53(12) pp 8775-8792, December 1982
- ¹⁸ B. Broberg and S. Lindgren “Refractive index of $\text{In}_{1-x}\text{Ga}_x\text{As}_y\text{P}_{1-y}$ layers and InP in the transparent wavelength region” J. Appl. Phys. 55(9) pp 3376-3381, November 1984
- ¹⁹ J. Carroll, J. Whiteaway, and D. Plumb, Distributed feedback semiconductor lasers, Volume 10, Institution of Electrical Engineers, 1998
- ²⁰ H. Kogelnik and C. V. Shank “Couple wave theory of distributed feedback lasers” J. Appl. Phys. 43, 2327 (1972)
- ²¹ W. Streifer, D. Scifres, and R.D. Burnham, “Coupling Coefficients for Distributed Feedback Single- and Double-Heterostructure Diode Lasers,” *IEEE J. Quantum Electron.*, vol. QE-11, pp. 867-873, Nov. 1975
- ²² W. Streifer, R. Burnham, and D. Scifres, “Analysis of Grating-Coupled Radiation in GaAs:GaAlAs Lasers and Waveguides – II: Blazing Effects,” *IEEE J. Quantum Electron.*, vol. QE-12, pp. 494-499, Aug. 1976.
- ²³ S.-C. Cho, B.-G. Kim, and N. Dagli, “Extended Additional Layer Method of Calculating the Coupling Coefficient of Arbitrarily Shaped Gratings,” *Microw. Opt. Technol. Lett.*, vol. 16, pp. 143-145, Oct. 1997.
- ²⁴ P. Correc, “Coupling Coefficients for Trapezoidal Gratings,” *IEEE J. Quantum Electron.*, vol. QE-24, pp. 8-10, Jan. 1988.
- ²⁵ R. R. Millett “Modelling, Fabrication, and Measurement of Laterally-Coupled Distributed Feedback Lasers” PhD thesis, University of Ottawa 2009
- ²⁶ Photon Design Ltd, Oxford, United Kingdom www.photond.com/products/fimprop
- ²⁷ L.M. Zhang, and J.E. Carroll, “Large-signal dynamic model of the DFB laser,” *IEEE Journal of Quantum Electronics*, vol.28, no.3, pp.604-611, Mar 1992
- ²⁸ Linh V. T Nguyen, Arthur James Lowery, Phillip C. R. Gurney, and Dalma Novak. A time-domain model for high-speed quantum-well lasers including carrier transport effects. *IEEE Journal of Selected Topics in Quantum Electronics*, 1(2):494–504, 1995
- ²⁹ C. F. Tsang, D. D Marcenac, J. E Carroll, and L. M Zhang. Comparison between power matrix model and time domain model in modelling large signal responses of DFB lasers. *IEE Proceedings-Optoelectronics*, 141(2):89–96, 1994
- ³⁰ Toshiaki Suhara. *Semiconductor laser fundamentals*. pages 77–103,255. CRC Press, 2004
- ³¹ John E Carroll, James Whiteaway, and Dick Plumb. Distributed feedback semiconductor lasers. volume 10, pages 22–24,58–66,97–162, 211–246,329–351. IET, 1998
- ³² L. M. Zhang, S. F. Yu, M. C. Nowell, D. D. Marcenac, J. E. Carroll, and R. G. S. Plumb Dynamic analysis of radiation and side-mode suppression in a second-order dfb laser using time-domain large-signal traveling wave model. *IEEE Journal of Quantum Electronics*, 30(6):1389–1395, 1994

-
- ³³ John E Carroll. Rate equations in semiconductor electronics. Cambridge University Press, 1990.
- ³⁴ Photon Design Ltd, Oxford, United Kingdom www.photond.com/products/picwave.htm
- ³⁵ W. S. Rabinovich and B. J. Feldman, "Spatial Hole Burning Effects in Distributed Feedback lasers," *IEEE Journal of Quantum Electronics*, Vol. 25, No. 1, January 1989.
- ³⁶ A. Akrouf, K. Dridi, and T. J. Hall, "Dynamic Analysis of High-Order Laterally Coupled DFB Lasers Using Time-Domain Traveling-Wave Model," *IEEE Journal of Quantum Electronics*, vol. 48, no. 10, pp. 1252-1258, Oct. 2012
- ³⁷ M. Grundmann, "The present status of quantum dot lasers," *Physica E*, vol. 5, pp. 167, 2000.
- ³⁸ D. Bimberg, M. Grundmann, F. Heinrichsdorff, N. N. Ledentsov, V. M. Ustinov, A. E. Zhukov, A. R. Kovsh, M. V. Maximov, Y. M. Shernyakov, and B. V. Volovik, "Quantum dot lasers: breakthrough in optoelectronics," *Thin Solid Films*, vol. 367, pp. 235-249, 2000.
- ³⁹ H. Ishikawa, H. Shoji, Y. Nakata, K. Mukai, M. Sugawara, M. Egawa, N. Otsuka, Y. Sugiyama, T. Futatsugi, and N. Yokoyama, "Self-organized quantum dots and quantum dot lasers (invited)," *Journal of Vacuum Science & Technology A: Vacuum, Surfaces, and Films*, vol. 16, pp. 794, 1998
- ⁴⁰ M. Sugawara, "Theoretical bases of the optical properties of semiconductor quantum nano-structures," *Semiconductors and Semimetals*, vol. 60, pp. 1-116, 1999.
- ⁴¹ P. Bhattacharya, S. Ghosh, and A. D. Stiff-Roberts, "Quantum dot opto-electronic devices," *Annual Review of Materials Research*, vol. 34, pp. 1-40, 2004.
- ⁴² F. Lelarge, B. Dagens, J. Renaudier, R. Brenot, A. Accard, D. F. van, D. Make, G. O. Le, J. G. Provost, F. Poingt, J. Landreau, O. Drisse, E. Derouin, B. Rousseau, F. Pommereau, and G. H. Duan, "Recent advances on InAs/InP quantum dash based, semiconductor lasers and optical amplifiers operating at 1.55 μm ," *IEEE Journal of Selected Topics in Quantum Electronics*, vol. 13, pp. 111-124, 2007.
- ⁴³ Y. Arakawa and H. Sakaki, "Multidimensional quantum well laser and temperature dependence of its threshold current," *Applied Physics Letters*, vol. 40, pp. 939, 1982.
- ⁴⁴ T. C. Newell, D. J. Bossert, A. Stintz, B. Fuchs, K. J. Malloy, and L. F. Lester, "Gain and linewidth enhancement factor in InAs quantum-dot laser diodes," *IEEE Photonics Technology Letters* **11**, 1527-1529 (1999).
- ⁴⁵ M. ASADA, Y. MIYAMOTO, and Y. SUEMATSU, "Gain and the threshold of 2-dimensional quantum-box lasers," *IEEE Journal of Quantum Electronics* **22**, 1915-1921 (1986).
- ⁴⁶ L.M. Miller, J.T. Verdeyen, J.J. Coleman, R.P. Bryan, J.J. Alwan, K.J. Beernink, J.S. Hughes, and T.M. Cockerill, "A Distributed Feedback Ridge Waveguide Quantum Well Heterostructure Laser," *IEEE Photon. Tech. Lett.*, vol. 3, pp. 6-8, Jan. 1991

-
- ⁴⁷ L.M. Miller, J.T. Verdeyen, J.J. Coleman, R.P. Bryan, J.J. Alwan, K.J. Beernink, J.S. Hughes, and T.M. Cockerill, "A Distributed Feedback Ridge Waveguide Quantum Well Heterostructure Laser," *IEEE Photon. Tech. Lett.*, vol. 3, pp. 6-8, Jan. 1991
- ⁴⁸ V.V. Wong, W.-Y. Choi, J.M. Carter, C.G. Fonstad, H.I. Smith, Y. Chung, and N. Dagli, "Ridge-waveguide sidewall-grating distributed feedback structures fabricated by x-ray lithography," *J. Vac. Sci. Technol. B*, vol. 11, pp. 2621-2624, Nov/Dec 1993.
- ⁴⁹ R.C. Tiberio, P.F. Chapman, R.D. Martin, S. Forouhar, and R.J. Lang, "Laterally coupled distributed feedback laser fabricated with electron-beam lithography and chemically assisted ion-beam etching," *J. Vac. Sci. Technol. B*, vol. 12, pp. 3746-3749, June 1994
- ⁵⁰ Y. Watanabe, N. Chen, K. Takei, K. Chikuma, N. Futakuchi, and Y. Nakano, "Laterally Coupled Strained MQW Ridge Waveguide Distributed-Feedback Laser Diode Fabricated by Wet-Dry Hybrid Etching Process," *IEEE Photon. Tech. Lett.*, vol. 10, pp. 1688-1690, 1998
- ⁵¹ N. Chen, Y. Watanabe, K. Takei, and K. Chikuma, "InGaAsP/InP laterally coupled distributed feedback laser," *Jpn. J. Appl. Phys.*, vol. 39, pp. 1508-1511, 2000
- ⁵² M. Müller, M. Kamp, A. Forchel, and J.-L. Gentner, "Wide-range-tunable laterally coupled distributed feedback lasers based on InGaAsP-InP," *Appl. Phys. Lett.*, vol. 79, pp. 2684-2686, 2001
- ⁵³ B. Reid, M. Poirier, S.R. Das, D. Ducharme, R. Dowlatshahi, S. Langstaff, N.S. Kim, R. Kuchibhatia, and S. Djavani-Tabrizi, "Narrow Linewidth and High Power Distributed Feedback Lasers Fabricated without a Regrowth Step," *ECOC 2003*
- ⁵⁴ A. Laakso, M. Dumitrescu, J. Viheriälä, J. Karinen, M. Suominen, and M. Pessa, "Optical modeling of laterally-corrugated ridge-waveguide gratings," *J. Optical Quantum Electron.*, DOI 10.1007/s11082-009-9292-3, April 2009
- ⁵⁵ M. Zanola, M. J. Strain, G. Giuliani, and M. Sorel, "Monolithically Integrated DFB Lasers for Tunable and Narrow Linewidth Millimeter-Wave Generation," *IEEE Journal of Selected Topics in Quantum Electronics*, vol. 19, no. 4, pp. 1500406-1500406, Jul.-Aug. 2013.
- ⁵⁶ R. Millett, H. Schriemer, T. Hall, and K. Hinzer, "Effects of Grating Order and Tooth Rounding in Laterally-Coupled Distributed Feedback Lasers," *J. Opt. Quantum Electron.*, 10.1007/s11082-009-9293-2, April 2009
- ⁵⁷ R. Millett, K. Dridi, A. Benhsaien, H. Schriemer, K. Hinzer, and T. Hall, "Fabrication-tolerant 1310 nm laterally-coupled distributed feedback lasers with high side mode suppression ratios", *American Institute of Physics (AIP) Conf. Proc.* 1288, 88 (2010), DOI:10.1063/1.3521380
- ⁵⁸ K. Dridi, A. Benhsaien, J. Zhang, and T. J. Hall, "Narrow Linewidth 1550 nm Corrugated Ridge Waveguide DFB Lasers," *IEEE Photonics Technology Letters*, vol. 26, no. 12, pp. 1192-1195, Jun. 2014

-
- ⁵⁹ K. Dridi, A. Benhsaien, J. Zhang, K. Hinzer, and T. J. Hall, "Narrow linewidth two-electrode 1560 nm laterally coupled distributed feedback lasers with third-order surface etched gratings," *Optics Express*, vol. 22, no. 16, pp. 19087-19097, Aug. 2014.
- ⁶⁰ K. Dridi, A. Benhsaien, J. Zhang, and T. J. Hall, "Narrow linewidth 1560 nm InGaAsP split-contact corrugated ridge waveguide DFB lasers," *Optics Letters*, vol. 39, no. 21, pp. 6197-6200, Nov. 2014.
- ⁶¹ A. Akrouf, K. Dridi, and T. J. Hall, "Dynamic Analysis of High-Order Laterally Coupled DFB Lasers Using Time-Domain Traveling-Wave Model," *IEEE Journal of Quantum Electronics*, vol. 48, no. 10, pp. 1252-1258, Oct. 2012
- ⁶² Ramón Maldonado-Basilio, Vahid Eslamdoost, Julie E. Nkanta, and Trevor J. Hall "Experimental Analysis of Laterally-Coupled MQW-DFB Lasers in Optical Feedback" CLEO, June 8-13, 2014, San Jose, USA
- ⁶³ A. Akrouf, K. Dridi, A. Benhsaien, and T. J. Hall, "Time-Domain Analysis of Third-Order Quantum-Dot-Based Laterally-Coupled Distributed Feedback Lasers Using Travelling-Wave Approach," *IEEE Journal of Quantum Electronics*, vol. 49, no. 5, pp. 491-498, May 2013
- ⁶⁴ A. Akrouf, K. Dridi, S. Abdul-Majid, J. Seregelyi, and T. J. Hall, "Numerical Study of Dual Mode Generation Using a Sampled-Grating High-Order Quantum-Dot Based Laterally-Coupled DFB Laser," *IEEE Journal of Quantum Electronics*, vol. 49, no. 10, pp. 821-828, Oct. 2013
- ⁶⁵ Philip J. Poole "Email conversation" November 2014, in copy Trevor J. Hall and Jessica Zhang
- ⁶⁶ Z. G. Lu, J. R. Liu, P. Poole, S. Raymond, P. Barrios, D. Poitras, G. Pakulski, X. P. Zhang, K. Hinzer and T. J. Hall "Low noise InAs/InP quantum dot C-band monolithic multiwavelength lasers for WDM-PONs" Proc. OFC paper JWA27 (March 2009)
- ⁶⁷ Z. G. Lu, P. Poole, P. Barrios, Z.J.Jiao, J. R. Liu, G. Pakulski, D. Goodchild, B. Rioux, A. J. Springthorpe and D. Poitras "Single-mode 1.52 μm InAs/InP quantum dot DFB lasers" Proc. OFC (2011)
- ⁶⁸ P. J. Poole, K. Kaminska, P. Barrios, Z. Lu and J. Lie "Growth of InAs/InP-based quantum dots for 1.55 μm laser applications" *J. Cryst. Growth* 311(2009) 1482-1486
- ⁶⁹ M. A. Ordal, L.L. Long, R.J. Bell, S.E. Bell, R.R. Bell, R.W. Alexander, Jr., and C.A. Ward, "Optical properties of the metals Al, Co, Cu, Au, Fe, Pb, Ni, Pd, Pt, Ag, Ti, and W in the infrared and far infrared," *Appl. Opt.*, vol. 22, pp. 1099-1120, Apr. 1983
- ⁷⁰ G.M. Smith, D.V. Forbes, R.M. Lammert, and J.J. Coleman, "Metallization to asymmetric cladding separate confinement heterostructure lasers," *Appl. Phys. Lett.*, vol. 67, pp. 3847-3849, Dec. 1995
- ⁷¹ J. H. Weaver, "Optical properties of Rh, Pd, Ir, and Pt," *Phys. Rev. B*, vol. 11, pp.1416-1425, Feb. 1975.
- ⁷² J. Carroll, J. Whiteaway, and D. Plumb, "Distributed feedback semiconductor lasers", SPIE Press, London, UK, 1998

-
- ⁷³ K. Williams, A. Hayes, S. DiStefano, O. Huang, and E. Ostan, "Reactive ion beam etching of ferroelectric materials using an RF inductively coupled ion beam source," Proc. 10th IEEE Symp. Appl. Ferroelectrics, vol. 2, pp. 783-786, Aug. 1996
- ⁷⁴ B.Fay, "Advanced optical lithography development, from UV to EUV," *Microel. Eng.*, vol. 61-62, pp. 11-24, July 2002
- ⁷⁵ Canadian Photonics Fabrication Centre (CPFC), "Standard PL measurement provided alongside the delivered fabrication lasers and SOA devices", Ottawa, Canada
- ⁷⁶ K. S. Mobarhan "Test and Characterization of Laser Diodes: Determination of Principal Parameters" 1996-2008, Newport Inc. USA
- ⁷⁷ Y. Suematsu, K. Kishino, S. Arai, and F. Koyama, "Dynamic single-mode semiconductor lasers with a distributed reflector," Chapter 4 in R.K. Willardson and A.C. Beer, eds., "Semiconductors and Semimetals, vol. 22, Academic Press, San Diego, 1985
- ⁷⁸ L. B. Mercer, "1/f frequency noise effects on self-heterodyne linewidth measurements," *Journal of Lightwave Technology*, vol. 9, no. 4, pp. 485-493, Apr. 1991.
- ⁷⁹ S. Spiessberger, M. Schiemangk, A. Wicht, H. Wenzel, O. Brox, and G. Erbert, "Narrow Linewidth DFB Lasers Emitting Near a Wavelength of 1064 nm," *Journal of Lightwave Technology*, vol. 28, no.17, pp. 2611-2616, Sep. 2010
- ⁸⁰ T. Okoshi, K. Kikuchi, and A. Nakayama, "Novel method for high resolution measurement of laser output spectrum," *Electronics Letters*, vol. 16, no. 16, pp. 630-631, Jul. 1980.
- ⁸¹ D. Derickson, "Fiber Optic Test and Measurement" Prentice Hall, New Jersey, 1998
- ⁸² U. Gliese, T. N. Nielsen, M. Bruun, E. Lintz Christensen, K. E. Stubkjær, S. Lindgren, and B. Broberg "A wideband heterodyne optical phase-locked loop for generation of 3-18 GHz microwave carriers," *Photon. Technol. Lett.*, vol 4, no. 8, p. 936, 1992
- ⁸³ N. Satyan, W. Liang, A. Kewitsch, G. Rakuljic, and A. Yariv, "Coherent power combination of semiconductor lasers using optical phase-lock loops," *IEEE J. Sel. Top. Quant. Electron.*, vol. 15, no. 2, pp. 240-247, Mar./Apr. 2009
- ⁸⁴ R. C. Steele, "Optical phase-locked loop using semiconductor laser diodes," *Electron. Lett.*, vol. 19, no. 2, pp. 69-71, 1983
- ⁸⁵ M. Poulin, S. Ayotte, F. Costin, A. Babin, D. Faucher, M. Aubé, C. Latrasse, S. Savard, G. Robidoux, M. Laliberté and F. Pelletier "Optically phase-locked lasers for RF photonics applications, Proc. OFC, Tu3F.1 (2015)
- ⁸⁶ J.-F. Cliché, M. Allard and M. Têtu "High-power and ultranarrow DFB laser: the effect of linewidth reduction systems on coherence length and interferometer noise," Proc. SPIE, 62160C (2006)
- ⁸⁷ Kartalopoulos, S.V., "DWDM: Networks, Devices and Technology", Wiley-Interscience, 2003.

-
- ⁸⁸ Tyler, E.J.; Kourtessis, P.; Webster, W.; Rochart, E.; Quinlan, T.; Dudley, S.E.M.; Walker, S.D.; Penty, R.V.; White, I.H.; "Toward Terabit-per-Second Capacities Over Multimode Fiber Links Using SCM/WDM Techniques," *Journal of Lightwave Technology*, vol.21, no.12, pp.3237-3243, Dec 2003
- ⁸⁹ Nagarajan, R.; Kato, M.; Pleumeekers, J.; Evans, P.; Lambert, D.; Chen, A.; Dominic, V.; Mathur, A.; Chavarkar, P.; Missey, M.; Dentai, A.; Hurtt, S.; Back, J.; Muthiah, R.; Murthy, S.; Salvatore, R.; Grubb, S.; Joyner, C.; Rossi, J.; Schneider, R.; Ziari, M.; Kish, F.; Welch, D.; , "Single-chip 40-channel InP transmitter photonic integrated circuit capable of aggregate data rate of 1.6 Tbit/s," *Electronics Letters* , vol.42, no.13, pp. 771- 773, 22 June 2006
- ⁹⁰ ITU-T G.694.2, "Spectral grids for WDM applications: CWDM wavelength grid", Dec. 2003, <http://www.itu.int/rec/T-REC-G.694.2-200312-I/en>
- ⁹¹ ITU-T G.694.1, "Spectral grids for WDM applications: DWDM wavelength grid", Jun. 2002, <http://www.itu.int/rec/T-REC-G.694.1-200206-I/en>
- ⁹² L. G. Kazovsky, Wei-Tao Shaw, D. Gutierrez, N. Cheng, and S.-W. Wong, "Next-generation optical access networks," *Journal of Lightwave Technology*, **25**(11), 3428-3442 (2007).
- ⁹³ K. C. Reichmann, P. P. Iannone, C. Briton, J. Nakagawa, T. Cusick, E. M. Kimber, C. Doerr, L. L. Buhl, M. Cappuzo, E. Y. Chen, L. Gomez, J. Johnson, A. M. Kanan, J. Lentz, Y. F. Chang, B. Palsdottir, T. Tokle, and L. Spiekman, "A symmetric-rate, extended-reach 40 Gb/s CWDM-TDMA PON with downstream and upstream SOA-Raman amplification," *Journal of Lightwave Technology*, **30**(4), 479-485 (2012).
- ⁹⁴ P. Vetter, "Tutorial: next generation optical access technologies," in *European Conference on Optical Communications (ECOC)*, 2012
- ⁹⁵ E. Trojer, S. Dahofort, D. Hood, and H. Mickelsson, "Current and next-generation PONs: a technical overview of present and future PON technology," *Ericsson Review*, **2**, 64-69 (2008)
- ⁹⁶ A. Banerjee, Y. Park, F. Clarke, H. Song, S. Yang, G. Kramer, K. Kim, and B. Mukherjee, "Wavelength-division-multiplexed passive optical network (WDM-PON) technologies for broadband access: a review [Invited]," *Journal of Optical Networking*, **4**(11), 737-758 (2005).
- ⁹⁷ International Telecommunication Union, ITU-T Recommendation G.984.5, "Gigabit-capable passive optical networks (G-PON): enhancement band," (2007).
- ⁹⁸ P. E. Green, Jr., "Fiber to the home: the next big broadband thing," *IEEE Communications Magazine*, **42**(9), 100–106 (2004).
- ⁹⁹ J.-M. Kang, and S.-K. Han, "A novel hybrid WDM/SCM-PON sharing wavelength for up- and down-link using reflective semiconductor optical amplifier," *IEEE Photonics Technology Letters*, **18**(3), 502–504 (2006).
- ¹⁰⁰ R. Bavey, J. Kani, F. Bourgart, and K. McCammon, "Options for future optical access networks," *IEEE Communications Magazine*, **44**(10), 50–56 (2006).

-
- ¹⁰¹ Corning Inc., “Suppressed water peak enhances long-haul networks,” White Paper WP7151, October 2005 <http://www.corning.com/docs/opticalfiber/wp7151.pdf>
- ¹⁰² P. Koonath, S. Kim, W.-J. Cho, and A. Gopinath, “Polarization-insensitive quantum-well semiconductor optical amplifiers,” *IEEE Journal of Quantum Electronics*, **38**(9), 1282-1290 (2002).
- ¹⁰³ K. Morito, M. Ekawa, T. Watanabe, and Y. Kotaki, “High-output-power polarisation insensitive semiconductor optical amplifier,” *Journal of Lightwave Technology*, **21**(1), 176-181 (2003).
- ¹⁰⁴ S. Ikeda, A. Shimizu, and T. Hara, “Asymmetric dual quantum wells laser-wavelength switching controlled by injection current,” *Applied Physics Letters*, **55**(12), 1155–1157 (1989).
- ¹⁰⁵ X. Zhu, D. Cassidy, M. Hamp, D. Thompson, B. Robinson, Q. Zhao, M. Davies, “1.4- μm InGaAsP–InP strained multiple-quantum well laser for broad-wavelength tunability,” *IEEE Photonics Technology Letters*, **9**(9), 1202-1204 (1997).
- ¹⁰⁶ V. V. Lysac, H. Kawaguchi, and I. A. Sukhoivanov, “Gain spectra and saturation power of asymmetrical multiple quantum well semiconductor optical amplifiers,” *IEEE Proceedings of Optoelectronics*, **152**(2), 131-139 (2005).
- ¹⁰⁷ M. J. Hamp, and D. T. Cassidy, “Critical design parameters for engineering broadly tunable asymmetric multiple quantum well lasers,” *IEEE Journal of Quantum Electronics*, **36**(8), 978–982 (2000).
- ¹⁰⁸ G. Eisenstein, G. Raybon, and L. Stulz, “Deposition and Measurements of Electron-Beam-Evaporated SiO_x Antireflection Coatings on InGaAsP Injection Laser Facets,” *Journal of Lightwave Technology*, vol. 6, no. 1, pp. 12–16, 1988.
- ¹⁰⁹ H. Ghafouri-Shiraz, *Fundamentals of Laser Diode Amplifiers*, Wiley, Chichester, 1996
- ¹¹⁰ Y. Boucher and A. Sharaiha, “Spectral properties of amplified spontaneous emission in semiconductor optical amplifiers,” *IEEE J. Quantum Electron.*, vol. 36, no. 6, pp. 708-720, June 2000.
- ¹¹¹ J. Shim, J. Kim, D. Yang, Y. Eo, and S. Arai, “Facet Reflectivity of a Spot-Size Converter Integrated Semiconductor Optical Amplifier,” *Journal of Quantum Electronics*, vol. 38, no. 6, pp. 665–673, 2002.
- ¹¹² T. Saito and T. Mukai, “Recent progress in semiconductor laser amplifiers,” *J. Lightwave Technol.*, vol. 6, no. 11, pp. 1656-1664, Nov. 1988.
- ¹¹³ L. A. Coldren and S. W. Corzine, *Diode Lasers and Photonic Integrated Circuits* (New York, NY: John Wiley & Sons, Inc., 1995),
- ¹¹⁴ N. Tessler, and G. Eisenstein “On Carrier Injection and Gain Dynamics in Quantum Well lasers,” *IEEE J. Quantum Electron.* vol. 29, pp. 1586-1596. Jun. 1993

-
- ¹¹⁵ B. W. Hakki and T. L. Paoli, "CW degradation at 300°K of GaAs double-heterostructure junction lasers. II. Electronic gain", *J. Appl. Phys.*, Vol. 44, pp. 4173, 1973.
- ¹¹⁶ D. T. Cassidy "Comparison of rate-equation and Fabry-Perot approaches to modeling a diode laser", *Appl. Opt.*, Vol. 22, pp. 3321-3326 , 1983.
- ¹¹⁷ D. T. Cassidy, "Technique for measurement of the gain spectra of semiconductor diode lasers", *J. Appl. Phys.*, Vol. 56, pp. 3096, 1984.
- ¹¹⁸ H. Wang, D.T. Cassidy, "Gain measurements of Fabry-Perot semiconductor lasers using a nonlinear least-squares fitting method.", *IEEE J. Quantum Electron.*, Vol. 41, pp. 532-540, 2005.
- ¹¹⁹ B. W. Hakki and T.L. Paoli, "Gain spectra in GaAs double-heterostructure injection lasers", *J. Appl. Phys.*, Vol. 46, pp. 1299-1302, 1975.
- ¹²⁰ P. Brosseau, "Analytical model of a semiconductor optical amplifier," *J. Lightwave Tech.*, vol. 12, no. 1, pp. 49–54, 1994
- ¹²¹ Niloy. K. Kutta and Qiang wang "Semiconductor Optical amplifiers" World Scientific Publishing, 1st Edition, 2006
- ¹²² D. M. Baney, P. Gallion, and R. S. Tucker, "Theory and measurement techniques for the noise figure in optical amplifiers," *Optical Fiber Technology*, 6, 122-154 (2000).
- ¹²³ A. W. Fang, H. Park, O. Cohen, R. Jones, M. J. Paniccia, and J. E. Bowers, "Electrically pumped hybrid AlGaInAs-silicon evanescent laser," *Opt. Express* **14**, 9203-9210 (2006).
- ¹²⁴ A. W. Fang, E. Lively, Y-H Kuo, D. Liang, and J. E. Bowers, "A distributed feedback silicon evanescent laser," *Opt. Express* **16**, 4413-4419 (2008).
- ¹²⁵ Y-L. Cao, X-N. Hu, X-S. Luo, J-F Song, Y. Cheng, C-M. Li, C-Y. Liu, H. Wang, L. Tsung-Yang, G-Q. Lo , and Q. Wang "Hybrid III-V/silicon laser with laterally coupled Bragg grating" *Opt. Express* **23**, 8809-8817 (2015).